FRACTURING AND SEALING IN GEOTHERMAL SYSTEMS

by

MICHAEL LEE BATZLE

B.S. Degrees in Geology and Geophysics
University of California at Riverside
(1973)

SUBMITTED IN PARTIAL FULFILLMENT
OF THE REQUIREMENTS FOR
DEGREE OF

DOCTOR OF PHILOSOPHY

at the

MASSACHUSETTS INSTITUTE OF TECHNOLOGY

Signature of Author..
Department of Earth and Planetary Sciences
20 March 1978

Certified by...
Thesis Supervisor

Accepted by..
Chairman, Departmental Committee on Graduate Students

Lindgren

WITHDRAWN

MAY 26 1978

FRACTURING AND SEALING IN GEOTHERMAL SYSTEMS

by

MICHAEL LEE BATZLE

Submitted to the Department of Earth and Planetary Sciences

on 20 March 1977 in partial fulfillment of the requirements

for the Degree of Doctor of Philosophy.

ABSTRACT

Repeated fracturing and fracture sealing were observed in core samples from six geothermal areas. Both fracture porosity and morphology vary widely. The minerals that seal fractures show significant temporal variations. Water-rock reactions and alteration often produce low density or hydrous phases that further seal and block cracks. Such parameters as hydraulic permeability and electrical conductivity that influence the geologic environment or serve as geothermal indicators are dependent on the fracture state of the rock. Cementation and sealing can lower permeability and conductivity by several orders of magnitude. Even a small value of crack porosity can significantly reverse this sealing effect. Conductivity is dependent also on the alteration and fluid characteristics and may not accurately indicate other rock properties. Fractures may serve as the only conduits for geothermal fluids. Sealed fractures and veins, however, may be effective barriers to further fluid migration. Sealed fractures are often the boundaries between regions of significantly differing physical properties.

Fracturing and sealing processes have both a cause and effect relationship with the geologic environment. The effect of the environment is to modify or seal fractures or cause alteration reactions along fracture walls. Induration and sealing harden rocks and make them more susceptible to brittle fracturing. Fracturing, on the other hand, can strongly influence such physical parameters as porosity and permeability. Cracks provide surfaces for water-rock reactions. Thus, the flow and chemical characteristics of hydrothermal fluids are strongly influenced by the same cracks and pores that these fluids will alter or modify.

Name and Title of Thesis Supervisor: Gene Simmons
                                       Professor of Geophysics

ACKNOWLEDGEMENTS

Numerous people and organizations were involved in supplying the samples and information that made this investigation possible. The thesis supervisor, Gene Simmons, was instrumental with financial and other support, including an indepth reading of this entire thesis. Professor T.R. Madden spent many hours discussing the geometric mean technique and the modeling results. Professor H. Einstein made several useful suggestions for clarification of portions of this thesis. Steven Shirey contributed several SEM micrographs and mineral analyses. Herman Cooper, Mike Feves, and Robert Siegfried of (or formerly of) M.I.T. provided assistance in collecting and reducing some of the strain data. W.A. Elders of the University of California at Riverside provided much information and insight into the problem as well as the Dunes samples. A. Timur of the Chevron Oil Field Research Company assisted in obtaining the Heber samples. Lloyd Mann of Chevron Resources Corporation described several aspects of the Heber system. H. Covington of the U.S. Geological Survey and R. Stoker and D. Goldman at the Idaho National Engineering Laboratory assisted in the acquisition of the Raft River specimens. David Blackwell of Southern Methodist University made the Marysville core samples available. Jim Bruce of Battelle Pacific Northwest Laboratories allowed many Coso samples and much well data to be appropriated. Jimmy Combs of GeoThermal Services, Inc. provided several core samples from shallow heat flow holes in the Coso region. C. Austin of the Naval Weapons Center and J. Hyde of the University of Utah both contributed significant information about the Coso area. The Phillips Petroleum Company, through G. Crosby, provided the Roosevelt Hot Springs

cores. Alfred Wendelin Chock, Jr. did most of the final drafting.
Financial support for this investigation was provided by a Penrose
Grant from the Geological Society of America and by NSF-RANN grant
AER75-09588.

I owe a very special debt of gratitude to Ann Harlow whose service as editor, collator, and typist went far beyond the call of duty ('What? Type another change in the figure caption?!').

TABLE OF CONTENTS

LIST OF FIGURES

Page

LIST OF TABLES

CHAPTER I

BACKGROUND

Introduction

Geothermal systems have been the object of considerable attention recently because of their potential use for energy production. The systems are dynamic and involve the interplay among rocks, fluids, and the local structural framework. As the result of numerous investigations, the basic nature of the generalized system has been determined to a great extent. However, the details of rock-water interaction, the importance of local geologic structures, and the effect on and of physical properties are still largely unknown. Fluid circulates in broad and complex convection cells. Water and rock properties change continuously in response to the variations in the physical environment. Circulation paths commonly occur along fault and fracture zones. Many episodes of fracturing and sealing by mineral precipitation and alteration are typical. A 'cap' or impermeable zone of sealed rock forms in many areas. The availability of economic near-surface hot fluids is often dependent on the stage of development of the system. The geothermal industry is in its infancy and techniques are still evolving. Usually exploration and drilling are done only where surface manifestations indicate anomalously high temperatures at depth. An improved understanding of the interactions within geothermal systems would lead to more effective exploration and evaluation in known geothermal areas and would permit exploration to be extended to areas lacking surface manifestations.

The purpose of this investigation is to examine geothermal systems,

the physical processes involved, and the variation of physical proper-
ties with time. In this study, we examine fracturing and sealing pro-
cesses and attempt to determine their significance. Fluid circulation
is greatly dependent on paths provided by fractures. Fractures, in
turn, are modified by alteration and mineral precipitation from the
contained fluids. The microfracture content of a sample matrix con-
trols to a large extent its resistivity and hydraulic permeability.
The variations of these properties with time can be estimated qualita-
tively from the morphologic changes of fractures with time which can be
observed with the optical and scanning electron microscopes. The results
have significant implications for surface geophysical measurements. The
examination of textures and physical properties can indicate if hot
fluids have been actively circulating in the sample and, therefore, may
be circulating presently in open, active fracture systems nearby.

This investigation is not primarily to determine the exact chemical
or mineralogical interactions or responses involved in geothermal sys-
tems. Temperature-pressure-mineral relationships are not the topic of
this study. Hence, detailed petrographic and mineral descriptions are
not presented. The mineralogy is examined in detail only where immedi-
ately pertinent to the physical characteristics and properties of the
sample. Most observations concern texture and surface morphology for
the determination of spatial and temporal relationships. Phase identi-
fications and analysis are used primarily to indicate fluctuations in the
geologic environment.

This thesis is structured to present a unified, integrated summary
of the investigation. Since the samples collected form an incomplete

set for any one area, the results will not be presented on an area by
area basis. Rather, a generalized view of geothermal systems will be
developed based on data from all the sampled localities. In a sense,
a 'typical' geothermal system will be constructed using parts from each
individual system. Within this framework, individual areas can be
compared and contrasted.

Definitions

Many terms in the literature pertaining to geothermal research have
very broad or ambiguous usage. Several important and frequently used
terms are defined below in order to restrict their meaning to the defini-
tions intended in this paper.

Geothermal area: A region of unusually high heat flow or thermal gradi-
ent resulting from high temperature hydrothermal convection or flow.

Geothermal system: The physical and chemical components of a geothermal
area. A geothermal system includes rocks, fluids, and thermodynamic
properties.

Geothermal fluid: Natural steam and hot water and any dissolved solids.
Geothermal fluid and hydrothermal fluid are considered synonymous
terms in this thesis.

Chemical and geochemical environment: The thermodynamic conditions and
active components of a system.

Physical environment: The physical properties and structural framework
not immediately involved in chemical reactions.

Aspect ratio (α): The ratio of the short dimension (width) to the long
dimension (length) of a void.

Fracture or crack: Breakage or separation of a formerly continuous

solid. Fractures have small (<<1) aspect ratios.

Pores: Approximately equant voids (α~1).

Healed fractures: Where a broken crystal lattice has reformed across

a fracture.

Sealed fractures or veins: Those fractures filled with precipitated or

alteration materials.

Fracture porosity: The volume fraction of open fractures determined

through stress-strain relationships.

Interconnected porosity: The volume fraction of connected voids deter-

mined by immersion techniques.

Total porosity: The total volume fraction of all void spaces including

all interconnected and isolated pores and fractures.

Samples

Almost ninety samples were obtained for this study from six dif-
ferent geothermal areas in the western United States (figure 1-1). The
suite of samples is excellent for examining many of the characteristic
properties and effects of geothermal systems. All specimens are portions
of well cores obtained during exploratory drilling. These cores range
in size from five to fifteen centimeters in diameter but several samples
are broken fragments retrieved from within a depth interval. Large vari-
ations in characteristics are expected both within single systems and
among the several sampled systems. The specimens are neither physically
unmodified nor representative of the entire geothermal system or strati-
graphy of any one region. Samples were chosen specifically for visible
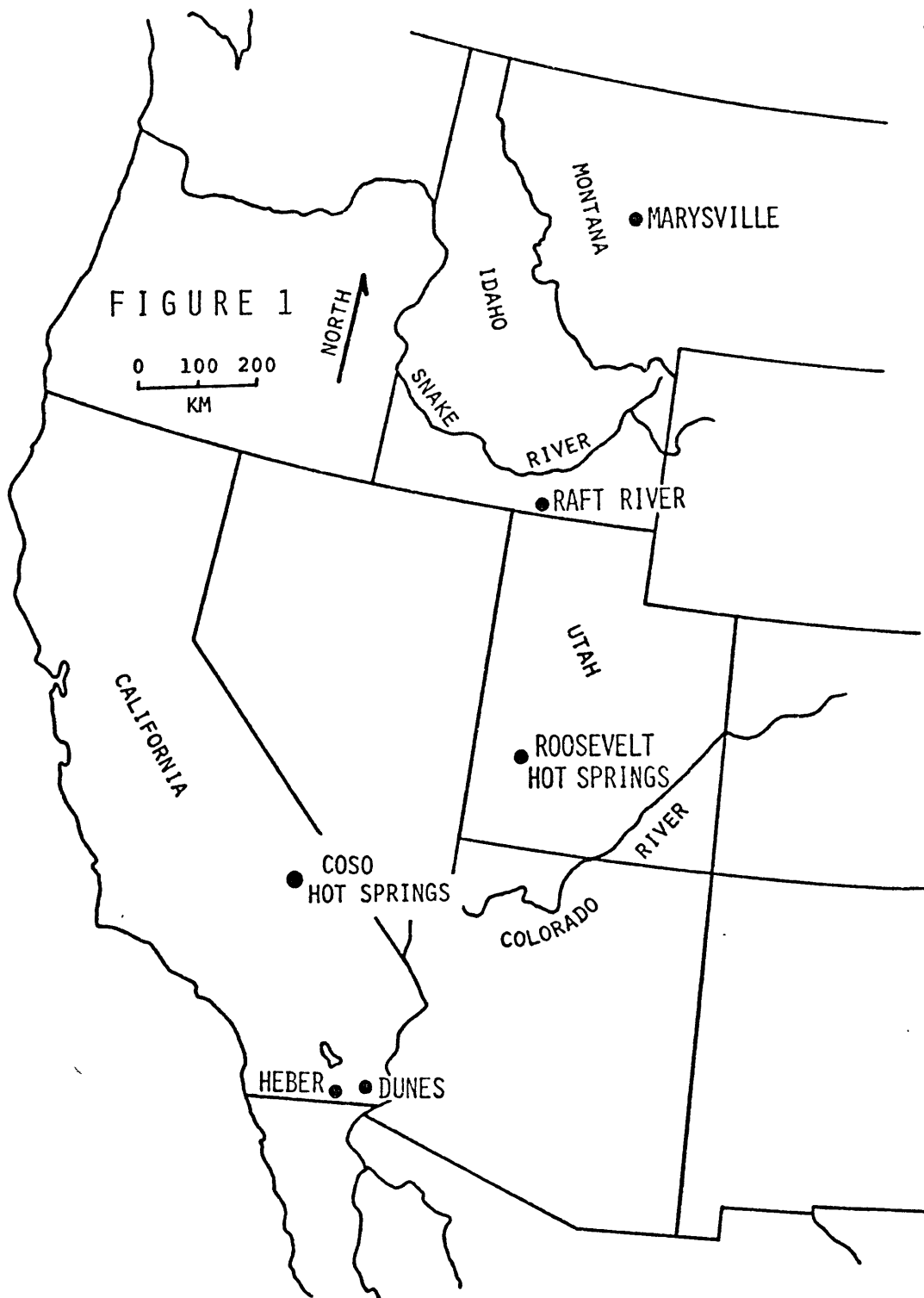
Figure 1-1. Index map of sampled localities.

fracture and vein content. Weak and friable samples were usually avoided due to preparatory or transportation problems. Because sample selection often involved considerable inconvenience to other agency and corporate personnel, preliminary examination and selection were often cursory and incomplete. Each sample is described briefly in the first appendix and the in situ settings are shown graphically in the geologic sections presented in Chapter II. Otherwise, detailed sample descriptions are not given.

Even under ideal conditions, the sampling process itself has a considerable affect on the properties of the sample. Friable and incoherent samples are difficult to core and retrieve intact. The open and continuous fractures which are extremely important to circulation are also not sampled intact by drilling. Pressure, temperature, and saturation conditions change drastically during sampling. Temperatures may drop more than 100°C. Pressure drops abruptly as samples are removed and brought to the surface. Fracturing may occur as a result of the strain release and differential mineral expansion (for example, at Marysville distinct 'popping' noises were heard as cores were uncased after core retrieval). Fluids originally in rocks are replaced during drilling and sample preparation. Although saturation has little effect on textural observation and fracture content, extrapolation of laboratory measurements to in situ conditions is difficult. Hence, the sample suite has gone through several stages of mechanical as well as conscious biasing.

The Geothermal System

This final section will introduce a basic conceptual model of a con-

vective geothermal system and outline the effects of fracturing and seal-
ing. The hypothetical sequence of events in the life cycle of a hydro-
thermal system will be presented. This sequence will then serve as a
framework for the following chapters, each concentrating on some specific
aspect of the cycle.

Detailed models of convective geothermal systems have been developed
both for specific sites as well as for systems in general (see, for
example, McNitt, 1973; White, 1968; White et al., 1971; White et al.,
1975; Elders and Bird, 1974; Muffler, 1976; Nathenson and Muffler, 1975;
Grindley and Browne, 1976; and Healy and Hochstein, 1973). A circulation
'cell' begins as cold dilute meteoric water descends either along fracture
zones or permeable rock units. This water is heated and the dissolved
solids become more concentrated. In some areas, connate water may be a
major source of the hydrothermal fluids. Fluid may then enter ascending
limbs of the cell, rise, and often mix with cool shallow ground water.
In some systems where temperatures are high enough and pressure and flow
rates are low enough, boiling may occur at depth to produce a vapor-
dominated zone (Renner et al., 1975; White et al., 1971). As the fluid
cools, chemically changes, or boils, it becomes supersaturated with dis-
solved solids and precipitates material interstitially and within frac-
tures. Rock-water reactions produce a host of alteration materials.
Precipitation and alteration then serve to 'self-seal' the system or
form impermeable 'cap rocks' (Facca and Tonani, 1967), entrapping the
hydrothermal fluids. This sealing process requires that the system be
fractured repeatedly to permit continued circulation.

Various heat sources have been postulated to drive convective sys-

tems. In some cases, such as Hawaii, Long Valley, Coso, and the Geysers in California, nearby young volcanics or shallow intrusives are obvious sources. The systems in the Salton Trough of California are undoubtedly the result of magmatic activity but the exact nature of the heat source or sources is unknown. For a system to be extensive enough and sufficiently hot to be economic places a restriction on the size and age of the magma body responsible. Modeling by many people, including Smith and Shaw (1975), Norton and Knight (1977), and Norton (1977) requires that these bodies be relatively young ($<10^6$ years) or very large ($>>10^3$ km^3). Some geothermal systems, such as the Raft River, Idaho and Marysville, Montana have no obvious igneous heat sources and deep and extensive ground water circulation has been postulated as a possible source. These systems would then be the result of the regional geothermal gradient which is abnormally high in many areas, such as the Basin and Range. Renner et al. (1975), however, do not believe that this type of deep circulatory source can support a sustained high temperature convective system.

Core samples for this investigation were obtained from wells drilled at the geothermal sites shown in figure 1-1. The individual systems are located in a wide variety of different geologic environments. Conditions range from a possibly vapor-dominated caldera structure at Coso to hot water systems circulating in alluvial sediments at Raft River, Dunes, and Heber; and circulating in fractured igneous rocks at Marysville. More detailed descriptions of each locality will be presented in Chapter II.

The basic components of a generalized hydrothermal system are shown

in figure 1-2. The model has been constructed to include numerous
features from each of the localities in figure 1-1. Figure 1-2 should
be considered a compilation of aspects of several systems and not cor-
responding to any one in particular. The figure is based on both exam-
ination of the obtained samples as well as on the material published
on each area. Meteoric water invades fractured crystalline rocks (1),
as is the case in Marysville, Roosevelt, and probably in the lower por-
tions of Raft River. Considerable fluid may also be derived from the
connate water in sediments. A heat source is shown (2) although in all
the studied areas the precise nature of this source is not known. After
heating and at least partial saturation with materials such as silica,
potassium, sodium, calcium, chlorine, etc., the fluid may then move
either laterally or vertically into other portions of the system. The
fluids will invade fracture zones and permeable units (3). Considerable
horizontal as well as vertical flow (4) can occur (Healy and Hochstein,
1973). Hot fluids will not uniformly enter permeable units and fracture
zones, resulting in stratified and alternating hot and cold water aqui-
fers. The thermal inversions encountered in many areas confirm this
stratification. Hot water may not reach the surface if circulation is
confined within lower units or if the pressure is insufficient to ele-
vate the thermal fluids. The circulation patterns can also be perturbed
significantly by local hydrologic conditions such as mixing with near-
surface ground water. As the hydrothermal fluids cool or chemistry
changes in response to pressure changes or water-rock reactions, materi-
als such as quartz, calcite, albite, adularia, etc. may be precipitated.
Fluid reactions with the surrounding rocks commonly form clays, zeolites,
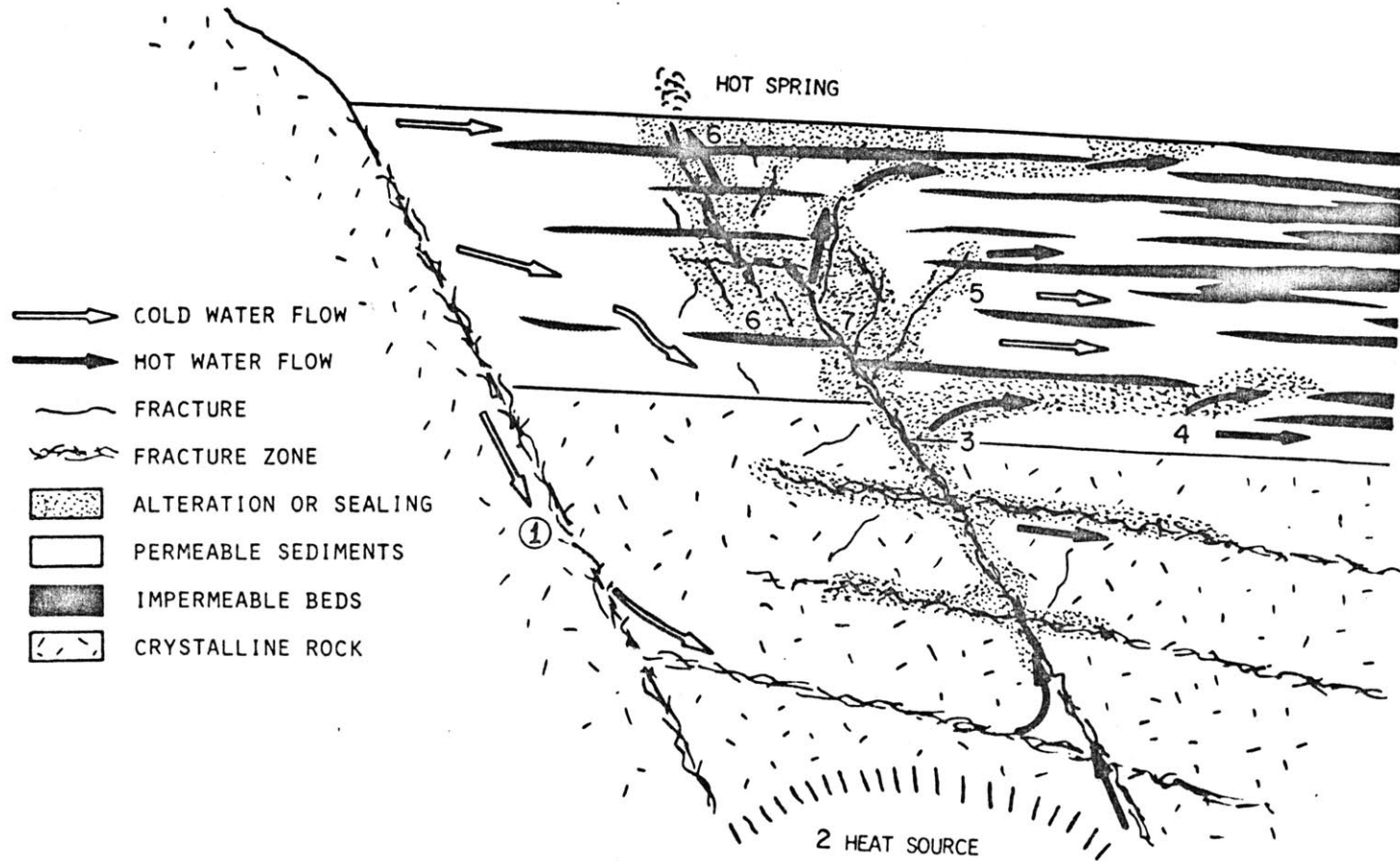
Figure 1-2. Generalized geothermal system. Numbers refer to processes discussed in text.

and other low density alteration materials. Both precipitation and al-
teration tend to seal the system (6). This sealing retards fluid move-
ment or may seal the system entirely unless fracturing and refracturing
occur to keep circulation paths open. Active systems are therefore
commonly confined to recently active fault zones and fractures (7).
Note that the fractures have both a cause and an effect relationship
with the system. The fractures are caused by faulting and local stresses
such as changes in pore pressure and are sealed and otherwise modified
by the environment. On the other hand, the fracture state of the rocks
controls many of the important physical properties, such as permeability,
which, in turn, strongly influence the geologic environment. The sealing
and resultant production of a 'cap rock' can be beneficial by confining
high temperature fluids to porous units that serve as reservoirs. The
highly variable flow patterns, the effects of local hydrology, and the
dependence on structure, particularly faults and fracture zones, must
be emphasized since all these factors interact to form extremely complex
systems rather than the simpified version of figure 1-2.

As mentioned previously, the cores obtained for this study vary
widely in the rock type and type of geologic environment they represent.
The locations of the samples in the generalized geothermal system are
shown schematically in figure 1-3. Samples from no single area span the
entire range of environments shown in figure 1-3. However, because of
the range of different rock types obtained, it is possible to fill gaps
that may occur in any one system. Samples are confined to the more
active areas of convection as this is the portion of the system that is
of economic value and therefore has been explored and drilled. Rocks
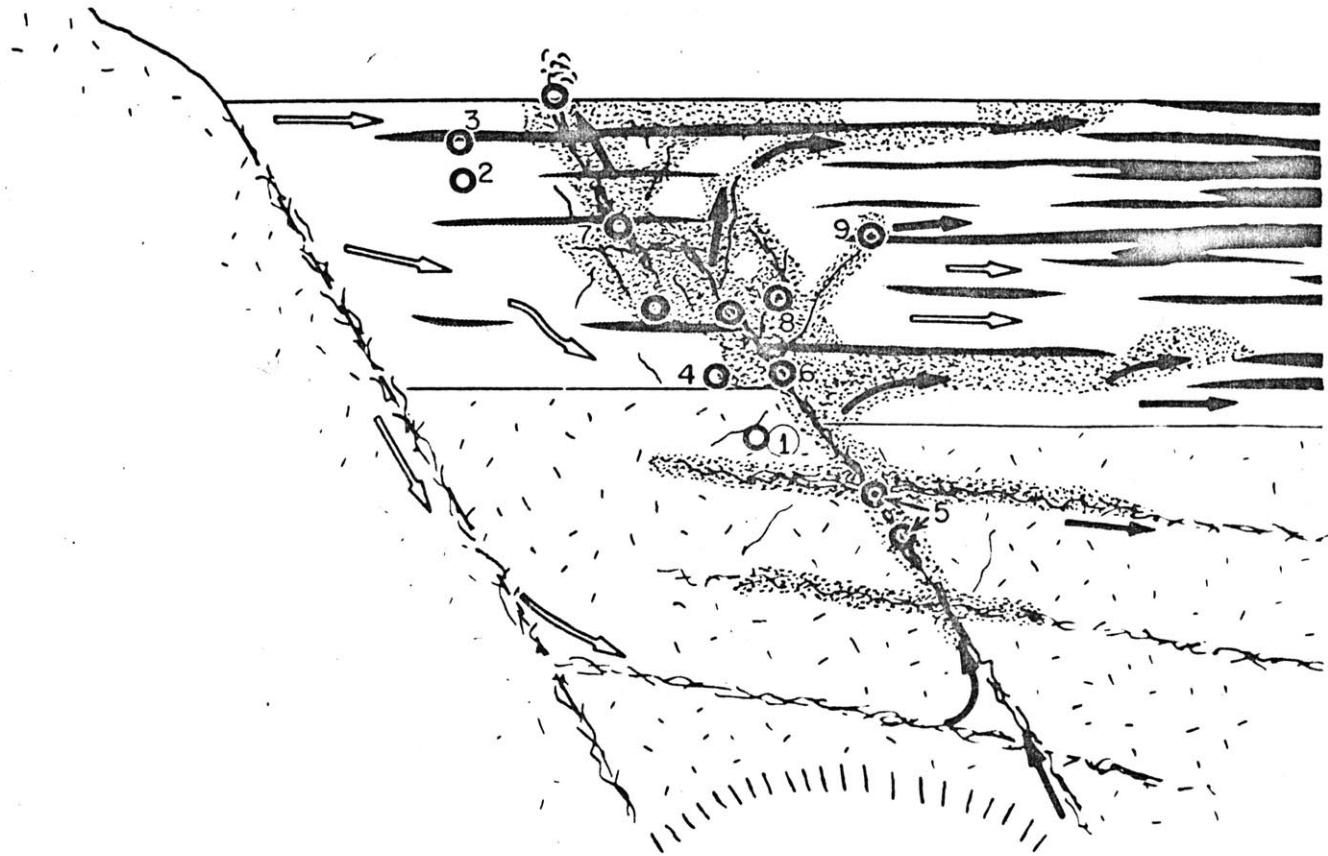
Figure 1-3. Deduced locations within the generalized geothermal system represented by the samples. Symbols are the same as in figure 1-2. Numbered circle locations are referred to in later chapters.

from recharge limbs of the hydrologic cycle would be little affected
and difficult to identify as parts of the system. In later chapters,
specimens will be described and the position that they are interpreted
to hold in figure 1-3 will often be pointed out and explained. The posi-
tions are obvious for some samples but in many instances, placement in
this generalized scheme is somewhat uncertain.

The data and observations from these several areas can be used to
produce a scheme describing the processes that can occur through time
within a geothermal system. Figure 1-4 is the resulting schematic 'flow
chart' for the generalized system. This figure represents the sequence
of events that often occur at single locations within the system. A
typical sample will be subjected to the processes and events as a func-
tion of time as indicated by the arrows of figure 1-4. The numerical
values on the chart are crude guides to the range and response of the
physical parameters to the various processes involved in the development
of a system. Any near-surface geologic environment can be a potential
site for the formation of a convective system. Sediments, if present,
are compacted and indurated. Igneous and metamorphic rocks reach steady-
state temperatures, fracture content, and porosity. These initial stages
of induration may be a direct result of the geothermal activity. The
introduction of hydrothermal fluids usually seals the rocks with preci-
pitated and alteration materials. Fracturing is necessary if the sealed
rocks are to be reopened to circulation. A new sequence of sealing and
alteration may occur, often confined to the region immediately adjacent
to the fractures. Thus, a cyclical behavior begins if the rocks are re-
fractured and reopened and subsequently invaded again by hydrothermal

PROCESS OR CONDITION	REMARKS	PHYSICAL PARAMETERS*			
		1	2	3	4

INITIAL GEOLOGIC SETTING
  Implacement (Igneous and
    Metamorphic)
	Geothermal sites occur in many
	different geologic settings
		.1 to .001	small	1 to 3	-5 to -10

Deposition (Sed) Sand		.3 to .05	small	1 to 2	-1 to -5
Clay		.3 to .05	small	0 to 2	-4 to -7
POSSIBLE FRACTURING			≤0.01	1 to 2	-2 to -5

LITHIFICATION AND INDURATION
  Cementation, Compaction
  Sealing
  Leaching (?)
	Usually results in hard, low
	porosity rocks susceptible to
	fracturing (lithification
	processes may not be related
	to geothermal processes)
		.1 to .01	~0	1 to 5	-4 to -9

FRACTURING	Macro- and microscopic breakage	.1 to .01	≤0.01	1 to 3	-2 to -4

FRACTURE REACTIONS
  Sealing.................
  Healing.................
  Alteration..............
 	
  Possible etching........
	Mineral precipitation
	Crystal reforming across frx
	Transformation to new (often
	low density) material
	Channeling
		.1 to .001	small	2 to 5	-3 to -9

SYSTEM SEALED		.1 to .01	~0	1 to 5	-4 to -9

*(1) Interconnected porosity; (2) Fracture porosity; (3) $\log_{10}$ formation factor; (4) $\log_{10}$ permeability (Darcys)

Figure 1-4. Schematic diagram of interpreted events at some single location within a geothermal system. General trend in occurrences indicated by arrows.

fluids. This requirement for episodic fracturing and sealing usually confines the regions of active circulation to fault zones capable of causing repeated fracturing (Elders, 1977; Elders and Bird, 1974; Grindley and Browne, 1976). Alternatively, sealing can block further fluid movement and a cap rock or impermeable boundary may form.

The chart of figure 1-4 will serve as the basic outline for the latter part of this thesis. Since figure 1-4 is based on the idealized processes occurring in a convecting hydrothermal system with time, chapters four through six will describe the events and processes roughly in a temporal framework. However, all the various processes may occur simultaneously at different locations within a single system. Figures 1-2, 1-3, and 1-4 are idealized and are not meant to represent any area in particular. Indeed, some systems (such as Heber) show wide variations on these generalized patterns. This thesis is intended to observe the processes involved in geothermal systems and to deduce the generalized fracturing and sealing behavior and not to describe any individual system.

CHAPTER II

SAMPLE LOCATION AND GEOLOGIC SETTING

Introduction

This chapter is to introduce and briefly describe each of the sampled areas. For each locality the general geology, the major structures, physical characteristics, and well stratigraphy are presented. The proposed geothermal systems for each region are discussed. The areas are presented in a rough progression from entirely sedimentary settings to igneous or metamorphic dominated settings. A casual examination of figures, particularly the well stratigraphy, will reveal the complex and varying fracture, alteration, and sealing interaction within each system. These local complexities should be kept in mind when the various processes are described in detail later.

Salton Trough Region

The Salton Trough* is a structural basin transected by the United States-Mexico border (see figures 1-1 and 2-1). The trough is approximately 200 kilometers long and up to 130 kilometers wide with an extensive portion of the valley floor below sea level. The region is a structural continuation of the Gulf of California. Several individual sites of high heat flow occur within the basin. Thermal manifestations in the form of hot springs and boiling mud pots occur at the Buttes-Salton site at the southern end of the Salton Sea and at Cerro Prieto in Mexico. The area has been explored for geothermal resources for more than a

―――――――――――――――――
*Also referred to as the Salton-Mexicali or Mexicali Trough.
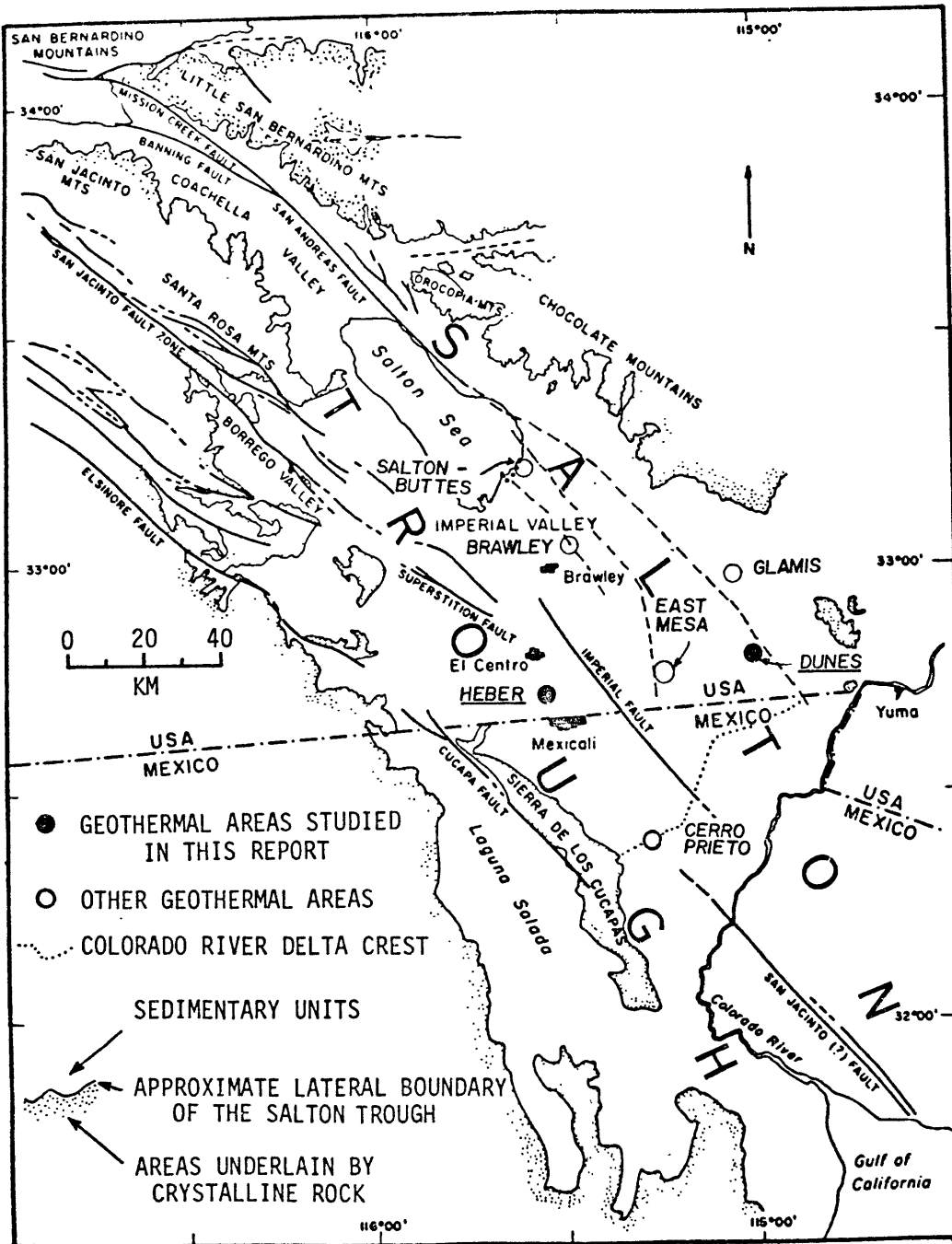
Figure 2-1. Geologic structures and geothermal areas of the Salton Trough (after Reed, 1972 and Biehler et al., 1964).

decade. Many test wells have been drilled at numerous recognized geothermal sites and several are shown in figure 2-1. A 75 MW generating plant is presently operating at Cerro Prieto.

The Salton Trough is filled with interbedded alluvial gravels and sands, eolian silts and sands, and lucustrine silts and clays. The sedimentary rocks comprised of this fill are complexly intertongued and have rapid lateral facies changes. The trough began opening in the Miocene (Hamilton, 1961) and was filled with alternating continental and marine deposits until mid-Pliocene when the growing Colorado River delta isolated the Salton Basin from the Gulf of California. The sedimentation has been exclusively continental since the mid-Pliocene (Van de Kamp, 1973). The maximum thickness of the valley fill is six kilometers with the thicker portions located near the southern end of the Salton Sea (Biehler et al., 1964). The sediments are at various stages of diagenesis and alteration. Low-grade metamorphism of greenschist facies grade is occurring at depths of only a few kilometers in the Buttes-Salton area (Helgeson, 1968; Muffler and White, 1969; Elders et al., 1972; Kendall, 1976). Cementation and low-grade metamorphism may be occurring at shallow depths at many of the geothermal sites in the region. Most of the valley fill is a mixture of deltaic and lucustrine deposits derived from the Colorado River. However, in the northern portion of the basin and around its margins, alluvial sediments derived from the local mountains frequently predominate (Van de Kamp, 1973). The fraction of mud and fine material in the sedimentary section increases away from the crest of the Colorado River delta toward the northwest (Randall, 1971). Several stages of lake filling

and evaporation occurred in the basin as the Colorado River shifted drainage between the Salton Trough and the Gulf of California. The occurrence of small settling ponds and deltas, beach features, reworking of sediments, channeling, cut and fill, etc. serve to make much of the stratigraphy complex on a fine scale. Because of the basin rifting, Miocene sediments are confined mostly to periphery of the basin with younger, thicker units occupying the center.

The structure of the Salton Trough is a result of complex interaction between faulting and rifting. Several major transform faults transect the region including the southern extension of the San Andreas fault system (see figure 2-1). Many of the faults are presently active and numerous large earthquakes have occurred in historic times. A magnitude 7.1 earthquake in 1940 along the Imperial Fault caused offsets of more than four meters. Many faults have been detected geophysically, have significantly offset subsurface units, and have disrupted ground water flow (Meidav and Furgerson, 1971; Rex, 1971; Combs and Hadley, 1977). The trough may be a region of incipient rifting and crustal spreading (Elders et al., 1972; Garfunkel, 1971, 1972). The trough was created when the North American Plate overrode the East Pacific Rise. Elders et al. (1972) postulated the sequence of events during rifting shown in figure 2-2. Segments of the ridge crest are offset in an en echelon pattern by northwest trending transform faults. Both tensional and compressional features are developed within the trough as a result of the interaction between the faulting and rifting (Garfunkel, 1971, 1972). Gravity data have been interpreted by Biehler et al. (1964) and Elders et al. (1972) to indicate crustal thinning under the

HEATING

UPLIFT AND
EXTENSION

SEDIMENTS

RISING GEOTHERMS

METAMORPHISM

BASALT MAGMA RISING

RHYOLITE MAGMATISM

BASALT
MAGMA

700°C
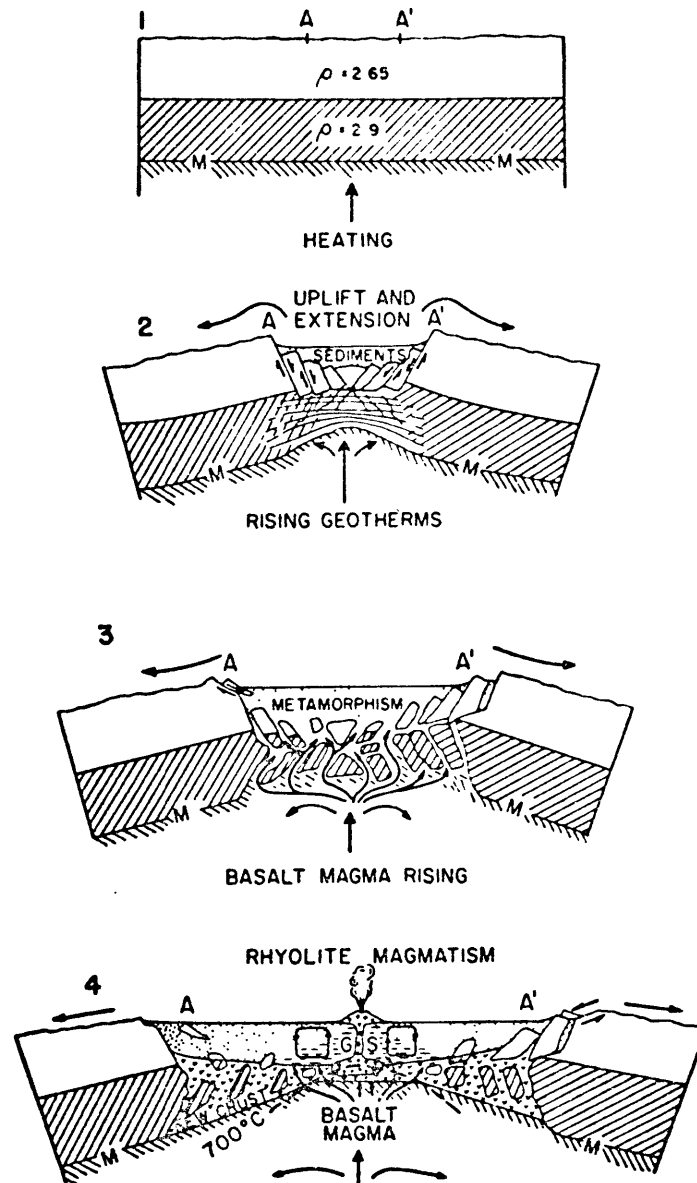
Figure 2-2. Sequential stages in the model of Elders et al. (1972) of rifting and growth of the Salton Trough. M, Moho; A, A', reference points for movement; GS, greenschist metamorphism caused by convecting hydrothermal fluids.

trough with implacement of basaltic magma at depth. Holocene volcanism occurred near the Buttes-Salton and Cerro Prieto areas, and a diabase dike was intruded at a depth of 1335 meters in the Heber area (Browne and Elders, 1976). The spreading mechanism is responsible for the high heat flow and the trough itself by the formation of 'rhombochasms' (Elders et al., 1972) along ridge crests. Mudie (1975) believes, however, that this rifting model is based too strongly on ocean ridge spreading. The Salton Trough is clearly tectonically active and dynamic.

The geothermal areas within the trough involve fluid circulation either in broad convective cells or channelled along faults and fracture zones. The original source of most of the ground water in the valley is the Colorado River although, to the north, around the Buttes-Salton area, and along the margins of the valley, water from local precipitation may predominate (Coplen, 1972; Rex, 1971). In general, ground water in the northern portion of the trough flows from the crest of the Colorado River delta toward the Salton Sea. There exists a significant salt concentration gradient along the axis of the valley. Ground water increases in salt content from about a thousand parts per million (ppm) near the delta crest to approximately 20 to 30 weight percent dissolved solids in the deeper portions of the Buttes-Salton area (Meidav and Furgerson, 1971; Furgerson, 1972). The ground water flow is inter-rupted by the several fault zones in the valley. At geothermal sites the deep ground water is heated and convects upward. In such areas as Buttes-Salton and Heber where permeable sediments are extensive or interconnected well enough by interbedding or fracturing, broad convection cells form (Randall, 1971; Helgeson, 1968; Kendall, 1976; Lloyd

Mann, personal communication, 1977). At other locations, such as Dunes,
East Mesa, and Cerro Prieto, impermeable cemented zones or shale layers
restrict significant fluid flow to fracture and fault zones. Hot
fluids invade the more permeable sand units encountered (Mercado, 1969;
Combs, 1972; Reed, 1972; Biehler, 1971). The hydrothermal systems in
the Salton Trough are self-sealing. Geothermal systems with no surface
expression can be recognized by the gravity and seismic anomalies asso-
ciated with the 'silicified cap rocks' developed by precipitated minerals.
The local heat sources and the details of the hydrology of most of the
hydrothermal systems in the valley are not known.

Dunes Area

The Dunes geothermal area is located approximately 38 kilometers
east of Holtville on the eastern side of the Imperial Valley (see
figures 1-1 and 2-1). The geothermal potential was indicated by high
heat flow (25 HFU), a positive gravity anomaly (2 mgal), and low resis-
tivity (2 Ωm) (Combs, 1971; Biehler, 1971; Combs, 1972; Black et al.,
1973). Several shallow holes were drilled in the early 1970's followed
by a 612 meter well drilled by the California Department of Water
Resources (DWR#1) in 1972. Ninety-six meters of core were recovered.
This well penetrated deltaic sand, channel fill, braided stream, dune,
and lacustrine facies sediments (Bird, 1975). The sediments have been
altered hydrothermally at seven distinct intervals of originally high
permeability. Alteration and precipitated minerals include quartz, adu-
laria, pyrite, and hydromuscovite. The well stratigraphy is presented
in figure 2-3. Ten core samples were chosen for this study that were

(1452)
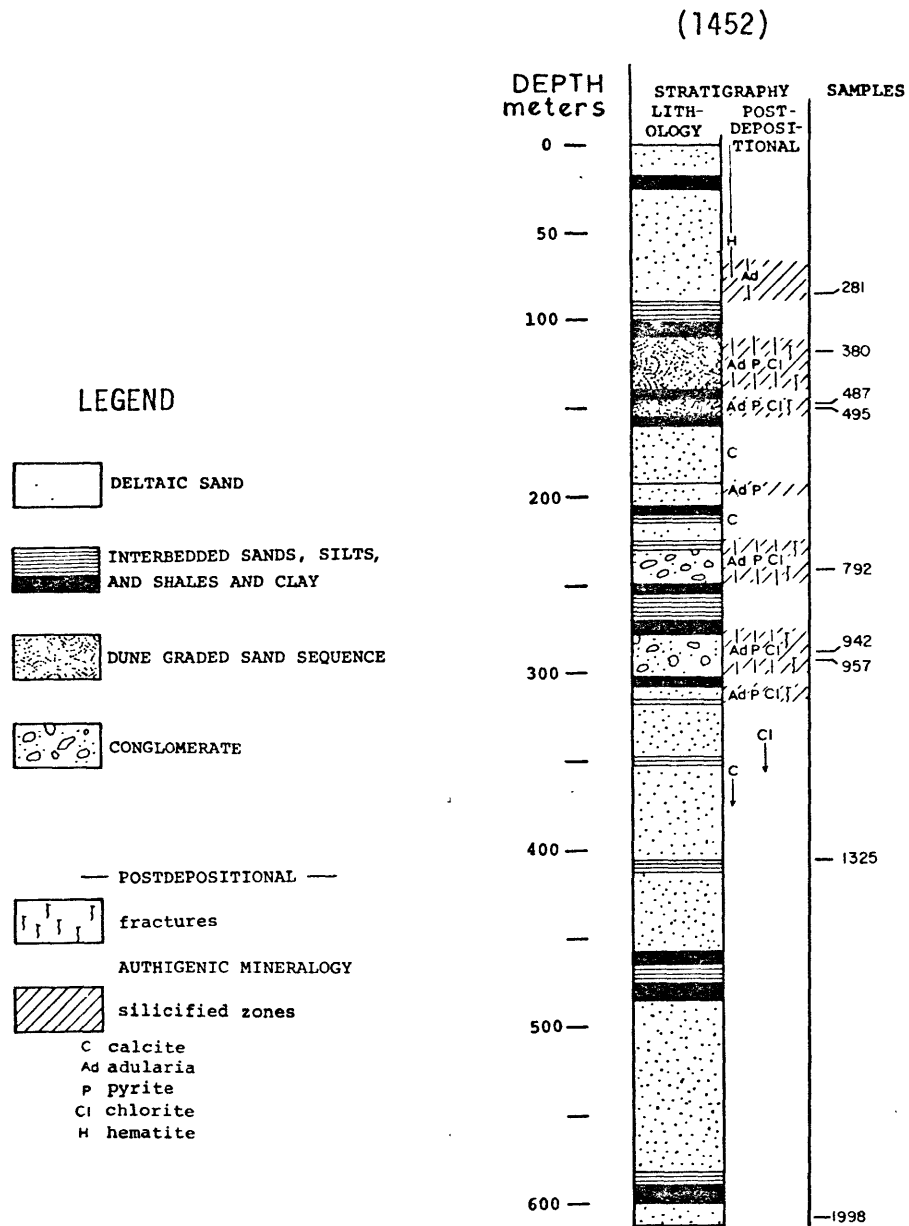
Figure 2-3. Dunes well stratigraphy modified from Elders and Bird (1974). Sample identification numbers (depth in feet) and positions are shown in the column furthest to the right.

either macroscopically fractured or representative of the local strati-
graphy.

High temperature fluids rise along fracture and fault zones to in-
vade several of the shallow permeable sand units. These rocks in the
Dunes site have been subjected to episodic fracturing and sealing (Elders
and Bird, 1974; Bird, 1975). Fracturing and geothermal fluid movement
are probably partially controlled by the San Andreas Fault which is
located only one-half kilometer to the east (Combs, 1971; Biehler, 1971;
Wilt, 1975). The temperature profile is complex and consists of five
temperature reversals with a maximum of 104°C reached at 280 meters
(see figure 2-4). The detailed temperature fluctuations are the result
of hot fluids flowing in various stratified permeable units and inter-
acting with shallow ground water flow. Temperature distributions in
shallow wells indicate that the hydrothermal system is disturbed by
ground water flow toward the northwest, away from the crest of the
Colorado River delta (Combs, 1972). Four liters per second of hot fluid
flowed from DWR#1 from the interval between 572 and 585 meters. Fluids
contained less than 4000 ppm total dissolved solids (Bird, 1975). Ten
core samples were chosen for this study (figure 2-3) on the basis of
either high visible fracture content or as representative of the geologic
section.

Heber Area

The Heber geothermal field is located in the central portion of
the Salton Trough midway between El Centro and Mexicali (figures 1-1
and 2-1). In 1945, Amerada Oil Company drilled an oil test well (Tim-
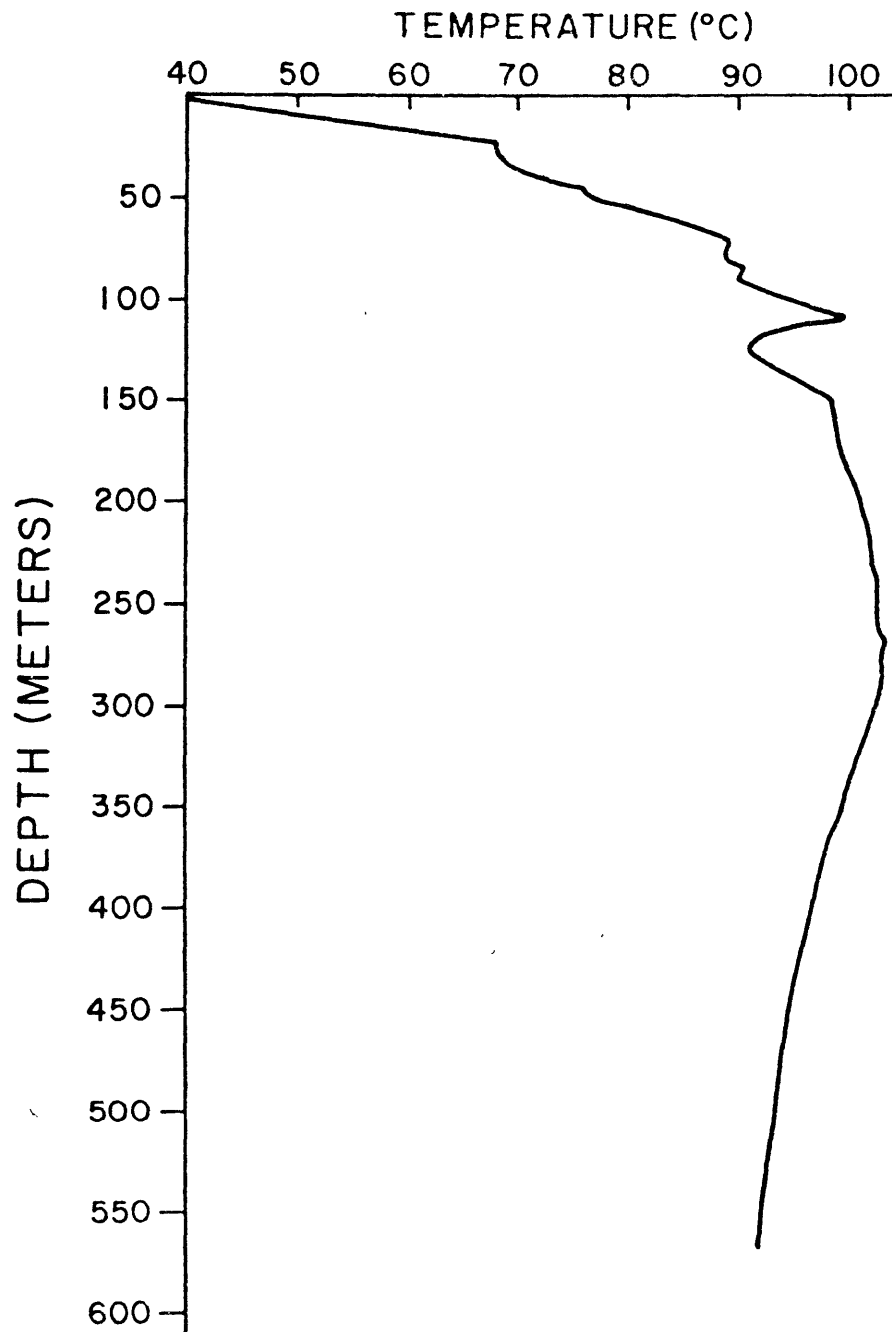
Figure 2-4. Dunes well temperature profile (from Elders and Bird, 1974).

kin #1) in the area which encountered abnormally high temperatures (Palmer et al., 1975). In the early 1960's, Chevron Oil Company confirmed the geothermal potential of the area with a series of shallow test holes. The Heber site is characterized on the surface by a positive gravity anomaly of 2 milligals, steep temperature gradients in excess of 180°C per kilometer, and a resistivity low of approximately one ohm-meter (Biehler, 1971; Combs, 1971; Furgerson, 1972). Several wells have been drilled in the area, including the Geothermal Wells (GTW) numbers one and three used in this study. The locations of several of the wells are shown in figure 2-5.

Sandstones, siltstones, and claystones compose the bulk of the strata at the Heber area. The upper thousand meters of the section are predominantly clays and shales which grade at depth into more sandy and hence more permeable units (Lambert, 1976). In the lower portions of the section, permeable horizons and lenses are apparently interconnected sufficiently to allow free circulation of hot water. Fractures are not needed to provide circulation links (Lloyd Mann, personal communication, 1977). The production temperature is approximately 185°C and the fluid is not extremely concentrated in dissolved solids (1.5 wt.%). The 'self-sealing' or mineralization process does not dominate in this area. Hydrothermal minerals have been encountered at depth and include chlorite, albite, calcite, epidote, and wairakite (Browne and Elders, 1976). A diabase dike was encountered in the Holtz #1 well between 1335 and 1366 meters and could be related to the heat source for the site. Data on fluid inclusions were interpreted by Browne and Elders (1976) to indicate that two thermal events had occurred at approximately 212°C and
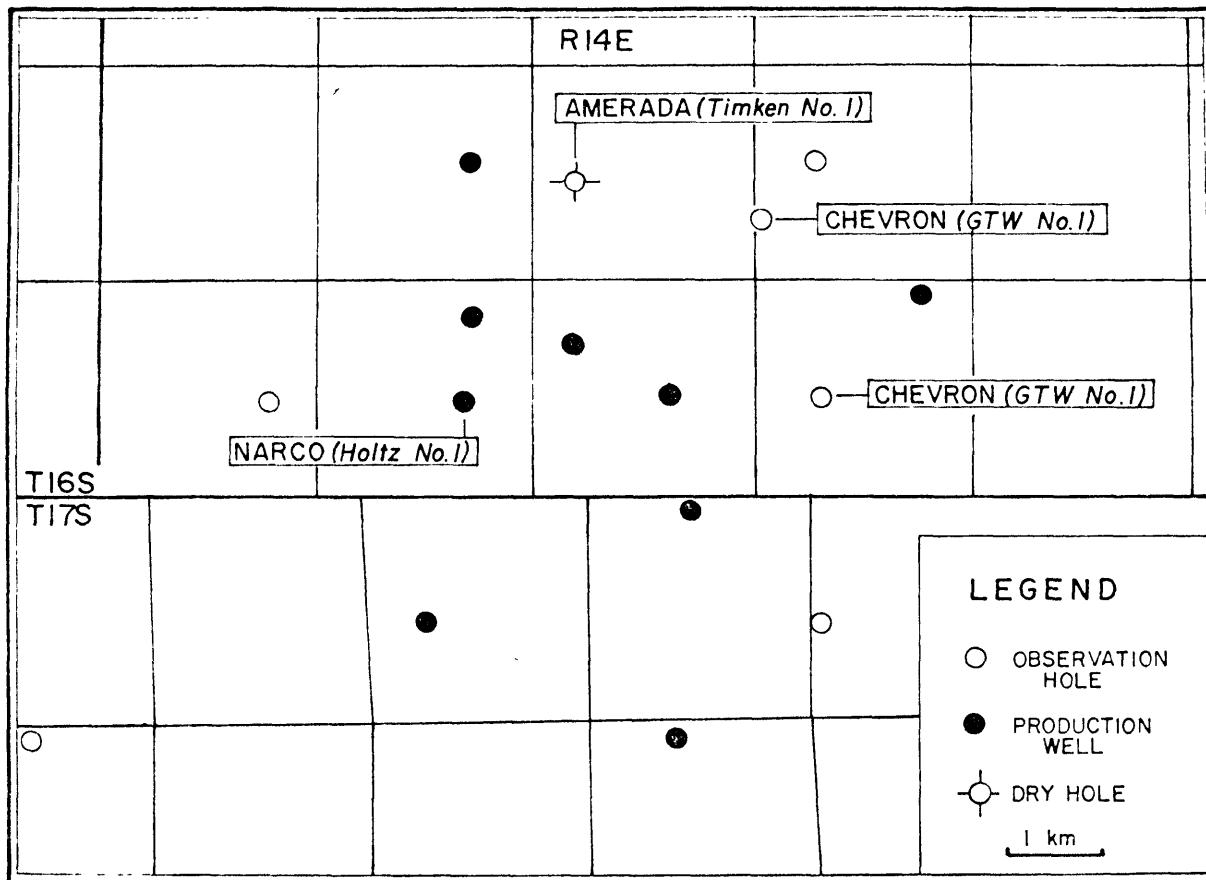
Figure 2-5. Well locations for the Heber geothermal area. The named wells are referred to in the text (from Lloyd Mann, personal communication, 1977).

235°C. Most data for the area are proprietary and therefore unavailable for this study. However, well logs from the Amerada test hole were used by Randall (1971) to determine the downhole stratigraphy. His interpretation of the sand versus clay content is shown in figure 2-6 along with the equivalent sample locations from wells GTW#s 1 and 3. Ten samples from these two wells were obtained from Chevron Oil Company. Samples were chosen for megascopic fracture and vein content and are predominantly shales and argillaceous siltstones. The samples occur in a very narrow depth range and are restricted in the types of geologic environment they represent.

Raft River Area

The Raft River geothermal area is south of the Snake River Plain in southern Idaho approximately nine kilometers north of the Idaho-Utah border (see figure 1-1). The area is in the Basin and Range physiographic province. The geothermal site is located on the western flank of the lower Raft River Valley. Natural evidence of hydrothermal activity consists only of (1) a warm seep (38°C) located in 'The Narrows' near INT#4 (see figure 2-7), (2) the altered alluvium around a former hot spring located on the Bridge Fault about one kilometer northwest of RRGE#1, and (3) minor green and yellow montmorillonitic alteration of volcanic rocks exposed in 'The Narrows'. Many of the shallow irrigation wells in the valley produce hot water and two such wells produce boiling water. Silica and Na-K-Ca fluid geothermometry applied to the well waters indicate a reservoir temperature of 150°C (Kunze et al., 1976; Williams et al., 1976). The U.S. Geological Survey initiated

AMERICAN PETROLEUM CORP.
TIMKIN WELL#1
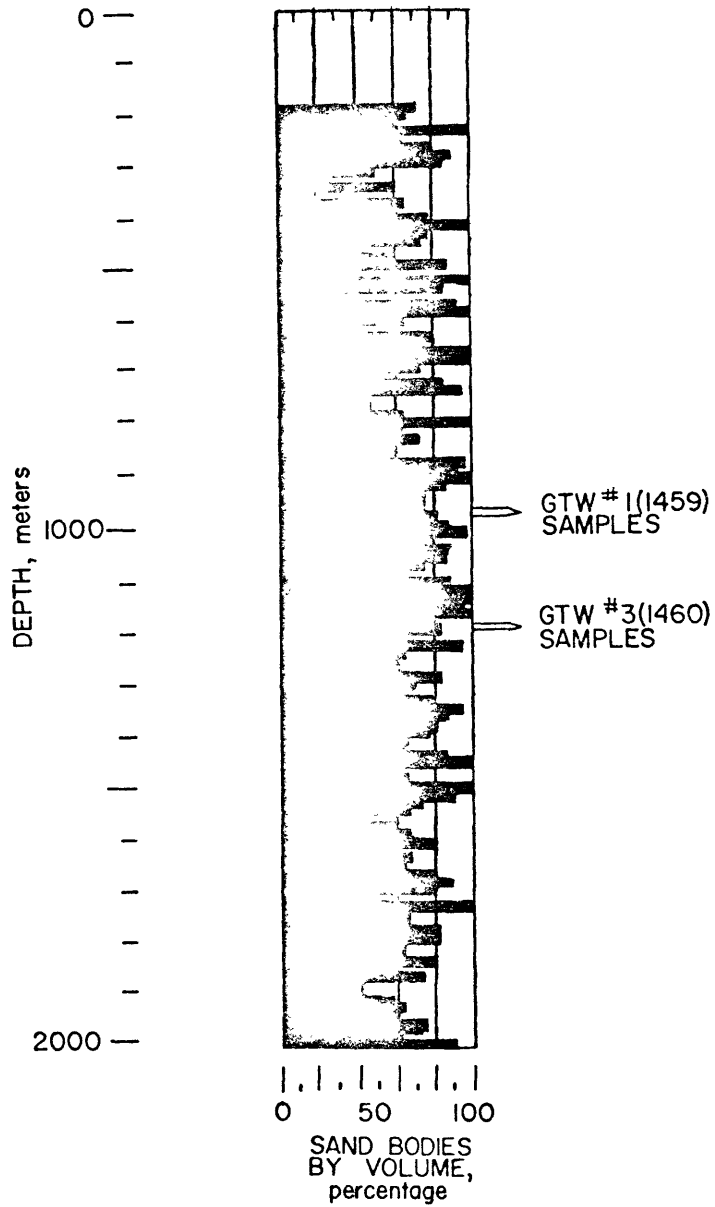
Figure 2-6. Sand versus clay content for the Timkin Well #1 as inter-
preted from well logs by Randall (1971). All of the samples from the
other Heber wells occur within the limits indicated by the small
brackets to the right.
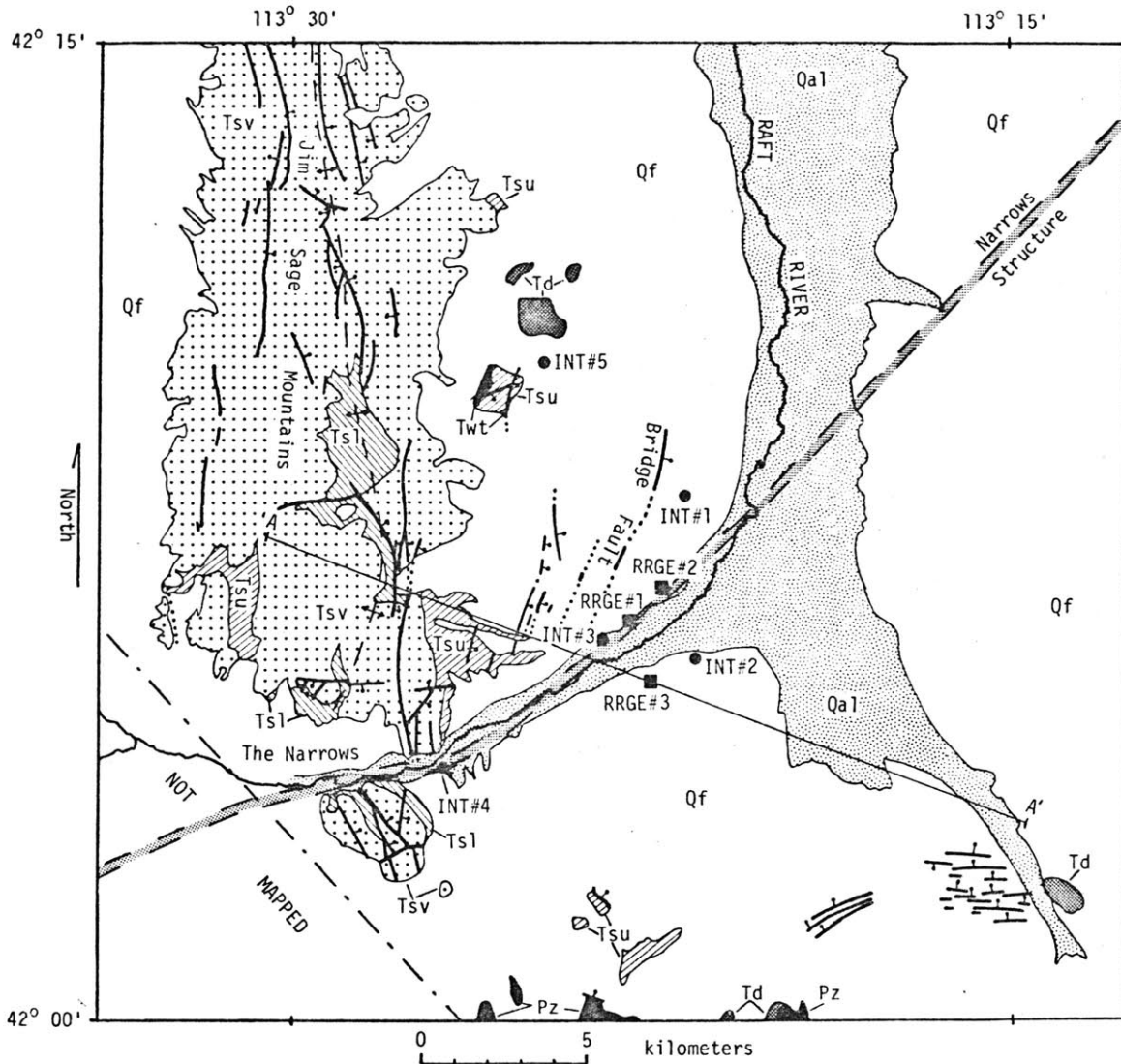
Figure 2-7. Geology, structure, and well locations for the Raft River area (adapted from Williams et al., 1974 and Williams et al., 1976).

A cross-section labeled A to A' showing the geologic structure from Jim Sage Mts through the Raft River Valley, with wells RRGE #1, RRGE #3, INT #3, Bridge Offset, and Bridge Fault, Narrows Structure, and formations Tsv, Tsl, Tsu, Qf, Qal, Raft Fm, Ts, Twt, Adamellite, Paleozoic and Precambrian rocks. Elevation scale from 2500 to 500 feet and Sea Level.

LEGEND

Qal	Alluvium and silt	SURFICIAL DEPOSITS	QUATERNARY
Qf	Fan gravels		
Td	VOLCANIC DOME		
Twt	WELDED TUFF		
Tsu	Upper member		TERTIARY
Tsv	Volcanic members	SALT LAKE FORMATION (Ts)	
Tsl	Lower member		

UNCONFORMITY

Pm	PALEOZOIC ROCKS	PALEOZOIC

- MAP SYMBOLS -

—— CONTACT

——⊥·· FAULT Bar and ball on downthrown side.
              Dotted where concealed.

NARROWS STRUCTURE

ANTICLINAL TREND

WELLS

■ Raft River Geothermal Exploration (RRGE)
● Intermediate depth well (INT)

Figure 2-7 (continued).

preliminary geologic investigations in the area in 1970 and in 1974 and early 1975 five intermediate depth test wells (INT#s 1 to 5) were drilled to depths from 76 to 434 meters (Williams et al., 1976). The deepest well, INT#3, encountered water at 97°C near the bottom. The Energy Research and Development Administration had three deep exploration wells (RRGE#s 1, 2, and 3) drilled during 1975 and 1976 to depths in excess of 1500 meters. The deep wells produce hot water with downhole temperatures of about 147°C (Kunze et al., 1976; Stoker et al., 1976, 1977, Kunze, 1977).

The Raft River area is typical of the Basin and Range province. Block-faulted mountains surround the Raft River Valley to the west, south, and east. The valley is a graben structure filled with approximately two kilometers of alluvial and tuffaceous detrital sediments. The generalized geology of the area is shown in figure 2-7. This geologic map and cross section, as well as most of the geologic descriptions presented below, were adapted from Williams et al. (1974) and Williams et al. (1976). The basement is a complex of Paleozoic sedimentary rocks, Cambrian and Precambrian metasediments, and gneissic porphyritic adamellites (quartz monzonite). The major sedimentary unit within the graben is the Salt Lake Formation. Pliocene and Miocene tuffaceous siltstones, sandstones, and conglomerates make up the bulk of the formation. Locally, volcanic flows and breccias may predominate and are used to divide the formation into upper and lower members. All members of the Salt Lake Formation outcrop in the Jim Sage Mountains (figure 2-7) where the volcanics are most abundant. The Pleistocene Raft Formation is the local subsurface unit overlying the Salt Lake Formation.

The Raft Formation consists of clay, silt, sand, and conglomerates. The surficial units in this area consist of alluvium and eolian silt in the central valley floor and alluvial fan gravels on the flanks of the surrounding mountains. The fan deposits adjacent to the geothermal well sites are composed of coarse subangular gravels derived mostly from the volcanic members of the Salt Lake Formation exposed to the west. More detailed information on the local stratigraphy is presented in the borehole stratigraphic columns in figures 2-8 and 2-9.

Several major structural features occur in the Raft River area. The mountain ranges are bounded by sets of subparallel dip-slip range front faults. The faults dip 60 to 70 degrees toward the valley. The north-trending Bridge Fault has the greatest offset locally, but apparently has not been active for several hundred thousand years. The 'Narrows Structure' that trends northeast through 'The Narrows' has regional geophysical expression and is probably a basement shear zone. A concealed fault zone lies juxtaposed on this structure. The precise nature and location of this 'Narrows Structure' is ambiguous. The Bridge Fault and similar north-trending faults do not cross the structure. The Jim Sage Mountains directly to the west show considerable faulting which may be intense in some locations. The rocks in these mountains are gently folded. The folding axis trends northward parallel to the general trend of the faults.

In their geothermal model, Williams et al. (1976) postulate deep circulation of meteoric water as the source of high temperature fluids. The local volcanics are too old to provide a heat source. The chloride content and low temperatures of well waters indicate a hot water system.

Heat flow data suggest that water would need to circulate to depths of about 4 to 5 kilometers to reach temperatures in excess of 145°C. Stanley et al. (1977) suggest a more prominent local heat source based on a resistivity low (0.9 Ωm) at a depth of approximately 7 kilometers as determined by a magnetotelluric sounding in the valley. Hot water rises along fracture and fault zones and through permeable zones in the lower sediments. The hot fluids invade the more permeable horizons in the upper sediments and result in the high temperature ground water being widespread throughout the basin. Calcite, silica, and other alteration and precipitated minerals in the well cores and cuttings indicate that the system is self-sealing.

Both shallow and deep core samples are available from the intermediate and deep exploratory wells in the Raft River area. One core sample was taken for this study from each of the INT#1 and INT#4 wells. An excellent sample suite was obtained from INT#3. Sample locations and well stratigraphy for INT#3 are given in figure 2-8. The deep exploratory wells (RRGE) had sparse coring and as a result few samples were obtained. Most of the samples taken from the deep wells were from the lower portions of the Salt Lake Formation. Deep well data are presented in Table 2-1. Detailed well stratigraphy and sample locations are shown in figure 2-9 for the RRGE wells. The RRGE#1 site was chosen so that the intersection of the 'Narrows Structure' and the Bridge Fault would be penetrated at depth. Samples were obtained from the region thought to be the fault intersection and two samples were taken from the lower metamorphosed quartz schist zone. RRGE#2 was also sited to intersect the Bridge Fault at depth. Several core samples were taken from the

INT. WELL #3 (1457)

DEPTH
METERS

LEGEND

STRATIGRAPHY
LITH- POST-
OLOGY DEPOSI-
TIONAL

SAMPLES

0 —

[ ] ALLUVIAL SAND

50 —

P

— 212

[ ] ARGILLACEOUS SANDS AND SILTS
SANDY CLAY

100 —

P
P
P

[ ] INTERBEDDED SANDS, SILTS,
AND SHALES AND CLAY

ſ

[ ] CONGLOMERATE

—

P   ſ   ſ

P   ſ   ſ

,507
5075

— 594

[ ] CALCAREOUS
TUFFACEOUS

200 —

ſ

POSTDEPOSITIONAL

PC

[ ] fractures

—

868

AUTHIGENIC MINERALOGY

300 —

C An
CbP

,982
991

[ ] silicified zones

ſ

1067
1107
1132
1159
1204
1217
12175

C   calcite
An analcime
P   pyrite
Cl chlorite
Cb carbonaceous material

—

PC·An
Cl

Cb   ſ

1247
1257

400 —

— 1387

—

Figure 2-8. Well stratigraphy and sample locations for the Raft River Intermediate well #3 (after Crosthwaite et al., 1974). Core sample identification numbers (depth in feet) and positions are indicated in the column furthest to the right.
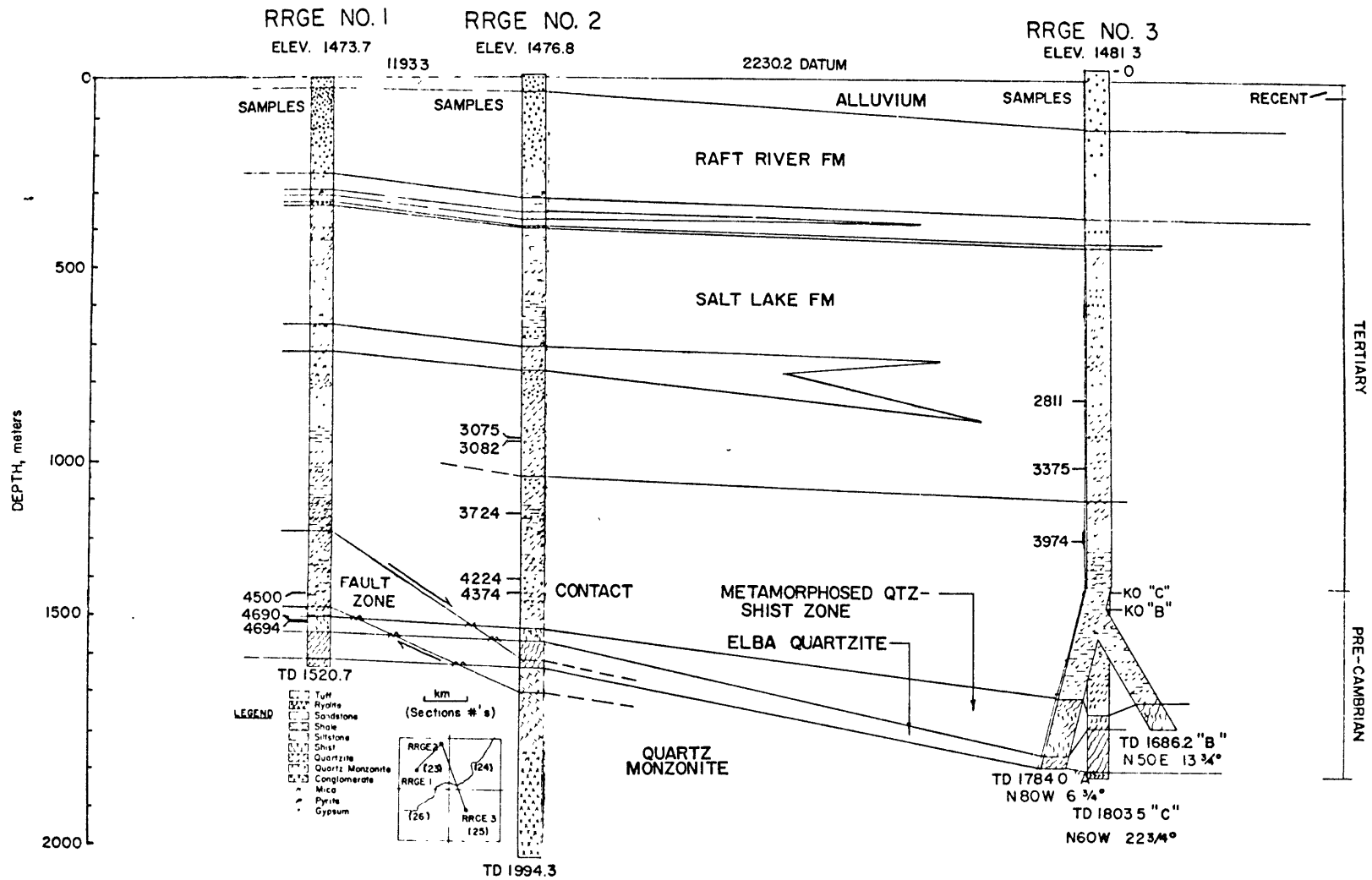
Figure 2-9. Well stratigraphy and sample locations with identification numbers (depth in feet) for the Raft River Geothermal Energy wells #s 1, 2, and 3 (from Kunze, 1977).

Table 2-1.

RAFT RIVER GEOTHERMAL EXPLORATION (RRGE) WELL DATA.

DATA	RRGE#1	RRGE#2	RRGE#3
Completed; depth	March 1975; 1524 m	June 1975; 1981 m	June 1976; 1804 m
Reservoir temp.	147°C	148°C	149°C
Artesian pressure	3.45 cold	4.14 cold	2.76 cold
(bars gage)	12.1 hot	11.4 hot	9.65 hot
Flow experience	25.2 l/s for many days with artesian pressure only. 54.9 l/s for 4 days pumping, drawing down 114.3 m below ground level.	31.5 l/s for several days with artesian pressure only. Three distinct production zones detected below 1200 meters.	85.2 l/s for one day under artesian pressure (145°C at surface).
Predicted after 10 years of production	69.4 l/s with 274.3 m drawdown below ground level.	94.6 l/s with 274.3 m drawdown below ground level.	31.5 l/s with 305 m of drawdown below ground level.
Total dissolved solids (ppm)	2000		4592
Cl	816		1626
SiO_2	52		69
Fe	trace		--
Mg	0.23		0.6
Na	400		?

Table 2-1 (continued).

DATA	RRGE#1	RRGE#2	RRGE#3
K	39		95
Ca	29		200
SO_4	54		34
HCO_3	<30		51
Specific conductivity (μmho/cm)	2700		9870

Well data modified from Kunze, 1977; Spencer and Hickman, 1976; Miller, 1976; and Stoker et al., 1977.

sediments above the postulated position of the fault (Kunze, 1977).

Reservoir tests on RRGE#1 and RRGE#2 indicate a porous reservoir of high

capacity and permeability (Narasimhan and Witherspoon, 1977). RRGE#3

was located over a resistivity low and a self-potential anomaly (Williams

et al., 1976). The physical parameters and water chemistry of the RRGE#3

well indicate that it has a separate, distinct reservoir from RRGE#1 and

RRGE#2. After completion of the initial leg in RRGE#3, two 'kick out'

legs were drilled to increase production. Three samples were obtained

for this study from the lower portion of the Salt Lake Formation above

the producing fracture zones.

Coso Area

The Coso geothermal area is located in the Mojave Desert in east-

central California (see figure 1-1). The area lies in the Basin and

Range Province near the boundary of the Sierra Nevada Mountains. The

region of major hydrothermal activity is contained within the Naval

Weapons Center at China Lake. The surface expression of the hydrother-

mal activity consists of hot springs, fumaroles, and sinter deposits

and alteration zones (see figures 2-10a and b). Early geologic inves-

tigations were concerned primarily with the low-grade and dispersed

mercury deposits associated with the fumaroles (Wilson and Hendry, 1940;

Ross and Yates, 1943; Dupuy, 1948). Geothermal interest in the area

began with preliminary geologic and geophysical investigations by the

Weapons Center staff. A 114 meter test well, Coso #1, was drilled in

1967. This well, located on the fault zone near Coso Hot Springs, en-

countered a maximum temperature of 142°C (Austin and Pringle, 1970).

NAVAL RESERVATION BOUNDARY

36°15'

COSO RANGE

COSO HOT SPRINGS

36°00'

SIERRA NEVADA

118°00'   117°45'   117°30'   117°15'

Alluvium and Sedimentary Rocks

Cenozoic Volcanics

Mesozoic Granitic Rocks

Faults associated with Coso caldera structure
(Bar and ball on downthrown side)

N

0   10
       Km
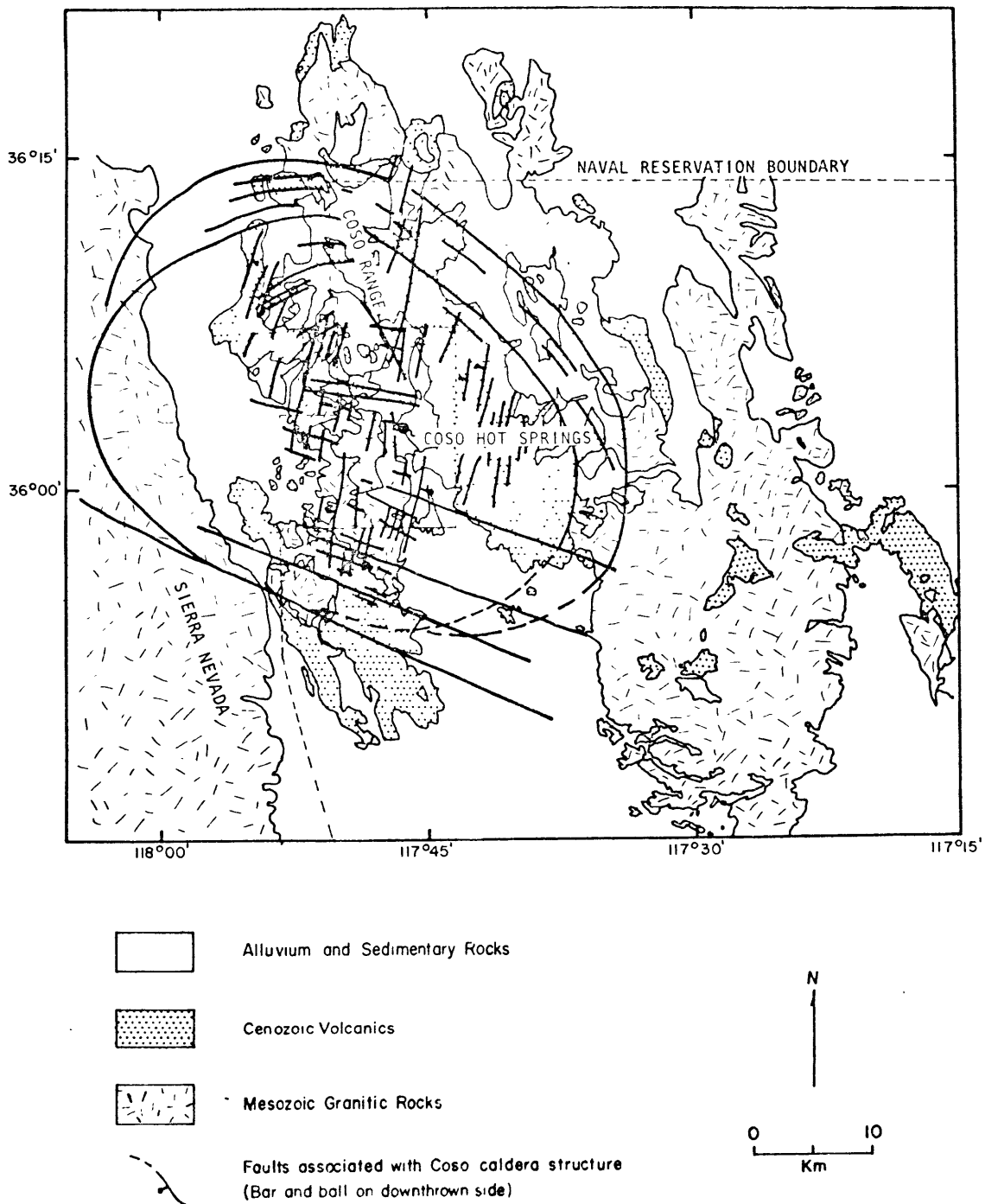
Figure 2-10a.   Regional geology and structures for the Coso Hot

Springs area.   See figure 2-10b for a detailed map of the area out-

lined by the solid rectangle (after Duffield, 1975; Jennings et al.,

1962; Jennings, 1958).
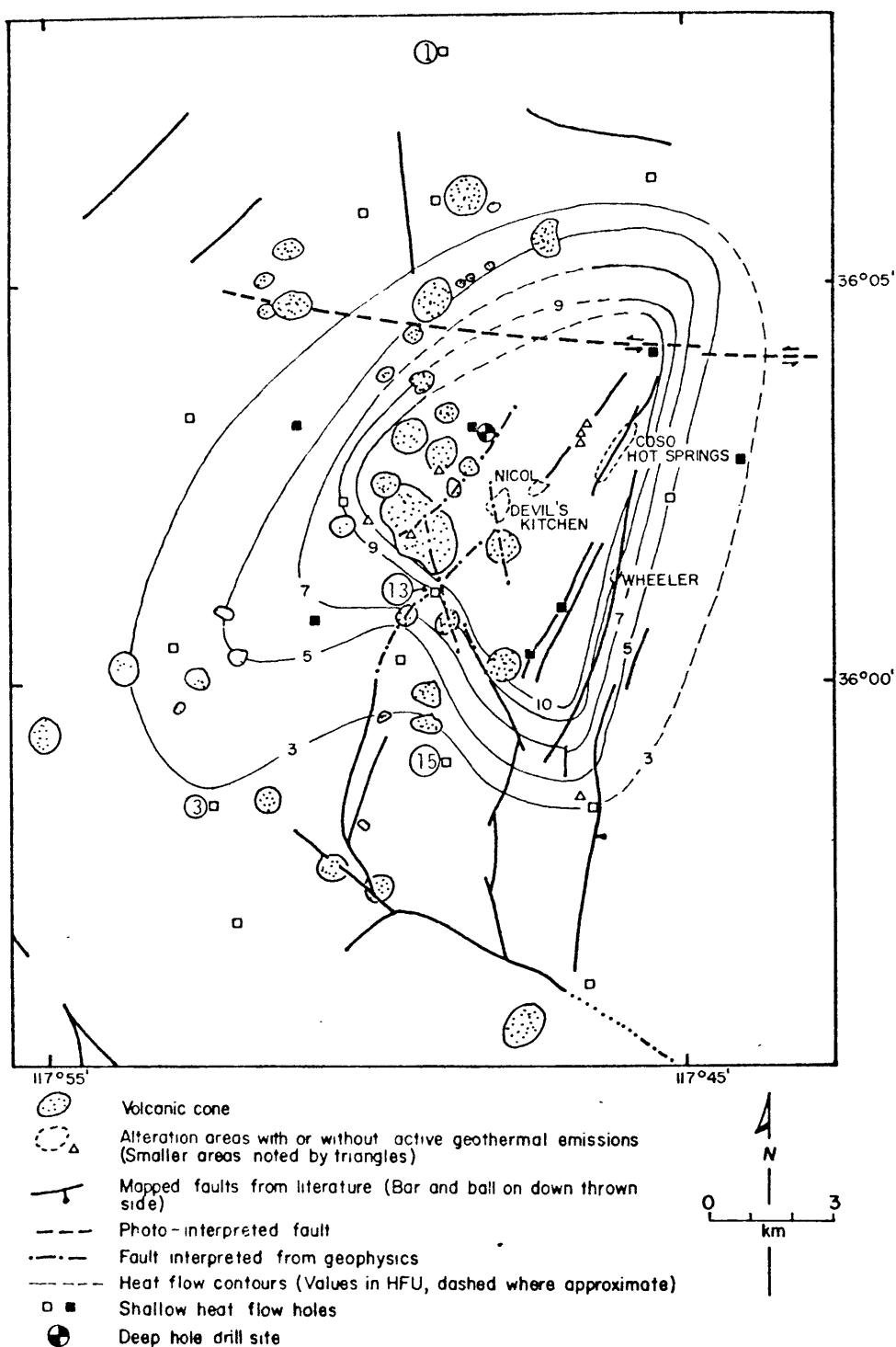
Figure 2-10b. Structure and heat flow map, Coso geothermal area, California. Samples were also obtained from the shallow holes identified by circled numbers (modified from Combs, 1976; Furgerson, 1973; and Lanphere et al., 1975).

More extensive investigations were begun in the early 1970's and drilling began for the 'Battelle Deep Hole #1' (BDH#1, see figure 2-10b) in late 1976. This well was badly mishandled and damaged. Drilling was suspended in early 1977. Drilling began on a new well, Coso Geothermal Exploratory Hole number one (CGEH#1) located on the same site, in late summer 1977. At the time of this writing, CGEH#1 had been completed to a depth of 1477 meters and downhole temperatures reached 193°C (Joy Hyde, personal communication, 1978). Well logging and testing are now in progress.

The general geology of the Coso area consists of young volcanics and alluvium capping metamorphic and plutonic rocks in a broad caldera structure (Duffield, 1975). Metamorphic and Mesozoic granitic rocks similar to those of the Sierra Nevada Batholith underlie the Coso Mountains (figure 2-10a). Late Cenozoic volcanics in the region include (1) basaltic and dacitic flows and cones, (2) tuffs, and (3) rhyolitic domes, flows, and ejecta. At least 31 rhyolitic domes and flows exist in the region and range in age from about 0.04 to 1 million years (Lanphere et al., 1975). The rhyolites retain their pumiceous and vitreous surfaces and, with the associated unconsolidated ejecta, have a total minimum volume of 2.4 cubic kilometers. Based on the homogeneous composition, Lanphere et al. (1975) conclude that all the rhyolites originated from a single magma body. The older (2-3 m.y.) dacites and basalts top ridges in the Coso Range. The dacite flows overlie late Cenozoic lacustrine sedimentary beds. The granitic rocks and alluvial deposits immediately adjacent to the hot springs and fumaroles are intensely altered. Feldspars have been completely altered to kaolinite

and alunite and the sediments are often indurated with layers of opal
and dispersed pyrite, hematite, and other hydrothermal minerals (Ross
and Yates, 1943; Austin and Pringle, 1970). The stratigraphy of BDH#1
is shown in figure 2-11. Preliminary downhole temperature data measured
during drilling are shown in figure 2-12.

The Coso geothermal area is not typical of the Basin and Range Pro-
vince. The hot springs are located near the center of a large caldera
structure defined by an arcuate 'ring' fault system (Austin et al., 1971;
Koenig et al., 1972; Duffield, 1975). These ring faults dip steeply
toward the interior of the caldera and vary from single fractures to
cataclastic zones tens of meters wide. The caldera extends westward to
include a portion of the Sierra Nevada Mountains and is concealed by
alluvium to the south. A dense rectilinear pattern of faults lies in the
interior of the caldera. These faults are steeply dipping, trend either
west-northwest or north-northeast, and have dip-slip components (figures
2-10a and b). This faulting is responsible for the linear distribution
of the hot springs and fumaroles. This caldera may be similar to the
calderas of Long Valley (Bailey et al., 1976) and Yellowstone (White et
al., 1971; Fournier et al., 1976). Duffield (1975) suggests that the
Coso area may be in a stage preceding large eruptions of ash flows and
major caldera collapse.

The Coso geothermal system may be steam dominated and heated by a
large magma body at depth. A region of high heat flow, up to 18 HFU,
encompasses the hot springs and fumaroles (Combs, 1976; Combs and Jar-
zabek, 1977). From seismic data, Combs and Rotstein (1976) calculated
low values of Poisson's ratio (0.16) under the heat flow anomaly and
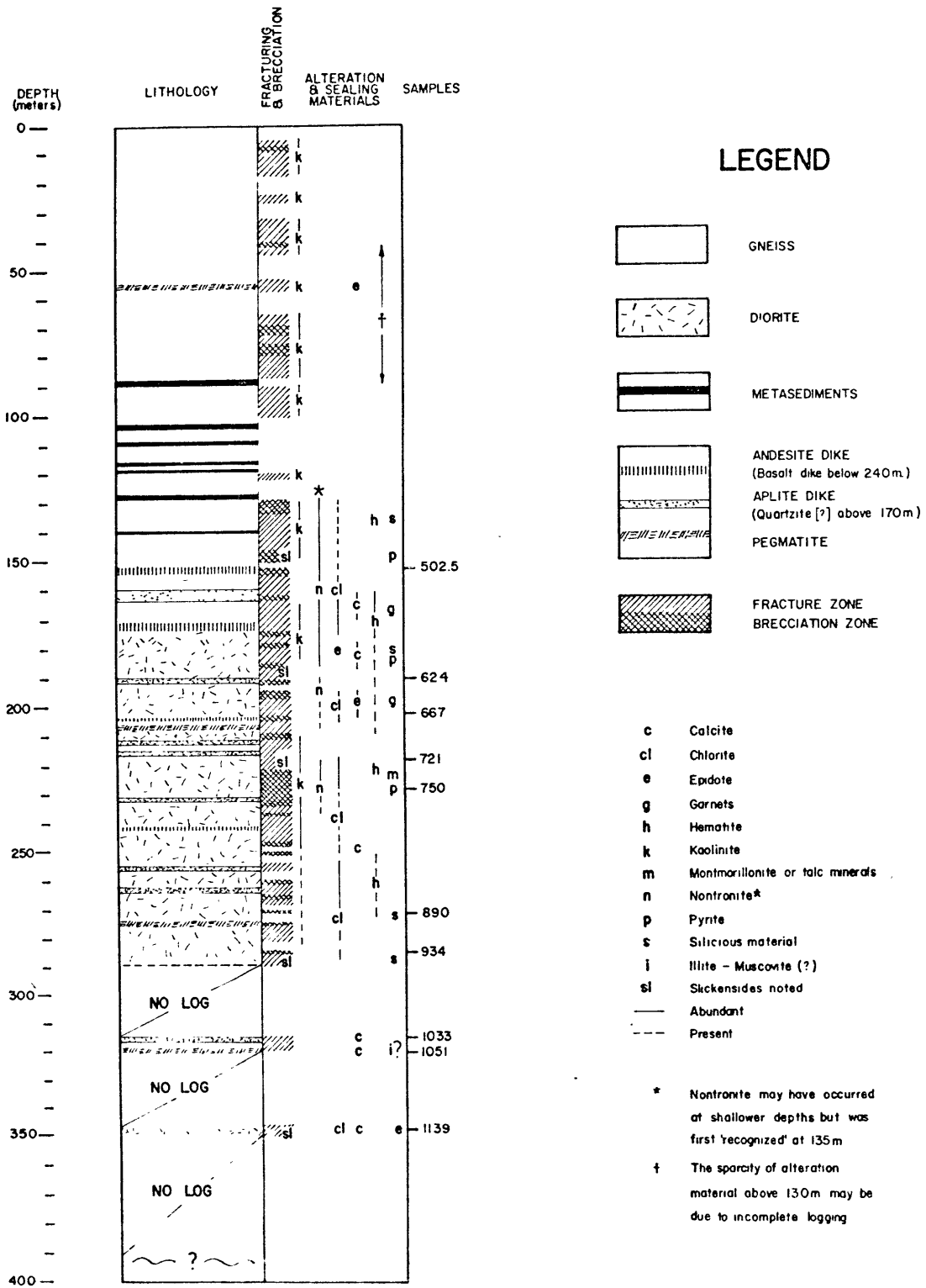
Figure 2-11. Well stratigraphy and sample locations for the Battelle Deep Hole #1 (from J. Bruce, personal communication, 1977).

COSO HOT SPRINGS
BDH [#]I
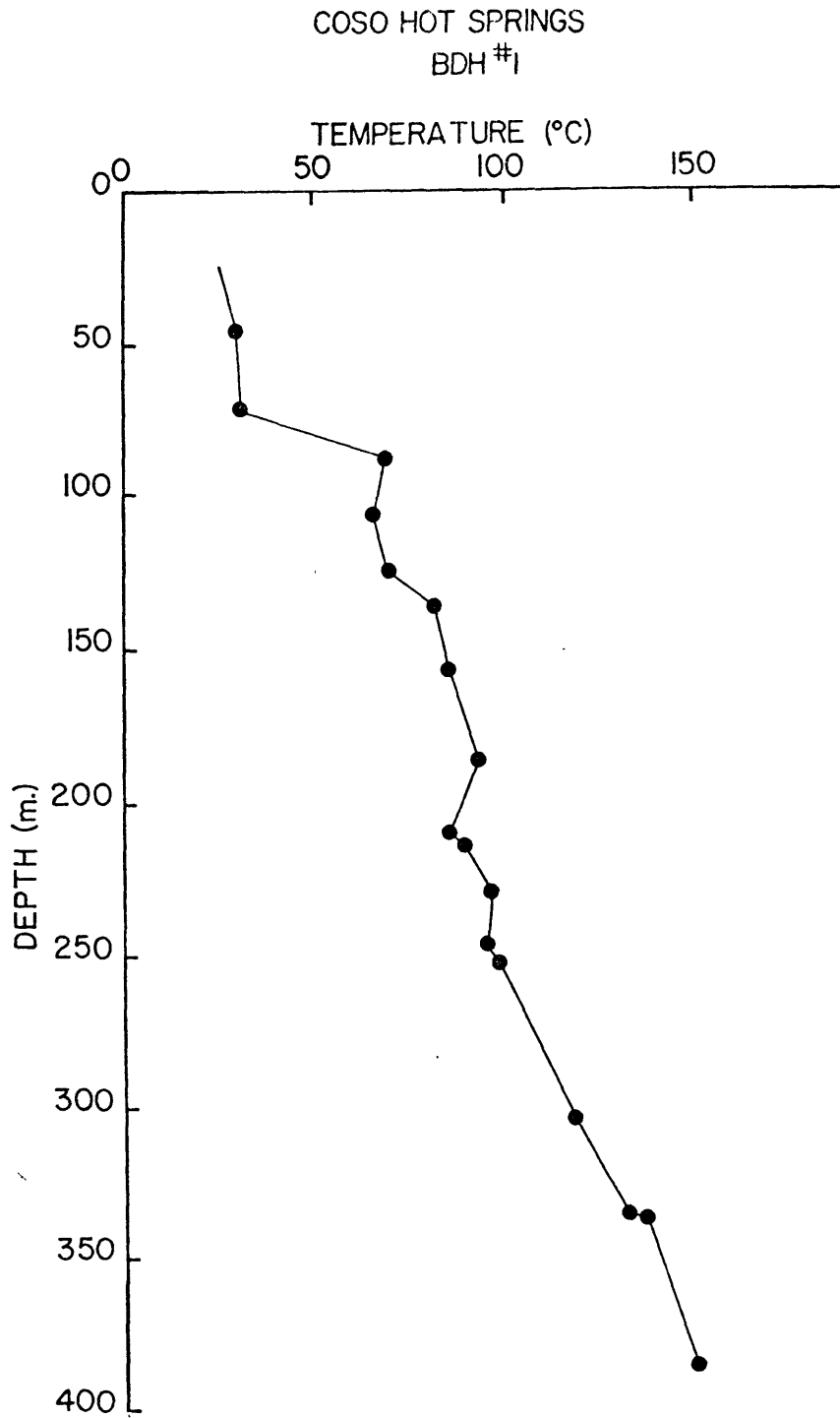
Figure 2-12. Preliminary downhole temperatures for the BDH#1 well measured between drilling intervals (C. Austin, personal communication, 1977).

suggested that the system is vapor dominated. Based on Schlumberger, audiomagnetotelluric, and telluric measurements, Jackson et al. (1977) also conclude that the system is vapor dominated and is capped to depths of a few hundred meters by a highly altered impermeable zone. If this model is correct, then steam would flow up along faults and fracture zones. The steam will then condense and the resulting hot water, possibly mixed with cold ground water, will feed hot springs and fumaroles and invade permeable rock units. However, the high chlorine content of up to 3681 ppm in the Coso #1 well water reported by Austin and Pringle (1970) seems inconsistent with a vapor-condensate source. Cores from BDH#1 are intensely fractured and brecciated. However, alteration products and precipitated minerals may be filling fractures sufficiently to inhibit fluid circulation and thus permit steep temperature gradients to exist (figure 2-12). P-wave delays and seismic attenuation under the caldera indicate that the ultimate heat source for the region is a deep magma chamber (Combs and Jarzabek, 1977).

Samples were obtained for this study from both shallow and deep holes. More than 20 shallow heat flow wells were drilled in and around the region of high heat flow (see figure 2-10b). One veined core sample was obtained from each of heat flow wells 1, 3, 13, and 15. The deep well, BDH#1, was drilled near the center of the heat flow anomaly over a highly resistive basement structure interpreted to be a steam-dominated zone (Jackson et al., 1977). Ten samples were taken from the interval between 153 and 347 meters depth.

Marysville Area

The Marysville geothermal area is approximately 30 kilometers north-
west of Helena, Montana (see figure 1-1). The area is located in the
Rocky Mountains on the continental divide. No natural surface expres-
sion exists indicating hydrothermal activity and Marysville has been
termed a 'blind' geothermal area. The geothermal potential of the region
was discovered in the course of a regional heat flow study (Blackwell
and Baag, 1973). A maximum of 19.5 HFU was measured in holes drilled
for mineral exploration. A wide range of geologic and geophysical in-
vestigations was initiated in the early 1970's to determine the exact
nature of the system. The project culminated with the drilling of the
Marysville Geothermal Exploration Well Number 1 (MGE#1; figures 2-13a
and b) in the summer of 1974. The well reached a maximum depth of 2.1
kilometers and a maximum temperature of 98°C. The low temperatures in-
dicate that the system is not economically viable and most geothermal-
related work in the area has been suspended. The information summarized
in this section comes primarily from the publications of Blackwell and
Baag (1973), McSpadden et al. (1975), Blackwell and Morgan (1976),
and Blackwell (1977).

The geology of the Marysville region consists of sedimentary and
metasedimentary rocks overlying igneous intrusives. A Precambrian
series of limestones, shales, and sandstones are the important sedi-
mentary units in the immediate area. The oldest sedimentary unit is
an argillite which is overlain by the biotite-rich siliceous to cal-
careous Empire Shale (see figure 2-13a). The next unit is a siliceous
limestone and dolomite with interbedded shales and sandstones. The
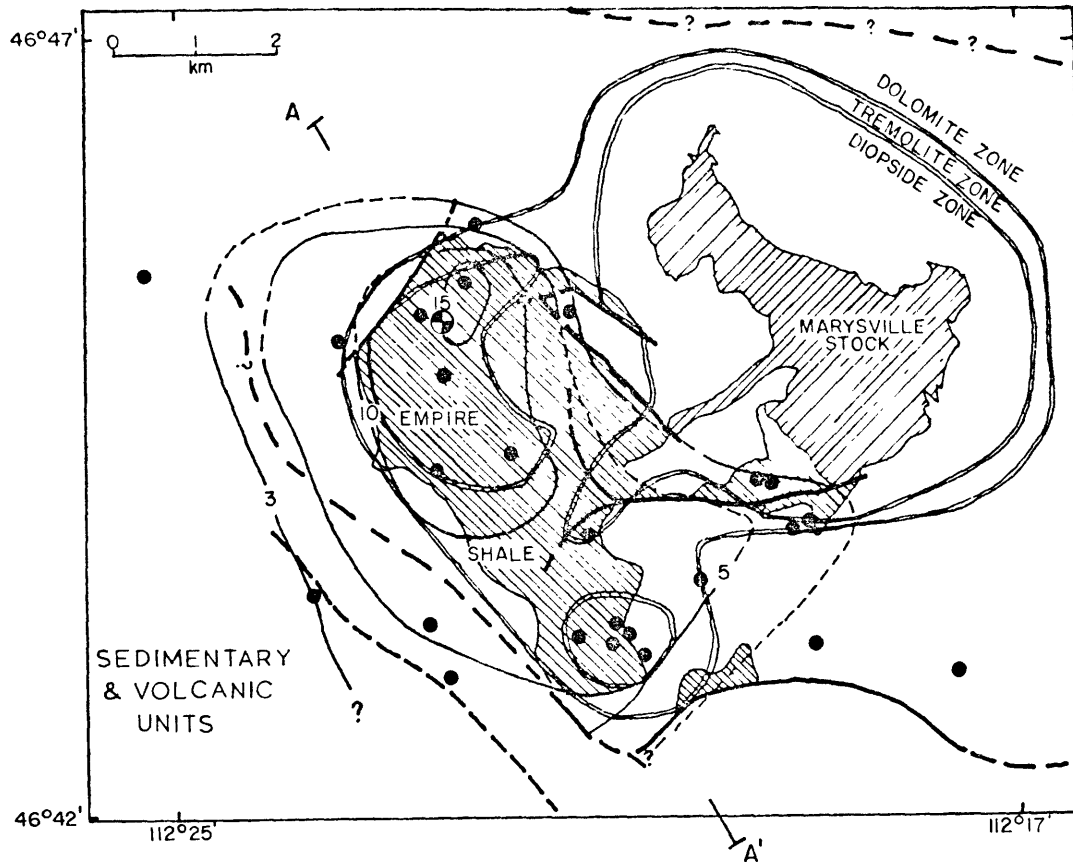
Figure 2-13a. Regional geology, structure, and heat flow for the Marysville area. See figure 2-13b for cross section A-A' (after Blackwell et al., 1975 and Blackwell and Morgan, 1976).
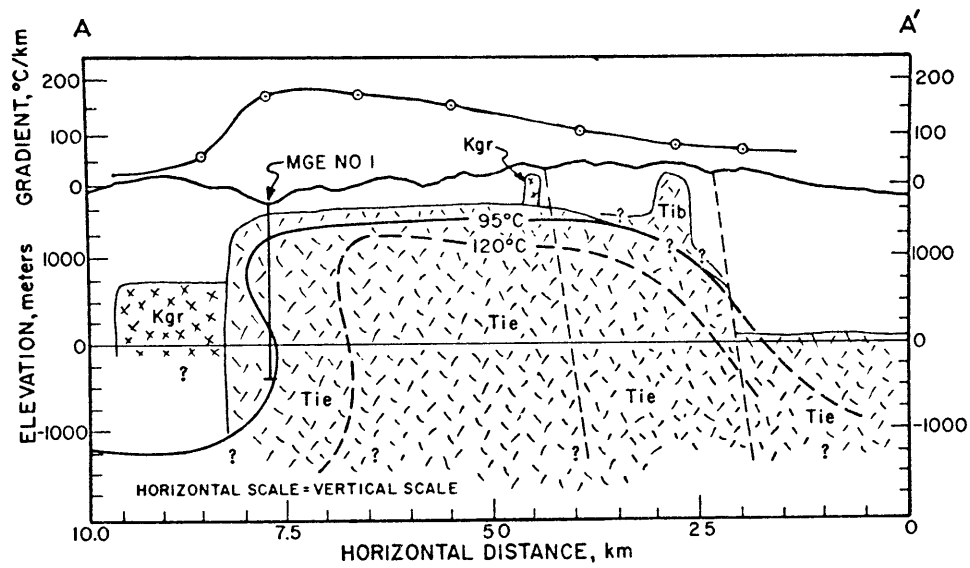
Figure 2-13b. Cross section A-A' from figure 2-13a including general structures, near-surface temperature gradients, and interpreted deep isograds. Tie = Empire Creek Stock, Tib = Bald Butte intrusive, Kgr = Marysville Stock (from Blackwell et al., 1975).

remaining overlying Precambrian rocks are dominantly shales and sand-
stones. Other sedimentary rocks ranging in age from lower Paleozoic
to Cretaceous rest unconformably above the Precambrian sedimentary series.
Several episodes of igneous activity have occurred locally. The Marys-
ville Stock is a Cretaceous (~79 m.y.) granodiorite and is probably re-
lated to the Boulder Batholith 20 kilometers to the south. The iso-
lated (figure 2-13a) Bald Butte quartz porphyry plug was emplaced about
49 million years ago. The Empire Creek Stock was intruded in the Oligo-
cene (~40 m.y.). This stock is a quartz-feldspar porphyry and has no
surface exposures. A few erosional remnants of rhyolite flows and tuffs
are located southwest of the Marysville area. The volcanics are about
37 million years old as are the numerous dikes and sills in the region.
The Marysville and Empire Creek plutons have produced contact metamor-
phism in the overlying Precambrian sediments. Metamorphism reached
diopside grade with temperatures and pressures estimated to be approxi-
mately 500°C and 500 to 750 bars. The diopside and tremolite contact
aureoles have been mapped (figure 2-13a) and indicate the lateral sub-
surface extent of the plutons.

The structure of the region is characterized by faulting and gentle
folding and doming. The folding and doming probably are a result of the
emplacement of the Marysville and Empire Creek plutons. The general
form of the folding is indicated by the extent and shape of the Empire
Shale exposure in figure 2-13a. North-south trending fracture cleavage
has been developed in the Precambrian sedimentary units. Faulting in
the area is usually poorly exposed and ambiguous. The major faults
are shown in figure 2-13a. Cutting relationships can prove only that

some of the faulting is younger than 79 million years. However, the latest faulting is probably much more recent. A zone of thrust faulting with displacements on the order of tens of kilometers is exposed approximately 40 kilometers east of Marysville. This thrust faulting may underlie the region at depth. Some of the major faults in the district have geophysical expression. The Empire Creek Stock and the geothermal area are characterized only by broad zones of high resistivity (10,000 Ωm) and low gravity (~-10 mgal). Heat flow and magnetics indicate that the Marysville pluton is bounded in the subsurface to the southwest near the limits of the outcrop. The Empire Creek Stock is responsible for the contact aureoles extending to the southwest.

The deep exploratory well, MGE#1, was drilled through the Precambrian metasediments and into the Empire Creek Stock. Fifteen sections of core were recovered from various depths (see figure 2-14). Samples for this study were obtained from each of the cored intervals. The well penetrated several major fracture zones. Large amounts of water began flowing into the well from fractures at approximately 450 meters depth. The upper fracture zones have highest fluid pressure, which resulted in water flow down the borehole to invade lower zones. The downhole temperatures reflect this flow and show a thermal inversion with a maximum temperature of 98°C reached at 1,000 meters. The measured well temperatures and flow rates are shown in figure 2-15. The maximum standing water level reached in MGE#1 was approximately 180 meters below the surface. The low fluid pressure may be responsible for the lack of surface thermal manifestations.

The hypothesized geothermal system in the Marysville area consists

DEPTH
(meters)

LITHOLOGY

FRACTURE ZONES

MEGASCOPIC VEIN
MINERALOGY
(from core logs)

CORES

MIT.
SAMPLE
NOS

0

c, q, f, p

1

1462,
1462A

q, a, c, f, cl, m

2

1463

q, f, c, a, cl, b, t, ph, b

3

1464

q, f, c, d, ch, a, ph, pl

4

1465

q, o, s, f, c, p, m

5

1466,
1467

LIGHT GRAY
GRANITE
PORPHYRY

q, p, m, s

6

1468

Kaolinized

Zone

q, f, b

7

1478

HIGHLY ALTERED WHITISH-GRAY GRANITE PORPHYRY

q, m

8

1469

q, ch, p, b

9

1470

1000

qc

10

1471

Koolinized Zone

qc, o, b

11

1472

qc, k

12

1473,
1474

LIGHT PINK
PORPHYRITIC
GRANITE

Fractures sparse

13

1475

q, o, pl, f, l

14

1476

Fractures not
mineralized

15

1477

2000

DARK PINK
PORPHYRITIC
GRANITE

TD=2070

LEGEND

LITHOLOGY

EMPIRE SHALE
(metamorphosed)

DACITE PORPHYRY

EMPIRE CREEK STOCK
(porphyritic to
equigranular granite)

HEAVILY ALTERED ZONE

VEIN MINERALOGY
(from core logs)

a	adularia
b	biotite
c	calcite
cl	chlorite
f	fluorite
k	kaolinite
l	limonite
m	molybdenite
o	orthoclase
p	pyrite
ph	phlogopite
pl	plagioclase
q	quartz
qc	cryptocryst quartz
s	sulfides
t	tremolite

Figure 2-14. Well stratigraphy and sample locations for the Marysville Geothermal Exploration well #1 (adapted from Blackwell et al., 1975).
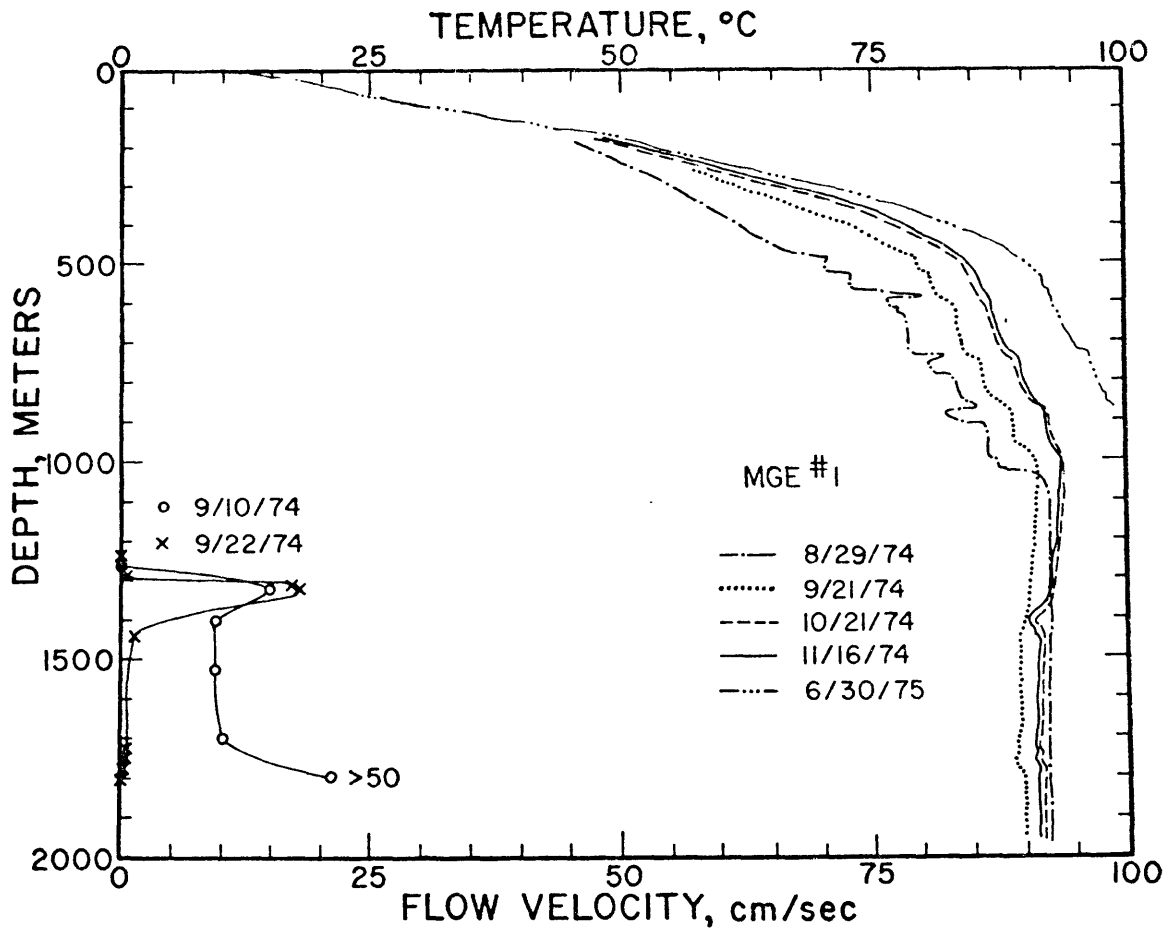
Figure 2-15. MGE#1 well temperature profiles and downhole flow
data taken at several different times (from Blackwell et al.,
1975).

of warm water circulating through fractures. The early exploration of the region was insufficient to differentiate between a 'hot dry' intrusive or shallow circulation of hot fluids as the source of the high heat flow. Based on the low fracture content and low permeability of the rocks exposed at the surface, the intrusive source was preferred. None of the igneous rocks located in the area are young enough to provide a shallow heat source. As is apparent from figures 2-14 and 2-15, the Empire Creek Stock has been heavily fractured at depth and circulation is pronounced. Fluid flow is significant within the fractures, but the individual fracture zones can form discrete non-interconnected systems. The isolation of individual fracture zones is demonstrated by the temperature inversions and copious downhole flow. The active circulation is apparently contained within the fractures of one pluton, the Empire Creek Stock, and bounded on the northeast by another pluton, the Marysville Stock. This area demonstrates the complex hydrologic conditions possible in geothermal systems. Based on fluid geothermometry, temperatures of 120 to 180°C should occur somewhere in the system. The interpreted positions of isograds, based on heat flow data, had been qualitatively located by Blackwell et al. (1975) on the cross-section in figure 2-13b.

Roosevelt Hot Springs Area

The Roosevelt Hot Springs geothermal area is in southwestern Utah (see figure 1-1). The site is located in the Basin and Range physiographic province on the western flank of the Mineral Range. In the early 1900's, the hot springs flowed at 88°C at a rate of about 0.6 liters

per second. The springs were dry by 1966 and a small 25°C seep is the only remaining active surface manifestation. A discontinuous chain of alteration and cementation zones roughly parallels the front of the Mineral Range. These zones consist mostly of alunite, opal, kaolinite, montmorillonite, and K-mica. Two samples were obtained for this study from wells (wells 9-1 and observation hole #2) drilled by Phillips Petroleum Company on opposite sides of this chain of alteration zones. Since only a pair of samples were obtained from this area, the region will not be discussed in detail; only a cursory description is presented. Most of the information presented here is summarized from the recent investigations by the staff at the University of Utah (Evans and Nash, 1975; Nash, 1976; Parry et al., 1976; Ward et al., 1976; Ward and Sill, 1976; Crebs and Cook, 1976; Bryant and Parry, 1977).

The region is dominated by a block-faulted mountain range of young igneous rocks flanked by alluvial fans. The Mineral Range Pluton (9.2 ± 0.3 m.y.) makes up the bulk of the mountains. This pluton varies in rock type from an altered granite to adamellite to granodiorite. The pluton gradationally contacts gneissic rocks to the west. Central portions of the Mineral Range are partially covered with rhyolitic vol-canics ranging in age from 2.30 ± 0.14 m.y. to 0.42 ± 0.07 m.y. The volcanics consist of 10 individual domes with associated deposits of rhyolite, perlite, obsidian, and ash. Tertiary and Quaternary alluvium blankets the plutonic rocks at the hot spring and alteration sites.

Numerous normal faults provide conduits for the circulating hydrothermal fluids. The Dome Fault is the most conspicuous of a series of north-south trending faults. The Dome Fault is traced by the chain of

alteration zones mentioned previously. This fault forms one side of a small buried horst in the Precambrian basement rocks west of the Mineral Range. The Dome Fault has been tentatively dated as pre-Pleistocene, but many of the less prominent parallel faults have been the sites of more recent movement. Another sequence of faults trends east-west, intersecting and crossing the north-south series of faults. The high temperature reservoir is postulated to consist of the faults, fractures, and joints in the Precambrian basement rocks and the plutonic rocks underneath the Mineral Range. Water samples from both wells and the warm seep are silica and sodium-chloride rich and acid-sulfate in nature with approximately 6,000 ppm total dissolved solids. Well temperatures reach 260°C and the Na-K-Ca geothermometers suggest system equilibrium temperatures of 240°C to greater than 294°C. The heat is probably derived from the same magma bodies that supply the young rhyolitic volcanics. The hot fluids flow along the faults and fractures and then into the alluvial sediments to the west. The Roosevelt Hot Springs system is therefore similar to the Marysville system in 'source' and the Raft River system in 'sink'.

CHAPTER III

EXPERIMENTAL AND OBSERVATIONAL TECHNIQUES

Introduction

The techniques used in this investigation will be discussed brief-
ly. The techniques included both direct and indirect measurements of
physical parameters, as well as direct observation of microscopic fab-
rics. Differential strain and interconnected porosity were measured on
almost all samples and hydraulic permeability and resistivity were de-
termined for several others. Observational methods included optical,
scanning electron, and cathodoluminescent microscopic examination.

Differential Strain Analysis

Differential strain analysis, abbreviated DSA, is a technique to
measure certain properties of open microfractures. This technique is
based on the pronounced effect fractures have on the compressibility
of rocks (see, for example, Walsh, 1965; Brace, 1965; Todd et al.,
1972). Strain versus pressure plots for dry fractured rock samples
often show two characteristic regions as in figure 3-1a. The 'straight'
portion of the plot at high pressure is a result of the intrinsic
compressibilities, β, of the constituent minerals. The curved por-
tion of figure 3-1a includes the additional strain due to the closure
of cracks and pores. Fracture porosity, ζ_c, is the amount of volu-
metric strain between the origin and the zero pressure intercept of
the 'straight' portion of the stress-strain plot (Walsh, 1965).
Morlier (1971) showed that the distribution of crack shapes could be
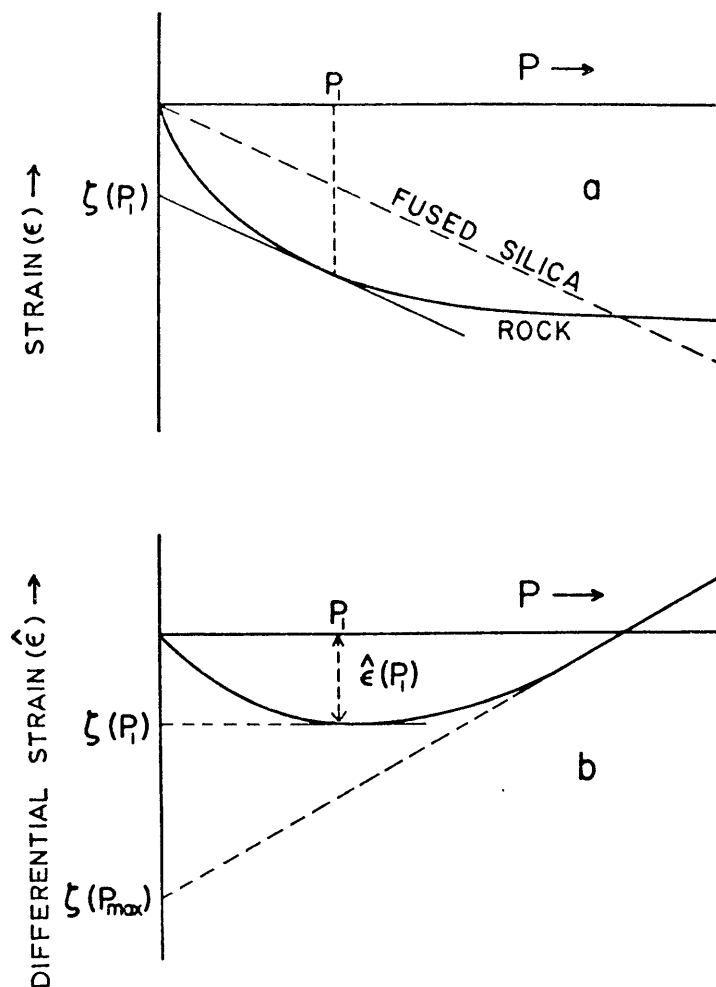
Figure 3-1. Differential strain analysis (DSA). In 3-1a the measured strain of a fused silica reference (dashed line) is subtracted from the measured rock strain (heavy solid line) to yield the differential strain in figure 3-1b. The zero pressure intercept of a line tangent to the strain curves at any pressure P_1 is the strain $\zeta(P_1)$ at zero pressure associated with cracks which have completely closed by pressure P_1 (after Feves et al, 1977).

obtained from plots such as that shown in figure 3-1a, provided that
a specific crack shape is assumed.

Differential strain analysis was used in this investigation to
obtain the fracture porosity with respect to closure pressure and in-
dications of fracture shape, spatial distributions, and orientations
in the core samples. DSA is described in detail elsewhere (Simmons
et al., 1974; Feves and Simmons, 1976; Batzle and Simmons, 1976;
Siegfried, 1977; Feves et al., 1977; Feves, 1977) so only a very
brief description will be presented here. The differential strain is
obtained by subtracting from the rock sample strain, the strain of a
fused silica standard exposed to the same high pressure (hydrostatic)
environment. With this technique, errors due to instrument drift,
changes in lead resistance, and many thermal effects are eliminated.
The result is a strain measurement with a precision of about 2×10^{-6}.
The process of plotting differential strains essentially rotates
plots such as in 3-1a into the form shown in 3-1b. In the transfor-
mation, the fracture porosity remains the strain between the origin
and the zero pressure intercept of the 'straight' intrinsic compres-
sibility portion of the DSA curve.

The precision of the DSA technique enables one to observe the
detailed behavior of the sample strain as a function of pressure.
Fracture closure with increasing pressure causes a strain normal to
the plane of the fracture. This strain or 'linear crack porosity'
can be measured in any direction and the distribution of fracture
orientations is often strongly anisotropic. The volumetric micro-
crack porosity is the sum of any three orthogonal linear crack

porosities or closure strains. With the penny-shaped crack model of
Walsh (1965), the stress-strain relations can be interpreted in terms
of fracture aspect ratio, α. In this model, fractures close linearly
with pressure. Fractures with aspect ratio α will be closed complete-
ly at a pressure, P_c, such that $\alpha = 4P_c(1-\nu^2)/\pi E$, where ν and E are
Poisson's ratio and Young's modulus of the rock matrix, respectively.
At this closure pressure, these fractures cease to contribute to the
sample strain. At P_c, the zero pressure intercept of the tangent to
the stress-strain plot will be increased by the porosity of this set
of closed fractures. Hence, such a model allows the interpretation
of DSA data in terms of the porosity of fractures with specific as-
pect ratios. Similar, though more elegant, models have been developed
by Toksöz et al. (1976) and O'Connell and Budiansky (1976). In all
of these models, however, the fractures are considered to be isolated
and of simple (elliptical) shape. The physical interpretations are
strongly dependent on the assumed models. To avoid this model depen-
dency, Simmons et al. (1974) have used the experimentally determined
values of closure pressure, P_c, and ζ_c, the strain due to all the
cracks (or segments of cracks) that have closed by P_c. A second de-
rivative of the DSA plot with respect to pressure and then multiplied
by the pressure yields the 'spectra' or rate of change with pressure
of the parameter ζ. This spectra indicates how the porosities of
microcracks of differing closure pressures are distributed.

The interpretation of DSA is not always straightforward. Fig-
ures 3-1a and b are highly idealized curves typical of fractured
plutonic rocks. For altered igneous and sedimentary rocks the behav-

ior can be complex. Large decreases in volume occur with samples
that are easily compacted. The compressibility can increase with
pressure and can be orders of magnitude greater than for dense crys-
talline rocks. Abrupt changes in compressibility are character-
istic of clay-rich rocks (Lambe and Whitman, 1969, p. 125). The
large amount of strain renders the correction from the fused silica
reference as trivial and obscures the effects of fractures. A
similar but less pronounced effect, shown in figure 3-2, occurs when
material is crushed in the vicinity of intergranular contacts (Lee
and Farhoomand, 1967). This effect may also occur when 'bridges' or
materials spanning open fractures are crushed. Several samples have
DSA curves that abruptly change curvature and become less compres-
sible. Such changes might be due to movement of small amounts of water
in the crack network during compression. All these effects are usually
insignificant for dense crystalline rocks. In pliable sedimentary or
altered rocks, several effects often combine to make interpretation
of DSA curves qualitative at best.

Permeability

A pressure decay technique was used for the determination of
sample permeabilities in this study. This permeability system is
patterned after that of Brace et al. (1968), but employs substantial
technical and analytical modifications. Basically, the system con-
sists of a chamber or vessel filled with fluid and sealed except for
a sample 'plug'. After pressurization and isolation, the only outlet
for the fluid is through the sample. From the pressure drop as a

STRESS   (bars)
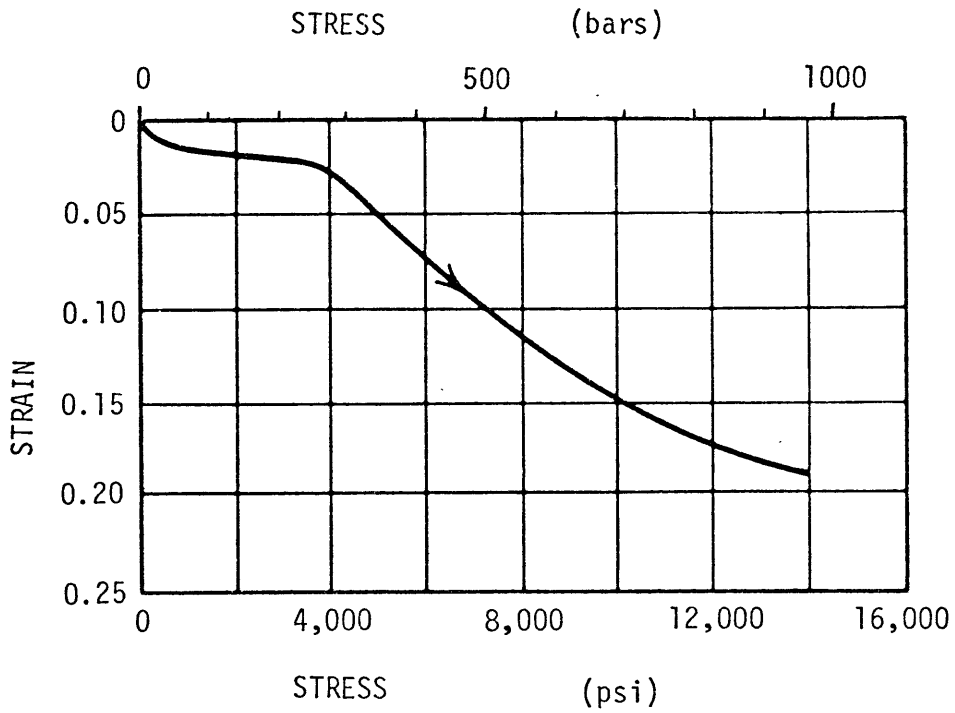
Figure 3-2. Generalized stress-strain curve for Ottawa Sand.
The differential strain curve would appear identical to this
curve because the sample strains are much larger than the strains
of the fused silica reference (from Lambe and Whitman, 1969).

function of time and the measured parameters of the system, the amount of water that has passed through the sample can be calculated. This method is useful for measuring samples with permeability below a few millidarcys.

The derivation of the basic permeability relationship is straight-forward. The fluid flow rate, Q, is related to fluid volume change, dV, and time, t, by

$$Q = dV/dt. \tag{3-1}$$

Darcy's law states that for isotropic materials

$$Q/A = (\frac{-k}{\mu})\nabla P$$

where A is the sample end surface area, k is the sample permeability, μ is fluid viscosity, and P is pressure. For samples of thickness h, Darcy's law is simplified to

$$Q/A = -k/\mu(\frac{P-P2}{h})$$

with P the internal vessel pressure and P_2 the pressure on the opposite side of the sample. In this study, P_2 was always approximately zero (gage pressure) and so this last equation can be combined with equation (3-1) to yield

$$dV/dt = \frac{-kA}{\mu}\frac{P}{h} \tag{3-2}$$

From the definition of compressibility, β,

$$dV = V\beta dP.$$

Substituting into equation (3-2) gives

$$dV/dt = V\beta dP/dt = \frac{-kA}{\mu}\frac{P}{h}$$

or

$$\beta\frac{dP}{P} = \frac{-kA}{\mu Vh}\ dt. \qquad\qquad (3-3)$$

In the present application, V represents the internal volume of the system.

Brace et al. (1968) used the compressibility of water in their relationship. However, this system includes o-rings, pressure fittings and packings, sample, sample holder and adhesives, pressure transducer, rupture disk, and entrapped air bubbles as well as water. These features have a large effect on the pressure dependence of the system. For a given change in the fluid volume, the pressure will not change simply according to the compressibility of pure water. This difficulty can be overcome by conceptually replacing the water with another fluid of different effective compressibility, β'. This effective fluid compressibility must then be determined to be able to relate a measured pressure drop to the quantity of fluid that has left the system through the sample. The effective fluid compressibility is strongly dependent on the pressure within the vessel, as shown in figure 3-3. The incremental change in pressure, ΔP, due to a known small reduction in the internal system volume, ΔV^*, is shown as a function of internal pressure for various material 'plugs' in figure 3-3. This pressure dependence can be described by one (or more) lines of the form

$$\ell nP = c + m\Delta P.$$
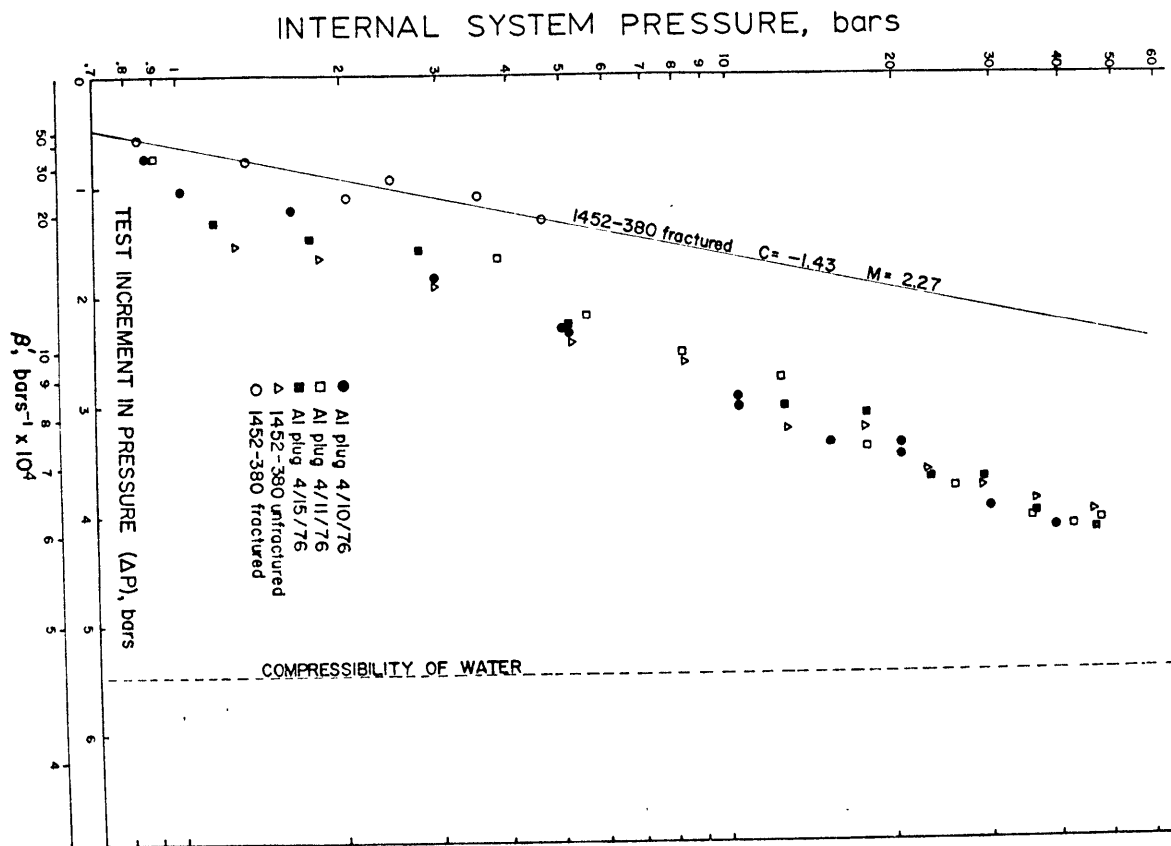
ιre 3-3. Effective fluid compressibility, β', as a function of the internal pressure of the

neability system.   β' is derived from the change in internal pressure, ΔP, due to a small

ιge in the system volume.   The thin solid line is an example of least squares curve fitting

determine the parameters c and m (see text).

where P is the internal pressure of the system.

If we define β' such that

$$\beta' = \frac{\Delta V^*}{V} \Delta P \qquad (3-4)$$

then

$$\ln P = c + m\left(\frac{1}{\beta'} \frac{\Delta V^*}{V}\right)$$

or

$$\beta' = \Delta V^* m / V(\ln P - c)$$

Putting this relation into equation (3-3) yields

$$\beta dP/P = \frac{\Delta V^* m}{V} \frac{dP}{P(\ln P - c)} = \frac{-kA}{\mu Vh} dt$$

or equivalently

$$\frac{dP}{P(\ln P - c)} = \frac{-kAVdt}{\mu Vh \Delta V^* m} = \frac{-kAdt}{\mu h \Delta V^* m.}$$

Integrating gives

$$\int \frac{dP}{P(\ln P - c)} = \frac{kA}{\mu h \Delta V^* m} \frac{dt}{} = \frac{-kA}{\mu h \Delta V^* m} t + const.$$

The pressure integral can easily be solved using the substitution x = $\ln P - c$ so that dP = $\alpha e^x dx$. Then,

$$\int \frac{dP}{P(\ln P - c)} = \int \frac{\alpha e^x dx}{\alpha e^x \, x} = \int \frac{dx}{x} = \ln x = \ln(\ln P - c)$$

Hence,

$$\ln(\ln P - c) = \frac{-kA}{\mu h \Delta V^* m} t = bt. \qquad (3-5)$$

The slope b of a plot of $\ln(\ln P - c)$ versus time yields the coefficient of time in the middle term of equation (3-5). After calculation of c and m, the only unknown variable is permeability k.

The dependence of compressibility on pressure requires that measurements such as in figure 3-3 be made frequently, usually before each permeability determination. This method has the disadvantages that several additional measurements must be made and the new parameters m and c introduce considerable error. However, there are several advantages to this method: (1) the exact system volume, V, for each determination is not needed; (2) the effects of the system components, air bubbles, etc. are measured directly so that the experimental set-up need not be precise and can be accomplished quickly; and (3) the sensitivity of the system can be varied enormously, as is required for the large variations of permeability encountered during this study.

Two basic modes of permeability determination were used: k as a function of confining pressure and k at zero confining pressure. The permeability versus confining pressure equipment is similar to that of Brace et al. (1968). The configuration of the sample, reservoir, and end plates is shown in figure 3-4. The plates are made of brass with stainless steel fittings soldered in place. A thin epoxy cylinder is molded around the sample to prevent fluid flow along the sides of the sample and to serve as a guide sleeve for the end plates. The screen and grooves allow even flow to the sample surface. Simultaneous measurements of resistivity can be made since the reservoir plate is isolated from the pressure vessel. The reservoir capacity is approximately 25 cubic centimeters of which 5 cubic centimeters
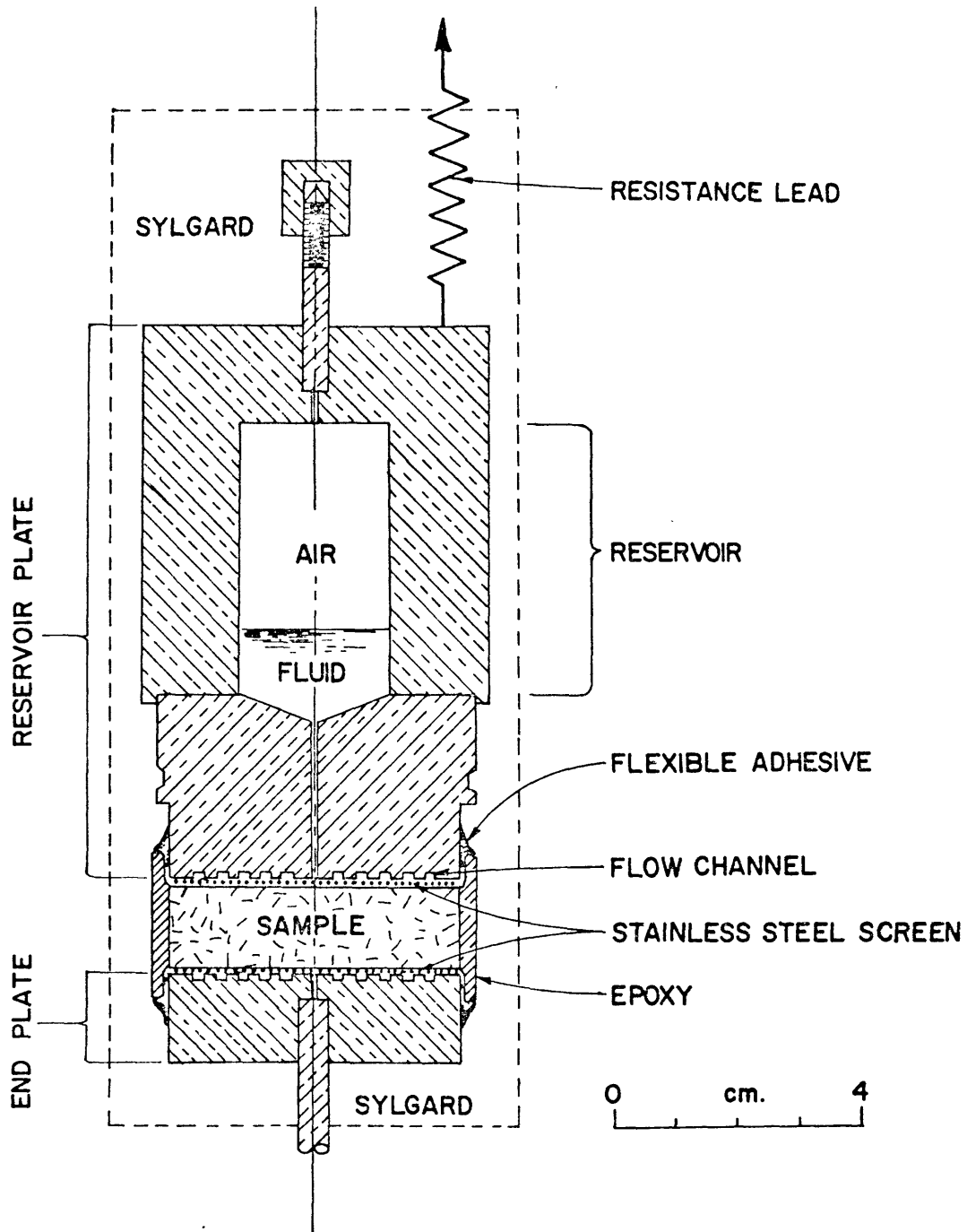
Figure 3-4. High pressure permeability assembly.

are initially filled with fluid to insure uniform wetting of the sample surface. During most permeability determinations, only a fraction of a cubic centimeter enters the reservoir. The air-filled volume is still large enough so that P_2 remains approximately zero. The entire assembly is encapsulated in silicon potting compound to exclude the pressure medium. Permeability can be measured as a function of hydrostatic pressure up to two kilobars.

The experimental arrangement is shown schematically in figure 3-5. During a permeability determination, the system is isolated by closing valve 4. Compressibility is checked at several fluid pressures by partially (but not completely) closing valve 5 with a specific number of turns. The valve needle moving in displaces the volume ΔV^*. The isolator is used to prevent mixing of the KCl solution moving through the sample with the distilled water in the rest of the system. Except for one fitting, the entire system can be leak-tested between determinations.

An example of a permeability determination or 'run' is shown in figure 3-6. The measurement of the effective fluid compressibility precedes the run. The large curvature in the record is due to both the decrease in the pressure gradient with time and the non-linear scale (due to the electronics) on the recorded graph. The initial portions of the determinations for low permeability samples were not picked to avoid the effects of fluid pressure equilibration.

Permeability measurements made with no confining pressure are quicker and less complicated in set-up than the high pressure determinations. A cross-secton of the zero confining pressure assembly
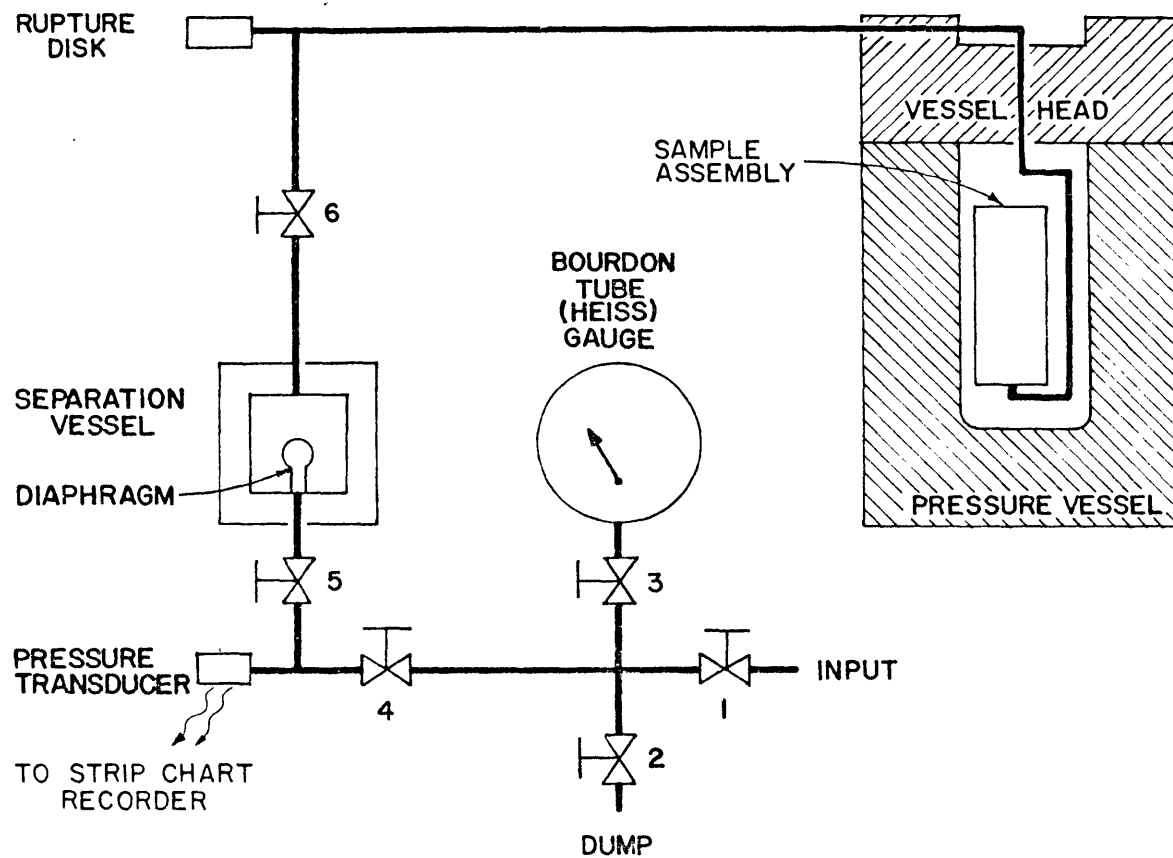
Figure 3-5. Experimental schematic for high pressure permeability determinations.
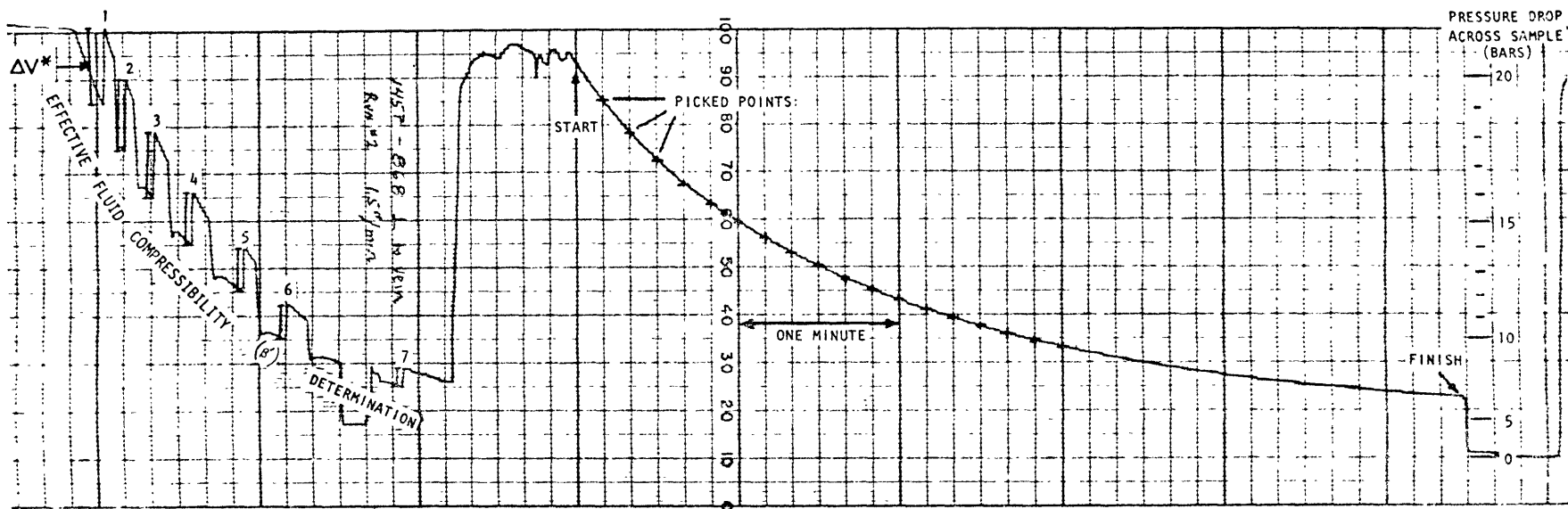
Figure 3-6. Annotated permeability and effective fluid compressibility determinations. The compressibility determination was made by injecting the amount, ΔV*, of the solution (1 to 7) into the otherwise closed system. 'Picked Points' refers to the data points used in the permeability determination.

is shown in figure 3-7. This assembly replaces the separation vessel in the schematic of figure 3-6. Valve 6 and the pressure vessel are disconnected. The zero pressure measurements use the same general procedure as in the permeability versus confining pressure determinations. Although the large fluid pressures can result in large negative values of effective pressure within the sample, the effect is countered by the constraining epoxy mount and sample ring and by the stress pushing the sample against the bottom plate. Figure 3-8 shows multiple runs made on three samples with pressure gradients that vary significantly. The permeability values vary somewhat during the determinations, but remain within the accuracy limits of about a factor of two throughout the entire range of pressure drops.

The major sources for errors in these permeability determinations arise from the measured parameters, temperature fluctuations, and leaks. The measured parameters are those in equation (3-5). The sample dimensions, fluid viscosity, pressure, and time measurements are all accurate to within a few percent. The viscosity of water varies less than one percent over the pressure, temperature, and salinity ranges considered here (Matthews and Russell, 1967). The compressibility slope, m, can vary by 10%. Variations in the compressibility intercept, c, are important because they are subtracted from the ℓnP term in equation (3-5). The inaccuracies in c can be as large as 50% of the calculated value. The absolute values of c are coupled with the value of pressure, however, so that ℓnP-c is always positive. The variations in c affect the left side of equation (3-5) and alter the determination of the slope b by as much as a factor of two.
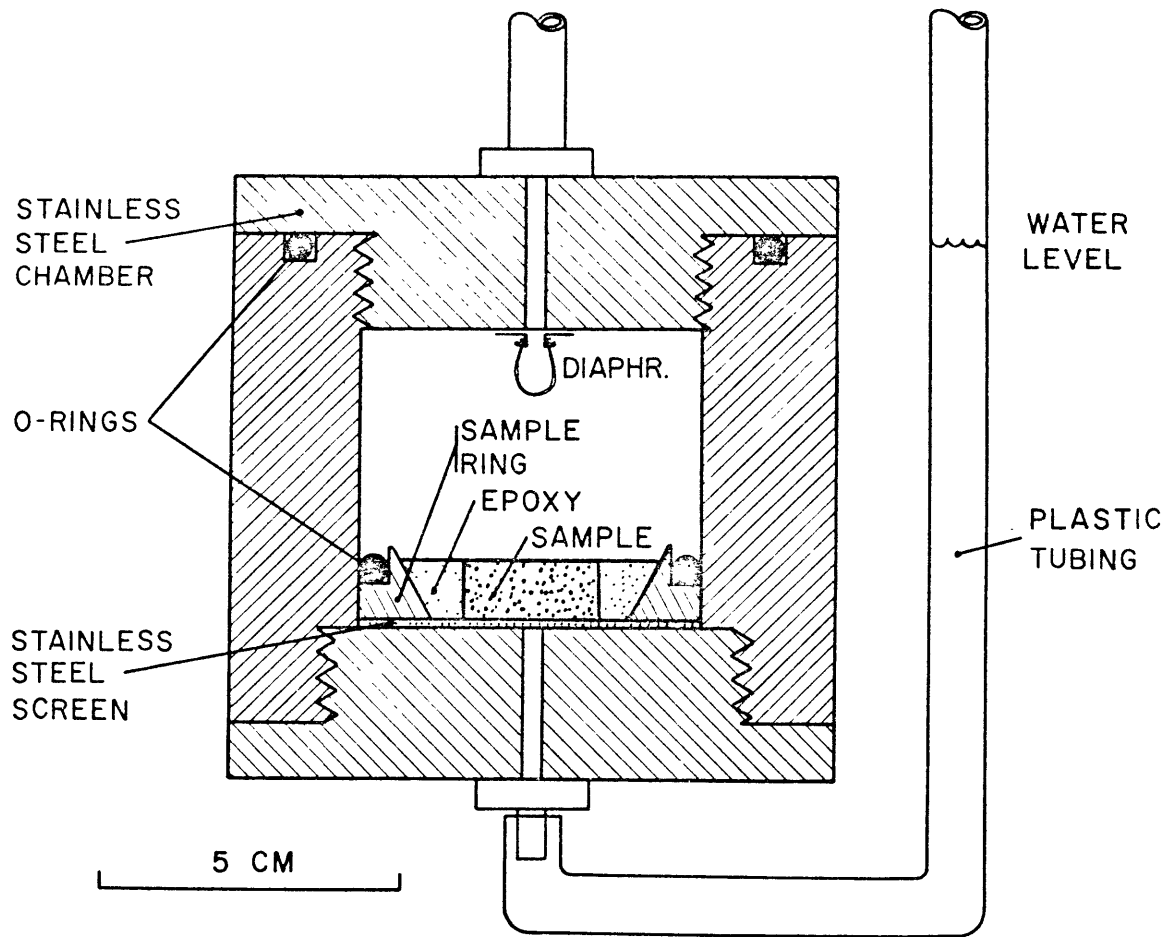
Figure 3-7.   Zero confining pressure permeability apparatus.
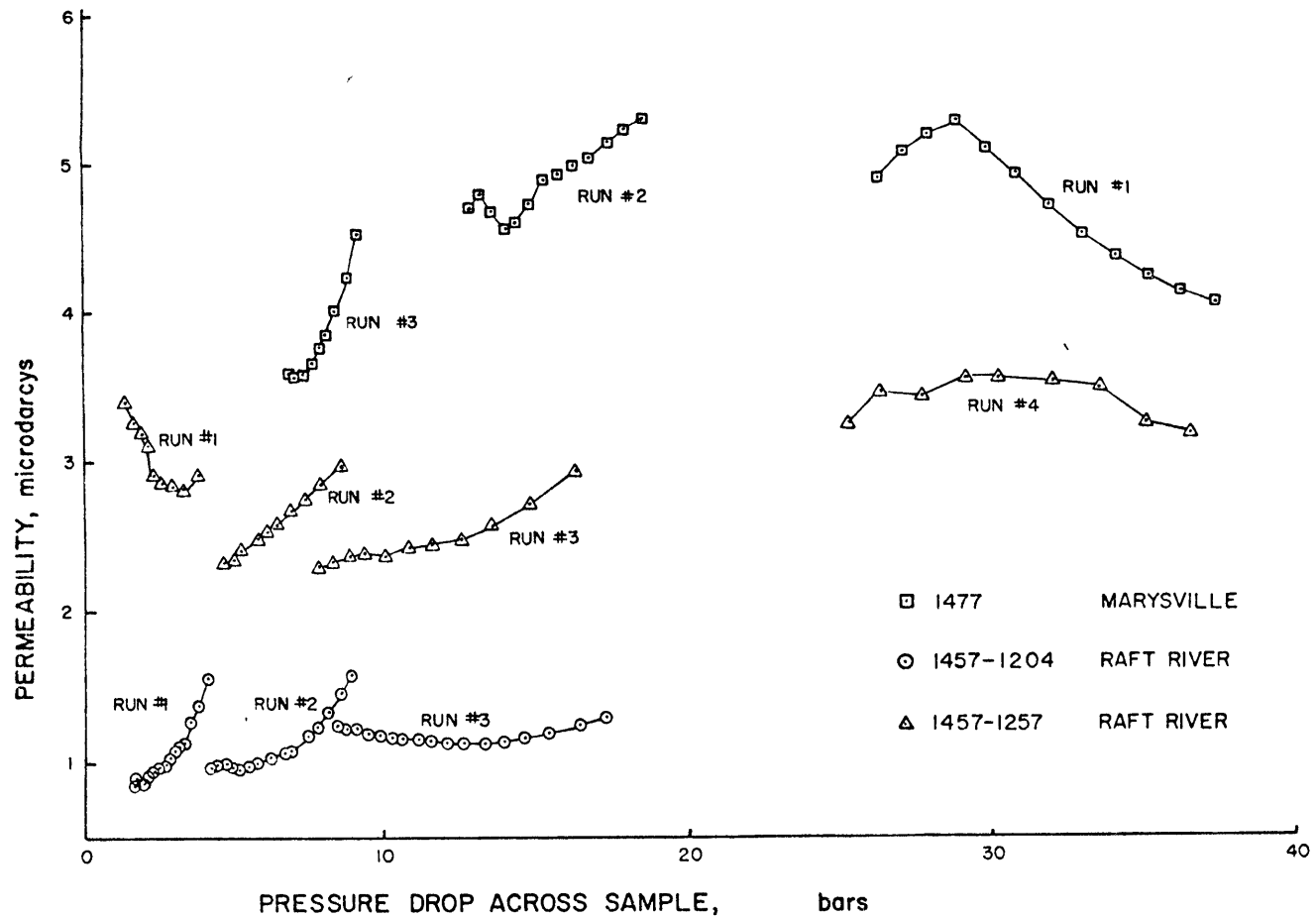
Figure 3-8. Multiple permeability determinations or 'runs' on three samples made at several different pressure gradients.

Temperatures in the laboratory can vary several degrees during a measurement. The effect of the temperature fluctuations depends on the magnitude of the fluctuation and the current value of effective fluid compressibility. The result of these variations is an uncertainty in the absolute measurement of k. When water is used as the flow medium, this uncertainty is on the order of half a nannodarcy. Hence, the temperature variations are important for low values of permeability and serve as a lower limit to the measurement of k.

The system is checked for leaks before most runs. Leakage effects can be measured and removed in the data reduction process. Leakage results in a limitation of the minimum measurable permeability similar to the temperature effects. With effort, leaks can often be reduced so as to have a smaller effect than temperature fluctuations. Again, the measured values of samples with low permeability are most affected.

The overall experimental error is a factor of two to three for samples with permeabilities above a few hundred nannodarcys. The error increases with decreasing permeability to the limit of resolution of approximately one nannodarcy for the fluid (water) used in this study. However, the precision of the technique is much better. During 'permeability versus confining pressure' runs, the only physical parameter to vary is the confining pressure. Measurements then have a precision of from 30 to 50%.

With few exceptions, the permeability measurements were made on right circular cylindrical samples. The diameters ranged from 2.5 to 4.75 centimeters and thicknesses from one to four centimeters. The end surfaces were ground parallel to one another to within a few

hundredths of a millimeter. During mounting and subsequent leak test-
ing, the ends were sealed with tape or teflon masking. If a sample
was longer than the holder ring, the sides were coated with epoxy to
prevent fluid flow through and along the sides.

Resistivity/Conductivity Measurements

Resistivities were measured on numerous samples saturated with
various solutions. A frequency of 100 Hertz was used in order to re-
duce electrode polarization. The samples were usually right circular
cylinders. The lateral surfaces of all samples were coated with epoxy
to prevent conduction along surfaces. Measurements were made after
(or during) permeability runs so that the samples were flushed and
saturated with the appropriate electrolyte, usually 0.02 or 0.04 molar
KCl solution. Other samples were saturated by being placed under
vacuum for several hours and then vented with the proper electrolyte.

Two different methods were used to determine resistivity. The
first method consisted simply of comparing the voltage drops across
the sample and a known resistor in series with the sample. These
measurements were taken at atmospheric pressure with sample contact
made through damp filter paper over copper screen electrodes. The
contact resistance was on the order of 100 ohms. The second method
used the bridge shown in figure 3-9 for measurements during permeabil-
ity versus confining pressure runs. The two channels of a dual trace
oscilloscope were subtracted for use as a null detector. This bridge
was used because the oscilloscope, oscillator, and sample assembly
all shared a common ground. One disadvantage of this last method over
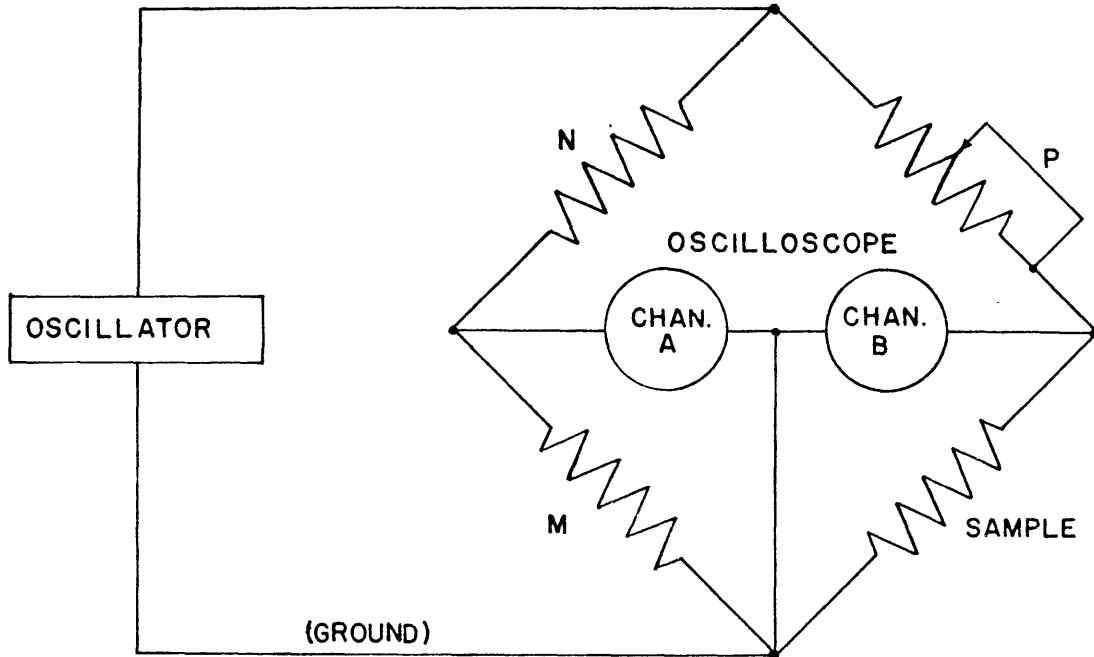
$$\text{SAMPLE RESISTANCE} = \frac{M}{N} \cdot P$$

Figure 3-9.   Resistance bridge used during permeability versus confining pressure measurements.

the first was the relatively low input impedance of the oscillo-
scopes (~1 megΩ) which limited the upper values of resistivities mea-
surable. For both techniques, measurements have an error of about
5 to 10% for most samples although this error increases to more than
20% for highly resistive samples.

Porosity

Sample densities and porosities were determined by immersion in
water. The specimens were evacuated for several hours at approximately
one torr and then 'vented' with water for saturated and submerged
weight determinations. Samples were evacuated again at 40°C and then
vented with dry nitrogen for dry measurements. Errors are 5 to 10%
for the better indurated rocks; for friable and unconsolidated rocks
which tended to break and crumble, particularly when damp, errors may
be as large as 20 or 30%.

Observational Methods

A variety of observational and analytical equipment was used in
this investigation, including the petrographic microscope, the scanning
electron microscope, a cathodoluminescence attachment, the electron
microprobe, and x-ray diffraction. Most of this equipment and the
associated techniques are described adequately in the literature. Only
the exceptional details pertinent to this investigation will be des-
cribed below.

The petrographic microscope was used predominantly to examine
the morphology and texture of the fractures and veins within samples.

Bulk rock mineralogy was usually only cursorily examined. Both
standard (30 μm) thin sections and 'crack sections' (100 μm) were
examined. The crack sections are valuable because they can be used
to get a three-dimensional view of the features contained in a slide.
As the microscope stage is raised and lowered, specific levels within
the section come into focus. Thus, features can be observed at dis-
tinct levels throughout the depth of the crack section. The opacity
of some samples, particularly clay-rich specimens, limited observation
to surface textures. Crack and thin sections must be prepared with
care to prevent adding or modifying cracks. Heating, rough sawing,
and stressing must be avoided. At least a one millimeter layer was
ground off each saw-cut face with a succession of fine grinding pow-
ders to remove any saw damage. Detailed descriptions of the prepara-
tion and observational techniques used in similar studies on igneous
and metamorphic rocks are given by Simmons et al. (1975), Simmons and
Richter (1976), and Richter and Simmons (1977).

The scanning electron microscope (SEM) was used to examine the
fracture and veining morphology. The SEM has been used extensively
recently to observe fractures and pores in many rocks (see, for example,
Sprunt and Brace, 1974; Montgomery and Brace, 1975; Richter and Sim-
mons, 1974). The same crack sections that were used on the petro-
graphic microscope were used with the SEM. Further preparation is
needed, as described in Sprunt and Brace (1974). A layer of several
tens of micrometers must be removed by bombardment with ionized argon.
This ion thinning gently removes any remaining damage due to grinding.
The thinning rate varies greatly among the various minerals from

relatively slowly for plagioclase to quickly for quartz and mica. The variations in thinning rate produce uneven sample surfaces. Numerous mounds up to 50 μm wide and perhaps a micron high cover the sample surface as thinning artifacts. The exact cause of these mounds is not understood but is related to the composition or impurities of the thinned phase. Exsolution twins, mineral zonation, and overgrowths often have characteristic mound densities and shapes. Fracture edges, grain boundaries, and mineral defects are not preferentially thinned. The topography produced by the mounding and variations in the extent of thinning are extremely useful for identifying minerals and locating grain boundaries. Large mosaics were constructed from individual Polaroid photographs with small fields of view but high resolution and magnification. Large mosaics could thus be used to examine in detail extensive portions of sample surfaces. Analyses could be made at specific locations using the energy dispersive analyzer attached to the SEM. These analyses are somewhat qualitative, however, due to the background effects and the lack of comparative compositional standards (Belk, 1974). The maximum resolution on the SEM is limited to a few hundred Angstroms due to the conductive coating deposited on the sections.

The electron microprobe was often used during this study both for point compositional analysis and analysis conducted along traverse lines. The microprobe technique is described in detail elsewhere (see, for example, Reed, 1975) and the following discussion serves only to describe the difficulties encountered in this study. The minerals examined during this investigation typically were hydrous or light

element phases such as clays and carbonates. The microprobe usually cannot be used to determine the content of elements lighter than sodium. Hydrous phases often decompose under the electron beam. Compositionally similar standards were usually not available so that correction factors had considerable error. Due to the fracture content and extremes in hardness, sample surfaces were often very irregular. Analyses of common non-hydrous minerals such as feldspars usually have errors of less than a few percent. Hydrous or light element phases can have errors which are considerably greater and analyses are often only qualitative.

Cathodoluminescence refers to the phenonemon that some materials emit light when bombarded with high energy electrons. A Nuclide Corporation Luminoscope was used in this study and consists of a high voltage source and a vacuum chamber. The chamber is mounted on a standard petrographic microscope. Electrons are accelerated through approximately ten to fourteen kilovolts in a partial vacuum of approximately 40 millitorr and focused on the sample. The light emitted is observed through the microscope. Details of the technique and applications have been described, for example, by Smith and Stenstrom (1965), Sipple (1968), and Sommer (1972). The intensity and color of the luminescence are dependent upon composition, particularly trace or contaminant elements. Cathodoluminescence is particularly useful for studying carbonates in which Mn^{++} serves as an activator or source. Zonation, overgrowths, and different veining mineralizations which cannot be observed under plane or polarized light often become apparent by cathodoluminescence. Because the luminescence is sensitive to trace

element variations, even coarsely crystalline and otherwise uniform calcite may display fine textures. Since the luminescence is a surface property, polished slabs can be used which are quickly and easily prepared. This technique does have several disadvantages: many minerals display no cathodoluminescence at all; iron, a common contaminant, quenches or prevents luminescence; and samples may overheat and be damaged and distorted during bombardment, particularly during the long exposures necessary for photography.

CHAPTER IV

INITIAL PROPERTIES AND PROCESSES

Introduction

The initial geologic environments encountered in a developing geothermal system will be discussed in this chapter. Igneous and metamorphic rocks such as those found in the basement of Marysville, Raft River, and Roosevelt Hot Springs will be described briefly. Next, examples of the more common unaltered sedimentary rocks that typify the Dunes, Heber, and Raft River will be presented. A description of the effects of the various stages of diagenesis and lithification will follow. These diagenetic processes can be either 'normal' or processes more directly related to the invasion and reaction of hydrothermal fluids. The results of the lithification necessitate the initialization of the fracturing-refracturing cycle to keep the system open to continued circulation.

Although the rocks in the geothermal system may be progressively modified, unaltered rocks will exist both at the periphery and within the system. Figure 1-2 illustrated how altered and unaltered rocks can be intimately mixed. Indeed, most of the samples discussed in this chapter as examples of unmodified rocks actually come from wells drilled over the most active parts of the geothermal systems. Appendix 1 contains a complete listing of the physical measurements made on each specimen.

Starting Materials

Geothermal systems can occur in almost any near-surface geologic

environment. The exact location of a convective system is dependent
on the location and type of heat source. Areas of abnormally high
heat flow and the regions adjacent to virtually all large siliceous
intrusives may have, or may have had at one time, an associated hydro-
thermal system. Evidence for this association is the ore deposits
and alteration zones commonly found around exposed intrusives (Smith
and Shaw, 1975). The placement of the heat source will be independent
of the surficial geology, although the precise flow patterns will be
controlled by local structures, stratigraphy, and hydrology. The
result is that a wide range of geologic materials, properties, and
conditions may be encountered by a developing geothermal system.

The geologic units in the Marysville area and the deeper units in
the Raft River, Coso, and Roosevelt areas are composed of igneous or
metamorphic rocks. These rocks usually have relatively low values of
matrix permeability, conductivity, porosity, and fracture content.
Their location in the generalized system is represented by circle 1 in
figure 1-3. The differential strain analysis (DSA) curves for a Marys-
ville sample from a depth of 1954 meters are shown in figure 4-1.
These curves are typical of curves of similar granitic rocks. The data
in figure 4-1a are differential strains versus pressure for three or-
thogonal directions. The curves are relatively smooth and continuously
concave upward. The second set of curves, figure 4-1b, is the cumula-
tive fracture strains or 'linear porosity' measured as a function of
closure pressure. Note that some of the fractures have closure pres-
sures below the approximate in situ pressure. This fracture porosity
would not exist at depth. Note that the cumulative linear fracture
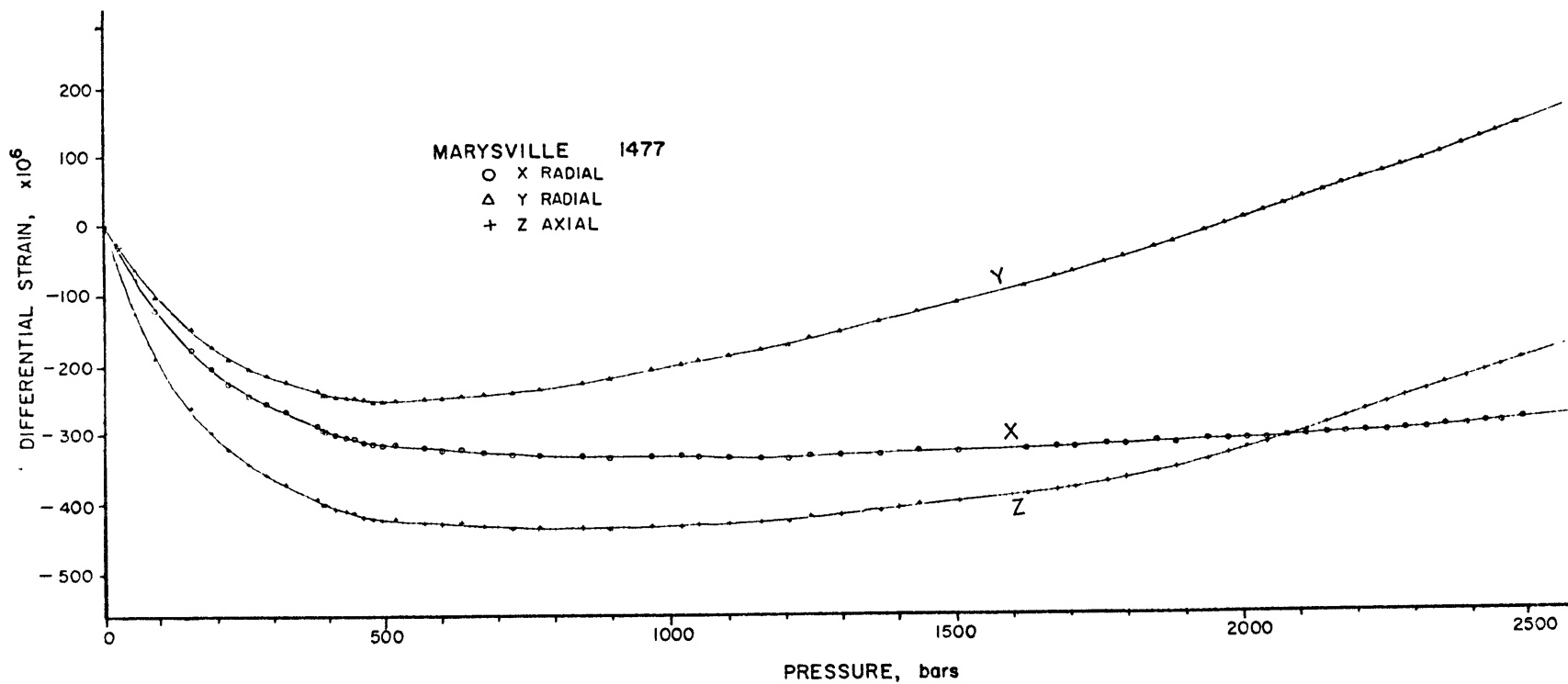
Figure 4-1. Marysville #1477, 1954 meters depth.

(a) Differential strain curves. Note: In this and following strain curves the Z direction is always axial to core, X and Y directions are perpendicular to Z and mutually perpendicular but otherwise arbitrary.
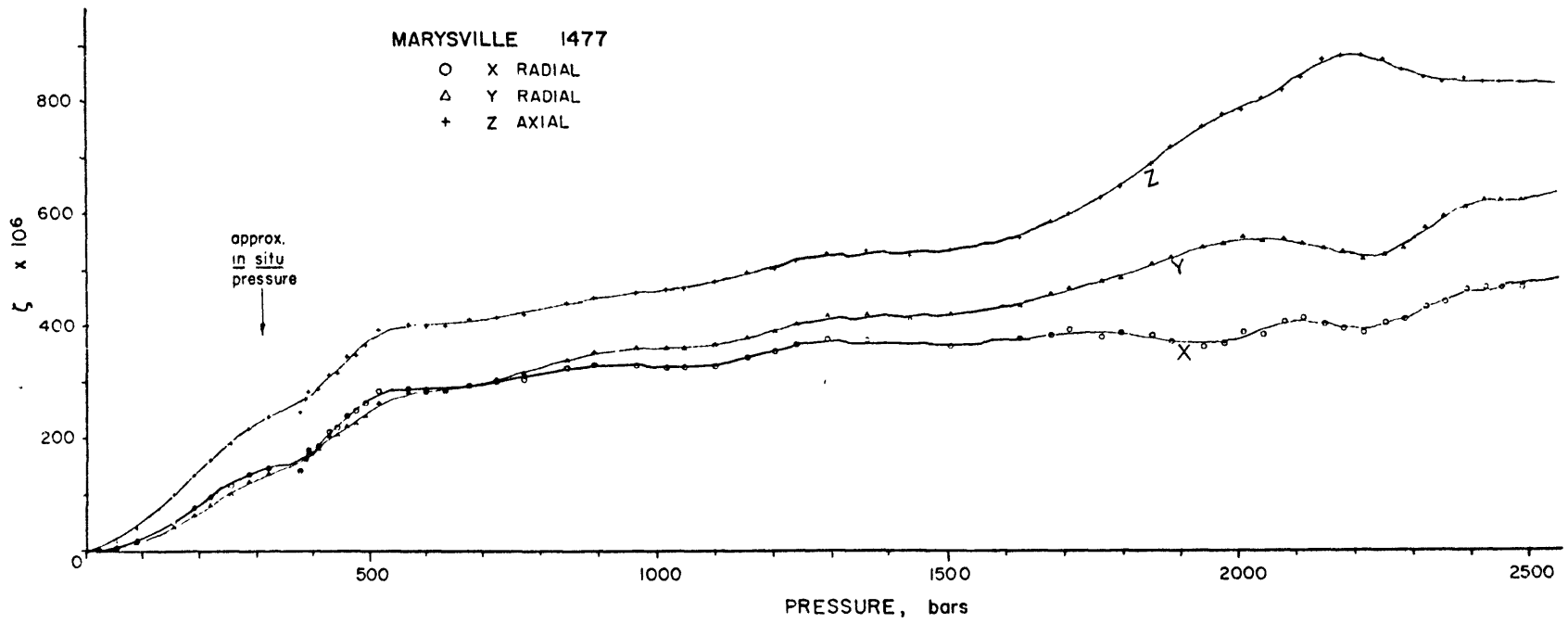
Figure 4-1b. ς (zeta) curves (= cumulative linear fracture strains versus fracture closure pressure).

porosity continues to increase with pressure. Summing the three or-
thogonal strains at high pressure and deducting the values at in situ
pressure indicate that an in situ volumetric fracture porosity in
excess of 0.14% exists. This 'background' fracture content means that
the rock in situ will also have non-zero conductivity and fluid per-
meability. Figure 4-2 shows the permeability and conductivity measured
as a function of hydrostatic confining pressure on another sample from
the same core as the specimen in figure 4-1. The rapid decrease in
permeability corresponds to the closing of fractures with pressure.
The exact relationships between fracture content and both conductivity
and permeability will be examined in detail in the next chapter.

Another set of DSA curves is shown in figure 4-3 for a sample from
a depth of 1525 meters in Roosevelt Hot Springs well. This curve also
indicates a 'background' fracture content. These plots are complicated
by the break in curvature marked by the brackets. This break may. be
due to small amounts of water remaining in the rock during compression
(Feves, 1977). The volumetric crack porosity for this sample is
2.28×10^{-3} at zero pressure or 1.93×10^{-3} when adjusted for in situ
pressure. The total interconnected (immersion) porosity is 2.6×10^{-3}.
Since the crack porosity comprises such a large fraction of the total
interconnected porosity, any fluids within the cracks cannot move into
more equidimensional voids. As fractures start to close with pressure,
the entrapped fluids would also increase in pressure and modify the
strain behavior. This is a possible explanation for the decrease in
rock compressibility indicated by the breaks in curvature at the brack-
ets. Corresponding curves have been obtained for several other unaltered
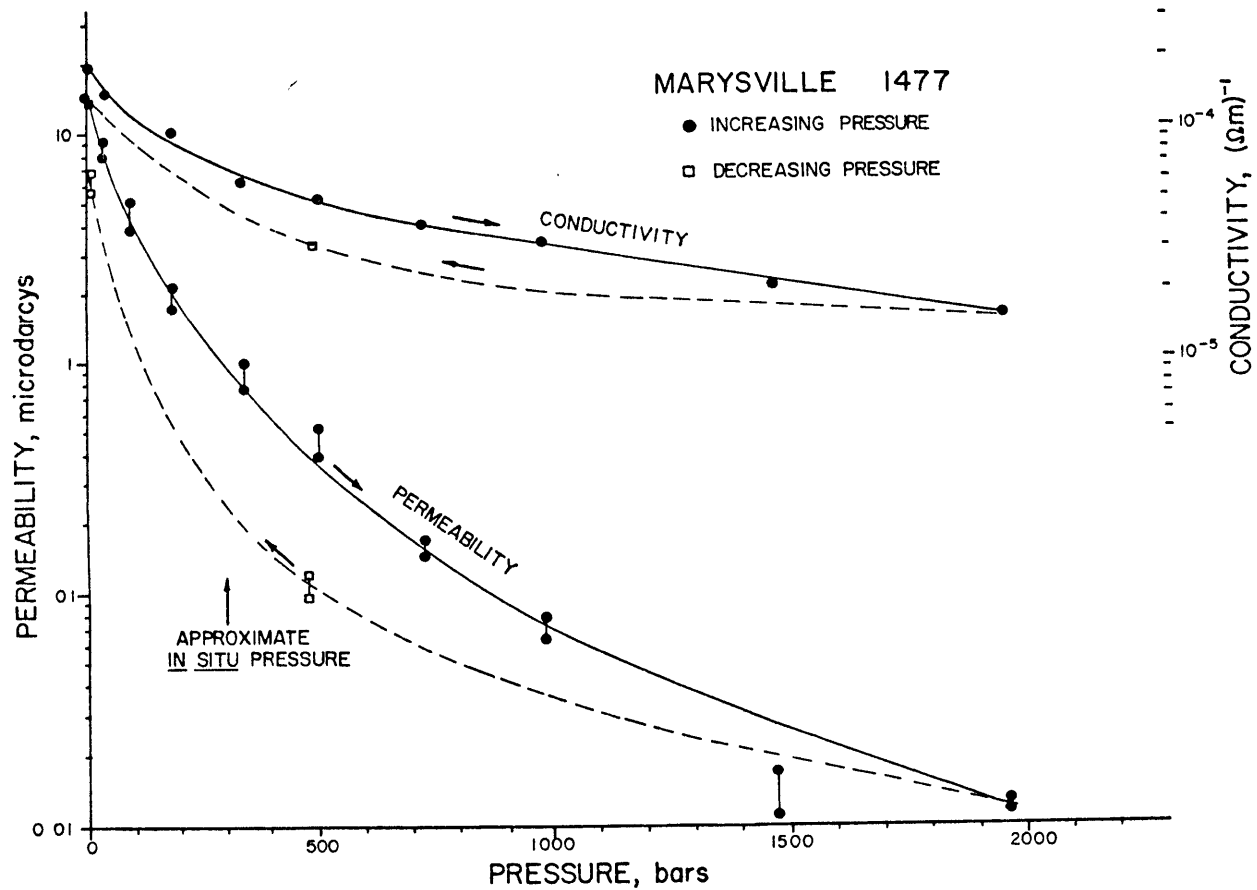
Figure 4-2. Marysville #1477, permeability and conductivity versus hydrostatic confining pressure.
Note: In this and following permeability and conductivity versus pressure curves, circles and
squares connected by thin vertical lines indicate the range of measured values and not estimates
of absolute error.
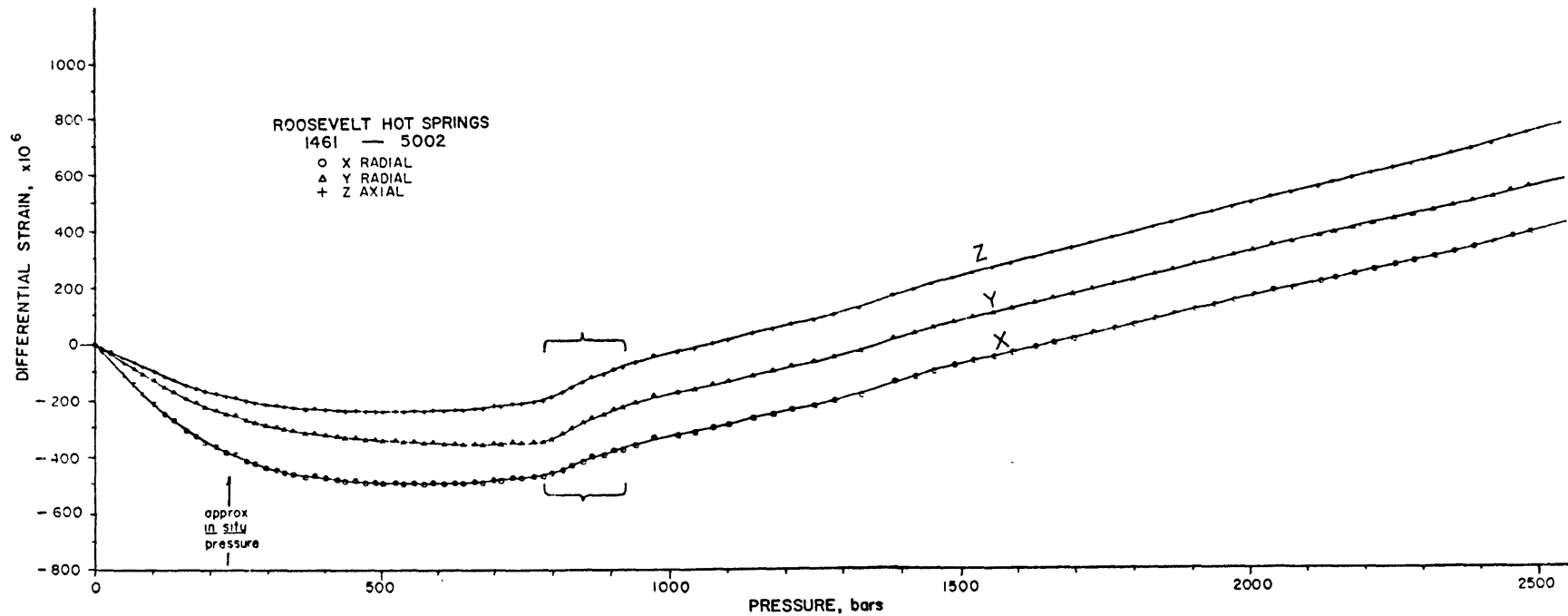
Figure 4-3. Differential strain analysis for Roosevelt Hot Springs sample #1461-5002, 1525 meters

depth. The break in slope on the curves at the brackets may be due to small amounts of fluids

remaining within the rock.

(a) Differential strain curves.
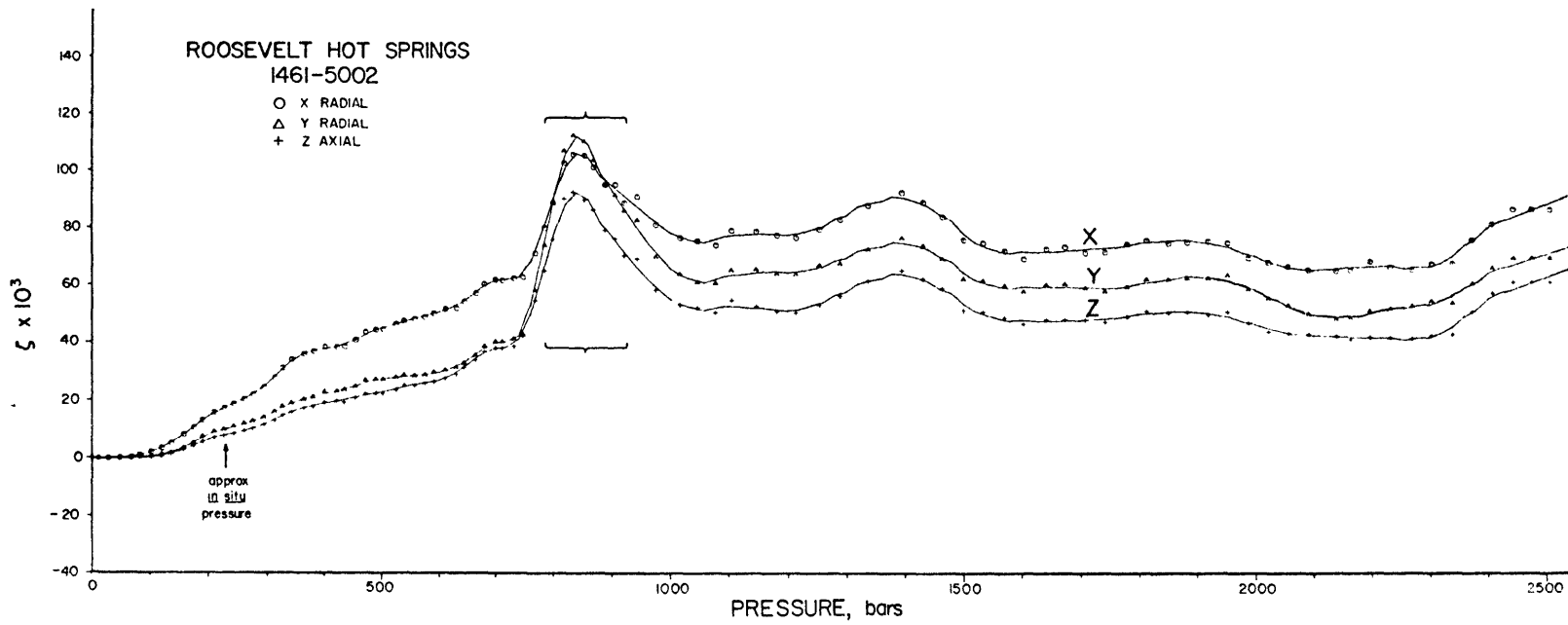
Figure 4-3b. ζ curves. These curves are dominated by the break in slope at the brackets and indicate no subsequent high pressure fracture closure.

igneous rocks. These measured behaviors are typical of many igneous

rocks. For example, the cores from the shallow heat flow wells in the

batholith near Coso Hot Springs, but outside the area of hydrothermal

activity, have curves similar to those in figure 4-1. The sheared

and altered rocks from the deep Coso well, described later, are almost

unrecognizable as originating from the same pluton.

An entirely different type of behavior is exhibited by a Marys-

ville sample from a depth of 179 meters. The nearly linear behavior

of the DSA curves in figure 4-4 is obvious. This linearity starting

from atmospheric pressure indicates a very small fracture content, about

1.2×10^{-4}, that is only poorly defined by the stress-strain plot. The

permeability measured on this core was on the order of a few nannodarcys.

The formation factor was correspondingly high, approximately 3×10^{4}.

This sample is a metamorphosed shale and may behave somewhat plastically.

The rock may be unable to physically support open fractures.

The preceding three paragraphs have described some of the variable

properties measured on the igneous and metamorphic rocks. The trans-

port properties such as permeability do not depend only on the matrix

properties and minute fractures, however. Major fluid transport will

occur through joints and macroscopic fractures that are difficult to

sample. Although the measured permeability for the Marysville sample

of figure 4-2 (#1477) was only a few microdarcys, copious amounts of

water flowed through nearby fracture zones (figure 2-15). Permeability

and other properties presented here are measured on the matrix and

serve to indicate trends and behaviors in physical properties and not

to predict absolute formation values.
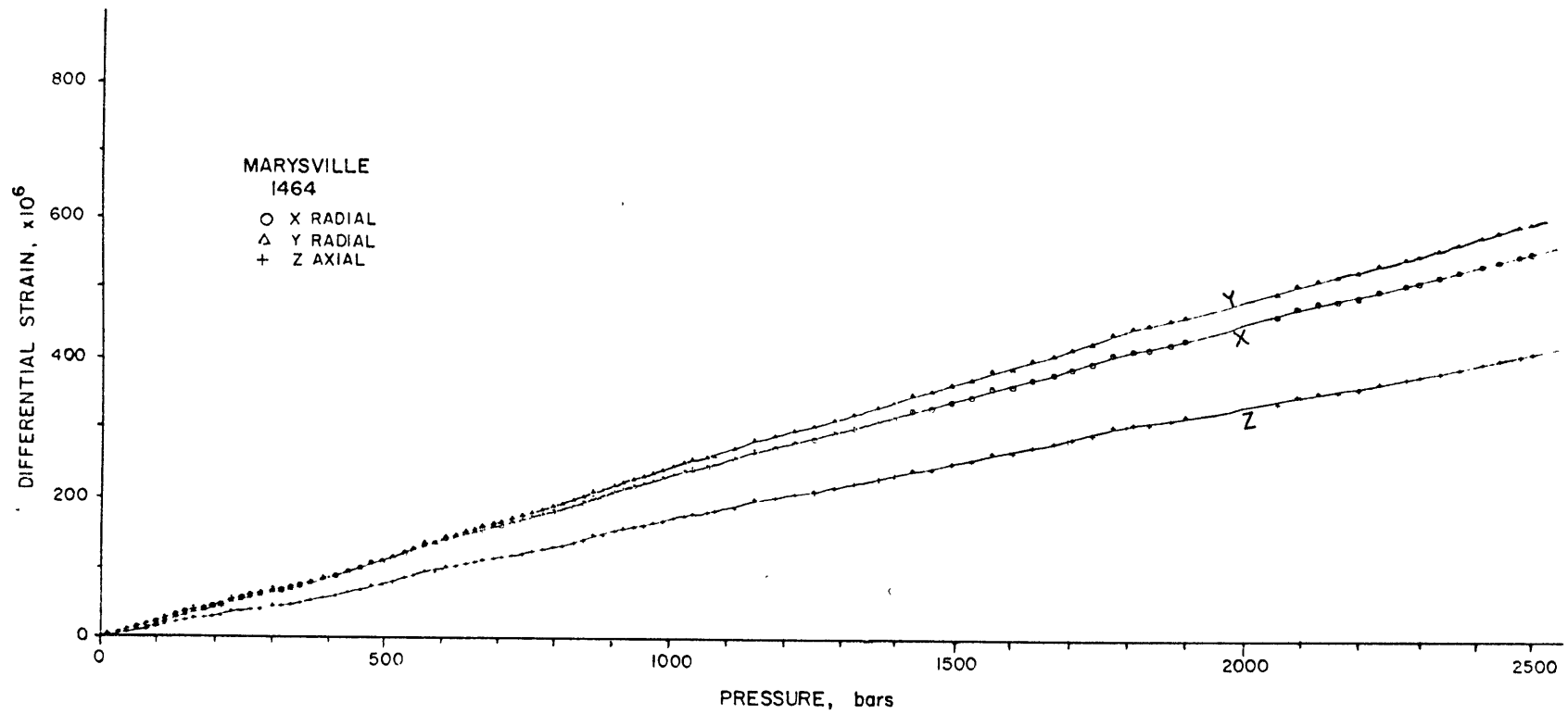
Figure 4-4. Marysville #1464, 179 meters depth, differential strain analysis.

(a) Differential strain. The nearly linear behavior of the curves indicates an almost constant rock compressibility and a low fracture content.
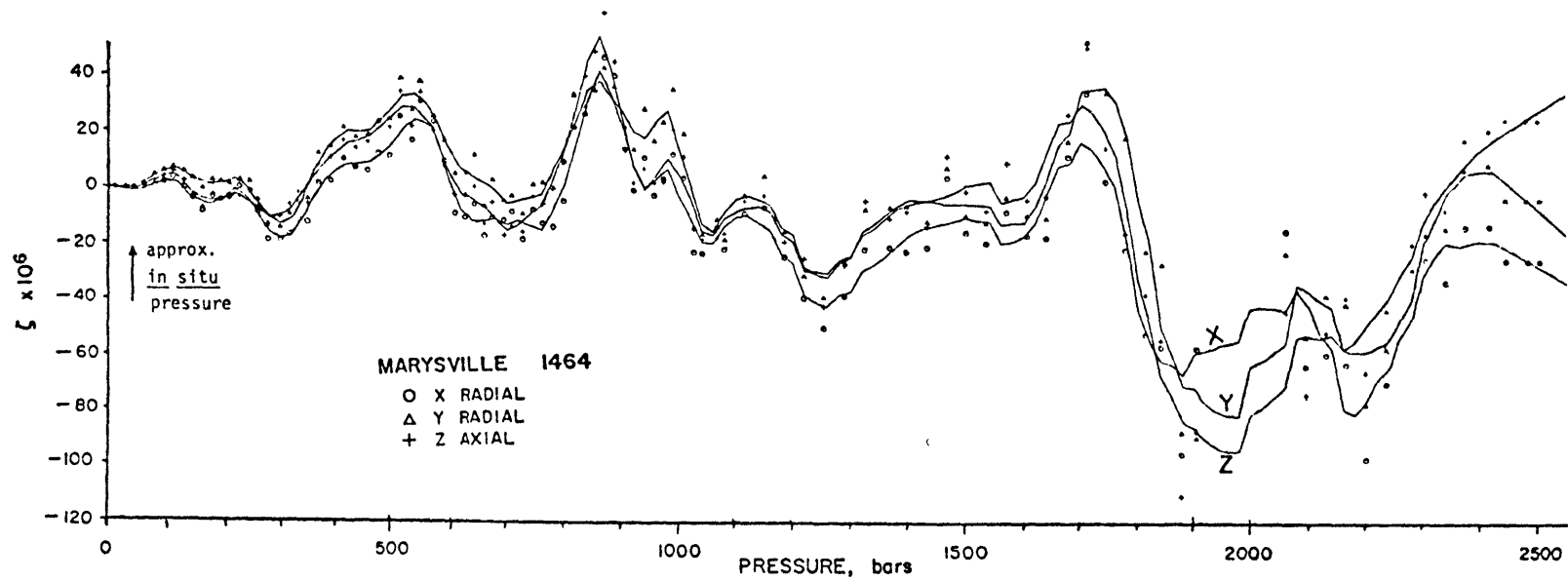
Figure 4-4b. ζ curves. The undulatory behavior of the curves, small magnitudes, and negative

values indicate that the measurement is dominated by noise. The roughly harmonic behavior is

due to thermal strains in response to diurnal fluctuations in laboratory temperature.

Sedimentary rocks are the most common type of rocks obtained for this study. Dunes, Heber, and all but a few Raft River samples are sedimentary. Most geothermal systems have been detected on the basis of surface manifestations. Since sedimentary rocks coat most of the earth's surface most of the discovered systems will be composed at least partially of such rocks. Sedimentary units are often very porous and permeable and can form conduits and reservoirs for hydrothermal fluids. Some of these fluids may be derived from the connate water in the sediments. The stratigraphy often encountered in exploratory wells consists of alternating sands and shales. The full range of mixtures of tuffs, argillaceous siltstones, sandy mudstones, and other sedimentary materials have also been penetrated. The properties of these rocks are extremely sensitive to the postdepositional conditions as well as to the original rock structure and composition. The remainder of this section will describe the properties of more or less unconsolidated and poorly lithified samples. Obviously, there is no definite line dividing lithified rocks from unlithified sediments.

Sands, silts, conglomerates, and other coarse-grained sediments generally dominate as the permeable units at depth. The location of the unaltered coarse-grained material is represented by circle 2 in the generalized system of figure 1-3. Porosity, permeability, resistivity, and compressibility are all dependent on the grading, granular structure or shape, and clay content of the sedimentary unit. These dependencies have been the subject of decades of intensive study by geologists and engineers interested in oil, gas, and water production and general settling properties (see, for example, Chilingarian and Wolf, 1975;

Bear, 1972; Lambe and Whitman, 1969). Several different types of behavior can occur during compaction of unconsolidated granular material. Several recent papers dealing specifically with this topic include Domenico (1977), Zoback and Byerlee (1976), and Raghavan and Miller (1975). Abey (1977) developed a model to describe both the loading and unloading behavior of partially saturated porous material. By use of the porosity, ϕ, data in Appendix I, the void ratio, e, for each sample can readily be calculated through the relation $e = \phi/1-\phi$. Plots of the change in void ratio versus pressure on a log scale are commonly used in the engineering literature. These plots are based on the assumption that all of the sample strain is due to a loss of void space. This assumption is valid for porous, easily compacted rocks. This type of curve is an alternative way to present the strain data obtained with DSA. The logarithmic plot of pressure places emphasis on the low pressure behavior of the sample. The low pressure responses of rocks are important to the economic development of a geothermal site. For example, effective pressure may increase several bars due to fluid production. Such small fluctuations in pressure can be important factors in land subsidence and changing reservoir characteristics. This void ratio-log pressure type of plot will be used for several of the sedimentary samples described below.

A Heber sample from a depth of 970.5 meters from GTW#1 exemplifies the behavior of many of the loose sandy samples. The stress-strain curves are reproduced in figure 4-5; the DSA curve is shown in 4-5a; the volumetric zeta curve is shown in 4-5b; and a plot of void ratio versus log pressure is shown in 4-5c. These curves can be divided into
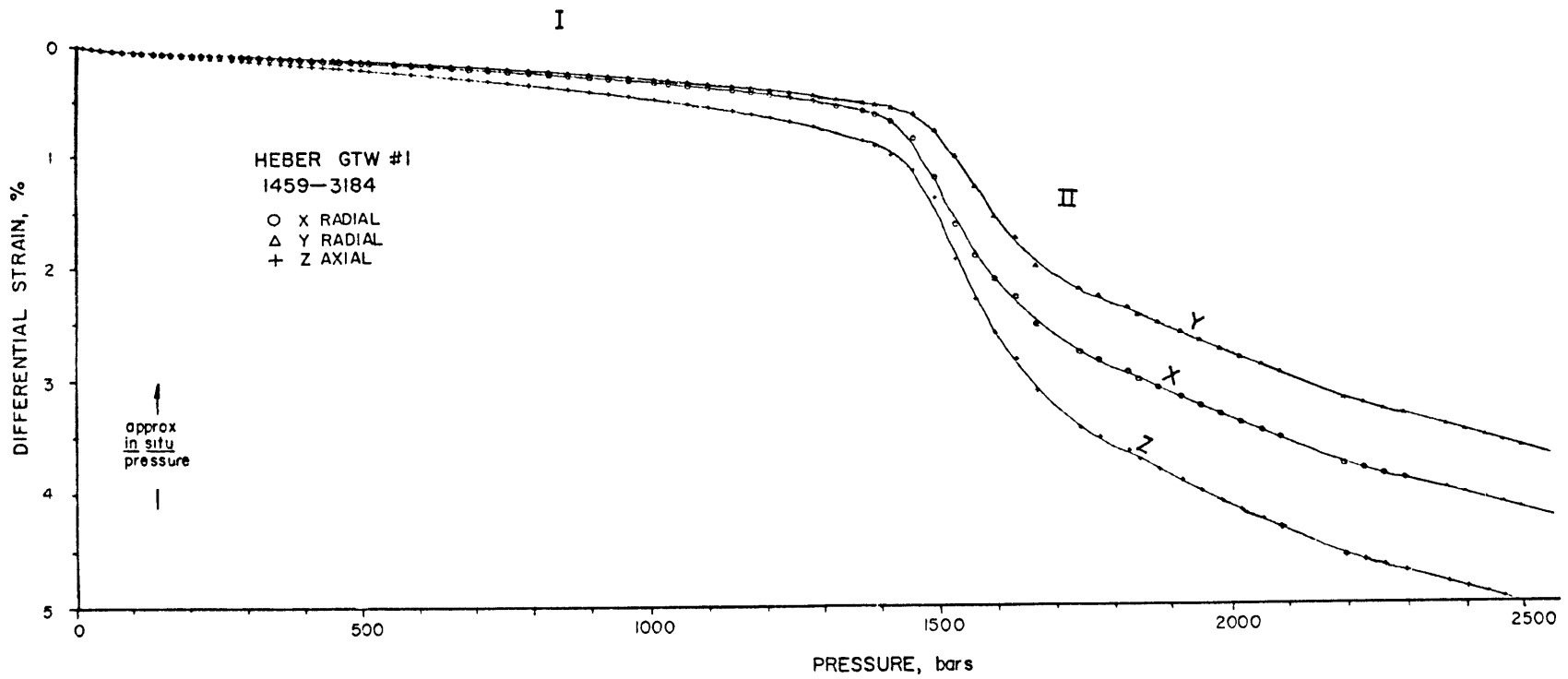
Figure 4-5. Heber GTW#1 sample #1459-3184, 970.5 meters depth. I - compaction region,

II - grain crushing region (see text).

(a) Differential strain curves.
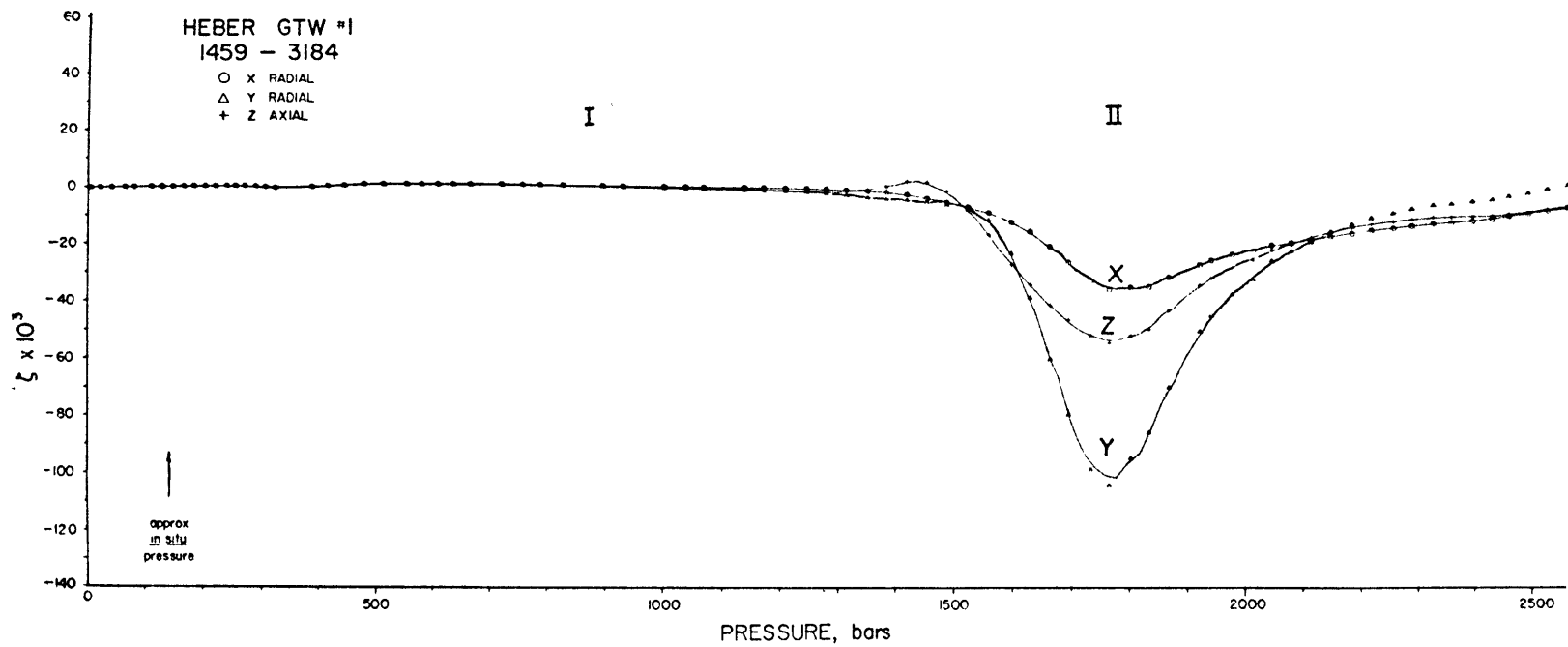
Figure 4-5b. ζ curves. Note how the compaction and crushing of the sample completely obscures the effects of any fractures within the rock.
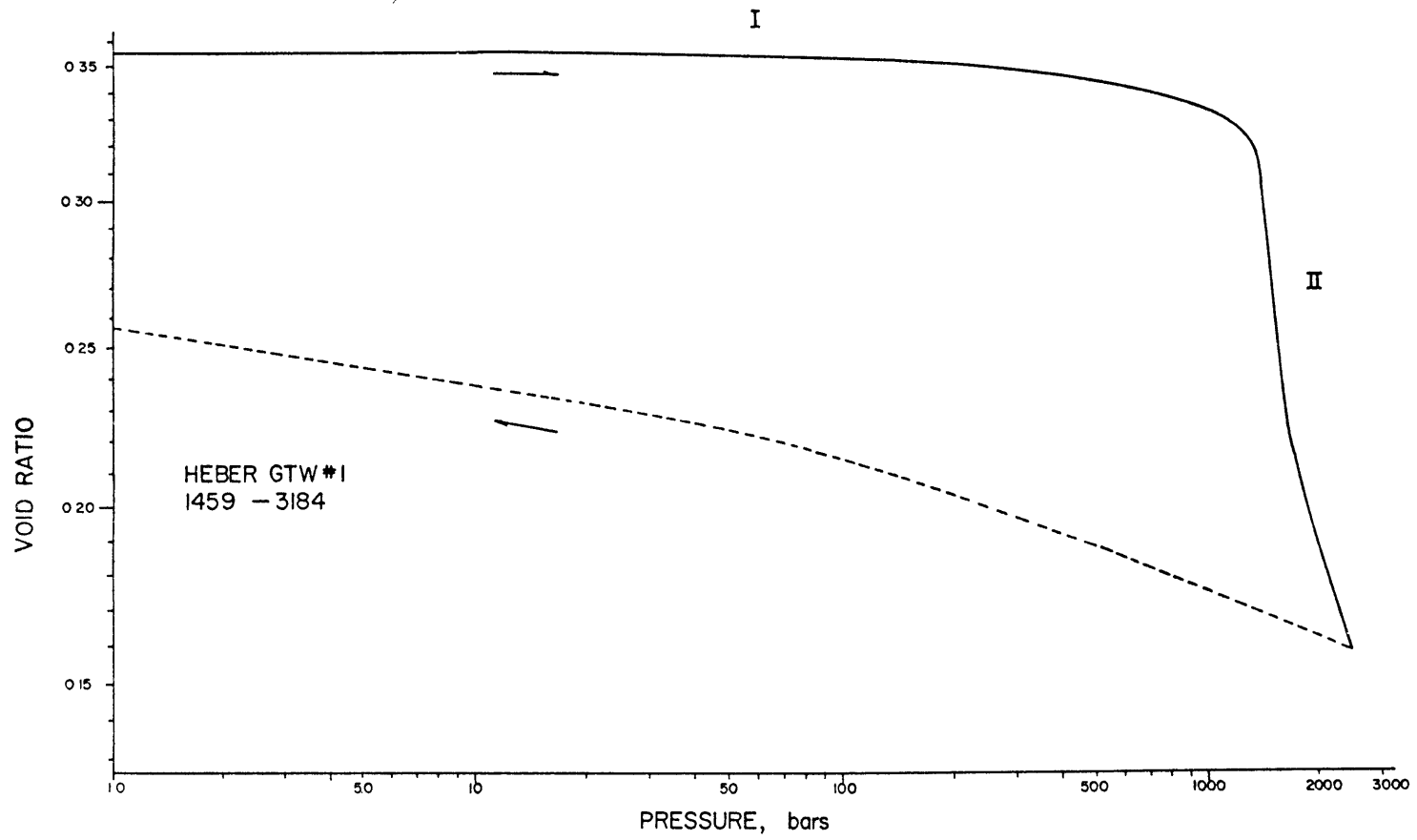
Figure 4-5c. Void ratio - logarithmic pressure plot.

distinct regions. Region I represents compaction due mostly to rear-
rangement of grains into a more dense packing (Lambe and Whitman, 1969).
This sample has probably already undergone some compaction so that the
magnitude of the strain in region I is relatively small. Grain crushing
dominates region II. Point contacts are broken and grains continue to
slide and rotate past one another as the entire skeletal structure slow-
ly collapses. As this process is highly non-elastic and requires con-
siderable grain motion, strains are time dependent. A very large hystere-
sis is developed as the sample is unloaded to atmospheric pressure.
This Heber specimen behaves very similarly to the loose Ottawa Sand
samples of Zoback and Byerlee (1976) and Domenico (1977). The agreement
is even closer if the in situ pressure is considered as preconsolidating
(precompacting) the sample and thus lowering the strain in region I.

Individual compressibility curves for similarly porous samples can
be considerably different from the curves of figure 4-5. For a loosely
packed sample, the magnitude of strain in region I is large and often
is a large fraction of the total high pressure strain. If grains are
very angular, the sediment will have sharper, more fragile point contacts
than sediments with more rounded grains. This will result in the initia-
tion of grain crushing at any pressure down to atmospheric. The strains
of the regions are additive and can overlap to the extent of forming a
single smooth curve continuously concave upwards.

During the compaction of granular materials, permeability and con-
ductivity will continue to decrease with decreasing pore volume. For
sands like the Heber sample in figure 4-5, one can expect an abrupt
decrease in the permeability after the onset of grain crushing. This

type of behavior was observed by Zoback and Byerlee (1976) for the
Ottawa Sand. Permeability changes associated with the compaction of
a very angular, loose, granular material were measured in the present
investigation during calibration runs with 120 grit silicon carbide.
The silicon carbide was loosely packed between a teflon sleeve and two
brass end plates in a similar arrangement to that shown in figure 3-4.
The results are shown in figure 4-6. The permeability decreases linearly
with pressure indicating that there is no abrupt onset of grain crushing
but rather a relatively uniform rate of compression including both con-
solidation or compaction as well as crushing.

Clays, mudstones, and shales are generally highly porous yet inhibit
fluid flow. Because of their flaky, layered and cohesive nature, clays
can form open but poorly interconnected structures. In spite of the low
permeability, the high porosity and large specific surface areas of clays
and clay-rich rocks will result in good electrical conduction due to
mineral surface conduction. Thus, the effects of the clays may dominate
exploratory geoelectrical measurements. Clays are also very compressible
and often behave plastically. During compaction, muds and clays can
lose water in excess of half the original sediment volume (Rieke and
Chilingarian, 1974). This water loss can be a significant source of free
water in deeply buried sediments. The high water content coupled with
the low permeability can produce zones with fluid pressures considerably
higher than hydrostatic (Weaver and Beck, 1971, p. 62; Papadopulos
et al., 1975). Clay units may therefore serve as the controlling factors
in natural subsidence. Circle 3 in figure 1-3 shows the position unal-
tered clay would represent in the generalized geothermal system.
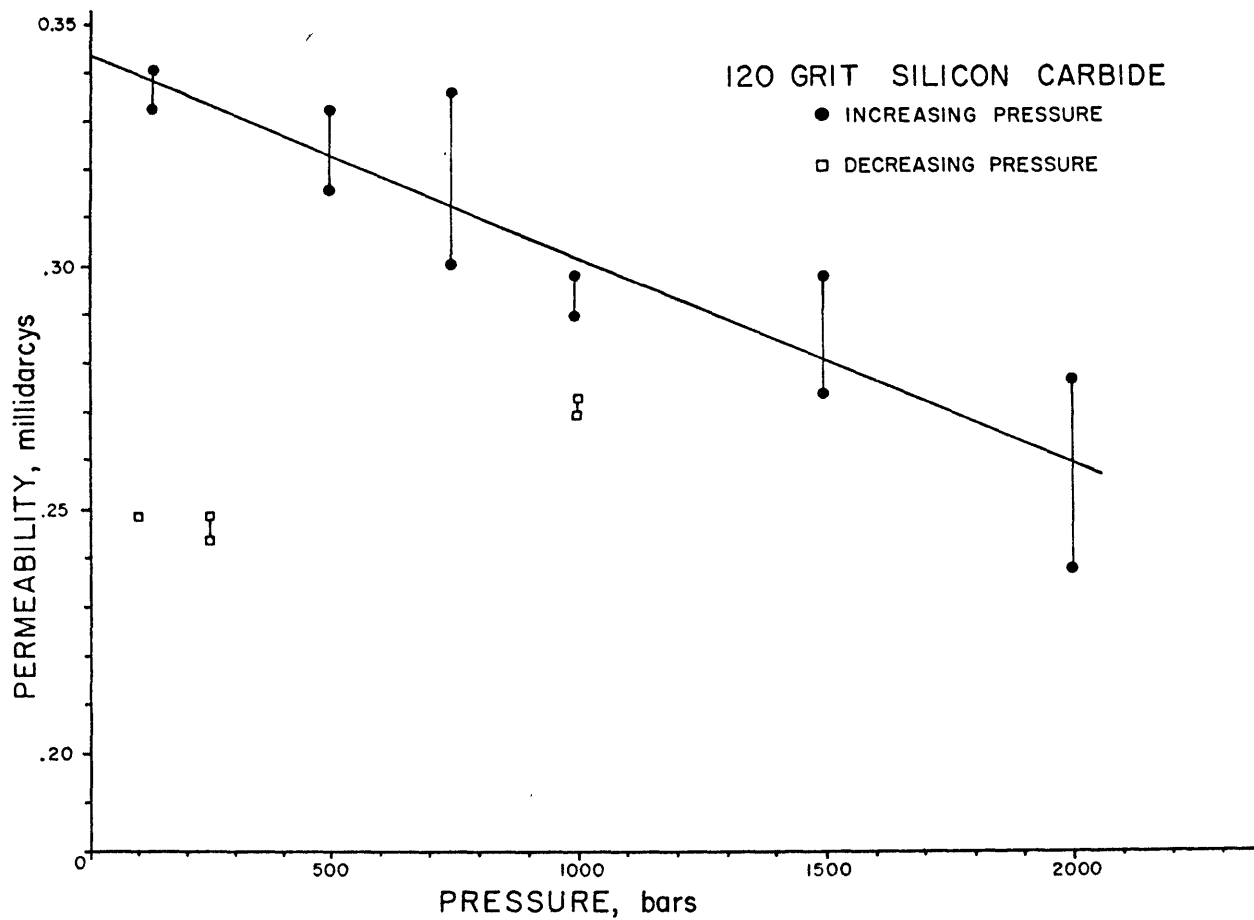
Figure 4-6. Permeability versus pressure for angular, granular silicon carbide.

The stress-strain curves for a sample from 93.9 meters in the Raft River Intermediate well #1 are shown in figure 4-7. This specimen is clay-rich, very porous (approximately 48%), unconsolidated, and very friable. The DSA curve in figure 4-5a displays the sample collapse at low pressure and subsequent compaction until an almost constant volume is reached at about 1300 bars. By 2500 bars, the specimen has decreased in volume by about 27%. The sudden collapse at about 70 bars is more vivid in the void ratio-log pressure diagram of figure 4-7b. This sample typifies the large amount of volume loss that can occur early in the burial history of clays.

The transport properties of permeability and conductivity differ widely from one another in their dependence on the clay content. Figure 4-8 demonstrates how even a small amount of clay can drastically lower the permeability of loose sand. Due to surface conduction, the sample conductivity can actually be enhanced by increasing clay content depending upon the saturating fluid properties. The conductivity dependence will be discussed in detail in another chapter. The permeability, conductivity, and DSA curves are shown in figure 4-9 for a poorly sorted, clay-rich sandy siltstone from a depth of 1287 meters in the Raft River RRGE#2 well. The large decrease in permeability below the in situ pressure may result either from the minor closing of fractures and pores opened as a result of drilling and sampling; or from the slight crushing of the specimen ends by the stainless steel screen. At higher pressure, there is an almost linear decrease of permeabilty with pressure. The conductivity, however, remains approximately constant indicating the dominance of conduction along clay surfaces even for the relatively con-
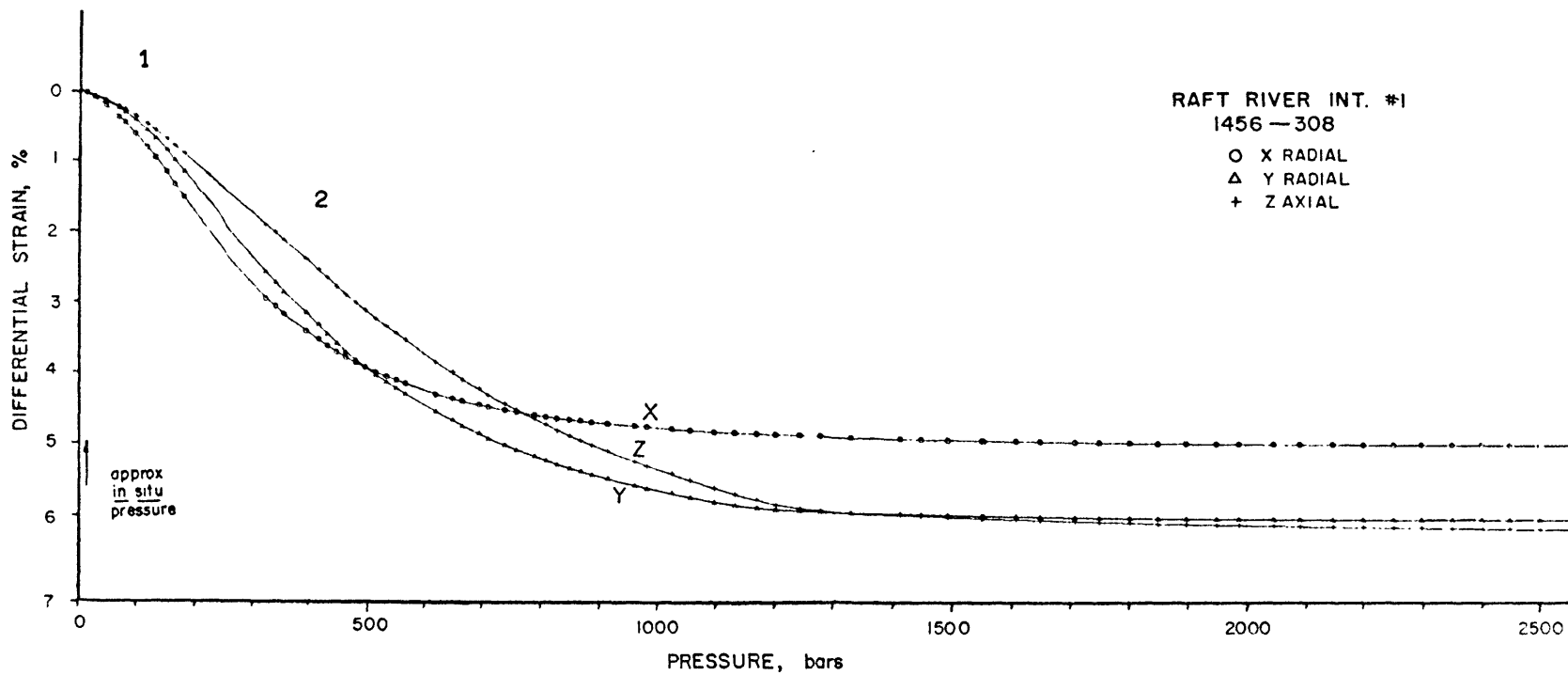
Figure 4-7. Raft River Intermediate well #1, depth 93.9 meters. 1 - recompression, 2 - virgin compression (see text).

(a) Differential strain curves.
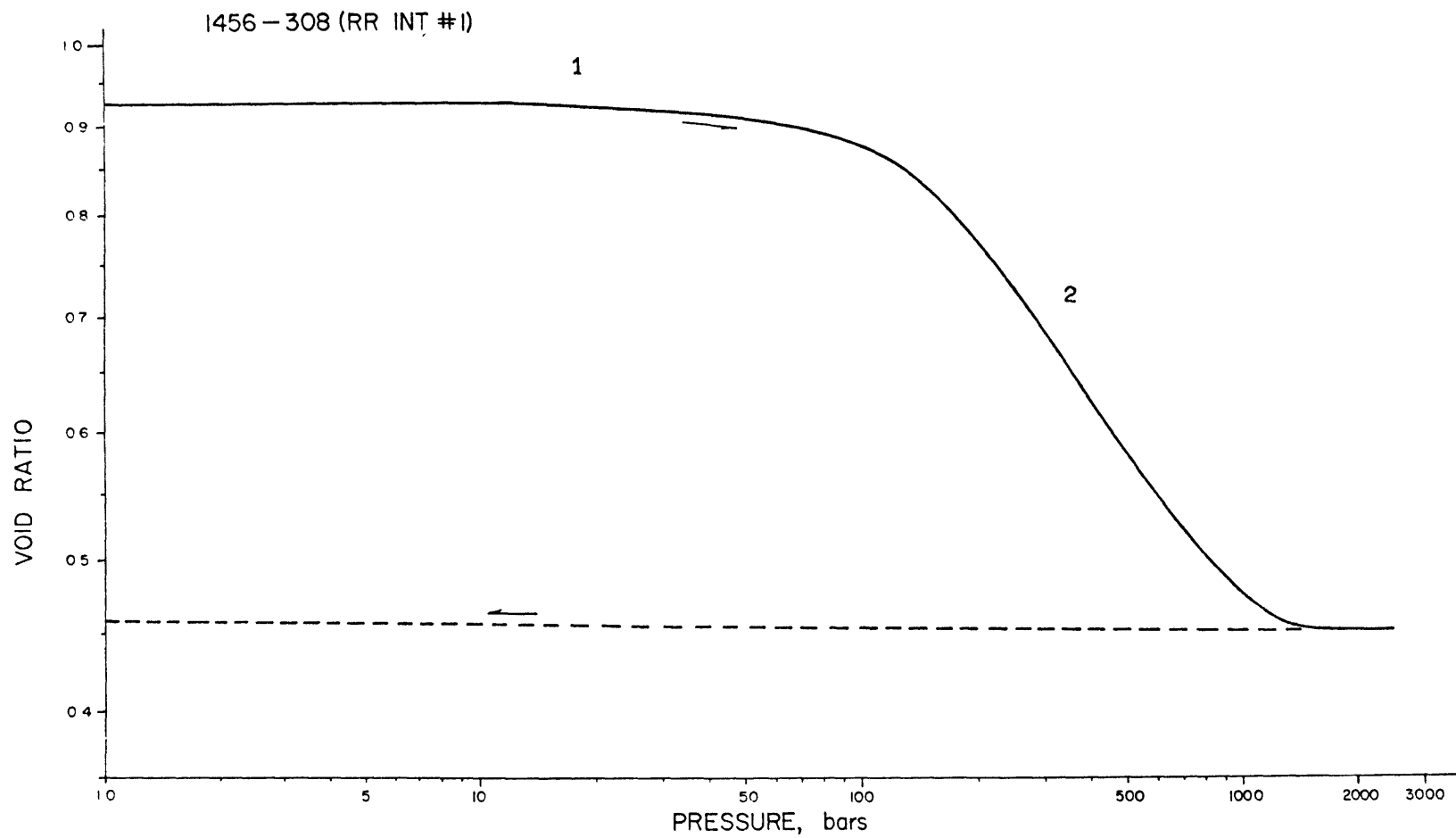
Figure 4-7b. Void ratio - logarithmic pressure curve.
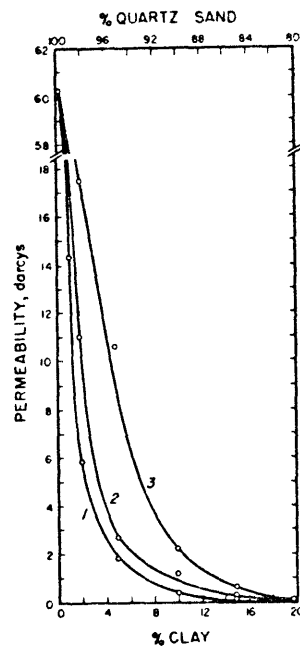
Figure 4-8. Permeability versus clay content for various clay types:
1 - montmorillonite, 2 - polymictic clay, 3 - kaolinite (after
Tsvetkova, 1954).
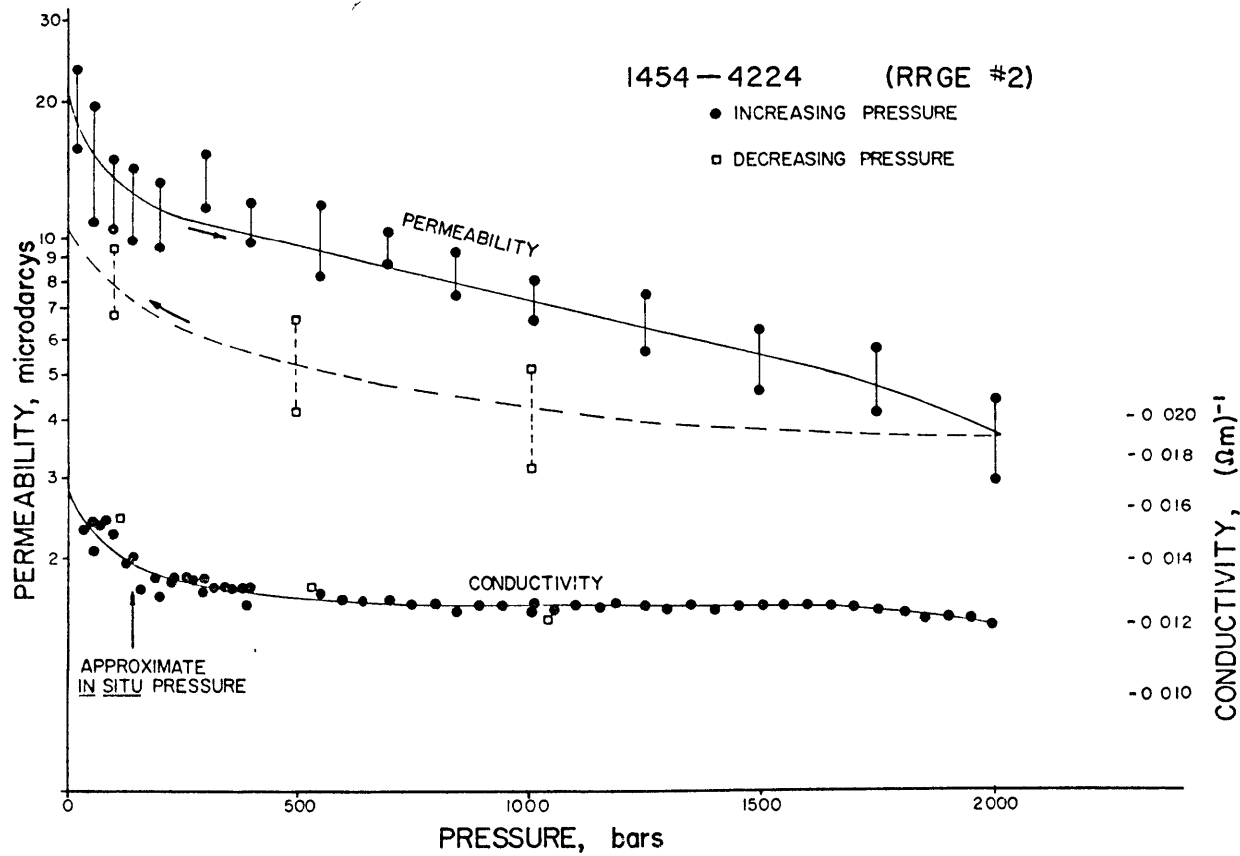
Figure 4-9. Raft River RRGE#2 well, sample 1454-4224, 1287 meters depth.

(a) Permeability and conductivity versus pressure.
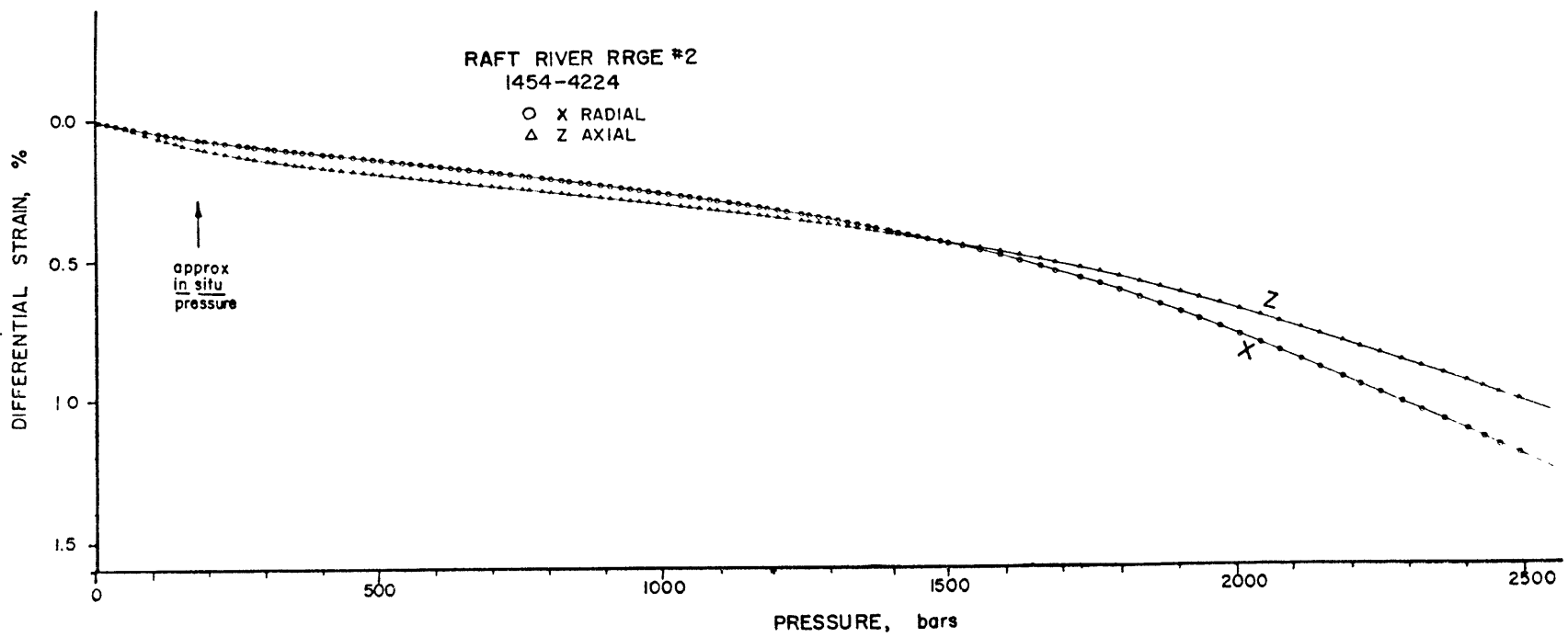
Figure 4-9b. Differential strain curves.
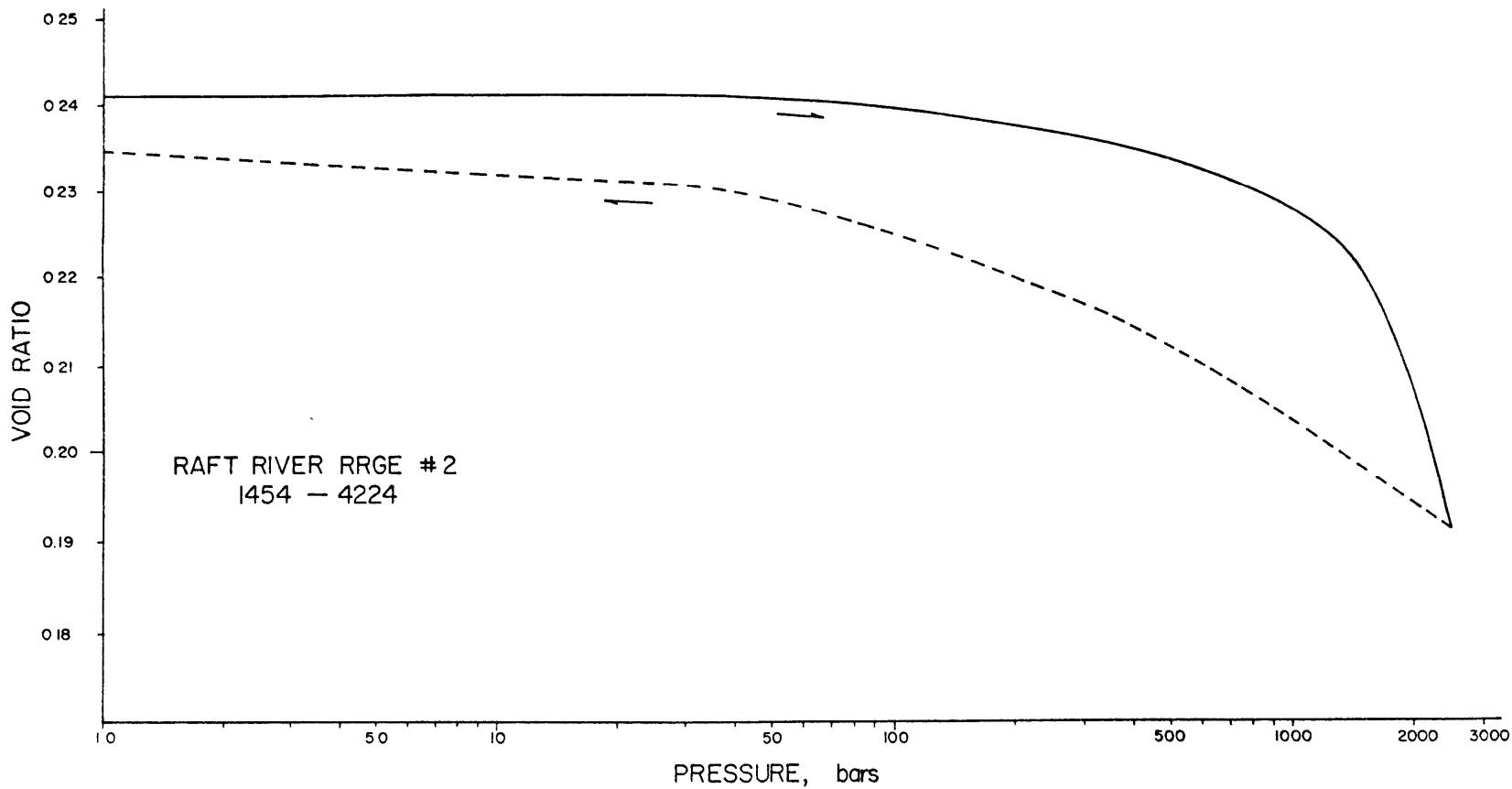
Figure 4-9c. Void ratio - logarithmic pressure curve.

ductive fluids of about 0.23 $(\Omega m)^{-1}$ used. The onset of crushing observed in the strain data at 1500 bars apparently has only minor effects on transport properties and these effects become vaguely visible above 1800 bars. Sands and clays and their mixtures obviously have complex properties and behaviors.

Diagenesis, Lithification, and Initial Stages of System Sealing

This section describes the processes that indurate and seal rocks, making them less permeable and less conductive. In the previous section, the enormous range of properties encountered in the developing geothermal system was briefly discussed. The lithification processes described below tend to narrow the range of properties. These processes will tend to close the system and increase the necessity for fracturing.

Compaction is one of the first and most obvious processes to occur in sediments. Compaction involves the reduction in bulk volume and water content as pressure is increased by the overburden of later deposited sediments. The overall fractional change in volume can range from nearly zero in some poorly sorted dense sediments to more than one-half in highly porous rocks. One effect of compaction was already described for the Heber sample from a depth of 970.5 meters shown in figure 4-5. The magnitude of strain of region I was reduced, which is indicative of a closer grain packing.

Another compaction effect is the consolidation and overconsolidation of clays. The initial compaction occurs along a 'virgin' compression line as porosity is decreased with increasing pressure. Grains and particles cannot recover their initial positions during unloading. The

strain curve will have a large hysteresis as both the relaxation (un-
loading) and recompression curves will have much different slopes than
the virgin compression (Ladd, 1971, 1973; Lambe and Whitman, 1969;
Rieke and Chilingarian, 1974). The result is that preconsolidated
clay-rich samples will also develop regions of distinct behavior on
stress-strain curves. The same specimen shown in figure 4-7 can be re-
examined in these different terms. Region 1 is the result of recom-
pression of the sample. In this region, the specimen has already been
compacted so that only a small reduction in pore space occurs. Region
2, however, has much larger compressibilities. The sample is now in
the virgin compression range. Grains are shifting and rotating to
become more densely packed. The pressure at which virgin compression
restarts can be interpreted as the maximum past pressure that the sample
had been subjected to. This pressure, approximately 60 bars, is in
considerable excess of the expected in situ pressure of about 14 bars.
This sample has been in effect 'overconsolidated'. The general shape
of figure 4-7 is very similar to the shape of figure 4-5. However, the
two curves are the result of different processes and the similarity in
shape is coincidental. The overconsolidation can be the result of
several factors. The overburden or effective pressure may have been sig-
nificantly higher in the past due to changes in fluid pressure, glacia-
tion, a thicker sediment sequence in the past, etc. In this case, how-
ever, the overconsolidation is almost certainly due to some lithifica-
tion process such as mild cementation which gives the appearance of over-
consolidation.

Induration and cementation occur when material is deposited in voids,

along grain boundaries, and at grain-to-grain contacts. Cementation results in a marked increase in the sample strength. An example of light cementation is a rounded lithic arenite from 85.7 meters depth in the Dunes well. A layer of microcrystalline quartz roughly 5 to 30 microns thick has coated the sand grains as can be seen in the photomicrograph of figure 4-10. The cement supports and bonds the grain contacts. This bonding inhibits relative grain motion and crushing. Note the fractures radiating from some of the grain contacts which are indicative of local stress concentrations. This unstressed sample demonstrates that microfractures do exist in weakly consolidated rocks. In fact, the core from this depth contained several large partially sealed fractures approximately one millimeter wide. The fractures are usually overshadowed by the much larger effects of compaction. The DSA curves are reproduced in figure 4-11. The cementation has had the effect of producing a smooth compaction curve with no abrupt onset of crushing. The rate of compaction continues to increase with pressure indicating that, as more grain contacts break, progressively greater amounts of material become available for further compaction and crushing. Permeability was determined as a function of pressure on a specimen from this same section of core. The permeability (figure 4-12) decreases at a much smaller rate than observed in other less-indurated samples. The smaller decrease is probably due to the large open framework being supported by the cement (Maxwell, 1960). To within measurement error, the permeability curve is smooth as is the case with compression. At about 900 bars, grains dislodged by the stainless steel screen plugged the narrow high pressure tubing preventing any futher measurements.
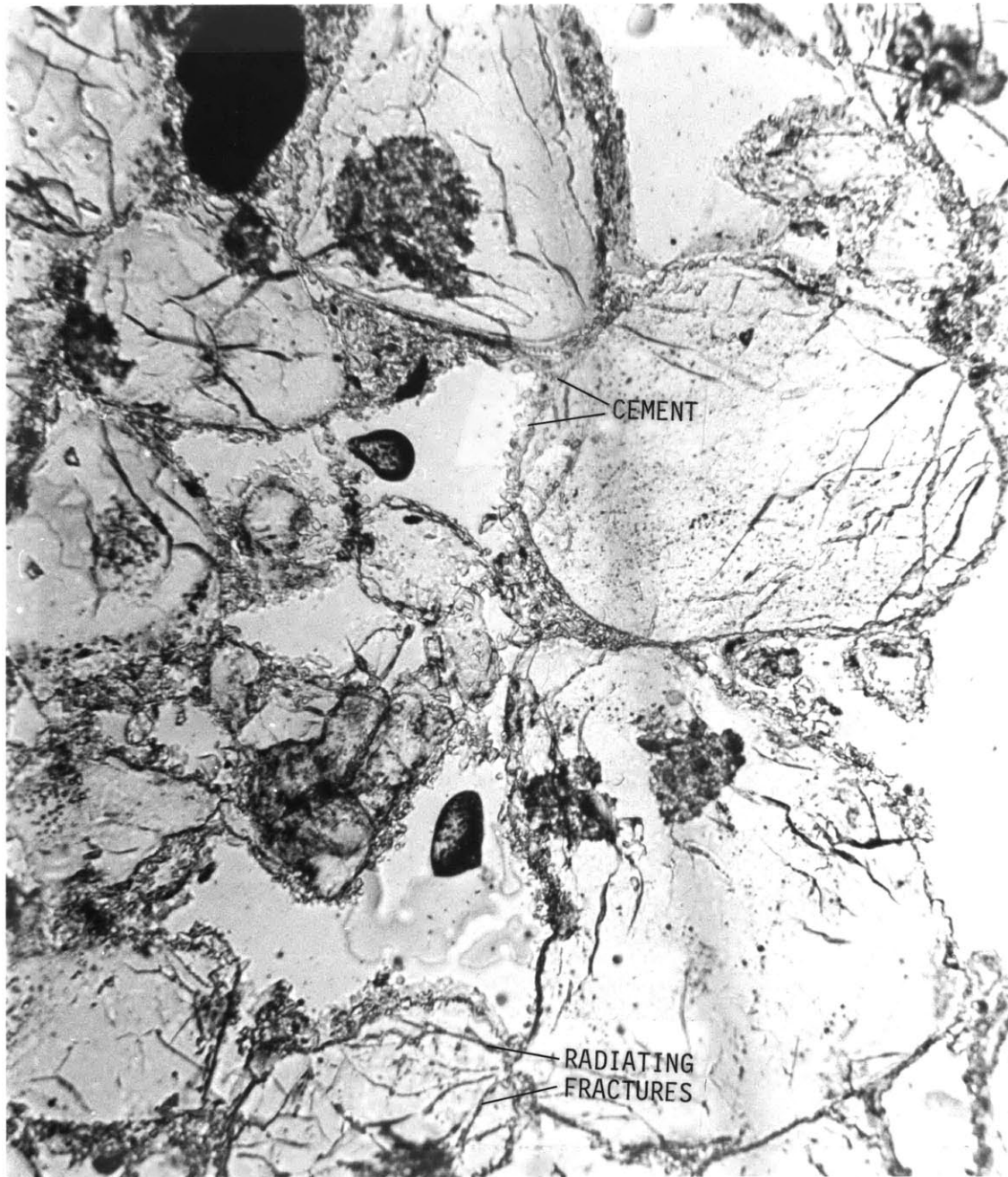
Figure 4-10. Dunes sample 1452-281 from a depth of 85.7 meters.
Standard thin section seen under plain polarized light displaying thin
cementation and point contact fractures. This sample has not been sub-
jected to laboratory stress.
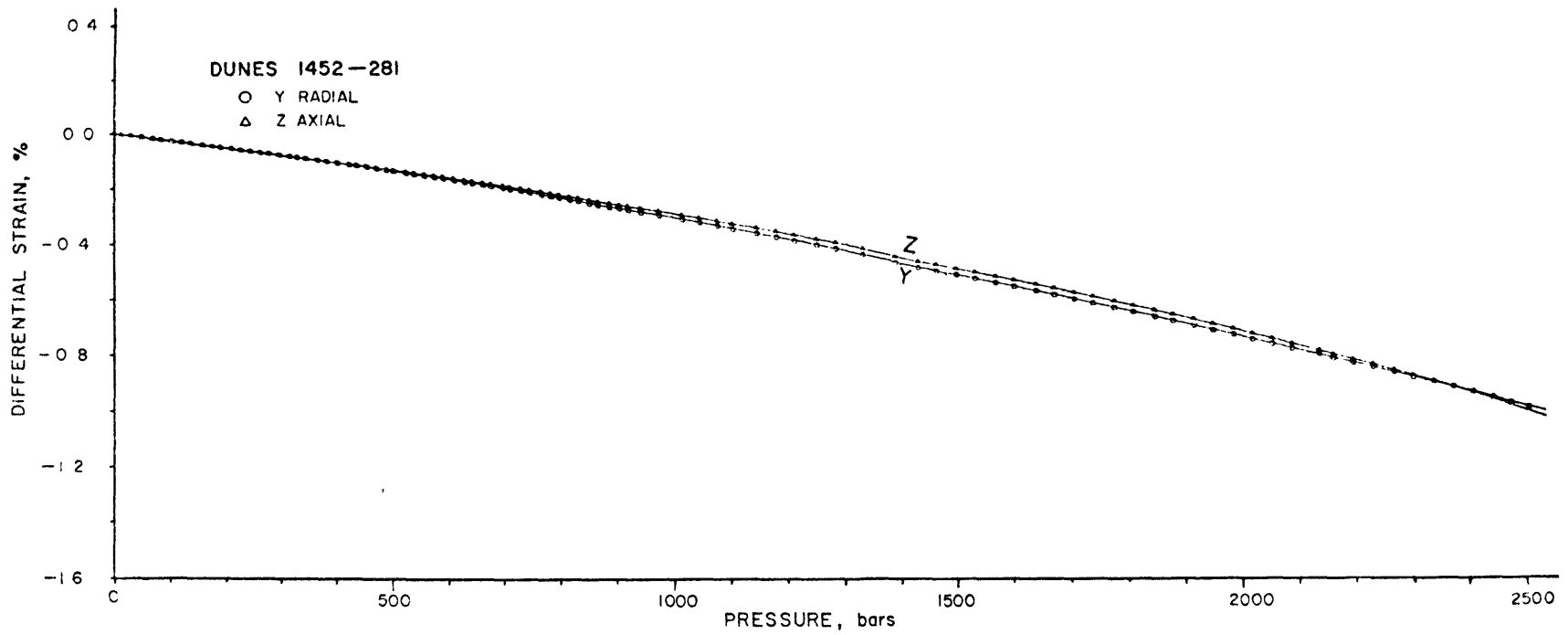
Figure 4-11. Dunes 1452-281, a sample from the same core as the specimen in figure 4-10.

(a) Differential strain curves.
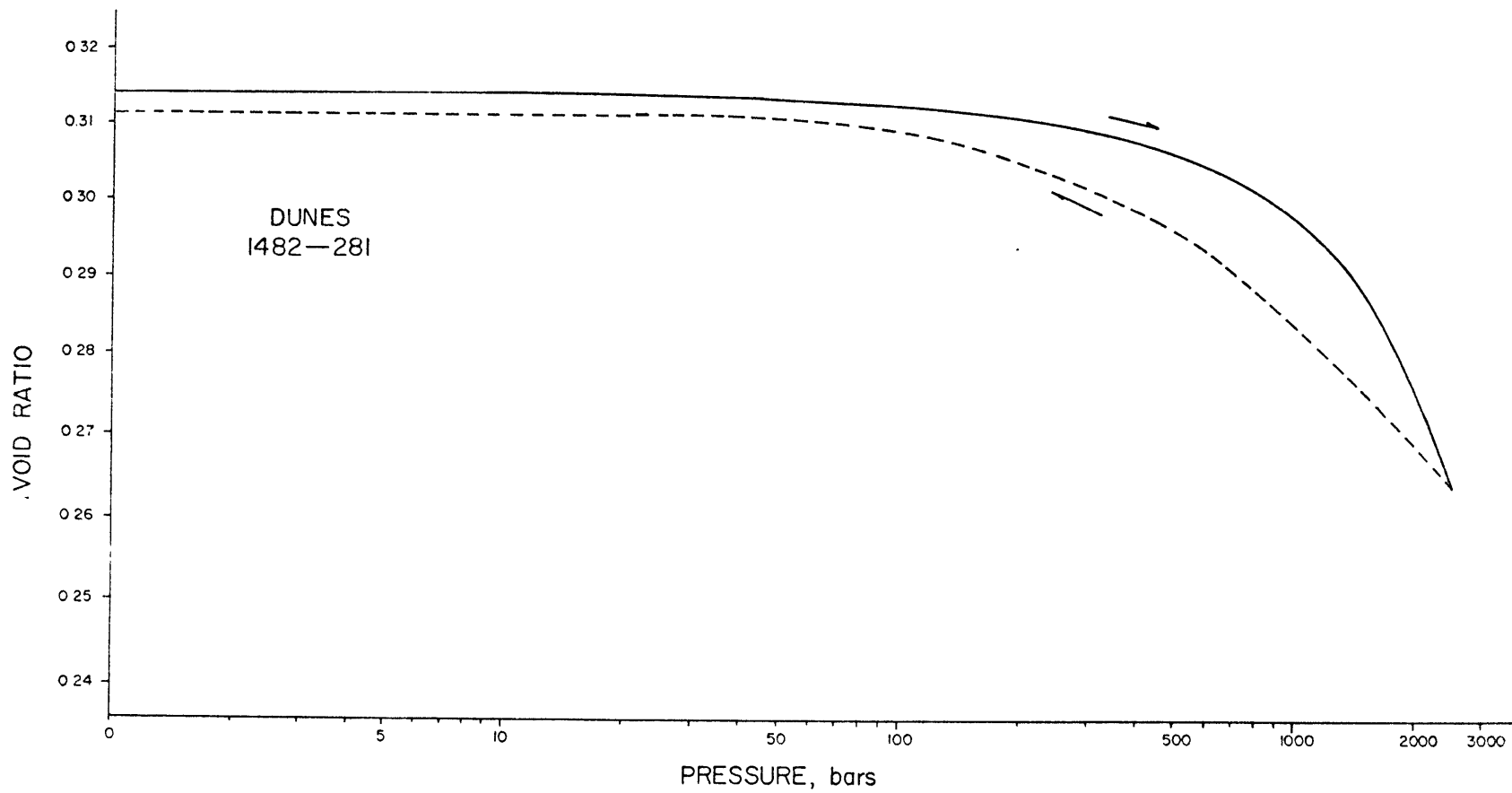
Figure 4-11b. Void ratio - logarithmic pressure curve.
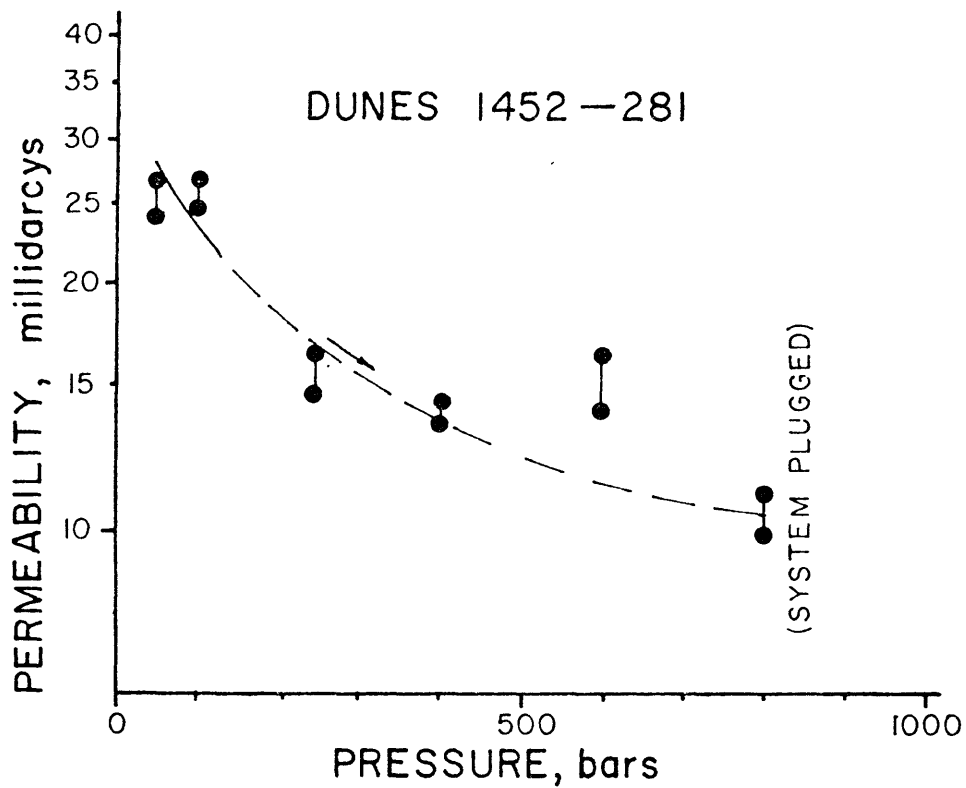
Figure 4-12. Dunes 1452-281, a sample from the same core as the specimen in figure 4-10, permeability versus pressure. The permeability system was blocked by loose sand particles above 900 bars.

More intensive but restricted cementation may be encountered
when material rapidly precipitates out of saturated hydrothermal fluids.
This process can result in a sharp boundary between cemented and non-
cemented regions. This feature can be similar to concretionary textures
except that irregular but interconnected fronts or boundaries are
formed. Similarly abrupt cementation boundaries are observed in many
of the samples obtained for this study. Such abrupt cementation boun-
daries may be a wide-spread phenomenon in geothermal systems. This
cementation texture may be an indication of the early stages of hydro-
thermal fluid invasion and resultant induration. Circle 4 in figure
1-3 represents the position of this cementation feature in the general-
ized geothermal system.

An argillaceous, felsic wacke from a depth of 609.2 meters in the
Dunes well serves as an excellent example of the abrupt cementation
boundary described above. The abrupt and concretion-like texture of the
front is easily seen in figure 4-13a. Figure 4-13b is a photomicrograph
of an area encompassing the boundary between the loose and well-indurated
portions. In the right half of 4-13b, the dark areas between grains are
open pores. This portion of the rock is friable and has a high porosity
of about 35%. To the left in figure 4-13b, the light areas between
grains are calcite cement. The porosity, approximately 6%, is greatly
reduced and this portion is dense and hard. Even on a microscopic scale,
the boundary is abrupt.

The physical properties differ substantially between the loose
and indurated portions of the sample. The DSA curves for the two portions
are presented in figures 4-14a and 4-14b. Significant strains occur at
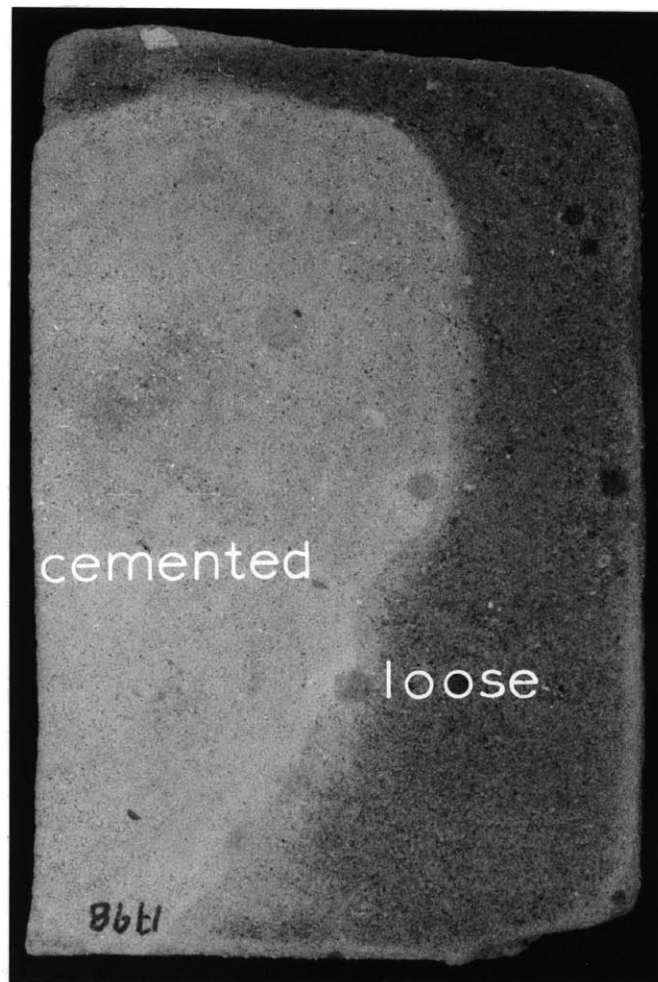
Figure 4-13. Dunes sample #1452-1998, from a depth of 609.2 meters.

(a) Overview of split core sample.
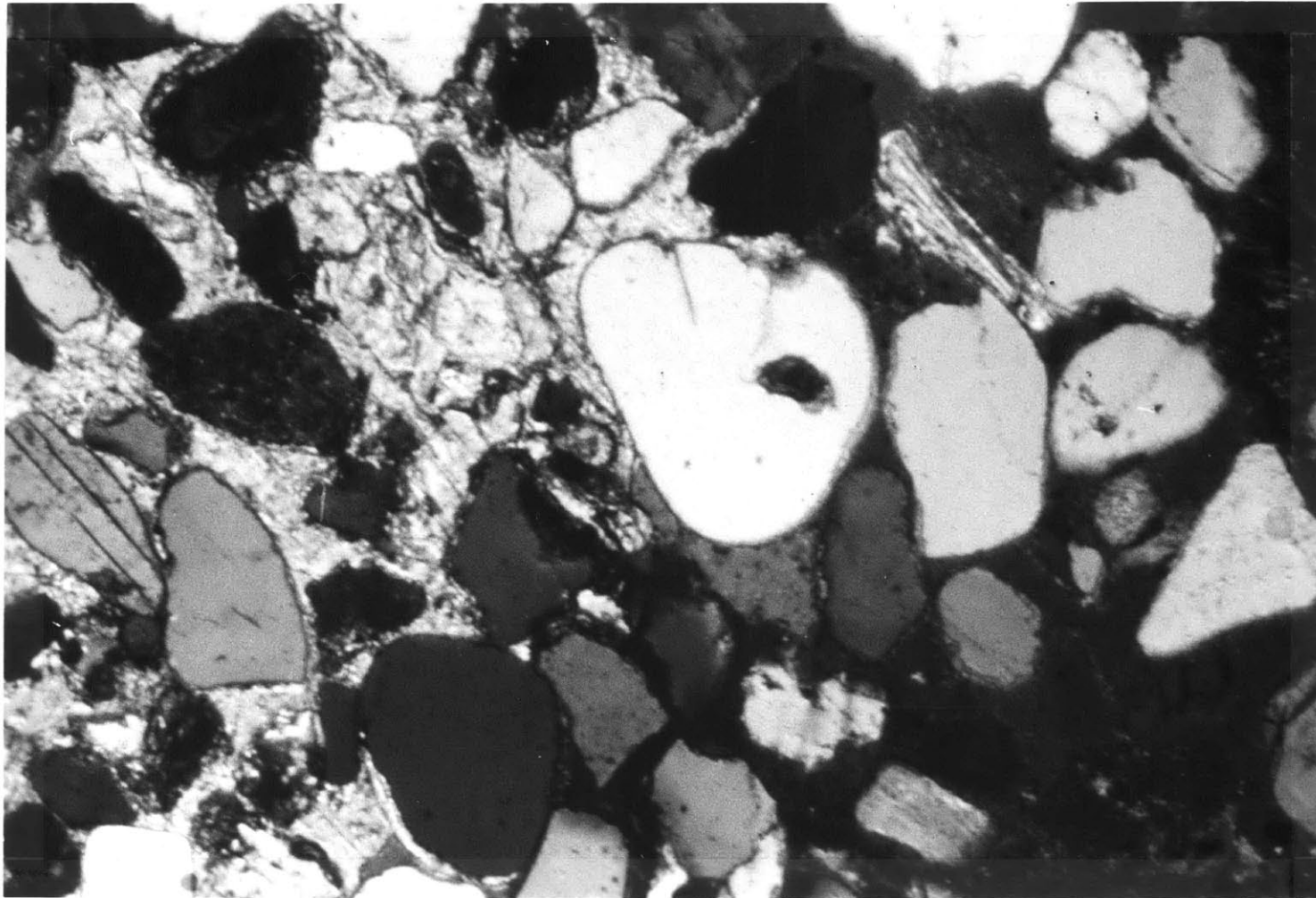
Figure 4-13b. Photomicrograph in crossed polarizers with calcite cemented portion to left (after Batzle and Simmons, 1976).

0.3   mm
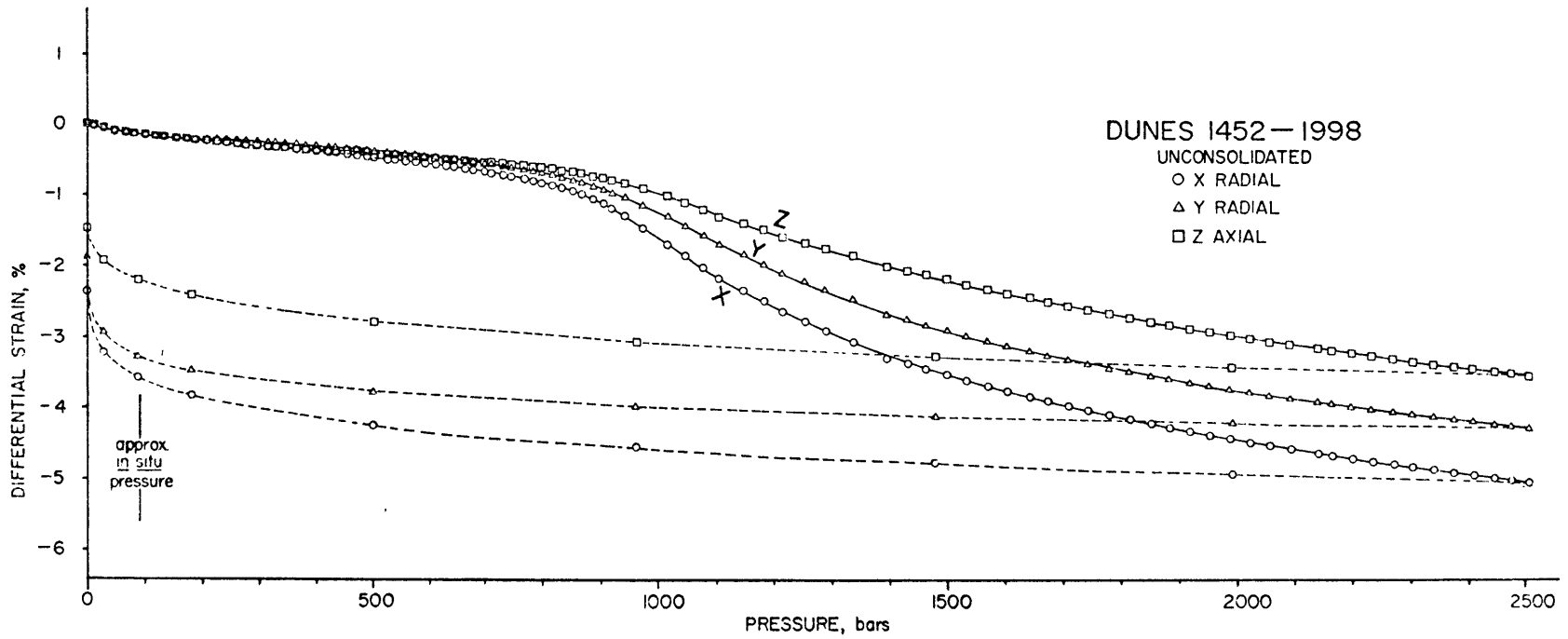
Figure 4-14. 1452-1998, differential strain.

(a) Unconsolidated portion.
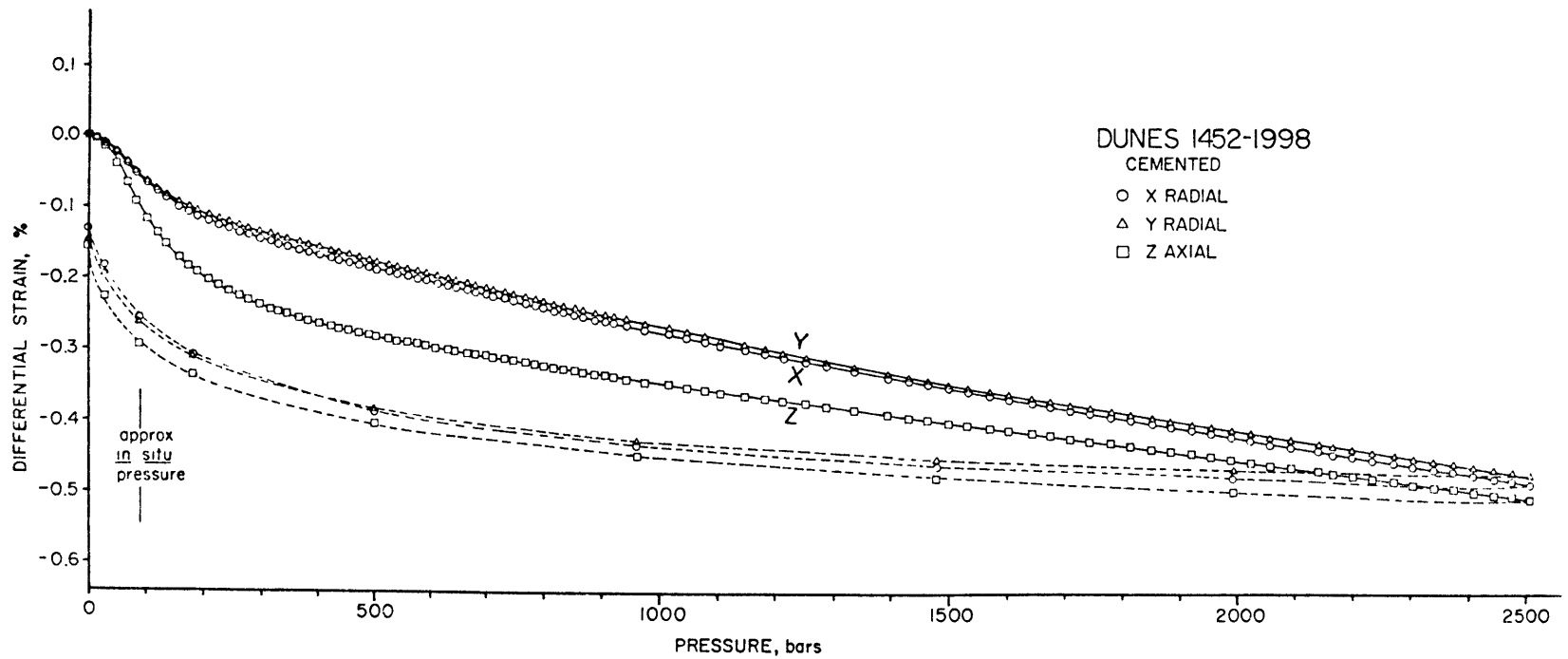
Figure 4-14b. Indurated portion.

the beginning of the runs below the approximate in situ pressure of 100
bars. These low pressure strains are probably due to fractures induced
by unloading, coring, and temperature changes resulting from drilling.
Note that the total strains below 100 bars are of the same absolute mag-
nitude for both the loose and cemented portions although this strain
has a much smaller relative effect in the former portion. Above approxi-
mately 100 bars, the loose portion undergoes crushing and becomes densely
packed. At 2500 bars, this poorly consolidated material has lost about
13% of its total volume or more than one-third of the initial porosity.
The high pressure structural collapse is prevented by the calcite de-
posited in the intergranular areas of the indurated section. The total
volumetric strain is approximately 0.6%, which represents a decrease of
only a tenth of the original porosity. The compactions of both the
well-cemented and unconsolidated portions are largely nonreversable as
demonstrated by the hysteresis.

Permeability and conductivity also differ drastically between the
two regions. A sample taken from the unconsolidated portion had a per-
meability of nearly 3 millidarcys. A similar sample from the cemented
region had a permeability of 340 nannodarcys, a difference of four orders
of magnitude. The formation factor is approximately doubled from the
loose to the cemented portions (28 Ωm fluid). The relatively small
change in conductivity is probably due to the clay content which provides
a large surface conduction contribution. This sample is an excellent
example of large changes in permeability being accompanied by only trivial
changes in resistivity. Thus, even in large and otherwise homogeneous
units, large-scale changes in permeability may thus be undetectable

geoelectrically.

Another example of an abrupt cementation boundary is a sample of a pebble conglomerate from a depth of 422.7 meters in the Raft River Intermediate well #3. A thin section of the boundary between the well-indurated and poorly-consolidated regions is shown in figure 4-15. This photomicrograph was made with cathodoluminescence as this technique emphasizes the texture of the calcite cement. The well-cemented portion is on the left. Calcite is the continuous light material between dark grains of sand. The dark region on the right of the figure is uncemented. The boundary is again distinct on a microscopic scale. Once again the calcite progressively cements or seals the rock along a front. The calcite does not form uniform grain coatings as would be expected for homogeneous circulation of calcite-saturated fluids. The uncemented portion is loose and crumbles easily when handled. This loose portion has a permeability of about 0.2 darcys and a formation factor of 20 (2.0 Ωm fluid). The permeability of the indurated portion is 2.1 millidarcys and the formation factor is about 47. The drop of two orders of magnitude in permeability but halving of conductivity indicates that larger pores are sealed but many smaller voids and cracks remain open. Smaller pores and clays once again result in relatively high electrical conductivity but low permeability.

Implications

In this section, the need for geothermal systems to remain open to fluid circulation is briefly discussed. For a convective system to be economic, severe restrictions are placed on the fluid production charac-
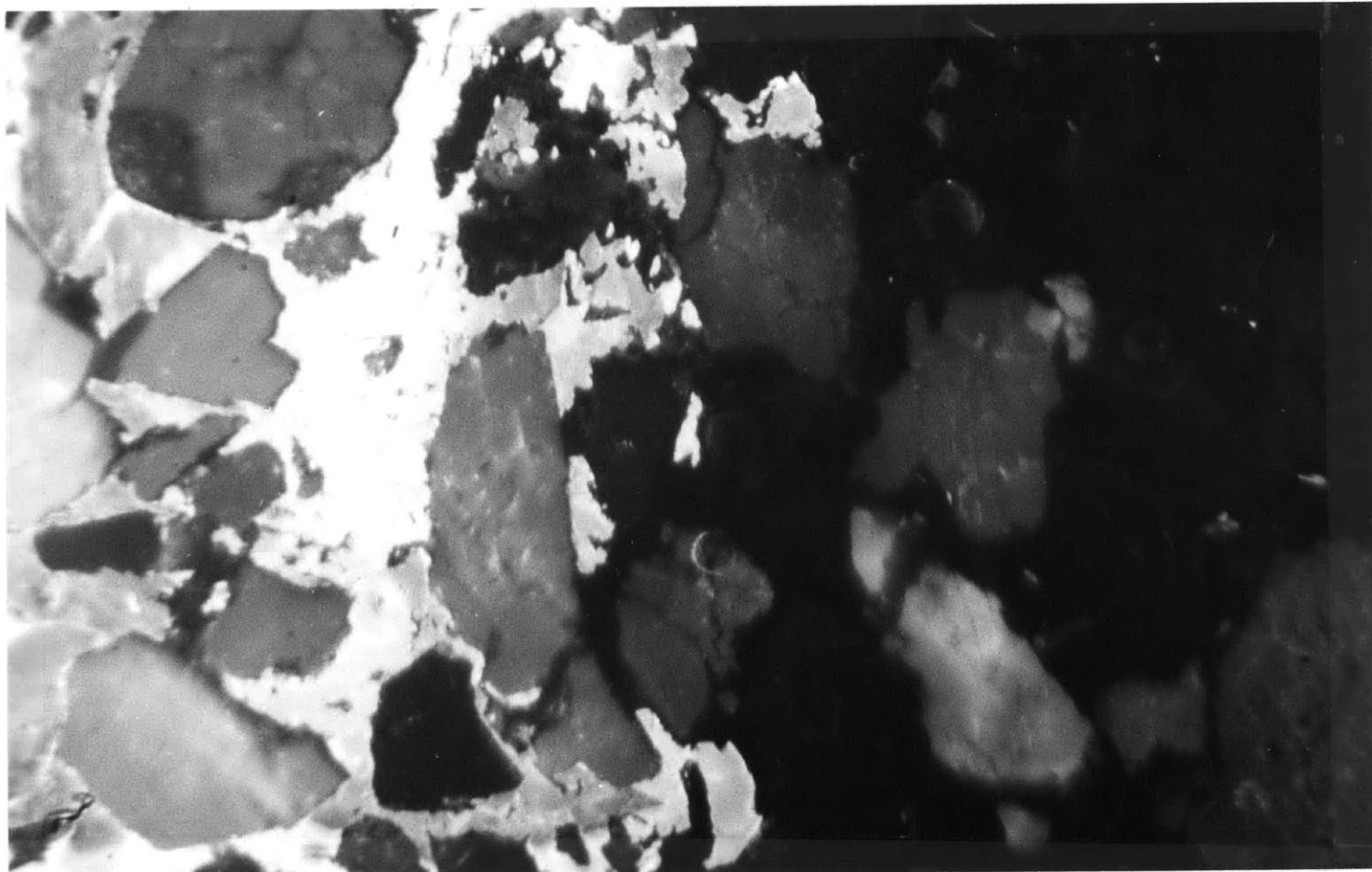
Figure 4-15. Raft River Intermediate well #3, sample #1457-1387, 422.7 meters depth. Cathodoluminescence. To the left the light material between grains is the calcite cement. The right half of this figure is uncemented.

0.4 mm

teristics of the local stratigraphy. Present economics require that the producing rock units have permeability-thickness products on the order of 10^5 millidarcymeters. To extract sufficient energy, roughly 20 to 100 kilograms per second flow is required per well in hot water systems (Nathenson and Muffler, 1975; Crosby, 1977). The wells themselves must be productive for several years and the reservoir must have a lifespan on the order of decades. These limits are very crude and depend largely on factors such as drilling costs and energy conversion factors. The production figures do require that the system remain open. Circulation must be continuous. Flow can occur through interbedded permeable horizons, such as at Heber, and through confined fractures zones as at Marysville.

Geothermal systems can become too impermeable even for slow fluid migration on a geologic time scale. Shale beds have permeabilities low enough to support overpressured zones. Nannodarcy permeability can inhibit equilibrium between fluid and rocks even at high temperatures (Kendall, 1976, p. 173). Although the formation of an impermeable cap rock is often beneficial, eventually the entire cooling portion of the system can become choked with deposited material.

In this brief chapter, it was possible only to give a very cursory introduction to the various physical parameters of rocks pertinent to this study. Examples were chosen to demonstrate the wide range of starting properties, results of lithification processes, and the effects of cementation brought on by the initial invasion by cooling hydrothermal fluids. The processes discussed, if carried out to a significant degree, significantly lower permeability. One overall conclusion to be drawn

from this chapter is that for a system to be economic or even to remain active in a geologic sense may require substantial fracturing.

CHAPTER V

FRACTURING

Introduction

In this chapter, the observed fracture content of samples is described and the effect of open fractures on rock transport properties is evaluated. Chapter IV examined initial rock properties and the processes of lithification and early stages of cementation that tend toward low permeability. Figure 1-4 indicated that fracturing is necessary to keep the system open to circulation. Evidence for the numerous fracturing and refracturing events that occur in geothermal regions will be presented first. The dependence of the fluid permeability and electric conductivity on individual fractures and fracture populations will be examined by direct measurement and fracture modeling. The dominant crack parameters and characteristics of porosity and shape will thus be determined. Relationships between in situ fracture and flow parameters will be briefly discussed. Finally, this chapter will conclude by noting several of the basic mechanisms that may be responsible for the repeated fracturing.

Observations

Episodic fracturing has been recognized in many geothermal regions. Samples were usually chosen for this study on the basis of visible macroscopic fracturing. A few examples will be discussed here as either typical or particularly illustrative of the fracturing-refracturing process. Much of the evidence of this section bears great similarity to the next chapter (sealing, healing, alteration) as evidence for frac-

turing is often in the form of alteration and veining textures.

Numerous types of evidence can be used to establish the temporal relationships of fracturing events. Etched non-matching surfaces indicate that the crack was open in situ. Cross-cutting relationships often allow fracture episodes to be dated on a relative basis. Younger fractures often terminate on older cracks. Overgrowths will enclose the older features but are transected by younger cracks as is seen in figure 5-1. Variations in veining materials, crystal habits, and zonation can also be utilized. Possible ambiguities arise when refracturing complicates the textural relationships. Textures can be obscured by crystal cleavage or habit. New fractures often follow older planes of weakness such as sealed or partially healed cracks as shown in figure 5-2. A wide variety of textures can thus be used to document the fracturing history and content of samples.

The first examples are drawn from the igneous and metamorphic rocks that make up the basements in hydrothermal cells. Several different fracturing ages and styles occur in a sample of quartz schist from a depth of 1431 meters in the RRGE#1 well. Figure 5-3a shows the earliest fracturing observed. The oldest fracture, f1, is cut by the younger fracture, f2. Both these fractures are surrounded by parallel sets of bubble planes, which is suggestive of strong shearing. The bubble planes are sites of former breakage where the crystal has healed or regrown across the crack. At other locations within the sample, the shearing is represented only by diffuse zones densely populated by fluid inclusions. Such zones can be several grains wide. This shearing may be related to the 'Narrows Structure' (figure 2-7 in Chapter II) that

50 μm
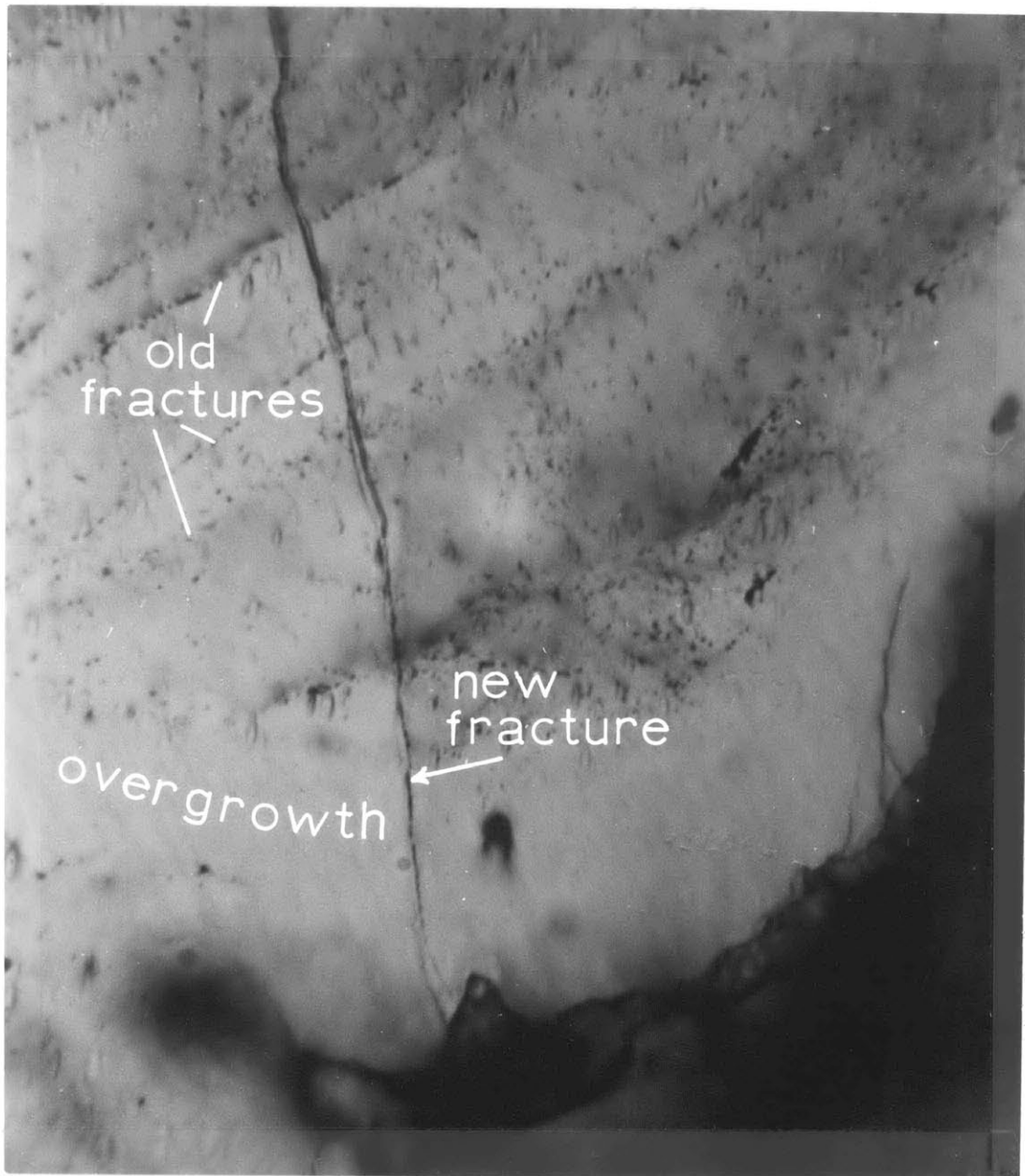
Figure 5-1. Fracture cutting relationships viewed in plane polarized light. Quartz overgrowth surrounds old fractures consisting of planes of fluid inclusions. New fracture transects both overgrowth and old fractures (from Batzle and Simmons, 1976).

0.1 mm
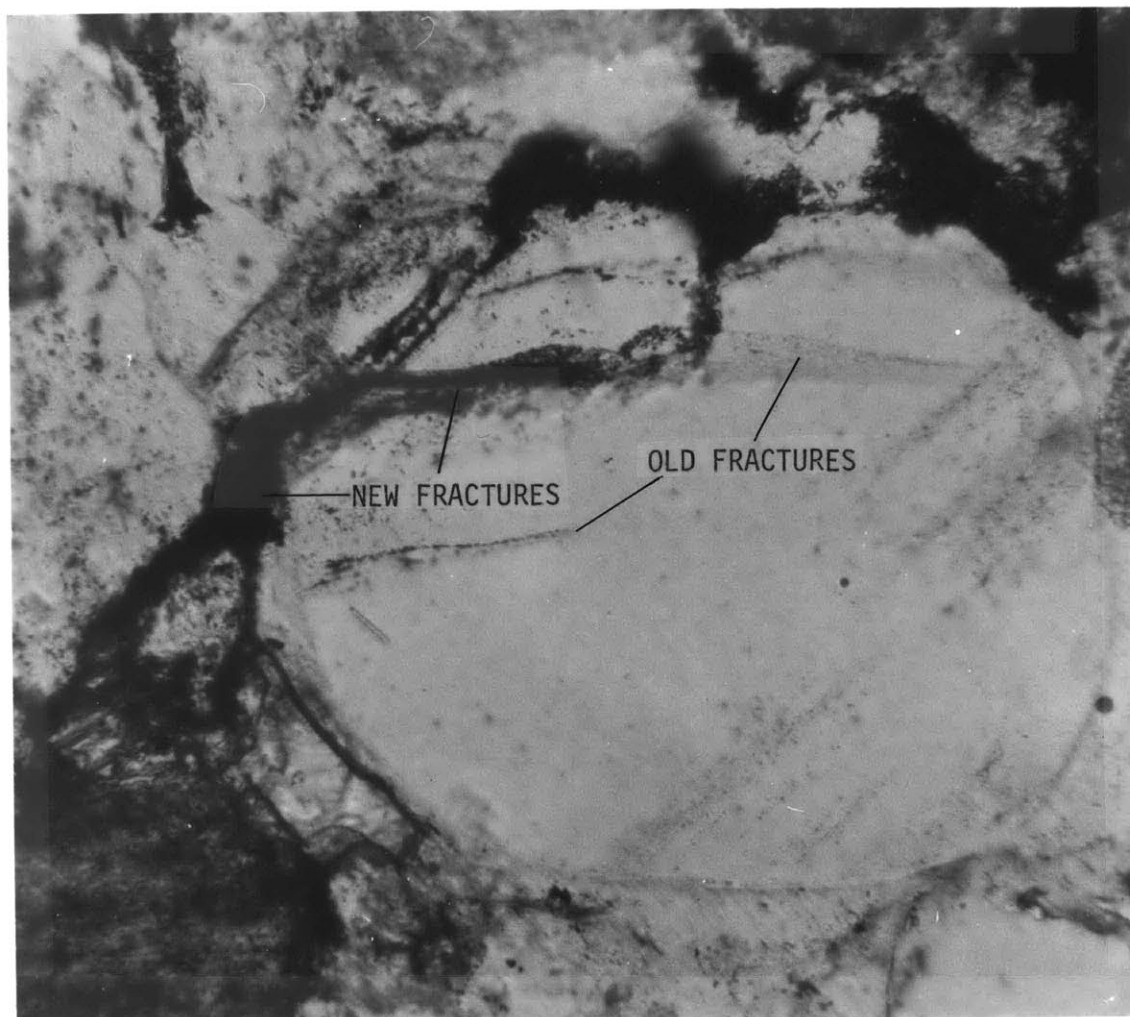
Figure 5-2. Refracturing along lines of weakness viewed in plane polarized light. Portions of old closed cracks consisting of planes of fluid inclusions are reopened by a new episode of fracturing (from Batzle and Simmons, 1976).
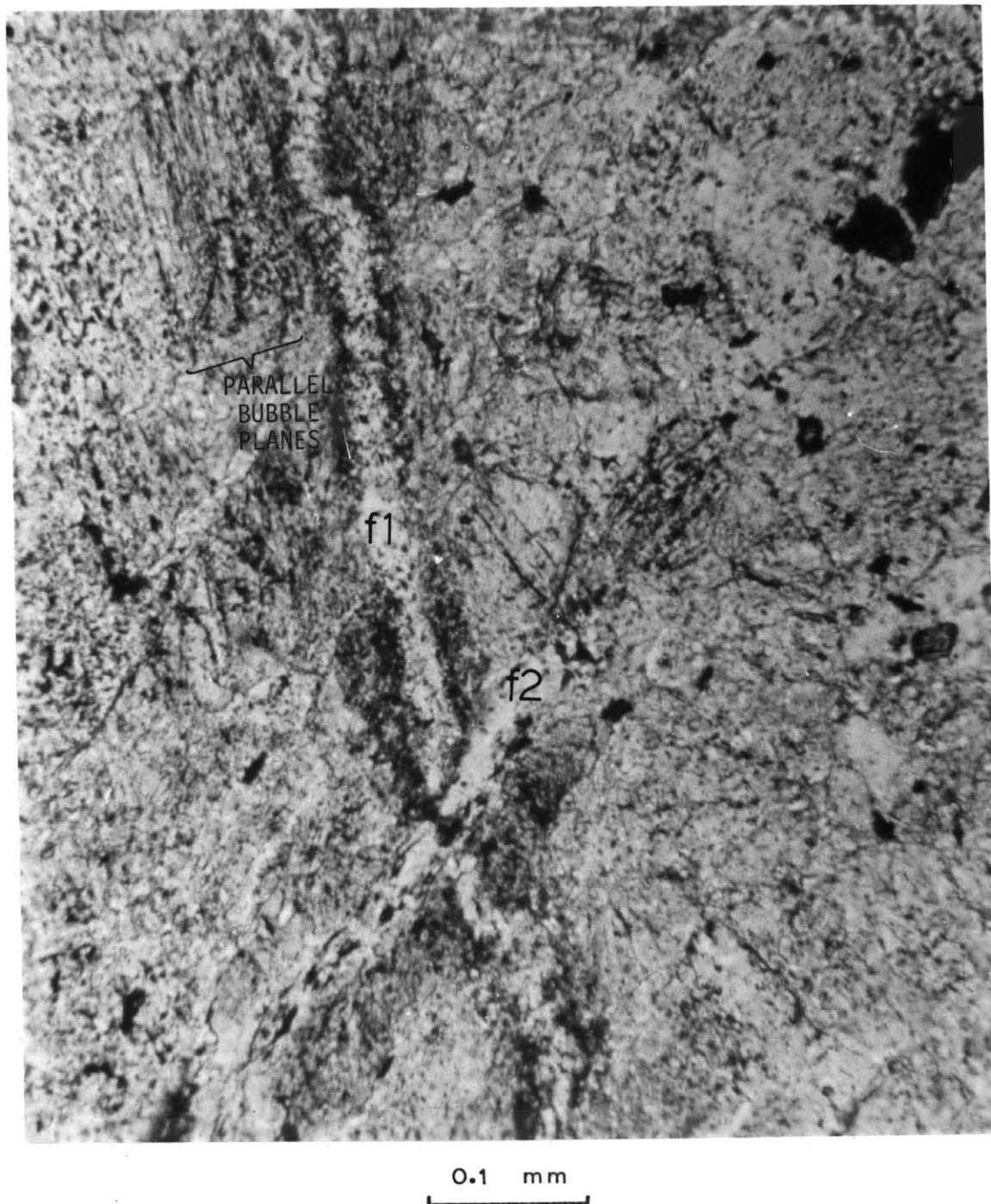
Figure 5-3. Multiple fracturing in a sample from a depth of 1431 meters
in the RRGE#1 well. Plane polarized light.

(a) Initial fractures, f1 and f2, with subsidiary parallel sets of
'bubble' planes.
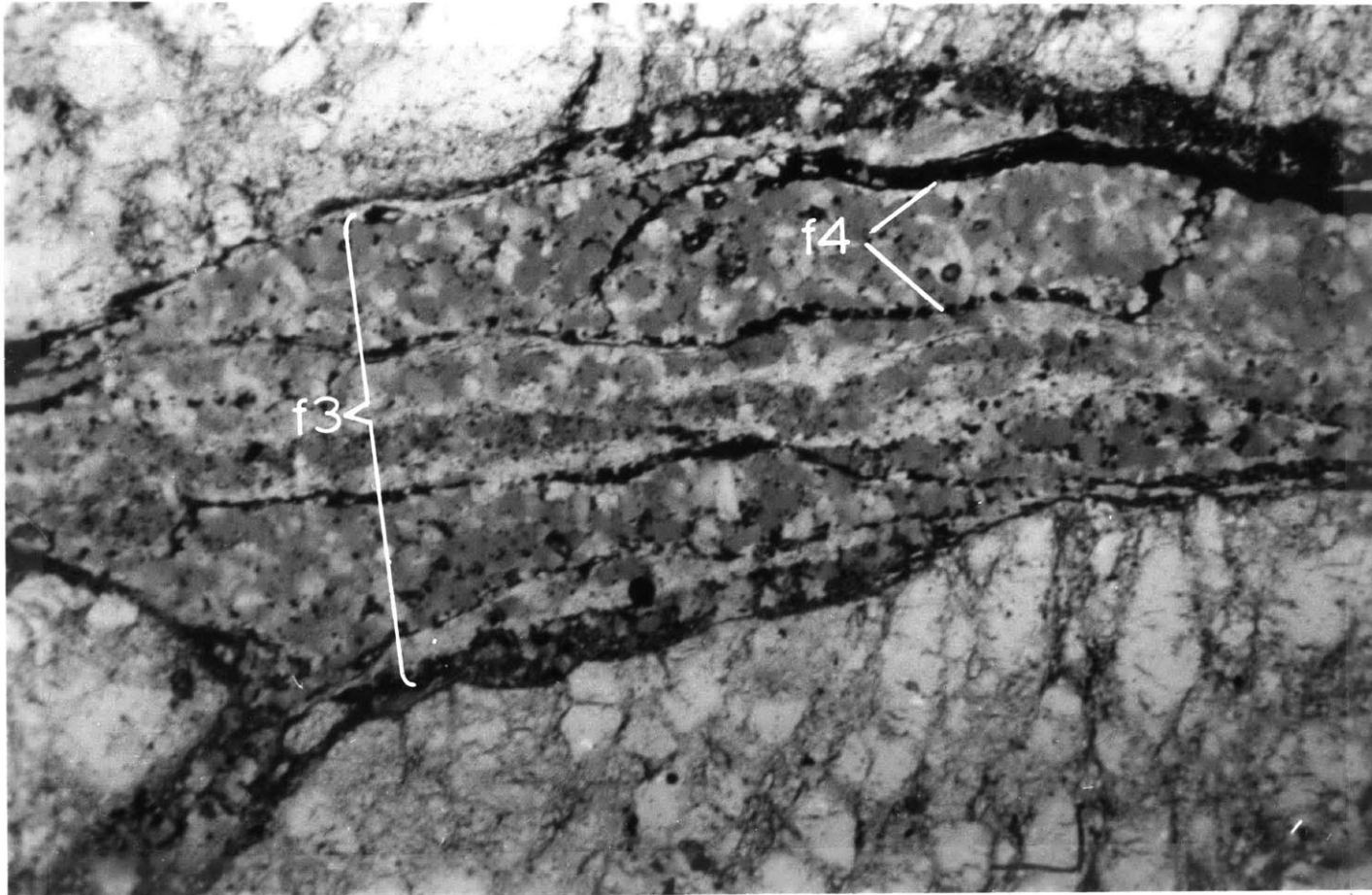
Figure 5-3b. Larger chlorite-filled vein, f3, that has been refractured and oxidized along f4.

dominates this region. If so, the healing indicates that the activity of this structure is very old. A completely different type of fracturing is represented by the vein, f3, in figure 5-3b. This vein is wide, undulating, and filled with chlorite. Not only is the sealing process different, but the basic fracturing mechanism has changed. Even f3 is later broken by a much narrower uniform crack, f4. The oxidation rim around f4 indicates that it was open in situ to oxidizing fluids. Hence, at least three distinctly different episodes of fracturing are obvious in this sample.

Massive shearing and breakage are evident in a sample from 285 meters depth in the Coso BDH well (figure 5-4). This rock has developed a cataclastic texture. The original leucogranite has been broken and crushed. Large porphyroclasts have granulated margins and are densely populated with fractures on a microscopic scale. These clasts are surrounded by a matrix of small granules of quartz and feldspar dispersed in brown-yellow mixed layer clays. Several shear zones with slickensides cut the core. The rock has become pliant and friable. The shearing has drastically altered both the macroscopic and microscopic properties.

The DSA curves for this Coso specimen are shown in figures 5-5a and b for two parallel gages in the axial direction separated by approximately 2.5 centimeters. The two locations have significantly different strains at high pressure, probably due to the compaction of varying amounts of clay. The sample is very inhomogeneous on a small scale. Many irregular clay-rich zones surround the larger clasts and account for the differences in strain values. The maximum cumulative
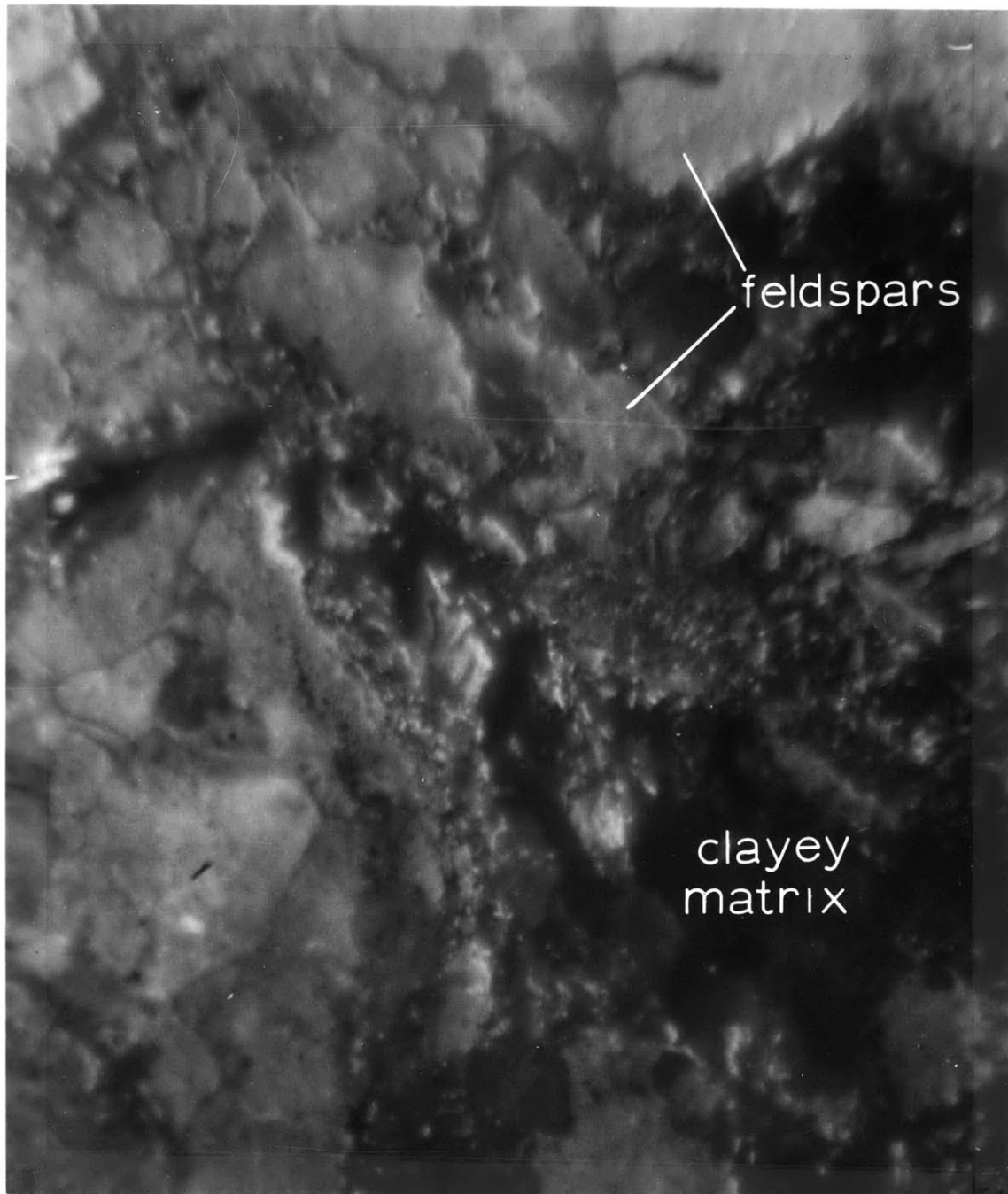
0.2   mm

Figure 5-4.   Coso BDH#1 well, depth 285 meters, cathodoluminescence.
Light-colored broken and crushed feldspar grains are embedded in the
dark clayey matrix.
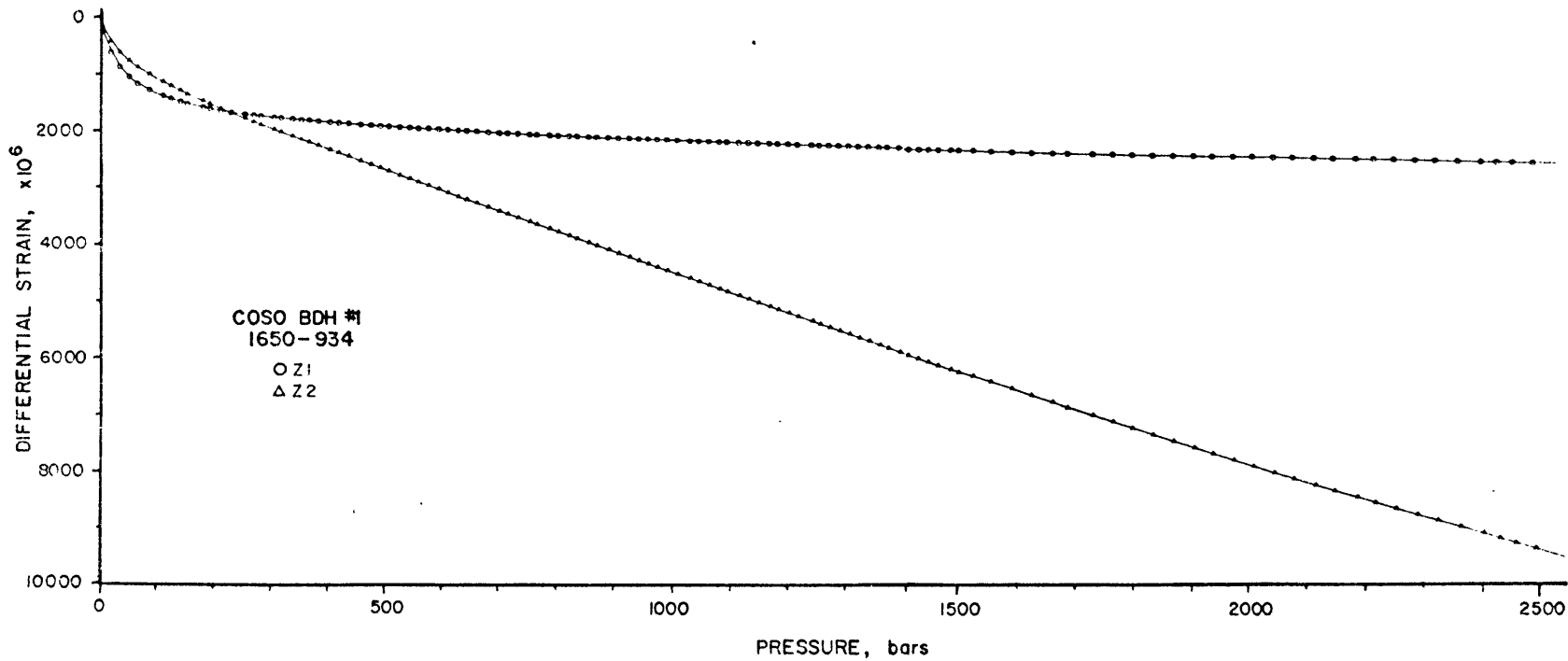
Figure 5-5. Differential strain analysis for a specimen from a depth of 285 meters in the

Coso BDH#1 well.

(a) Differential strains for two parallel gages in the axial directions.
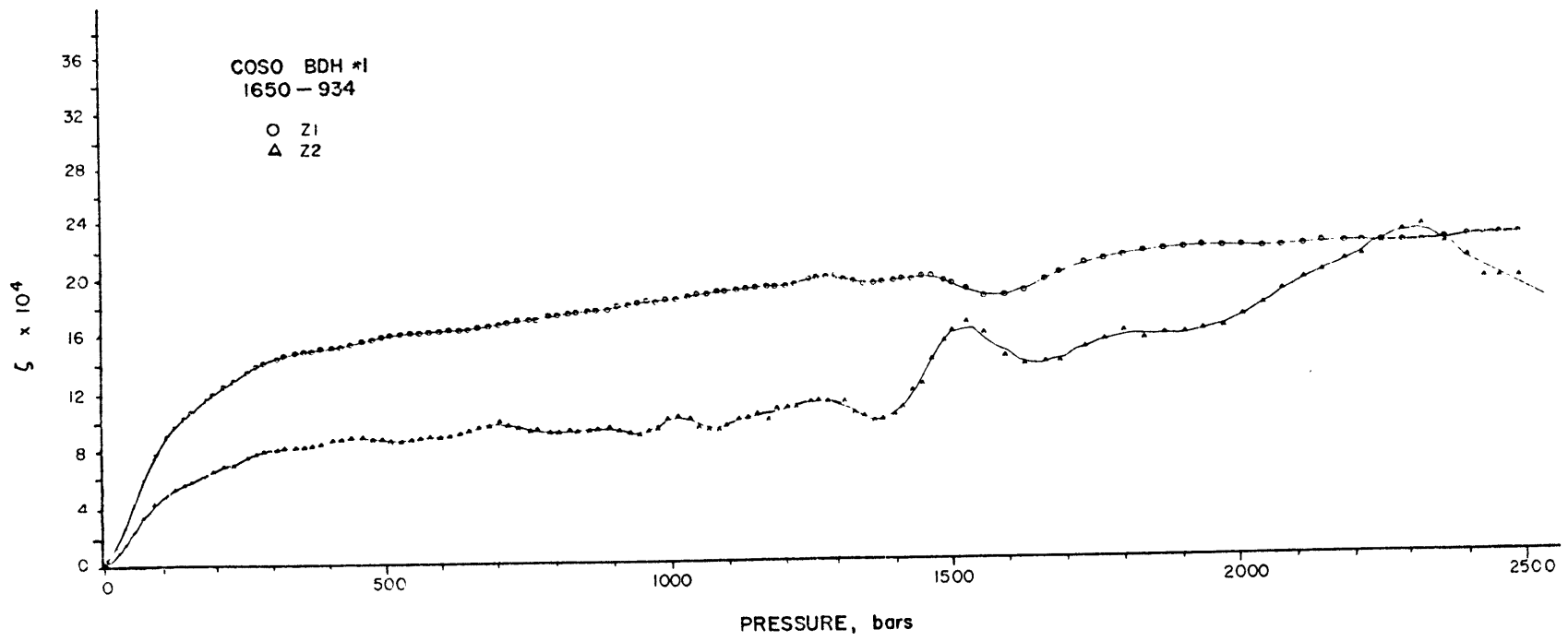
Figure 5-5b. ζ curves for the same gages as in figure 5-5a.

linear fracture strains (high pressure ζ values) for the two locations
are approximately equal at 0.22 percent each in spite of the large
differences in strain. The total average sample fracture porosity ad-
justed for the in situ pressure is 1.0 percent. This value is obtained
by averaging the strain measured by parallel gages and then summing
these average strains for three orthogonal directions.

The permeability and conductivity curves are presented in fig-
ure 5-6. The change in permeability is much smaller than in previous
examples in spite of the large amount of compaction. The conductivity
shows almost no variation. The compaction and fracture closure behavior
may be the result of the collapse of the clayey matrix until the angular,
'poorly sorted' clasts contact and support the structure. Loose, open
material between the coarser grains permits relatively high permeabili-
ty. This mechanism plus the clay content combine to prevent any signi-
ficant decrease in the conductivity.

A porphyritic granite from a depth of 1298 meters in the Marysville
well illustrates the type of fractures developed in dense igneous rocks.
Two episodes of fracturing can be clearly resolved in the scanning elec-
tron micrographs of figure 5-7. The light-hued pyrite-filled vein at
A is transected by a younger open fracture set. Etched surfaces, dis-
continuities, and 'bridges' or material spanning the open fracture such
as at B are indicative of the fracture being open in situ. At C,
this fracture merges with an open crack near the boundary of a plagio-
clase grain. The more equidimensional pores in the plagioclase may be
similarly interconnected with the fracture system although it may not
appear as such in the two-dimensional view of figure 5-7. Open cleav-
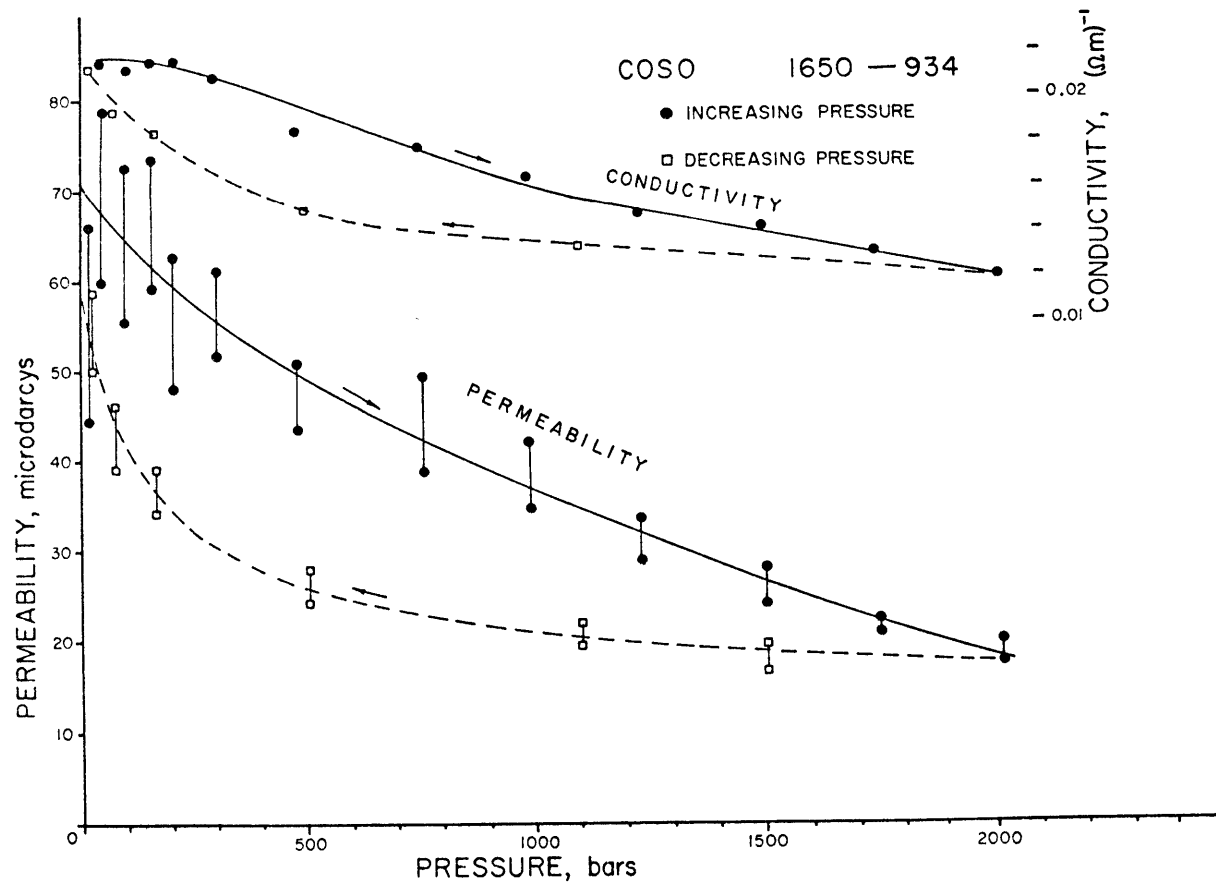
Figure 5-6. Coso BDH#1, depth 285 meters, permeability and conductivity versus confining pressure.
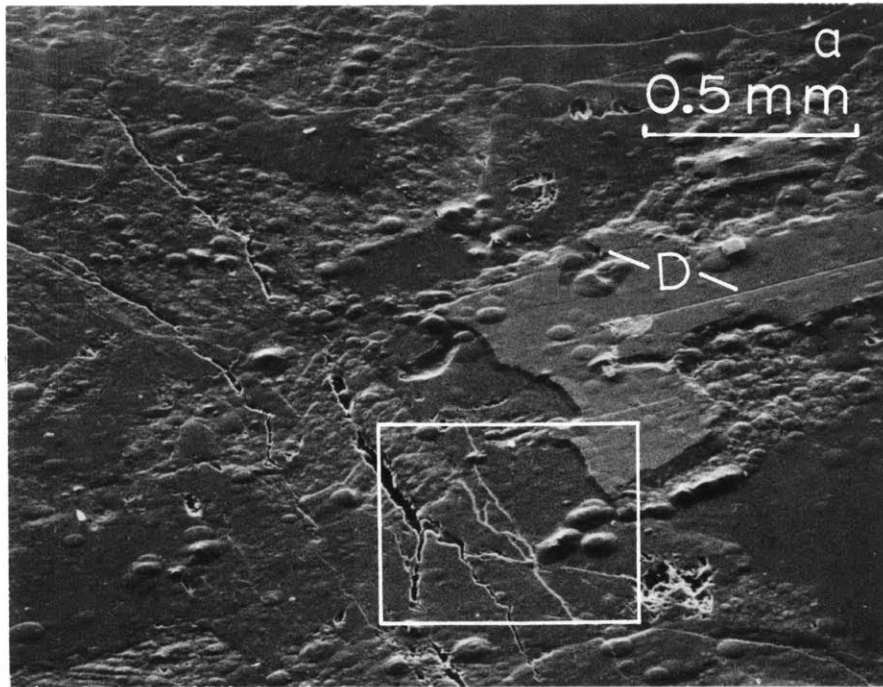
Figure 5-7. SEM photomicrographs of sample #1474 from a depth of
1298 meters in the Marysville well (photographs by S. Shirey).
(a) Overview showing several grains and a large open fracture.
See figure 5-7b for an enlargement of the area outlined by the
white rectangle. C, fracture in plagioclase; D, cleavage crack.
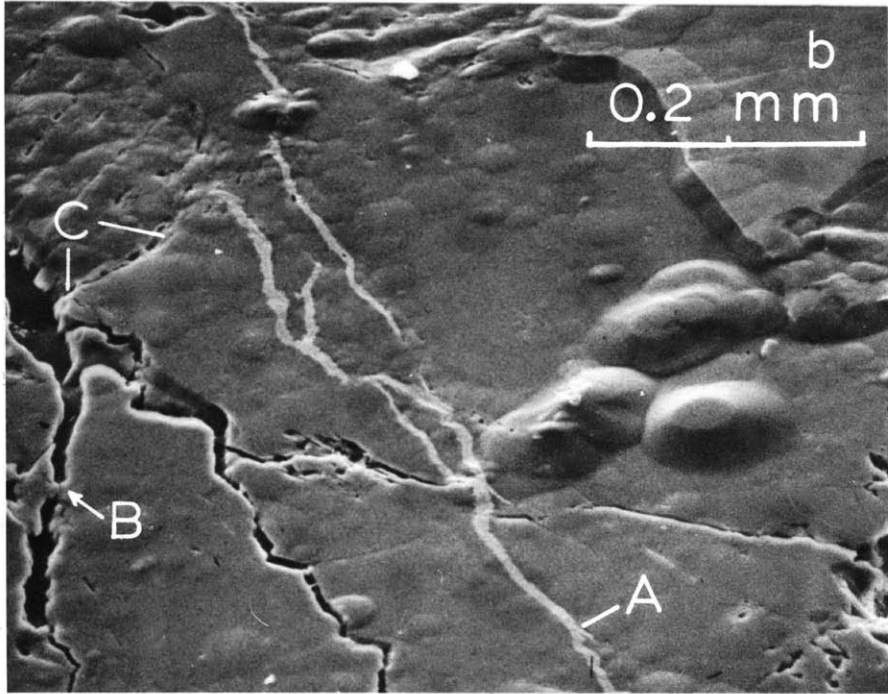
Figure 5-7b. Enlargement of the outlined area of figure 5-7a.

A, pyrite-sealed crack; B, bridging of open fracture.

age cracks are visible at D in figure 5-7a. Once again, numerous frac-
turing episodes are observed, each with distinct characteristics. These
three fractured and shear specimens are interpreted to represent circle
5 in the generalized system of figure 1-3.

Sedimentary rocks can also possess complex fracture histories. Det-
rital grains may have been fractured at their source or in transporta-
tion and deposition. Figure 4-10 demonstrated how compaction can cause
fracturing and crushing. Major fractures often permeate and transect
entire core samples. A specimen from a depth of 116 meters in the Dunes
well serves as an excellent example. Figure 5-8 is an SEM mosaic of
this sample, a well-sorted lithic arenite. Intergrown grain boundaries
result from the formation of overgrowths. In figure 5-8, the cutting
relationships suggest at least four different episodes of fracturing.
All but the final episode show some sign of healing or sealing by miner-
al precipitation. The episodes begin with the major fracture denoted
f1 and end with the small fracture f4, possibly due to drilling. An
ambiguity in the relative ages of fracturing events exists among f2,
f3b, and f3c. Apparently, f2 formed first followed by f3b and f3c.
The similarities in morphologies and merging near D of f3b and f3c
indicate that they are due to the same fracturing event. At location
K, f3c terminates on f2. This termination implies that f3b is younger
than, or at least the same age as, f2. On the other hand, the two
cracks f3b and f2 merge at L. Here at L, f3b probably represents the
refracturing of f2. Hence, this sample has a complex fracturing his-
tory developed within an area of only about one square centimeter.
This sample would hold a position such as circle 6 in the system shown
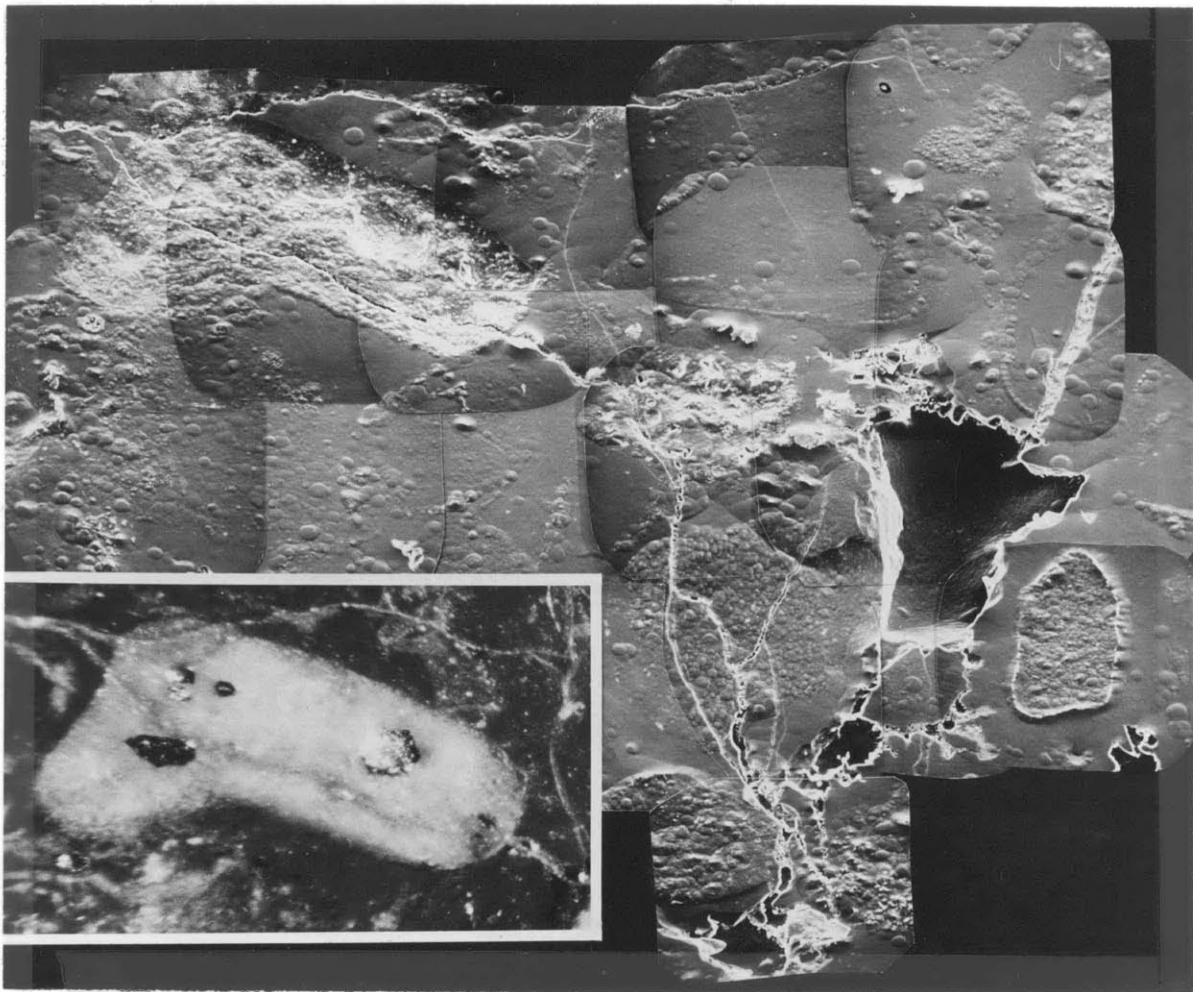
0.1 mm

Figure 5-8. Dunes sample from 116 meters depth (from Batzle and Simmons, 1976).

(a) SEM mosaic of an area of fracture intersections. In the inset, the clay fragment is viewed in reflected light. See figure 5-8b for an index sketch of the principle features.
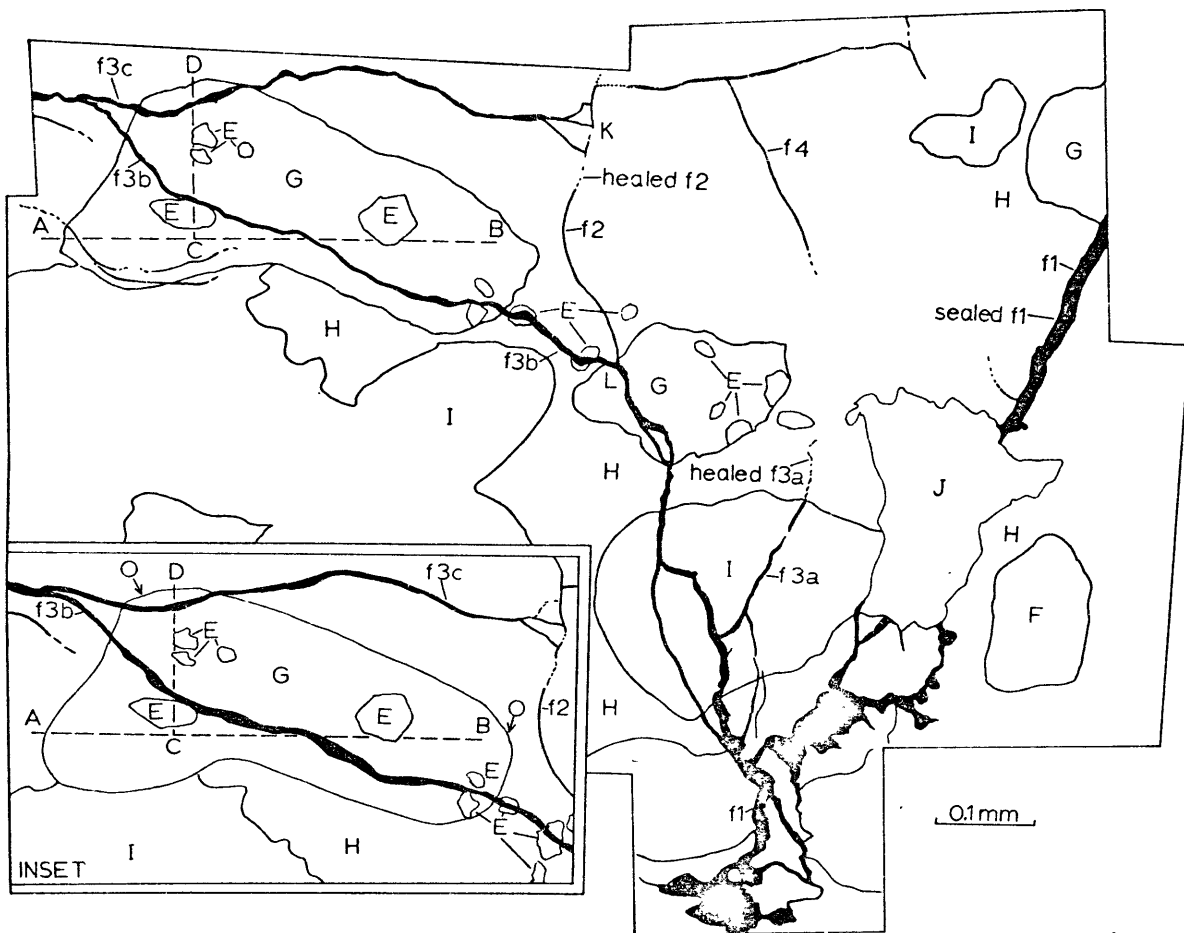
Figure 5-8b. Index sketch of the principle features of figure 5-8a. A-B = microprobe traverse line through altered feldspar; E = pyrite grains; F = lithic fragment; G = altered clay fragment; H = authigenetic quartz overgrowth; I = interior of detrital quartz grain; J = void now filled with epoxy; K, L = fracture intersections; f1 to f4 = fractures (see text).

in figure 1-3.

A more dramatic and straightforward example of multiple refracturing is presented in figure 5-9. The rock is an argillaceous siltstone from a depth of 968 meters in the Heber GTW#1 well. The figure is a view of a calcite-filled vein. The outstanding characteristic of this sample is the development of layering which exactly parallels the vein wall. Most of the vein in the area of the figure is occupied by a single crystal of calcite. The dark wavy bands are made up of clay and silt grains (confirmed by microprobe analysis) remaining on the calcite when the vein and matrix separated during fracturing. This texture is not due merely to the deposition of successive layers of calcite along the boundaries of an open vein. The precise repetition and duplication of the shape of the vein wall at A can only occur as a result of successive fracturing and sealing cycles. The composition of the calcite remains uniform throughout these several veining events to within the error of microprobe analysis. At least a dozen separate fracturing events have occurred. This sample and the following specimen would well represent location 7 in the generalized hydrothermal cell pictured in figure 1-3.

This veined Heber sample is exceptional but not unique. An example of a very similar texture occurs in a specimen from a depth of 403.9 meters in the Dunes well. This Dunes specimen is an indurated, lithic wacke with several large clay clasts embedded within an otherwise uniform sandstone. A photomicrograph is presented in figure 5-10 of the boundary between a clay clast and the surrounding sand matrix. Again, a calcite vein demonstrates numerous episodes of fracturing by the develop-

0.3 m m

Figure 5-9. Calcite veining in a siltstone from a depth of 968 meters in the Heber GTW#1 well. Viewed with crossed polarizers. Note the uniform curvatures at 'A' indicating repeated fracturing.
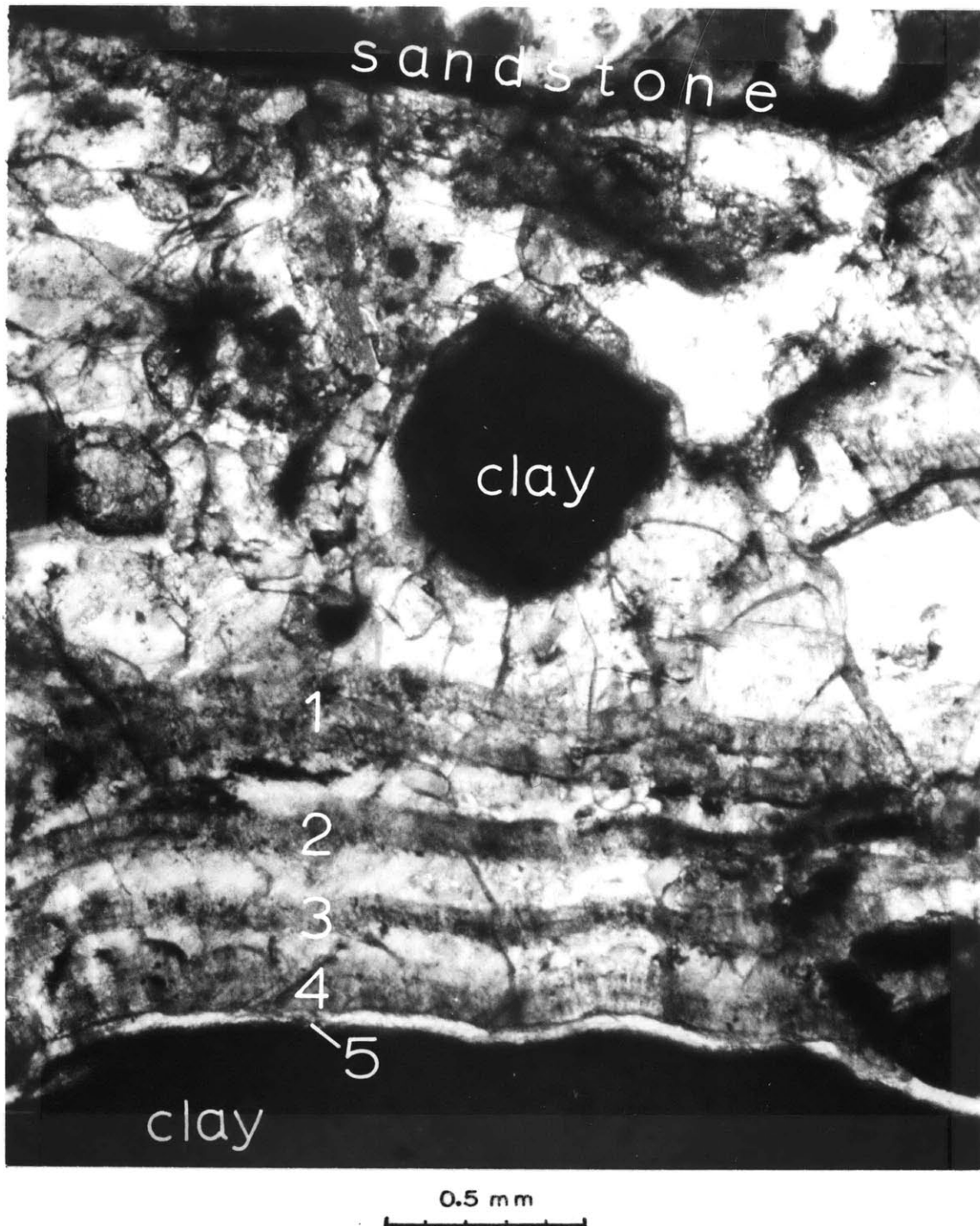
Figure 5-10. A Dunes sample from a depth of 404 meters. Multiple fracturing events recorded in a calcite vein. This is a thick section (100 μm) viewed with crossed polarizers (from Batzle and Simmons, 1977).

ment of banding parallel to the vein wall. In this case, five episodes
of fracturing are indicated. The refracturing textures in figures
5-9 and 5-10 are exceptionally well-developed. Less straightforward
but similar features are found in several specimens from most of the
regions of this study.

Crack Porosity

There exists an obvious need to determine the exact fracture con-
tent of the rocks. The method used here to measure the open fracture
porosity is differential strain analysis (DSA). DSA was performed on
almost the entire sample set and the detailed results are tabulated in
the first appendix. Several examples of DSA have been presented pre-
viously. A few illustrative analyses will be described here. The
Dunes sample from 116 meters can be examined again to observe how the
fracture content measured on the matrix material corresponds to the
several open fractures visible in figure 5-8. Figure 5-11 shows the
DSA curves for the axial and radial directions. The two curves differ
significantly, indicating a substantial anisotropy in physical proper-
ties. The larger radial strain is a result of fractures having a pre-
ferred orientation parallel to the core axis. The constantly changing
slopes, even at high pressure, imply that not all of the fractures are
closed by the maximum of 2000 bars reached during this particular measure-
ment. The measured fracture porosity will therefore be minimum values.
The linear segments in the radial direction are probably due to sets of
fractures closing completely at distinct pressures. In turn, such
closures imply that fractures are grouped into sets with discrete values
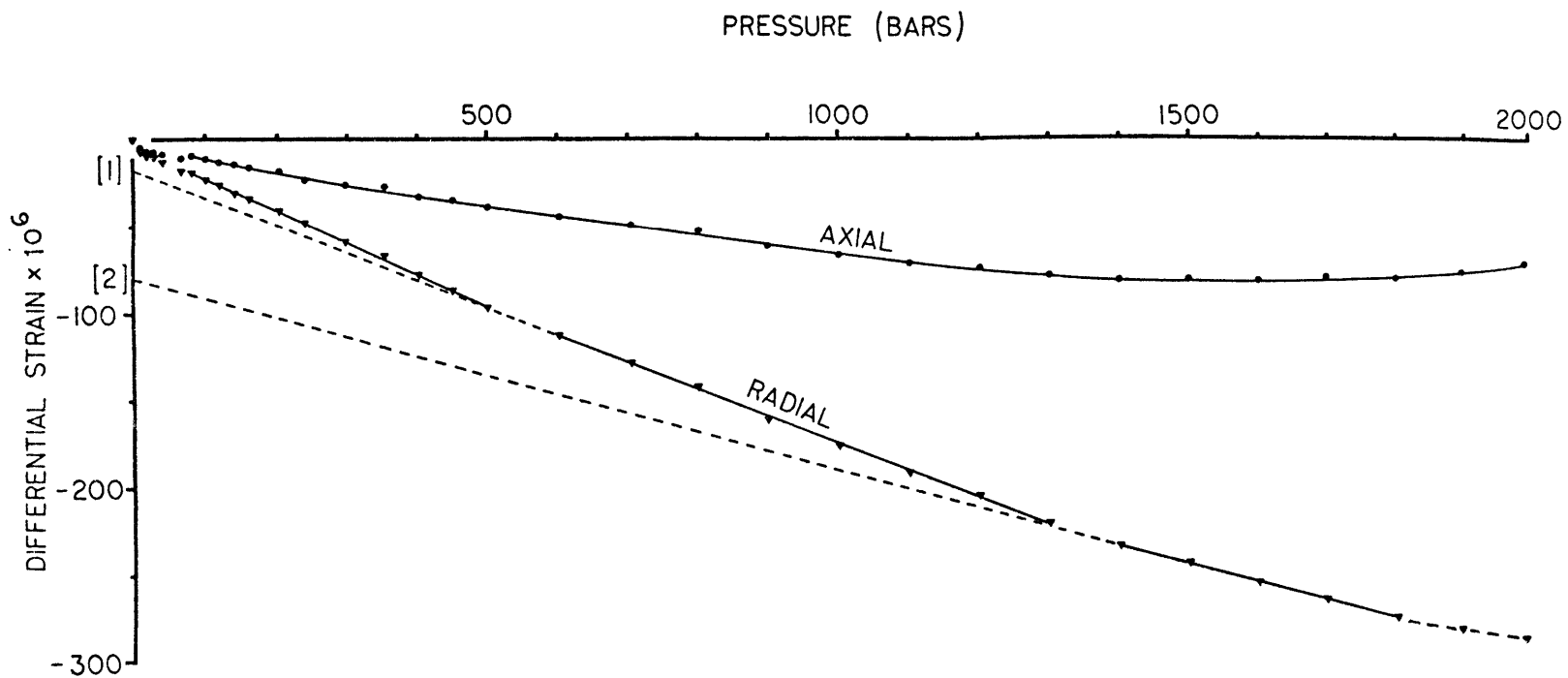
Figure 5-11. Differential strain curves for the Dunes sample from a depth of 116 meters of

figure 5-8. Note the large anisotropic behavior and the linear segments [1] and [2] in the

radial direction (from Batzle and Simmons, 1976).

of aspect ratios. The smoother axial curve probably measures fractures
with more continuous shape distributions. If radial symmetry is assumed,
then the total fracture porosity is twice the radial zero pressure inter-
cept of the high pressure strain plus the axial value: i.e. 0.0507.
The open fracture porosity is small compared to the numerous fractures
visible in figure 5-8.

To test the effects of anisotropy and drilling on fracture content
several strain gages were placed on a single sample from a depth of 241
meters in the Dunes well. This specimen is a well-sorted medium-grained
sandstone with no apparent bedding or directional fabric. The sample
has several macroscopic steeply-dipping fractures that penetrate approxi-
mately two centimeters radially inward from the edge of the core. These
fractures may have been caused by drilling. The top of the core is a
single fracture surface coated with fine adularia crystals. The DSA
curves are shown in figure 5-12. The curves are smooth and show no
linear segments to within the measurement error of approximately 2μ
(2×10^{-6}). Irregularities exist at the low pressure ends of the curves
which are probably due to the crushing of grain contacts and material
spanning fractures. The curve for the axial direction at the edge of
the core (AE) parallels the curve for the same direction at the center
(AC). The edge strain is greater in magnitude by 50μ at high pressure.
The larger strain at the edge is perhaps due to an increased number of
fractures near the drilled surface. The stress due to drilling would
tend to produce tensional cracks with surfaces perpendicular to the
core axis. The strain was also measured in two perpendicular radial
directions X and Y. The Y directions differ by only 26μ at 2000 bars
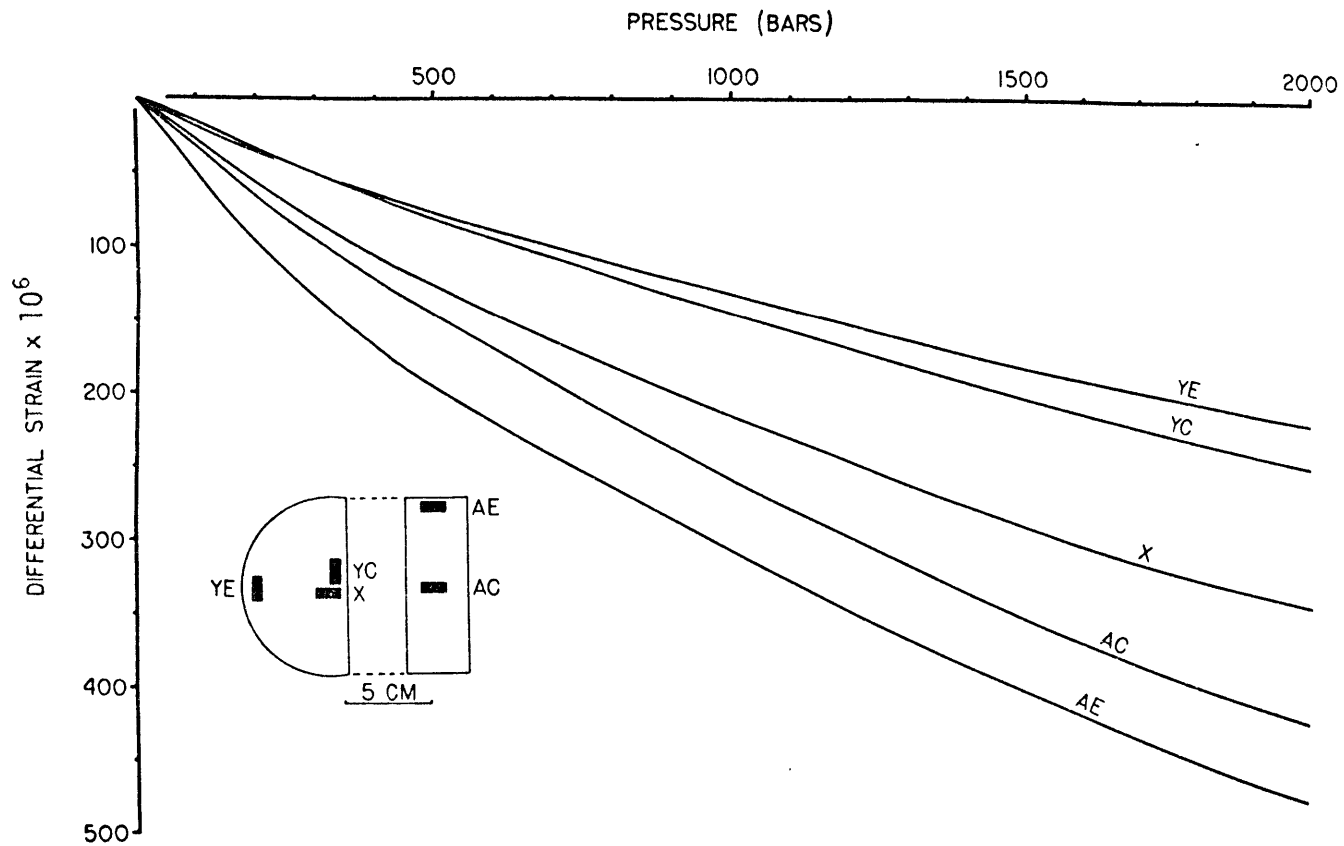
Figure 5-12. Differential strain curves for a Dunes sample from a depth of 241.4 meters. Datum points have been omitted for clarity. Sample size and shape is represented at the lower portion of the figure. The dark rectangles represent the size, position, and orientations of strain gages (from Batzle and Simmons, 1976).

with the center measurement (YC) having the larger value. The differential strain for the X direction at the center (X) is greater in magnitude than for YC. This difference is not due to preparation and must be due to sample anisotropy. The total crack porosity, 0.037%, is the sum of the intercepts of the three central linear strains.

In most of the softer sedimentary rocks, particularly at Heber and Raft River, the effects of fractures are obscured by the much larger compaction effects. Several examples of compaction were discussed in the previous chapter (figures 4-5, 4-7, 4-14). One very interesting example of mixed behavior occurs in a Raft River sample from a depth of 937 meters in the RRGE#2 well. The DSA plots are shown in figure 5-13. Note how in the initial low pressure stages of compression the plot has a curvature typical of fractured rocks. Above 270 bars, crushing apparently starts between grains and dominates the high pressure strain. The fracture characteristics dominate the strain properties of the rock under the low pressure conditions encountered in situ. This sample probably represents a transitional region between compaction-like behavior and fracture-like behavior. We have seen, therefore, a complete progression from the soft sediment compaction and crushing in figures 4-5, 4-7 and 4-14a; to the smaller compression of cemented sand in 4-14b; to the transition behavior displayed here; and finally to the well-indurated sediments of 5-11 and 5-12 with strain curves typical of fractured igneous rocks. In such a progression, strain becomes smaller but the relative contribution of fracture closure and the influence of fractures in general become much larger.

Several conclusions can now be drawn. Evidence for fracturing and
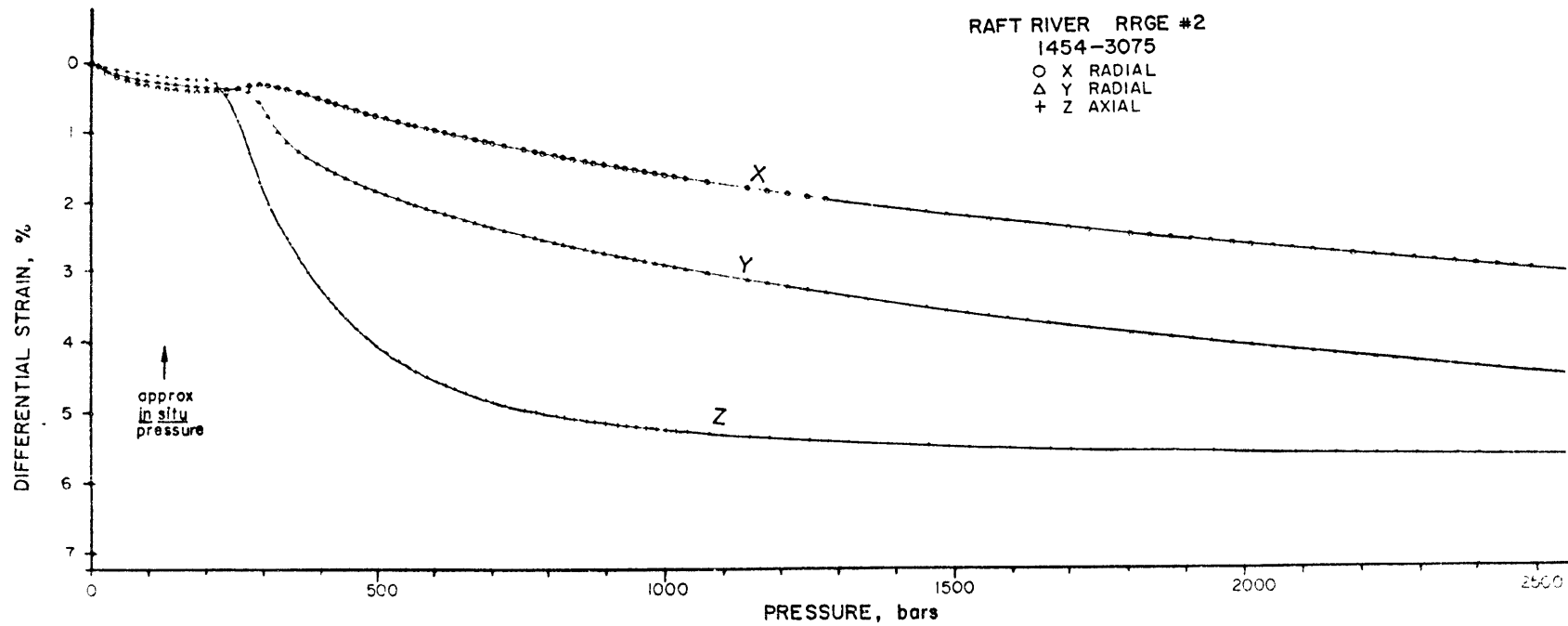
Figure 5-13. Differential strain curves for a sample from a depth of 937 meters in the Raft River RRGE#2 well. Note mixed 'fracture-like' and 'compaction-like' behavior.

refracturing has been seen both in the form of several distinct fracture
sets as well as in the form of multiple breakage along the same vein.
The same general processes and textures are visible in almost all of the
samples obtained for this study. In spite of the repeated breakage,
crack porosities measured on the matrix by DSA remain small, usually
from 10^{-3} to 10^{-5}. The fractures, therefore, are either (1) confined
to the major cracks and veins unsampled by the strain technique or
(2) quickly closed by healing and sealing, the topic of the next chapter.
Fracture distribution is inhomogeneous and anisotropic. Brittle frac-
ture textures are observed even in pliant sediments still susceptible
to large amounts of compaction. Because of the interbedded and zoned
nature of the geothermal systems, the measured crack porosity has no
simple consistent behavior as a function of depth. Each sample has
properties independent of samples only a few meters distant. The frac-
turing is mainly a function of local stresses associated with joints
and fault zones. Fracture porosity may be changed by local sealing and
alteration. The fracturing and refracturing is common and widespread
in the systems studied. The fracturing processes may be responsible
for the numerous 'nanoearthquakes' occurring in some geothermal systems
(Combs and Hadley, 1977).

Effects of Fractures on Permeability and Conductivity

The episodic refracturing observed in the geothermal systems neces-
sitates the examination of the general effects of fracturing on the
transport properties of rocks. Fractures and joints dominate the flow
characteristics of most dense crystalline rocks. A large fracture

content can increase the permeability sufficiently to render otherwise dense plutonic rocks porous and important as aquifers. As an example of the effect of a single fracture, we can once again re-examine sample 1452-380 of figure 5-8. The permeability of the sealed, unfractured matrix is approximately 2.8 nannodarcys. A sample containing the single, partially-sealed fracture fl in figure 5-8 has a permeability of about 8.2 millidarcys - an increase of six orders of magnitude. The conductivity was similarly increased by approximately one order of magnitude. Such a strong dependence on fractures will also occur on a large scale. At Marysville, for example, a specimen from a depth of 1010 meters has the transport properties shown in figure 5-14. The permeability is on the order of 100 nannodarcys at in situ pressure conditions. Similar properties were measured on the sample from 1954 meters shown in figure 4-2. However, a large amount of fluid flow occurs in nearby fracture zones (figure 2-15). Obviously, even a trivial fracture porosity can have a major impact on the economics of a geothermal system.

Numerous mathematical treatments of flow through fractured media have been developed (see, for example, Snow, 1968; Parsons, 1966; Sharp and Maini, 1972; Norton and Knapp, 1977). The simplest and most straightforward analogy is with flow between parallel smooth plates. The flow rate, q, is dependent on the width, w, of the fracture to the third power

$$q = \frac{\ell w^3}{12\mu} \nabla P \qquad (5-1)$$

where μ is the fluid viscosity and ℓ is the length of the fracture nor-
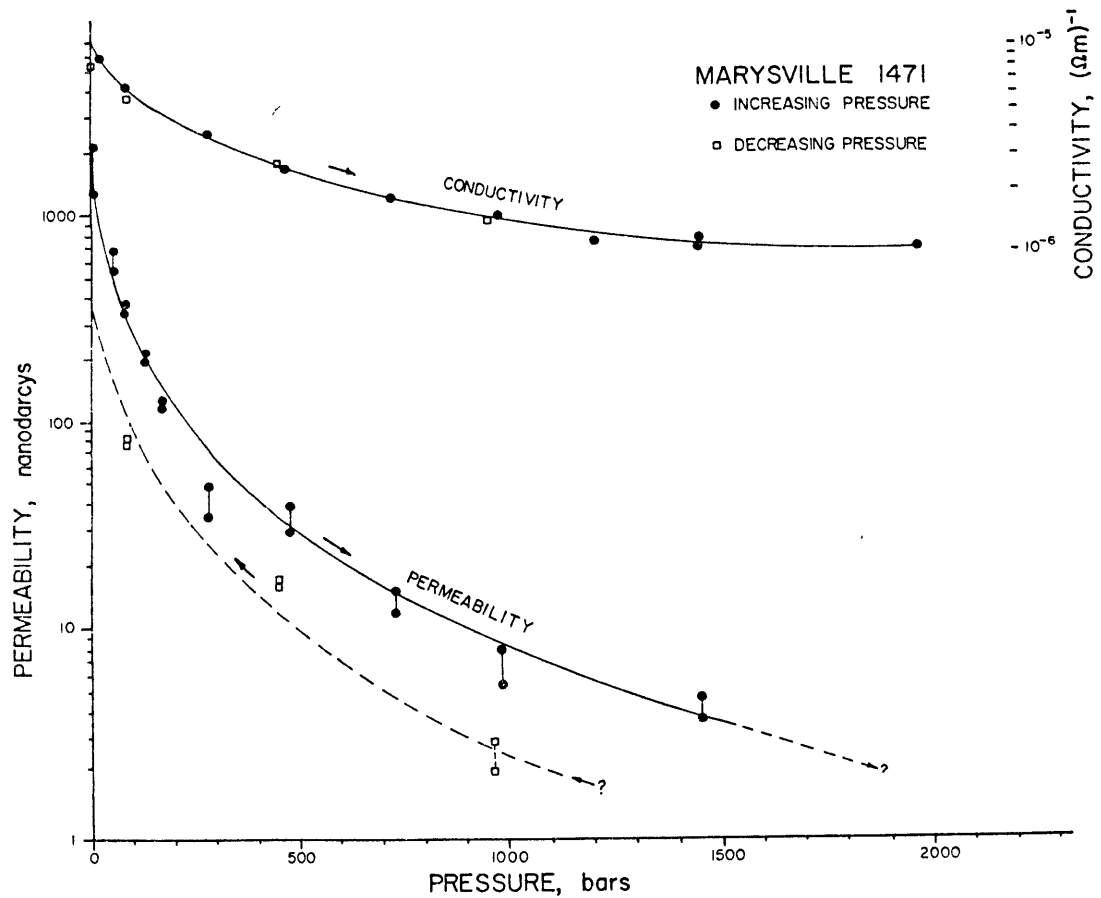
Figure 5-14. Permeability and conductivity versus confining pressure for a sample from a depth of 1010 meters in the Marysville well (sample #1471).

mal to the direction of maximum pressure gradient, ∇P. This width

dependence is by far the most common assumption made to model flow

through fractures. Other developments (see, for example, Hubbert, 1956;

Bear, 1972; Brace, 1977) dealing with more generalized flow through

porous media relate flow to mean hydraulic radius and porosity or to

the mean specific surface of the conduction path. The other treatments

usually reduce to equation (5-1) in the idealized parallel plate case.

Two difficulties immediately arise when applying idealized flow to real

fractures in rocks. Flow may not be laminar. A Reynolds number can

be derived for fractures ($2wv\rho/\mu$) where v and ρ are the fluid velocity

and density, respectively. The extremely small size of the cracks dealt

with in this study ($w \ll mm$) insures that flow is below the threshold of

the turbulent flow regime of a Reynolds number of about 2000 to 5000

(Parsons, 1966). In larger fractures and joints, however, the tur-

bulent regime may be entered. A far more serious difficulty is that

fractures are definitely not smooth or parallel. This difficulty can

be documented by an examination of real fractures in rocks such as in

figures 5-7 and 5-8. Although the regime of classical turbulence may

never be entered, rough surfaces, changes in width and direction, and

obstructing materials can give rise to cross currents that disturb laminar

flow. The result will be a more homogeneous and mixed flow throughout the

fracture. This mixed or non-laminar flow will behave similarly to

truly turbulent flow. Sharp and Maini (1972) suggest that the flow

dependence on width be w^n where $1.5 < n < 3$. Gale (1975) argues that the

change in width dependence is not necessary if surface roughness is

taken into account. Flow through a single fracture is complex and

poorly understood. Obviously, less is understood about the complex inter-
actions between the entire fracture populations in real rocks.

Geometric Mean

Many investigations have modeled fractures by embedding discrete sets
of slits in a permeable or impermeable matrix. Warren and Price (1961),
Parsons (1966), Madden (1976), and Madden et al. (1977) conclude that the
geometric mean of individual fracture contributions gives a good overall
estimate of the entire system values. Madden used a network analogy sim-
ilar to the techniques used previously by Parsons. Originally, Madden
(1976) developed the geometric mean model for rock conductivity and this
development has been adapted in Appendix 2 for calculations of permeabil-
ity. The technique of Appendix 2 can utilize fracture parameters mea-
sured on samples with DSA. From the measurement of the fracture poros-
ity, ϕ_i, aspect ratio, w_i/ℓ_i, and estimates of length, ℓ_i, single frac-
ture permeability, k_i, and conductivity, Y_i, can be calculated:

$$k_i = \frac{w_i^3 \ell}{18\mu} \sum_j (\frac{\phi_j}{w_j \ell_j}) \qquad (5\text{-}2)$$

and

$$Y_i = \sigma_f \frac{2}{3} w_i \ell_i \sum (\frac{\phi_j}{w_j \ell_j}) \qquad (5\text{-}3)$$

Here μ and σ_f are the fluid viscosity and conductivity, respectively.
The overall geometric mean values of the system will be

$$<<k>> = \prod_i k_i^{P_i}$$

$$<<\sigma>> = \prod_i \gamma_i^{P_i}$$

where P_i is the probability of the 'i' fractures. The model is applied directly to Westerly granite because it is a fine-grained, homogeneous, approximately isotropic (to within the measurement error of permeability and conductivity) rock with well-known properties and is frequently used in other geophysical research. Though specifically applied to Westerly granite, the results can be extrapolated to other rocks.

The model developed in Appendix 2 involves several important assumptions and simplifications. The assumptions are involved with the flow and conduction dynamics and with the shape and size of the fractures. Darcy's law is assumed valid even for flow through fractures with apertures on the scale of a few tens of Angstroms. Conduction along mineral surfaces is ignored here but becomes significant for small crack widths and low fluid conductivities. The effective width is used with no adjustments for surface roughness or boundary effects. The pores and cracks are assumed to interact simply, to be well-interconnected, and to be independent of connective topography. The rock is considered as homogeneous and isotropic. Accordingly, permeability and conductivity, which are actually tensor properties, will also be considered isotropic in this analysis. The fractures are modeled as rectangular voids with one dimension common to all sizes. The other two dimensions are allowed to vary. The fractures are grouped together into sets according to aspect ratio with a corresponding porosity. Each set is assumed to have a single effective width, length, and closure pressure. The aspect ratio and porosity are determined with the DSA data in accordance with the

relationship developed by Walsh (1965) and Morlier (1971) for the closing

of idealized cracks. Aspect ratios above 0.01 cannot be measured with

strain data and so the porosity of the more equidimensional pores must

be estimated in accordance with the total rock porosity. The resulting

model is obviously crude. Through the use of this technique, important

fracture parameters can be constrained and identified and some basic

insights into flow interactions can be gained.

Permeability and conductivity curves are fit by combining measured

values and estimated parameters in a crude inversion procedure. The

model is not well-constrained and requires that several important pa-

rameters be estimated. First, from DSA, porosity as a function of as-

pect ratio is determined. Since conductivity and permeability have dif-

ferent sensitivities to width and length (equations 5-2 and 5-3) these

flow values can be used to estimate both relative fracture shape as well

as absolute size. The relative length distribution is altered until the

conductivity is matched. The absolute size can then be increased or

decreased until the permeability is similarly matched. Ideally, the

best method to investigate the effects of the fracture content would be

to keep the matrix (i.e. unfractured rock) properties constant and ob-

serve the effects of altering the fracture porosity. One simple approxi-

mation to this technique is to make observations as fractures close under

increasing pressure. In the model, cracks will be closed by pressure by

means of two different types of mechanisms. These mechanisms will model

crack closure by changing fracture widths and flow properties.

The geometric mean model is applied to a sample of virgin Westerly

granite. The observed and calculated permeability and conductivities are

shown in figure 5-15. The porosity versus aspect ratio distribution

is shown in figure 5-16. Note that the porosity decreases rapidly at

small aspect ratios. The porosity must be extrapolated for $\alpha > 10^3$

and the two largest sets of aspect ratios must be expanded in order

to increase the total porosity to the value measured by immersion. The

total interconnected porosity includes both the fractures and the more

equidimensional pores. In Westerly granite, the plagioclase grains in

particular are filled with pores which comprise a large proportion of

the measured immersion porosity of approximately 1%. The estimated

length distribution requires that cracks shorten as aspect ratios in-

crease, otherwise too many narrow cracks exist and the probability dis-

tribution is overdominated by small aspect ratios. Large quantities

of narrow cracks result in overestimating the effects of confining pres-

sure and necessitate unrealistically large lengths and widths. The

model fractures are closed by increasing confining pressure via two types

of mechanisms. Type 1 consists of closing down each width to a small

fraction of the initial value. The 'best fit' fraction found was 1/25

of the initial width and the resulting curve is shown in figure 5-15b.

This type of closure is what would be expected for smooth parallel

plates. Figure 5-15b demonstrates the poor fit that ensues. The con-

ductivity and permeability diverge: too large a decrease in permeability,

too small a change in conductivity. Other closure fractions could match

either conductivity or permeability values, but not both. Improving the

fit of one value greatly increases the error in the other. Another

type of mechanism needs to be utilized. Type 2 is a somewhat ad hoc

mechanism that simply forces all cracks to collapse such that they all
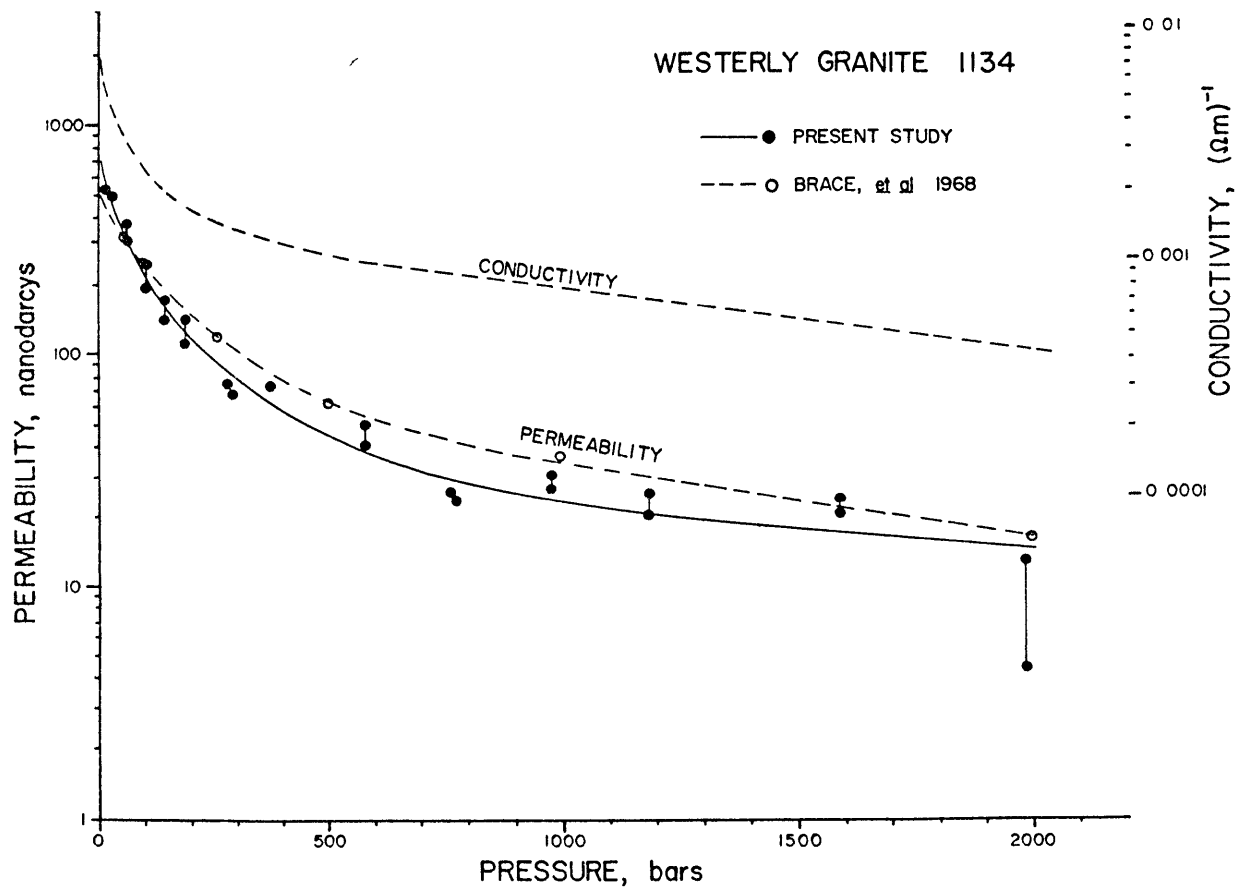
Figure 5-15. Permeability and conductivity as a function of confining pressure for Westerly granite.

(a) Measured values.
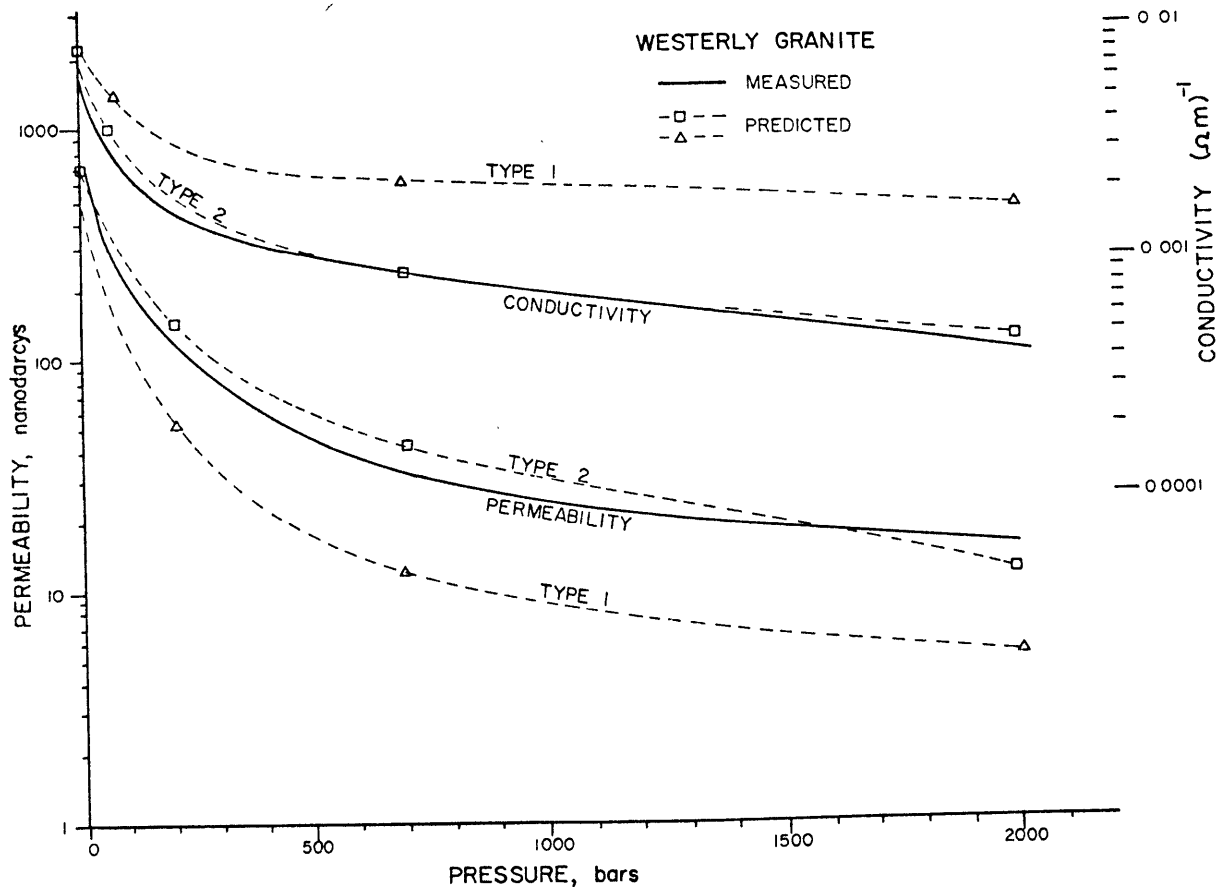
Figure 5-15b. Comparison of calculated versus measured values. Type 1 and Type 2 refer to different model mechanisms for fracture closure (see text).
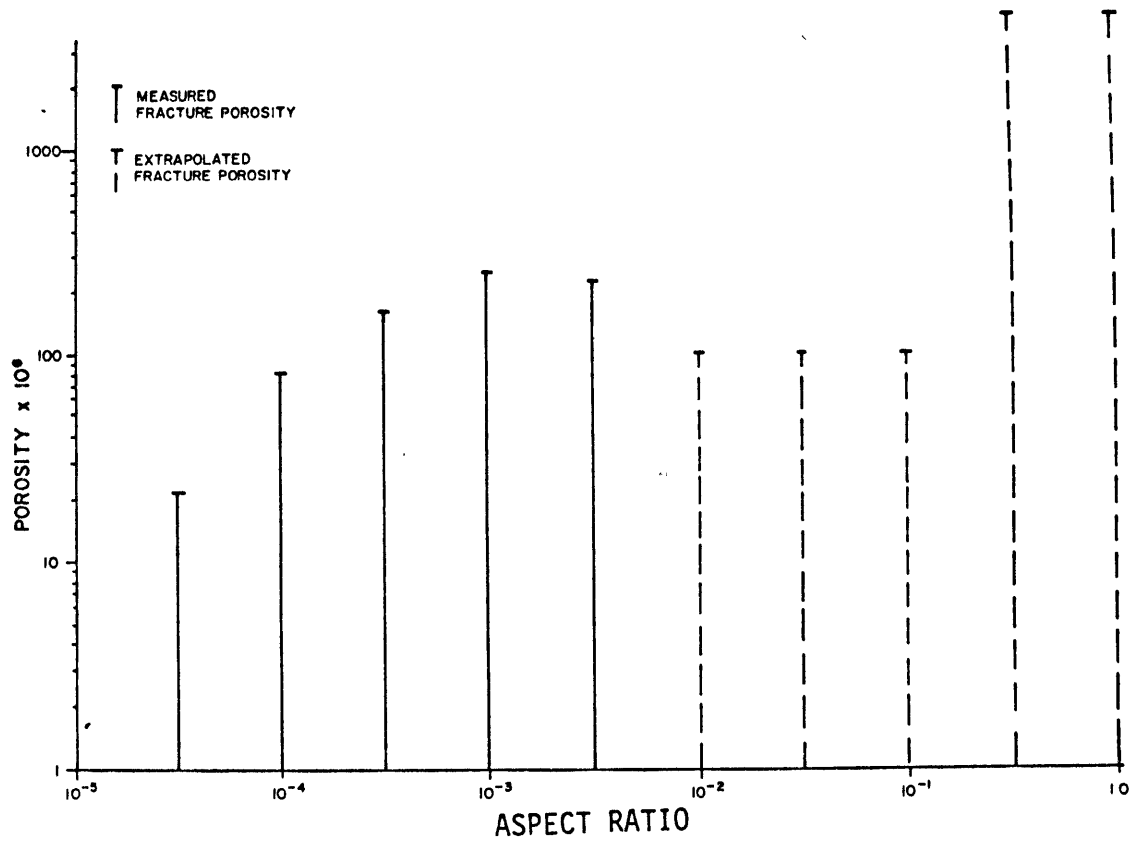
Figure 5-16. Fracture porosity versus aspect ratio for Westerly granite (derivation in Appendix 2).

have the same small values of transport properties at closure. This latter type would be the behavior expected for rough irregular fractures with very inefficient closure. The effective lengths are closed as well as the widths. The resultant 'best fit' curve is shown in figure 5-15b. The fit to the observed data is entirely within the error limits of measurement. This latter type of closure is an important result and indicates that closure is not simple for Westerly granite.

The model developed above specifically for Westerly granite contains numerous assumptions and estimations. The absolute magnitude of the calculated values of both the conductivity and permeability could be shifted by changing the initial size and shape of the model fractures. Most of the significance should be placed on the good agreement between the shape of the type 2 closure and observed curves. The agreement indicates that the rock behavior can be modeled by simple fracture inter-action and closure. The more equidimensional voids must play a significant role in the flow, otherwise permeability and conductivity would be too small at high pressure. The inefficient closure indicates that fractures do not behave like the isolated smooth ellipses frequently used as a model shape. As can be seen in the photomicrographs of this thesis (figures 5-3, 5-4, and 5-8) as well as in other observational investigations (Brace et al., 1972; Sprunt and Brace, 1974; Richter and Simmons, 1977; Simmons and Richter, 1976), fractures are typically rough, irregular, and often partially sealed and bridged. The DSA porosity determination cannot differentiate between smooth, simple, elliptical fractures with corresponding simple complete closure, and irregular, undulatory fractures which close in several separate stages.

Some of the porosity attributed to small aspect ratio cracks is almost certainly due to the early closing stages of wider irregular cracks. These observations indicate why fractures seem so well-interconnected and independent of specific connective topographies. The decrease in the transport properties with pressure is smooth and continuous. A large number of independent narrow cracks in the conducting network of the rock would cause a catastrophic decrease in permeability and conductivity when a critical probability of closure is reached (Madden, 1976). The dependence on small aspect ratio cracks explains, for example, the large influence of pore pressure on flow properties. Changes in fluid pressure during injection and withdrawal tests in wells give significantly different rock permeabilities. Small decreases in effective pressure will have a large effect on the small aspect ratio fractures critical to permeability and conductivity at low confining pressure. Lowering the effective pressure widens the original fractures and opens new ones. The new open cracks are placed in the fracture network at better than parallel efficiency. In other words, not only do the new fractures conduct fluids and electric currents as an independent set, but these new fractures also serve to interconnect pre-existing cracks. Modeled crack closure is consistent, therefore, with rock properties measured both in the laboratory and in the field.

The geometric mean model developed above is idealized, highly specific to Westerly granite, and most applicable to fractured crystalline rocks. Almost as much insight can be gained by examining the relationship between conductivity and permeability. Brace (1977) discussed the simple relation derived from flow equations and Archie's

law:

$$k = (m^2/k_0)\phi^3 = (m^2/k_0)(\sigma_f/\sigma_r)^{-1.5}$$

where m and σ_r are the mean hydraulic radius and rock conductivity, respectively, and k_0 is constant shape factor. The equation can be re-written

$$\frac{k}{\sigma_r^{1.5}} = c_1 \cdot m^2$$

with c_1 a constant. Similarly, equations (5-2) and (5-3) can be combined to form

$$k = \frac{w^2}{12\mu} \frac{\sigma_r}{\sigma_f}$$

or equivalently

$$\frac{k}{\sigma_r} = c_2 \cdot w^2$$

and c_2 another constant. Applying this equation to Westerly granite in figure 5-15 gives only a small variation in the ratio of permeability to conductivity which requires m or w to remain approximately constant. This result again is indicative of inefficient closure. The technique may be applied to other samples such as the Marysville #1471 (figure 5-14). The ratio k/σ_r decreases by two orders of magnitude which implies a similar decrease in w^2. The decrease suggests less dependence on the more equidimensional voids in this sample, not a surprising result because the total porosity of this rock is less than 0.002. The indicated decrease in width requires that a large portion of the flow occur in the small aspect ratio cracks that close completely below the

in situ pressure. This behavior may be typical of low porosity crystal-
line rocks that are damaged during sampling. A similar conclusion may
be drawn for the Marysville sample #1477 presented in Chapter IV. The
Dunes sample from 116 meters also demonstrated the marked dependence
on fracture width. The difference in permeability of six orders of
magnitude coinciding with the order of magnitude changes in conductivity
between the fractured and unfractured samples implies that the mean
width changes by 2 to 3 orders of magnitude. The large partially-sealed
fracture, f1, in figure 5-8 has an observed width of about 15 μm. The
decreased 'mean' width of the unfractured sample is then approximately
0.05 μm. The smaller width is in agreement with the observed small frac-
tures such as f3 and f4 in figure 5-8 that permeate the core. The com-
paction, grain crushing, and dependence on clay content make the extrapo-
lation to other sedimentary samples difficult.

Large Scale Properties

Any measurement on small samples will fail to include the flow
contributions of large faults, joints, and fracture zones. These large
features often dominate the overall flow values, as observed in the
Marysville well. Direct application of the geometric mean model is
difficult not only because of the larger scale, but also because of
differences in the basic characteristics and dependence on physical
parameters. Joints may be wider but poorly interconnected. The depen-
dence on the more equidimensional void indicated for the Westerly
granite samples is probably not valid for a jointed pluton. A more
analogous comparison for the small Westerly samples might be with a

fractured sedimentary unit where both the matrix and fractures contrib-
ute significantly to the total permeability. In situ measurements are
the only way to adequately account for such features if the absolute
flow capabilities of the system are to be determined. Two methods for
in situ observations are direct fracture and joint measurement and
injection-withdrawal tests. Snow (1968) estimated the fracture widths
and spacings from pumping tests in drill holes at several dam sites.
He concluded that the fracture porosity and crack apertures decrease
logarithmically with depth with simultaneous increases in spacing
between fractures. Pratt et al. (1977) performed tests on an outcrop
of granite by measuring flow along joints in an isolated block. The
results suggest a permeability on the order of millidarcys in otherwise
intact igneous rock. Direct measurements of fractures in wells have
been accomplished with devices such as impression packers and downhole
cameras. Norton and Knapp (1977) made a survey of porosity by both
field and laboratory measurements. Total porosity was defined as con-
sisting of major flow porosity, diffusion (i.e., 'dead end') porosity,
and non-interconnected residual porosity. They concluded that, although
total rock porosity is commonly 0.2 to 0.01 in hydrothermal systems,
most porosity is contained in the residual pores. Flow and diffusion
porosities are small, on the order of 10^{-3} to 10^{-5}. These values of
porosity are in agreement with the fracture porosities measured by DSA
(Appendix 1). The flow-diffusion porosity hypothesis of Norton and
Knapp can be applied to several veins observed in this present study.
For example, in a Dunes sample from 148 meters depth (figure 5-17),
pyrite is developed in the matrix adjacent to a pyrite-filled vein and
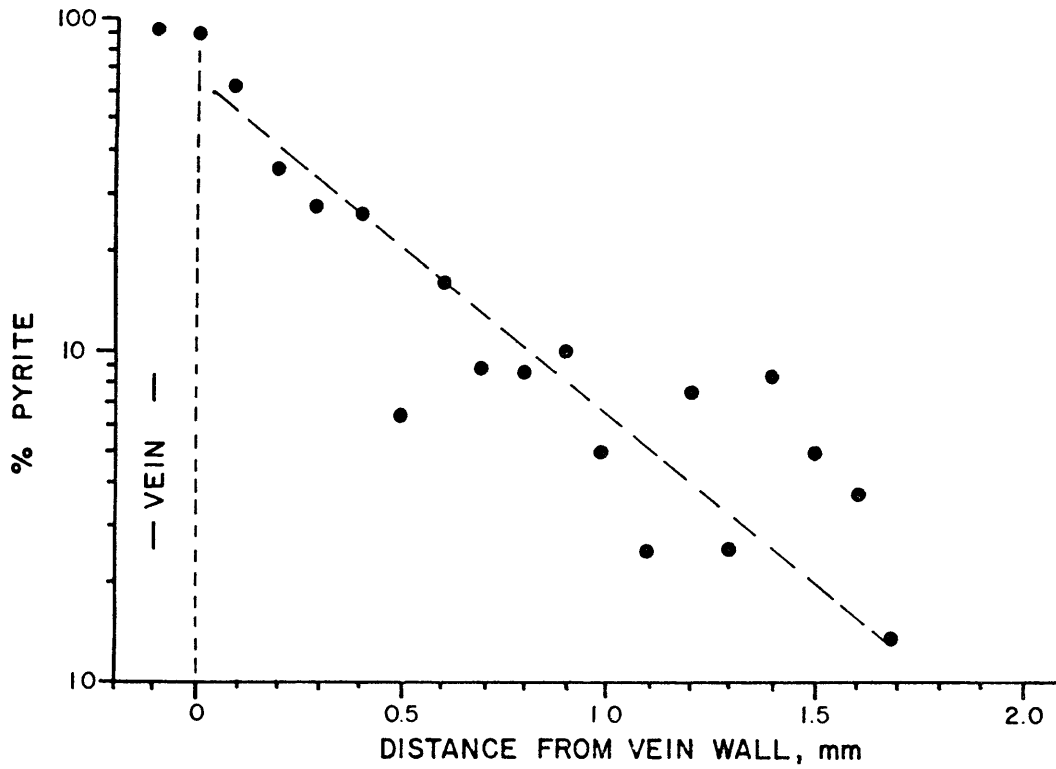
Figure 5-17. Dunes sample from a depth of 148.4 meters. Matrix pyrite content as a function of distance from a pyrite-sealed fracture. Content determined from 80 point count traverses running parallel to the pyrite vein at successive distances of 0.1 millimeters.

decreases in abundance with distance, as would be expected for dif-
fusion transport away from the vein. On the other hand, the results
of the modeling in the last section contradict the conclusion of
Norton and Knapp of little or no flow contributions from the more
equidimensional 'residual' pores. The discrepancy may be due to the
relatively open nature of Westerly granite porosity. The conclusion
drawn from most in situ investigations is that the normal near-surface
permeability of even dense crystalline rocks is on the order of micro-
to millidarcys rather than the nannodarcy values measured in the labora-
tory.

Causes

This section briefly examines the different mechanisms used to
explain the origin of fractures in hydrothermal systems. The most ob-
vious mechanism is faulting. With the exception of Marysville, all the
systems in this study are located on or near large faults. Most sys-
tems in general are associated with fracture and fault zones. Permeable
conduits are provided and kept open by continued fault motion. Normal
faults, common in the Basin and Range Province, may be particularly
efficient in this respect. Another mechanism is natural hydrofracturing.
Grindley and Browne (1976) conclude that hydrofracturing is important
in producing permeable breccia zones in the geothermal fields of New
Zealand. In many of the samples obtained for the present study, soft,
pliant sediments are filled with veins which are often many millimeters
wide. These veins are common in the Raft River and Heber areas. The
Heber sample from a depth of 968 meters (figure 5-9) is one example.

At Heber, the lithostatic pressure at the sampled depth is approximately 200 bars. The only way to tensionally open fractures in such soft rocks would be by the development of high fluid pressure. However, such high fluid pressures are not presently observed in the wells. Thermal cycling of rocks has caused significant increases in the fracture porosity on a laboratory scale (Cooper and Simmons, 1977). Moskowitz and Norton (1977) believe that increasing temperature can cause the fluid pressure in isolated pores to increase sufficiently to cause hydrofracturing on a small scale. They conclude that such fractures significantly alter the flow properties of the rocks in geothermal systems. Several other mechanisms may be possible, including the differential compaction of sediments, settling, and movement occurring in reponse to changes in fluid pressure. Stress relief may be important in the formation of the near-surface joints described by Snow (1968). It is difficult to distinguish among these different causes on the laboratory scale, but all will contribute to the transport properties of the rock.

Conclusions

This chapter discussed a wide variety of evidence, methods, and results concerning fractures. Observations were made on a microscopic scale of fracturing histories and characteristics. The effects of microfractures on the transport properties of rocks were both measured and modeled. Both in situ studies and extrapolation of model parameters indicate that major fractures and joints are widespread and dominate the overall flow properties in crystalline rocks. These large features could not be sampled in this investigation. Several general

conclusions can still be drawn:

(1) Evidence for fracturing is widespread and abundant in the geothermal areas.

(2) Many episodes of fracturing and refracturing occurred with differing age, intensity, and morphologies.

(3) The fractures have a drastic effect on the transport properties. Permeability can be increased by several orders of magnitude by even single partially sealed fractures.

(4) The effects of the fractures can be modeled by the geometric mean of a population of small idealized cracks.

(5) Naturally occurring fractures are irregular, undulatory, and clogged with material making the flow characteristics complex and resulting in inefficient closure under pressure.

CHAPTER VI

SEALING, HEALING, ALTERATION

Introduction

Sealing, healing, and alteration processes tend to reverse the effects of fracturing. These modifying processes can lower permeability and conductivity by several orders of magnitude and require new episodes of fracturing to keep the geothermal system open to circulation. Such modifications are caused by crystal regrowth across cracks, by material precipitation out of solution, and by water-rock interactions. The changing physical conditions within a system generally make hydrothermal fluids supersaturate with respect to numerous compounds. The fluid-rock reactions often produce low density hydrous phases. Any open fractures will therefore have a strong tendency to be sealed and filled quickly in most systems. The result is the development of complex histories of repeated fracturing and fracture sealing. The nature and characteristics of both fracturing and subsequent modification may vary significantly with time.

In this chapter, we will examine the processes that alter and fill the cracks, fracture zones, and nearby matrix. The evidence presented will be predominantly in the form of fabric and textural observations. The fluid properties typical of many hydrothermal systems will be discussed briefly since these properties are critical to the reactions that occur. Several examples of sealing and alteration will be presented. The effects of these processes on the physical parameters will be investigated through both direct measurement of physical properties and

examination of rock textures. The chapter will conclude with generalizations on the results of fracture closure by sealing and alteration. Although several examples are cited, the chapter will not be an exhaustive survey of all textures and fabrics observed in all the samples obtained. Since the purpose of this investigation is not to define the pressure-temperature conditions in general or to deduce phase relations or equilibria, the detailed mineralogy will be discussed only when it pertains to physical characteristics.

Fluid Properties

The fluids in geothermal systems are extremely variable in composition. The composition is dependent on numerous factors, including temperature, country rock, circulation history, and contamination by near-surface ground water. The dominant ionic characteristics of solutions of most systems are sodium chloride, acidic sulfate chloride, acidic sulfate, and calcium bicarbonate (Sigvaldason, 1973). The systems studied in this thesis are of the sodium chloride type except for the sodium sulfate bicarbonate fluids at Marysville. All types of solutions also can contain significant amounts of silica, sulfate, bicarbonate, sulfides, and dissolved gases, as well as the dominant sodium and chloride ions. The pH values of the fluids are usually about 7, approximately neutral. The total dissolved solid content ranges from about 4000 parts per million at Dunes and Raft River to less than 800 ppm at Marysville.

The chemical characteristics of hydrothermal fluids change in response to the changing physical and chemical environment. The general-

ized geothermal system described in Chapter I involves heating and cooling cycles. As temperature increases, fluids saturate with components derived from the surrounding rocks. As the temperatures drop in ascending limbs of the system, fluids become supersaturated. This temperature dependence is the basis of the several chemical geothermometers applied to geothermal fluids. Chemical changes also occur, for example, when the fugacities of oxygen or carbon dioxide fluctuate or the pH and ionic concentrations vary as a result of gas venting, mixing with ground water, or rock reactions. Fluids and rocks are frequently not in equilibrium (see, for example, Hoagland, 1977). Water-rock reactions often produce hydrous minerals such as zeolites, clays, and hydromicas with low density. Unstable minerals may alter or be replaced. For example, dispersed iron and organic sulfur can combine to form pyrite which is later oxidized to hematite or limonite. The fluctuations in fluid properties result in a wide variety of possible reactions. At various stages sealing, leaching, or metasomatism may occur within and around the same fracture (Batzle and Simmons, 1976). The interpretation of such sealing textures may be ambiguous as several processes can give rise to the same results. As an example, calcite may be precipitated due to changes in temperature, pH, partial pressure of carbon dioxide, or gross fluid chemistry. The typical result of fluid and rock interactions is a sealing of fractures with precipitated and alteration materials.

Examples of Fracture Sealing, Healing, and Alteration

The evidence for healing, sealing, and alteration is abundant throughout the complete sample set. The processes are interrelated and

there is no sharp division defining the three types. Healing results when the broken crystal lattice reforms across a crack. The texture produced is often chains and planes of fluid inclusions such as in figures 5-1 and 5-2. Sealing refers to the process of filling fractures with precipitated materials. A large variety of minerals can be involved in sealing and numerous species were indicated in the well stratigraphies shown in Chapter II. Textures typical of sealing were already shown in figures 5-9 and 5-10. Alteration is also common and ranges from subtle replacement such as albitization of existing feldspars to the more obvious development of clays or oxide rims around unstable minerals. All three processes often occur simultaneously within a single specimen.

The several modification processes can be observed in the Dunes sample from 116 meters of figure 5-8. Examples of healing are shown in figure 5-8 at 'healed f2' and 'healed f3a'. Sealing by mineral precipitation occurs at 'sealed f1'. The sealing minerals are mostly quartz with the addition of a few pyrite grains. The sharp, unetched nature of the fracture boundaries within quartz grains indicates that the fluids were always silica-saturated.

This Dunes specimen shows the effects of time-varying fluid chemistry. The fluids in the rock were in the process of oxidizing pyrite. Both oxidized rims around many pyrites and varying degrees of pyrite oxidation exist throughout the sample. At some locations within the major fracture f1, pyrite grains are almost completely altered to hematite. At other locations within this same fracture, unaltered euhedral pyrite grains still exist. Hence, fluid flow is restricted to specific sites within the fracture.

The progressive oxidation occurs in a particularly significant form within the altered clay (A-B). The oxidation reaction is poorly understood. Apparently, pyrite is oxidized to hematite and a highly soluble sulfate or hydrogen sulfate complex (Barnes and Czamanske, 1967). The sulfate is removed from the sample in solution. The hematite coats the pyrite grains and, more importantly, is distributed along the fractures. The active fractures, or fractures open to oxidizing fluids, appear as an abrupt rise in the iron background in microprobe analysis.

This correlation is seen in the microprobe traverse A-B in figure 6-1. Proceeding from B to A there is an abrupt rise in the iron content when crossing the first fracture f3b. The traverse then parallels the fracture for about 0.04 mm. This juxtaposition results in the gradual decrease in iron to the left side of the peak. Therefore, active fractures can be recognized on the basis of the local iron content. The iron in the fracture cannot be due to broken pyrite grains emplaced there during grinding because the sulfur content remains essentially zero within the fracture.

Zones of progressive oxidation can also be seen. These zones appear as shaded areas (brick red in color) in the clay as indicated in the inset of figure 5-8. The red hematite is obvious along f3b but also occurs as a broad zone around fracture f3c near D. Several of the pyrite grains within the clay fragment are fresh. The presence of strong oxidation gradients within the clay is interpreted to mean that oxidizing fluids are restricted to the vicinity of fractures.

A specimen from a depth of 1187 meters in the Heber GTW#3 well has a complex history of calcite veining. The dark argillaceous siltstone
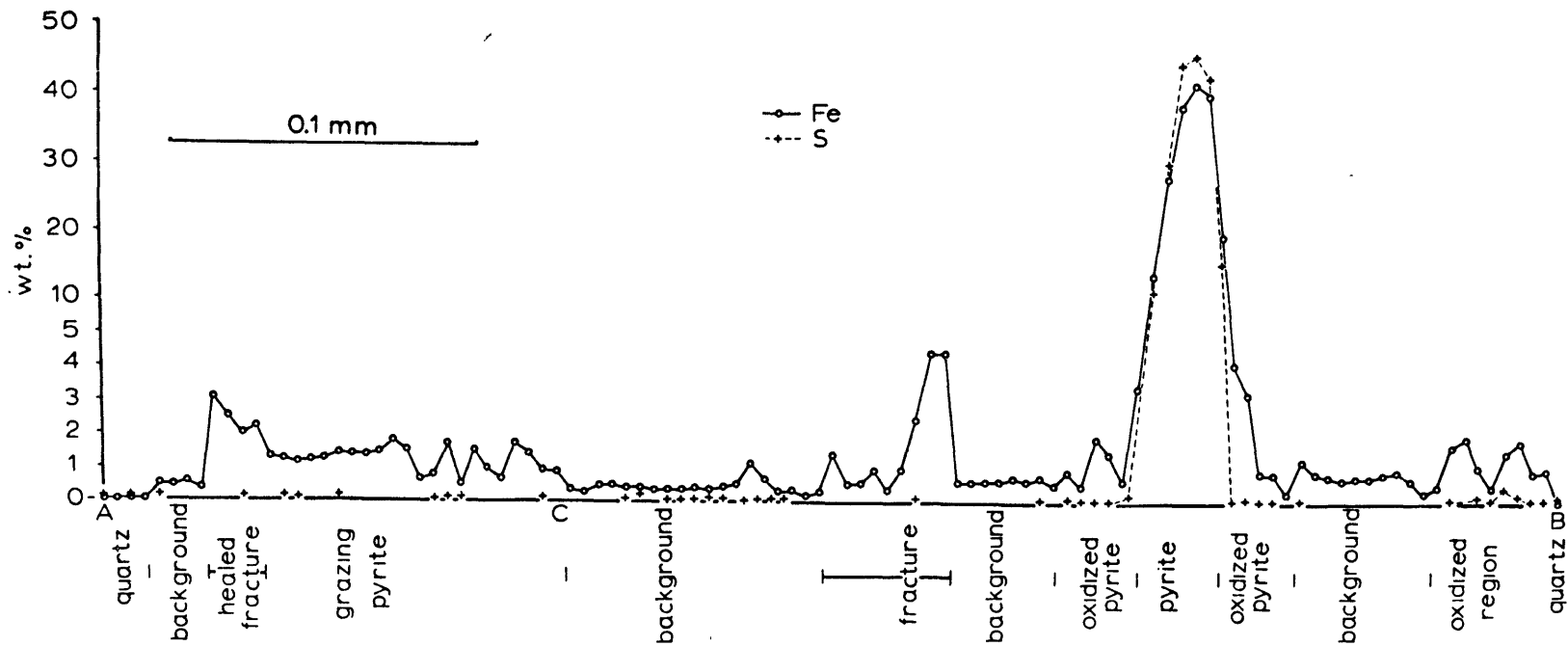
Figure 6-1. Microprobe traverse A-B of measured iron and sulfur content across the clay fragment in figure 5-8. Note change of scale in ordinate after '5 wt.%' (from Batzle and Simmons, 1976).

matrix is shown in figure 6-2 cut by several veins. The veining is so intense in this core that the view of figure 6-2 is actually a small chip surrounded by larger veins. The cutting relationships allow four episodes of fracturing and sealing to be distinguished, numbered 1 to 4 in the photomicrograph. Two distinctly different types of luminescence are shown by the veins. The increase in intensity of the later two veins corresponds to an increase in the trace content of manganese. Variations in the composition of sealing phases indicate two different fluid compositions or distinctly different physical conditions. Fluid inclusion work by Elders (1977) on similar samples from this region indicates two different thermal events occurred at 212°C and 235°C. Perhaps the two types of luminescent veins correspond to the two separate temperature events. The two events may represent invasion and flushing of this portion of the system by two solutions with different compositions. This specimen would be representative of position '8' in the idealized geothermal system of figure 1-3.

Multiple episodes of fracturing superimposed on variations of sealing mineralogies can be observed in the sample shown in figures 6-3a and b. The rock is an argillaceous, poorly-sorted sandstone from a depth of 345 meters in the Raft River Intermediate well #3. Several sealed and open fractures are visible to the unaided eye. The high clay content makes observation by transmitted light difficult except for areas of translucent fracture mineralization. The sample is divided by the fractures into two regions. One region is well-indurated with siliceous cement and minor carbonate cement. The other region is friable and easily crumbles when handled. This division indicates that the sealed
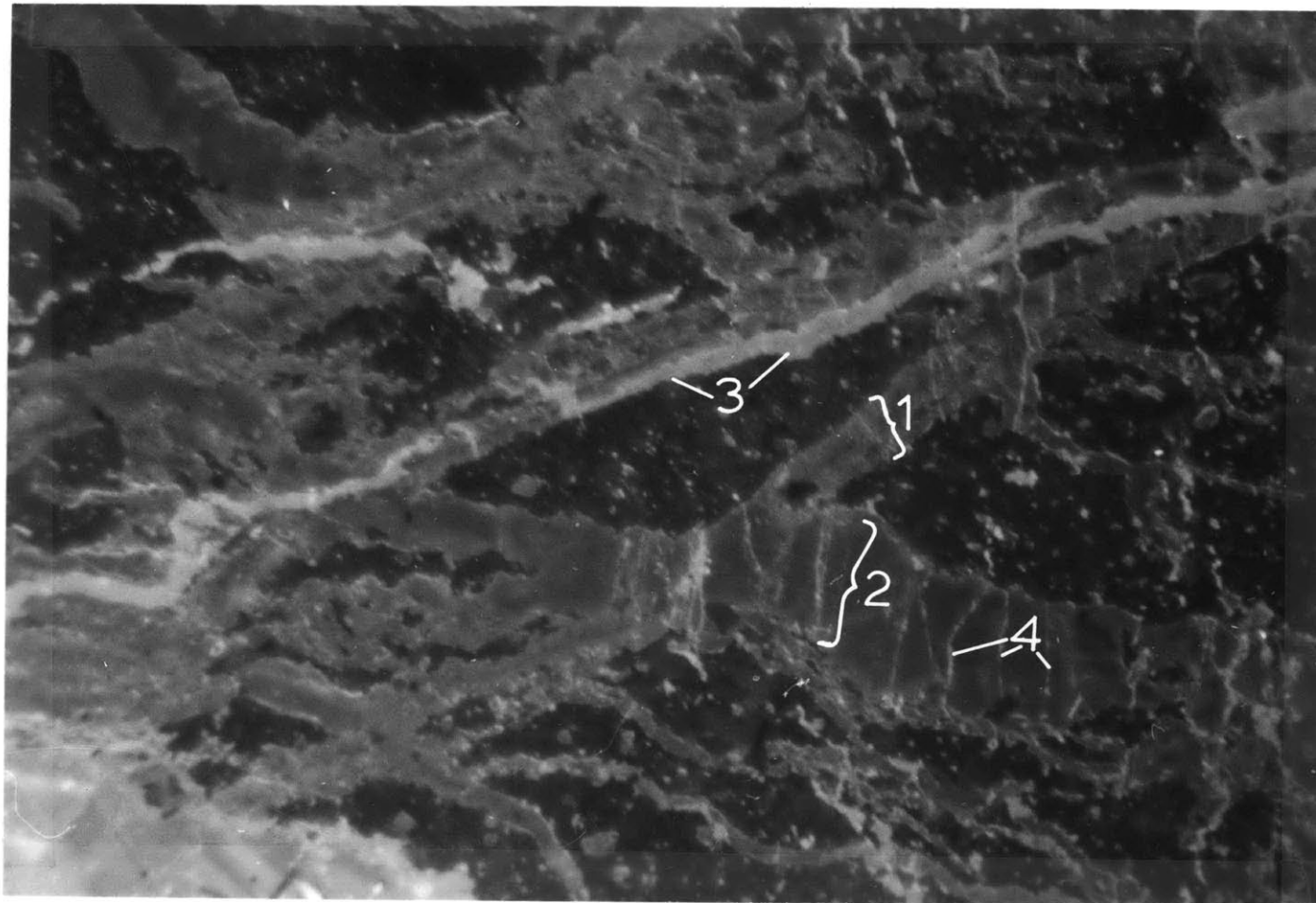
Figure 6-2. A sample from a depth of 1187 meters in the Heber GTW#3 well. Calcite veins in siltstone viewed with cathodoluminescence. Numbers refer to relative ages of veins: 1 to 4, oldest to youngest.

1 mm
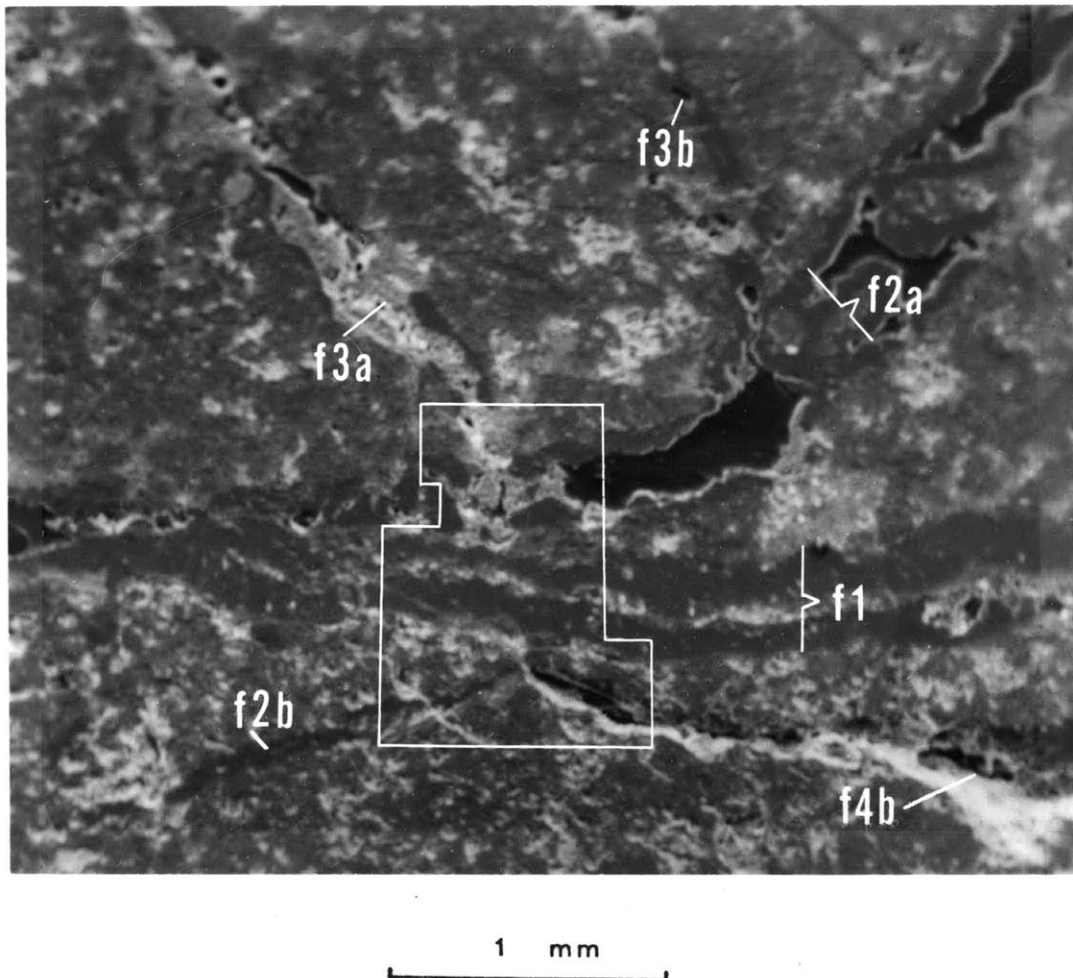
Figure 6-3. Sample from a depth of 345 meters in the Raft River
Intermediate well #3.

(a) SEM photomicrograph. f1 to f4b = fractures (see text). See 6-3b
for enlargement of outlined portion.

(b) See following page. SEM micrograph (mosaic). Enlargement of the
outlined portion of 6-3a. B = analcime plates (?) in matrix; C = cal-
cite; D = analcime; E = void; F = void now filled with epoxy; f1 to
f4c = fractures (see text) (from Batzle and Simmons, 1976).
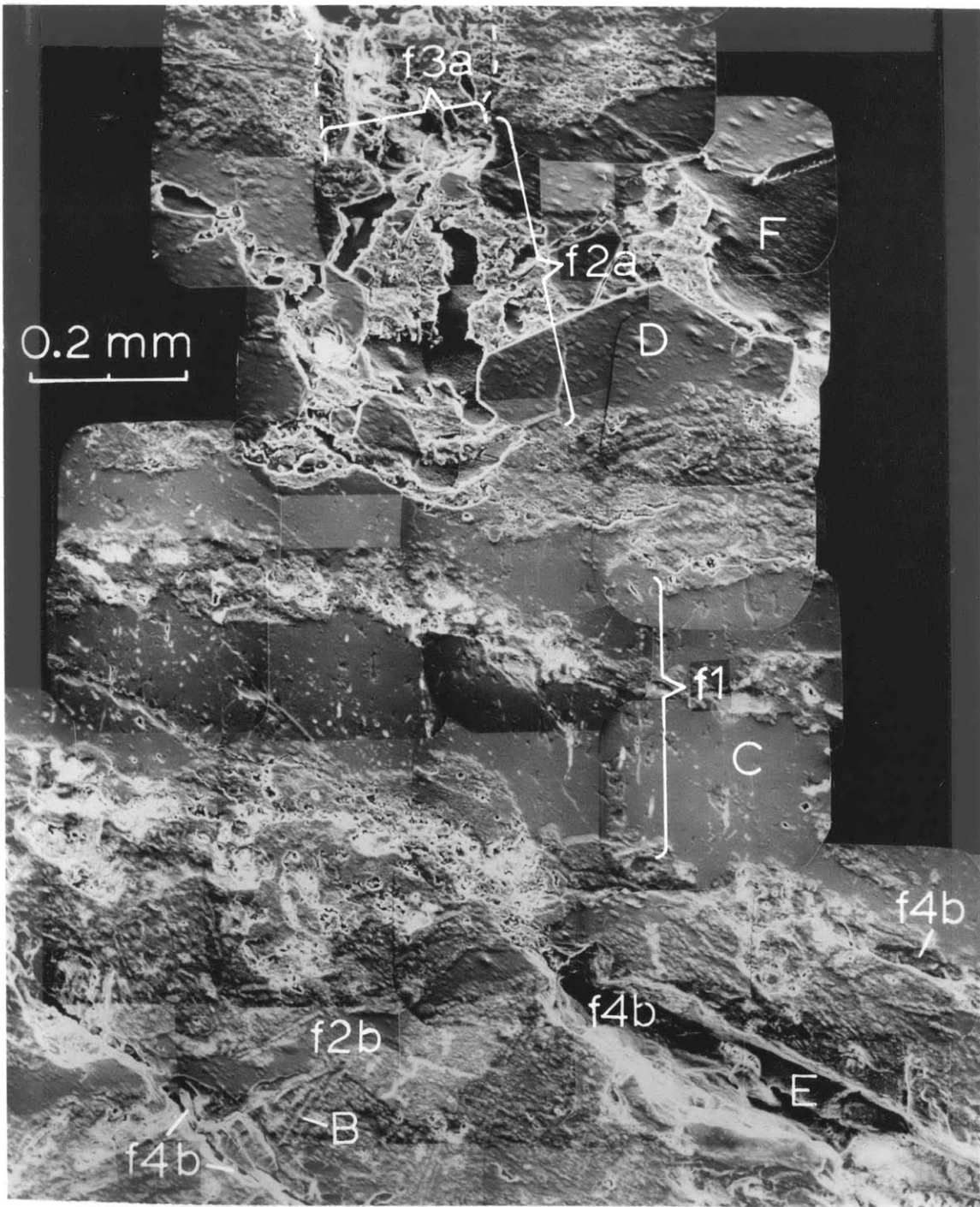
Figure 6-3b. See caption on preceding page.

fractures have acted as effective boundaries to the circulating fluids responsible for the induration. Continuity of bedding across fractures indicates that there has been no significant movement along fractures.

Five episodes of fracturing are indicated in figure 6-3. The first to occur, fracture f1, is now filled with calcite. The calcite tends to grow inward in small tablets perpendicular to the fracture walls. The sealing is complete except for a discontinuous chain of cavities at the center. A second series of fracturing, f2a, angles down from the upper right-hand corner of 6-3a to join f1 at the center of the figure. Fracture f2a then continues toward the left paralleling and crosscutting f1. Fracture f2b most likely occurred during the same fracturing episode that produced f2a. The evidence for this similarity in relative ages is that f2a and f2b trend in the same general direction, but are perpendicular to the later set of fractures, f3a and f3b. Fracture f2b is completely sealed with analcime, reflecting a change in the fluid chemistry from calcite to analcime supersaturation. Fracture f2a is lined with euhedral growths of analcime. The sealed and ingrown natures are clearly shown in 6-3b. Fractures f3a and f3b occurred next propagating downward from the upper left until terminating on f2a. Fractures f3a and f3b are partially filled with analcime.

A more substantial change in fluid chemistry is recorded in fractures f4a, f4b, and f4c which crosscut f1 and f2b. Most of the original void spaces of f4a, f4b, and f4c have remained open cavities. They conspicuously narrow when cutting the analcime of f2b. The fluids within these cracks have become undersaturated with respect to the matrix or

cement. The undersaturation does not affect the analcime already deposited in f2b but causes large voids in the clayey matrix. Hence, the various modes of fracture modification reflect changes in fluid properties. This sample would be another example of circle 6 in the generalized system of figure 1-3.

An example of the sealing and cementing developed as hydrothermal fluids invade permeable sediments along fractures is shown in figure 6-4. The core section is from 154.5 meters in the Raft River Intermediate well #3. The core contains a fault contact between an argillaceous sandstone and a claystone. The faulting is evidenced by cut bedding and slight sympathetic folding. Apparently, the sealing fluids penetrated upward along the fault and invaded the sandstone. The sandstone is cemented to a distance of approximately fifteen centimeters from the fracture. The cemented portion terminates abruptly and irregularly in a fashion similar to the samples seen previously in figures 4-14 and 4-15 of Chapter IV. The cementing fluids could not penetrate the less permeable clay which remained soft and pliable. This core is a striking example of the importance and interrelationship of fracturing and subsequent sealing. This specimen typifies circle 9 on figure 1-3 of the generalized system.

Complex veining textures are observed in several Coso samples. A veined specimen from a depth of 190.2 meters is presented in figure 6-5. The matrix is a gray-green metashale that has been faulted into direct contact with an equigranular diorite. Several episodes of veining can be seen in figure 6-5a, each characterized by a specific mineralogy. The first episode involved fracturing, then growth of euhedral steller-
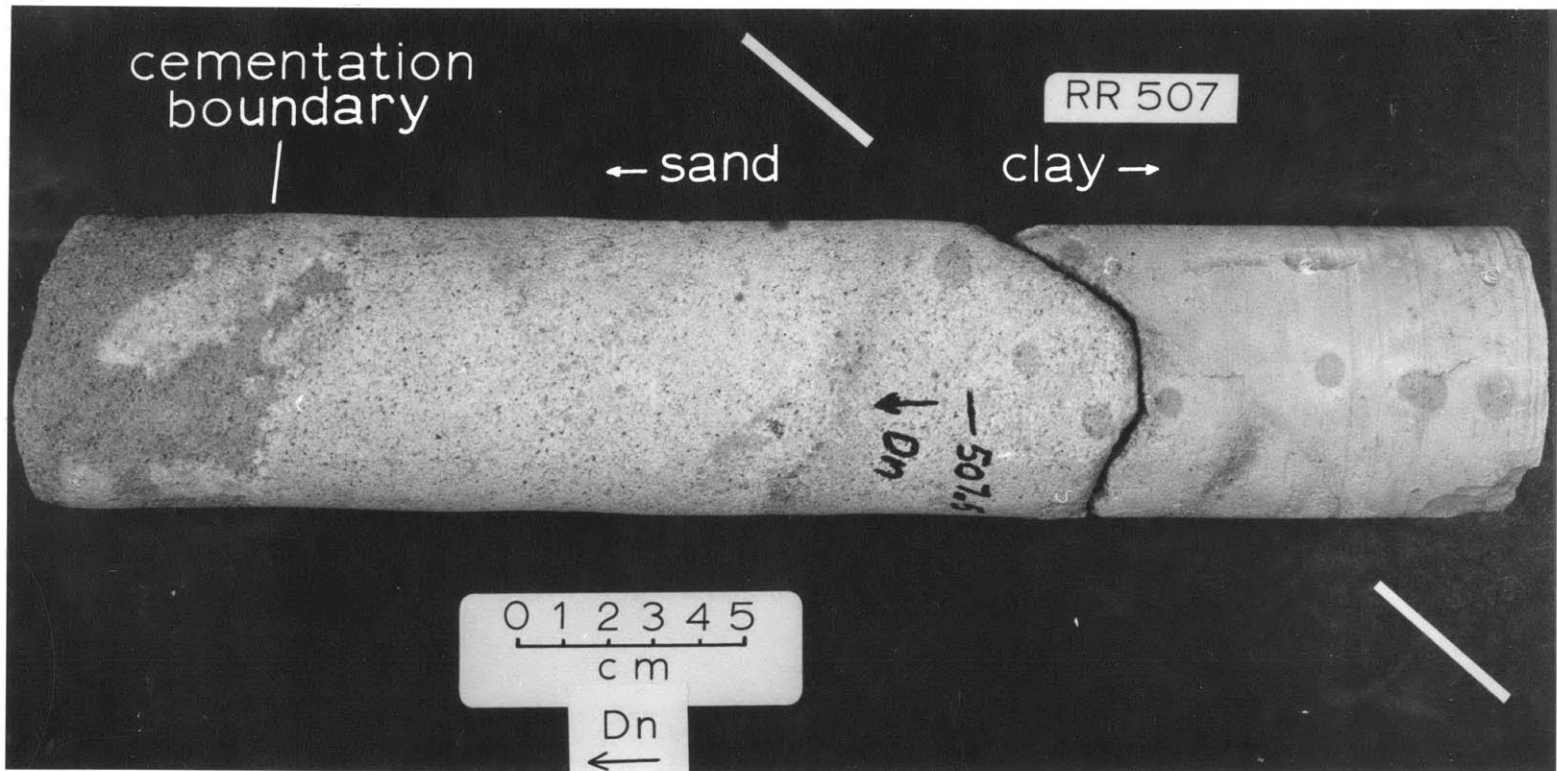
Figure 6-4. A core sample from a depth of 154.5 meters in the Raft River Intermediate well #3. The white line indicates the fault plane. Laminated clay is to the right of the fault, argillaceous sand is to the left. The calcite cementation terminates about 15 cm from the fault and may have resulted when saturated fluids invaded the sand from the fault.

5 mm
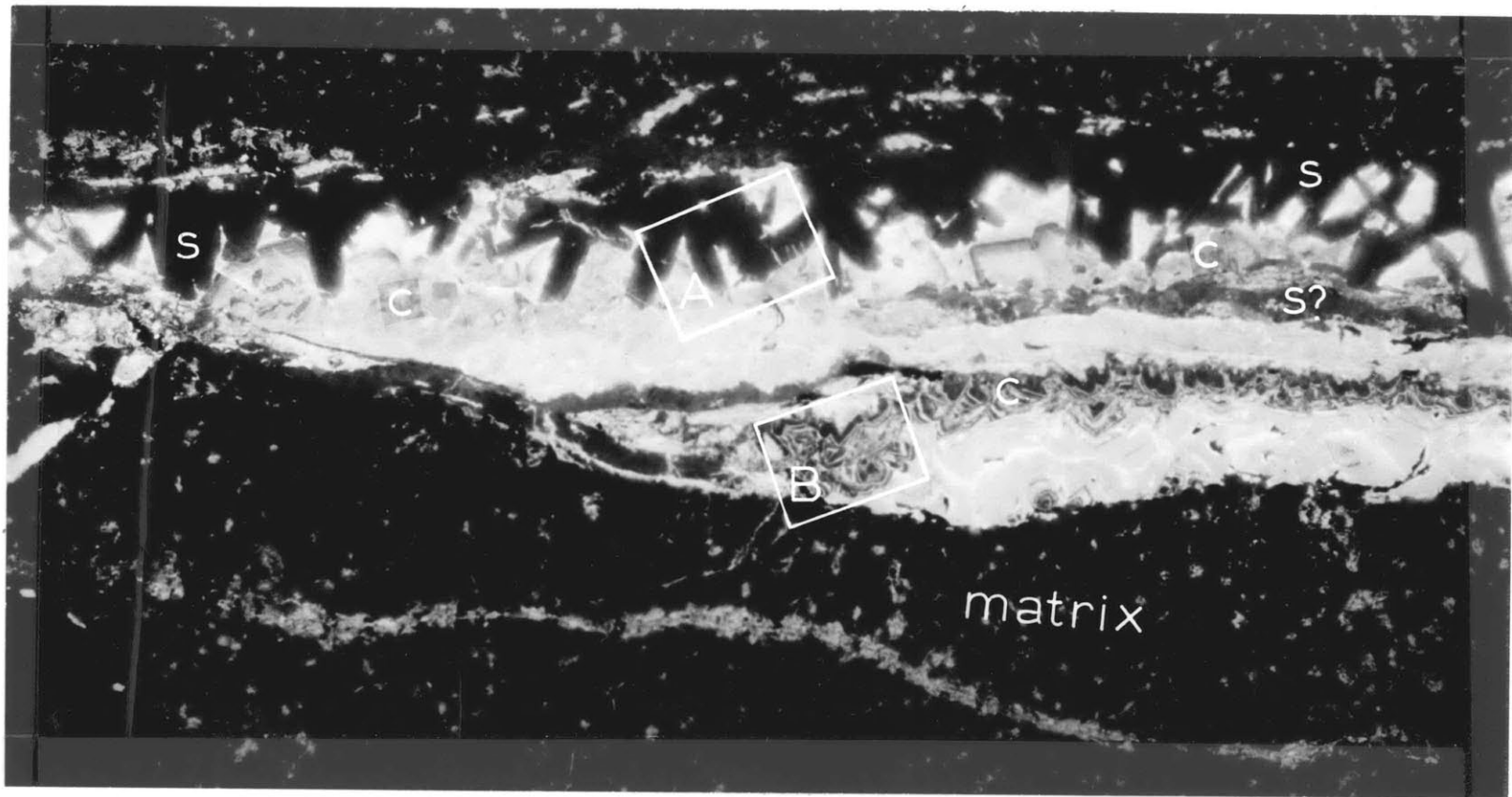
Figure 6-5. A veined metashale from a depth of 190.1 meters in the Coso BDH#1 well. All four photomicrographs in this figure were taken of cathodoluminescence.

(a) Overview of the sample. The light-hued vein occupies the center of the figure with dark metashale on either side. See figures 6-5b and 6-5c for enlargements of outlined areas A and B, respectively.
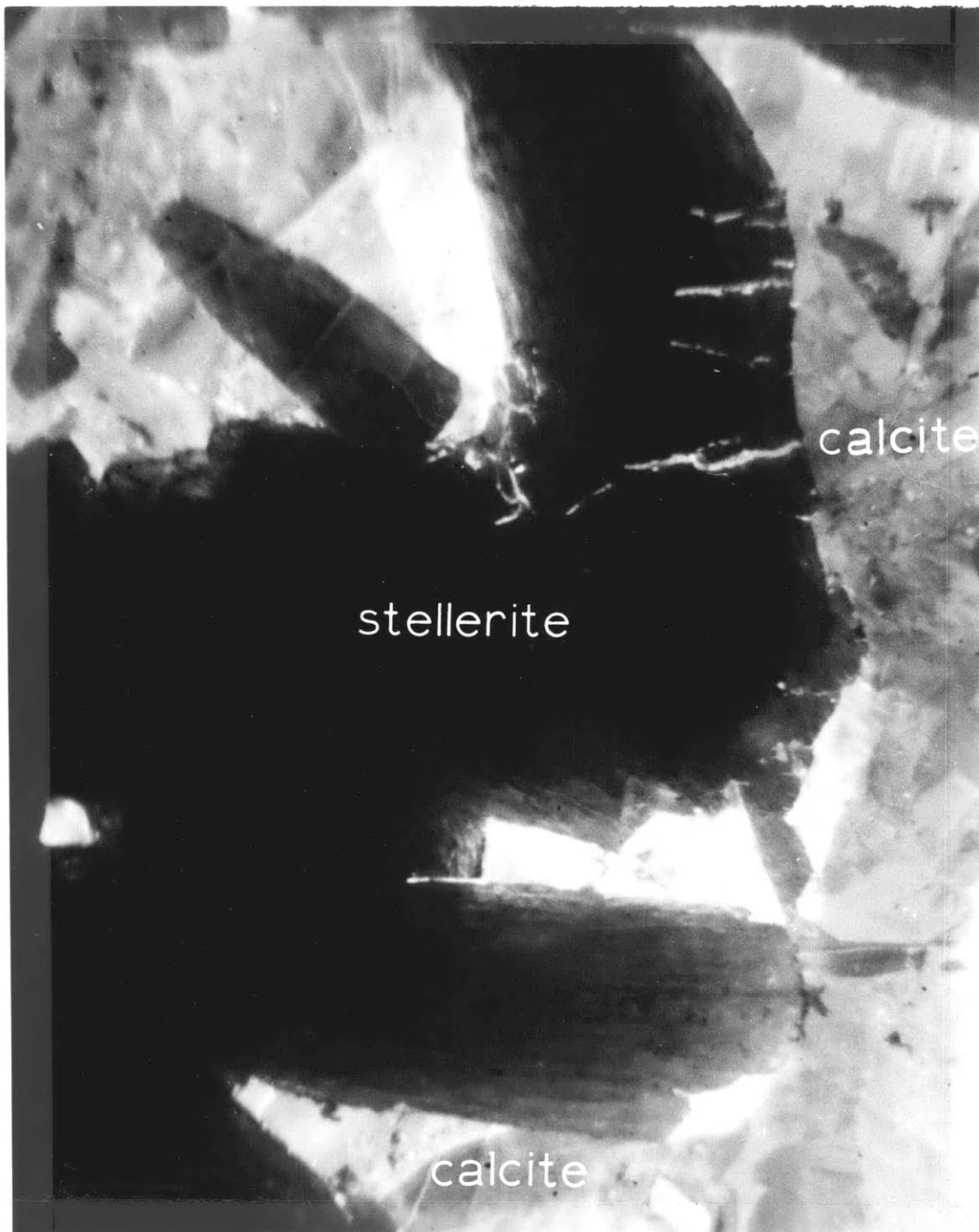
Figure 6-5b. An enlargement of a portion of figure 6-5a showing details of the calcite (light) and stellerite (gray) intergrowth. Note the bright calcite sealing the microfractures within the stellerite.

0.4 mm

Figure 6-5c. An enlargement of the heavily-zoned calcite within the vein of figure 6-5a. The intensity of the luminescence varies frequently and abruptly. The intensity is dependent on the Mn^{++} content and may represent the periodic flushing of the sample with fluids of varying composition.

0.3 mm
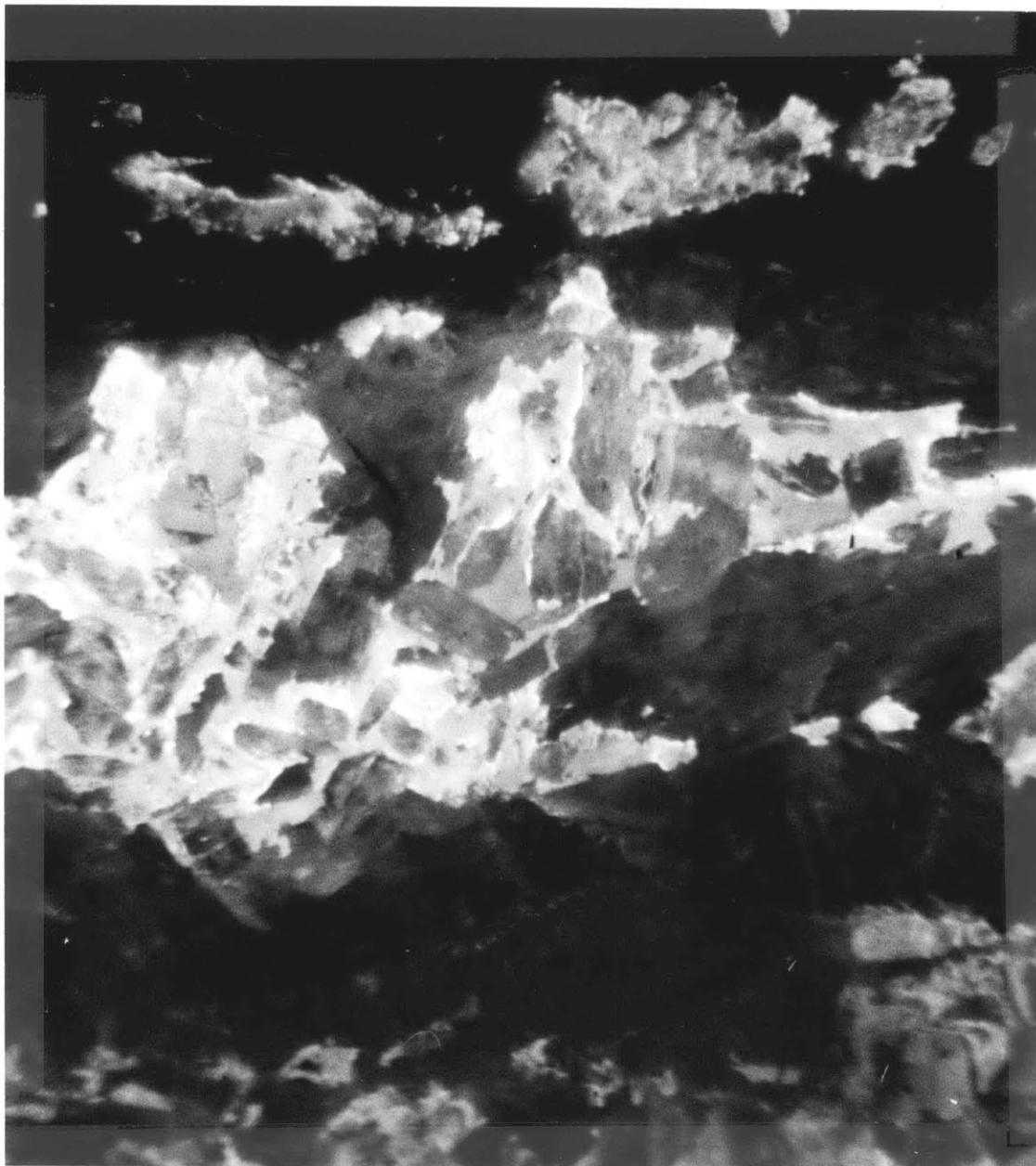
Figure 6-5d. Cataclastic texture in calcite. Dark hued, broken cal-
cite crystals are embedded in a lighter calcite matrix. This portion
of the vein is not in the field of view of figure 6-5a.

ite (a zeolite). Later, calcite formed in the vein and in microfractures developed within the stellerite (figure 6-5b). The calcite was followed by renewed deposition of a zeolite (?) similar in composition to stellerite. Finally, heavily zoned calcite formed in another portion of the vein (figure 6-5c). The refracturing of the vein involved some breakage of the pre-existing veining material as shown by the broken and clastic texture of the calcites with various luminescent intensities (figure 6-5d). The numerous changes in mineralogy and intense zoning indicate rapid fluctuations in the chemical or physical environment. Many smaller calcite-sealed fractures of uniform composition have also been formed in the rock. The exact age relationships between the later zeolite and calcite stages within the vein are ambiguous.

Deposition and alteration occur simultaneously in a sample of granodiorite from a depth of 608.7 meters in a Roosevelt Hot Springs well. A zone of alteration surrounds the sealed fracture or vein diagonally crossing the field of view in figure 6-6. Two distinct types of veining material can be distinguished in the fracture (numbered '1' and '2' in figure 6-6). The zone marked '1' is quartz and feldspar-rich. Zone '2' is predominantly hematite. The zones indicate that two distinct episodes of fracturing and sealing may have occurred. The relative ages between these two events is not known. The fluids circulating in and around the fracture have produced a zone of alteration within the local matrix. The biotite grains along the fracture (at 'A') are being altered and only hematite remains. Farther from the fracture, the mafic minerals are fresh. At 'B', an albitization rim has formed along a plagioclase crystal split by the fracture. The narrow zones of alteration around
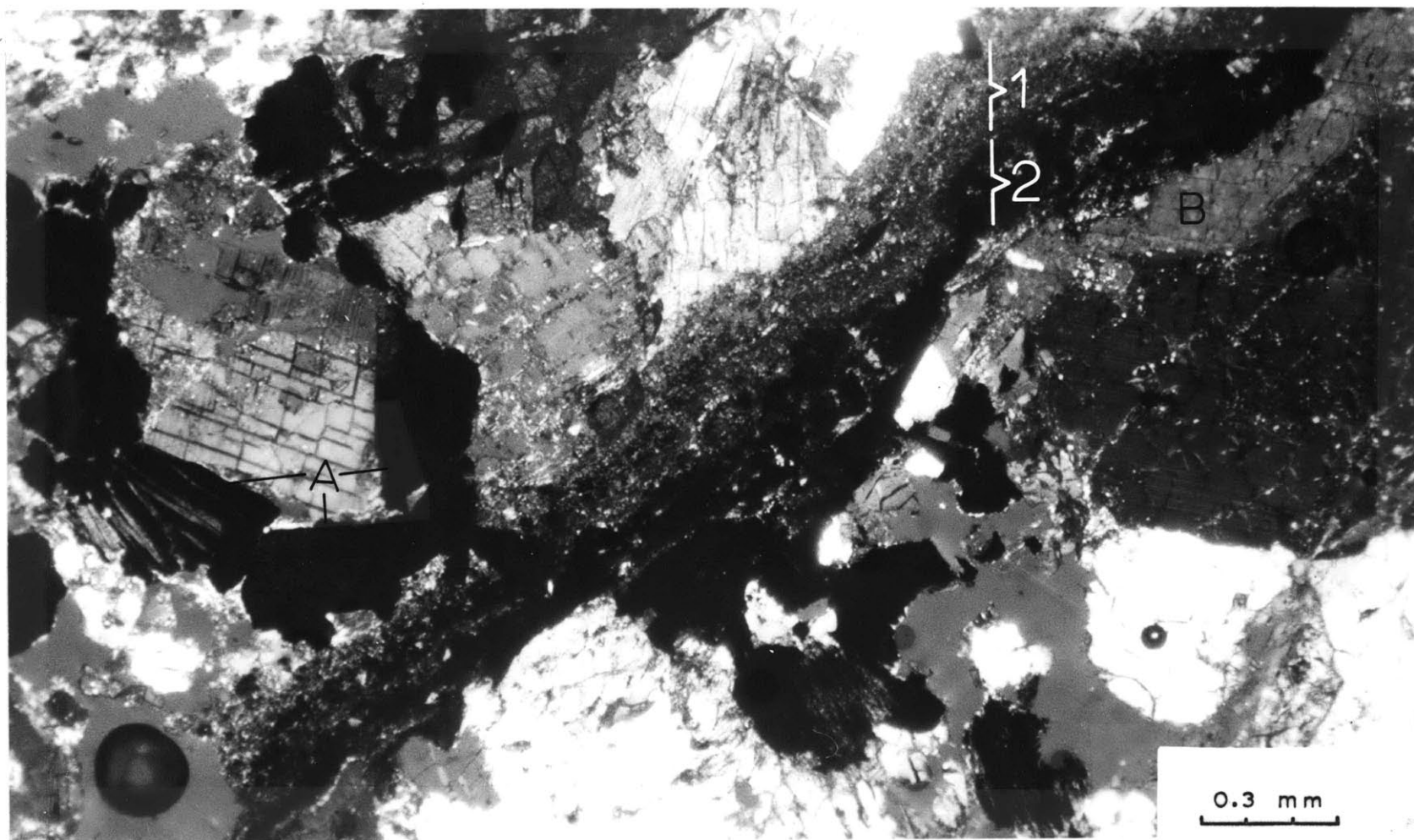
Figure 6-6. Roosevelt Hot Springs sample from a depth of 608.7 meters, photographed with crossed nicols. The dark band marked '1' and '2' is a sealed fracture. 'A' and 'B' are alteration zones (see text) (from Batzle and Simmons, 1977).

this vein indicate that the fluids are largely confined to the regions immediately adjacent to fractures in crystalline rocks.

Effects on Physical Properties

The sealing and alteration of rocks usually reverses the effects of open fractures. Permeability can be reduced by several orders of magnitude. Conductivity can be lowered significantly, but the change depends on the mineral content and specific type of alteration. The sealing and alteration can fill pores and voids making the rocks dense and brittle. On the other hand, development of clays can so severely alter rocks as to make them soft and porous. In this section, several more examples will be examined that demonstrate some of the specific effects that sealing and alteration have on physical properties.

An indurated, argillaceous wacke from a depth of 1184 meters in the Heber GTW#1 well is cut by several branching calcite veins a few millimeters wide. The initially open fracture must have increased the permeability and conductivity significantly. However, the precipitation of calcite had the opposite effect, reducing both of these transport properties to values lower than the prefractured values. Permeability and conductivity were measured with flow both parallel and perpendicular to a vein in the same rectangular sample. Flow in the rock parallel to the vein will be predominantly through the matrix. In this direction, the permeability is 15 microdarcys and the formation factor is 40 (2 Ωm fluid). Flow perpendicular to the vein will be blocked by the crystalline coarse and interlocking texture of the calcite in the vein. The measured permeability and formation factor in this direction are

5 microdarcys and 120, respectively. The decrease in both permeability and conductivity is thus due to the blockage by the vein. Hence, although the initial fracturing will increase the flow characteristics, the subsequent veining and sealing can lower overall values below the initial matrix properties.

Similar anisotropic characteristics are observed in a veined sample from a RRGE#2 core. This porous, argillaceous, tuffaceous wacke from a depth of 937 meters has a several irregular diffuse veins. Permeability (figure 6-7) and conductivity were measured in a sample that contained one dominant planar albite vein approximately half a millimeter wide. The permeability and formation factor measured parallel to the vein were 22 millidarcys and 6.8, respectively (2.3 Ωm fluid). Perpendicular to the vein, the permeability is decreased to 6 millidarcys. The formation factor measured in this direction was changed only to 7.3. The factor of three drop in permeability, but negligible change in conductivity, may be due to small breaks and discontinuities in the vein which conduct electric currents more efficiently than fluid. The permeability measurements for the parallel and perpendicular directions are shown as a function of pressure drop across the sample in figure 6-7. The two curves indicate the dependence of the measured permeability on the pressure gradient. Non-darcy flow dependence is frequently observed in clay-rich samples. This dependence has been variously attributed to mechanisms such as a 'threshold' pressure needed to start flow, variations of fluid viscosity within clays, and the chemical and bonding properties of clays (Bear, 1972; Low, 1959; Lambe and Whitman, 1969; Reed, 1972). The large hysteresis with pressure suggests that the higher velocities at large
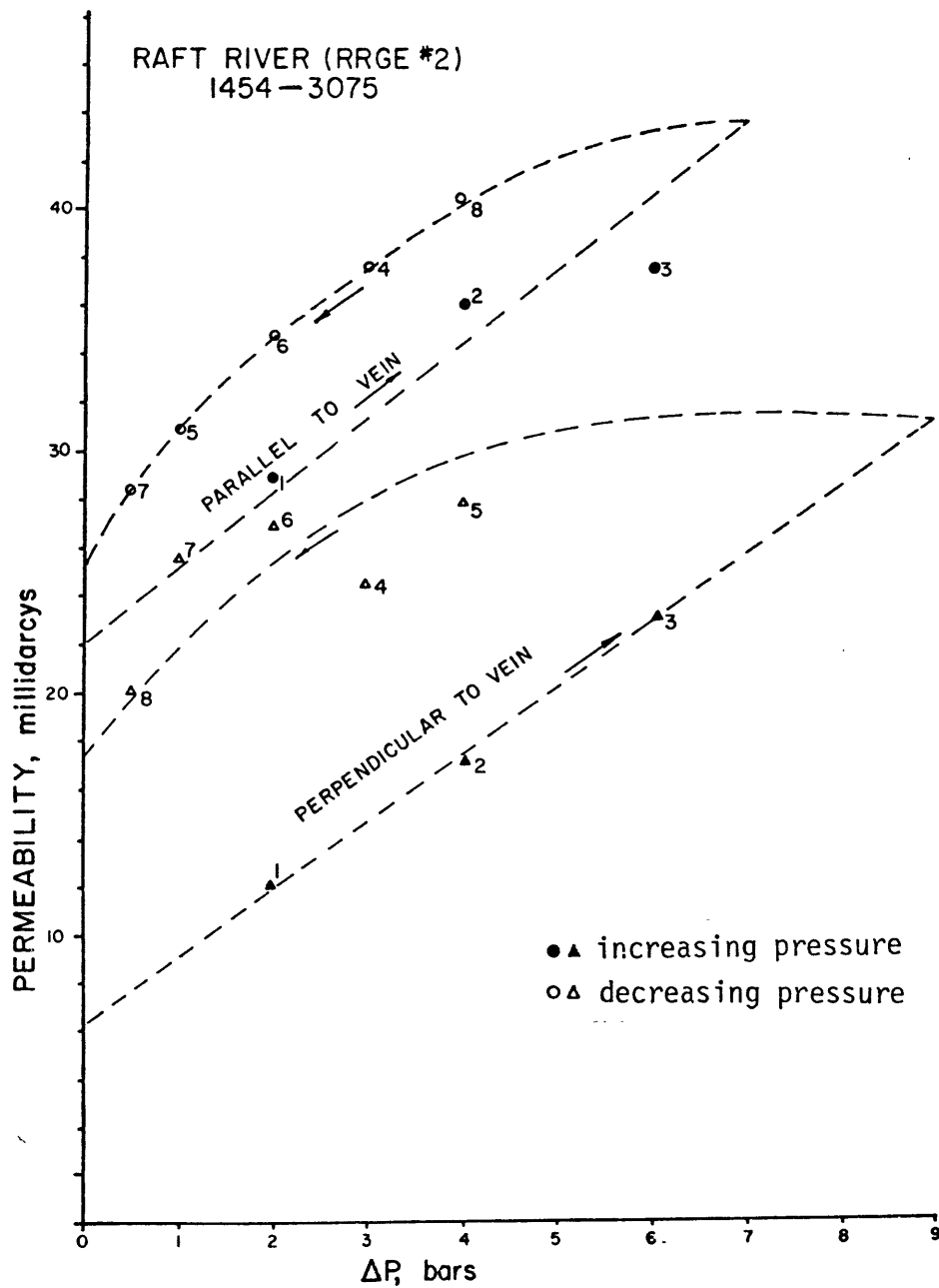
Figure 6-7. Permeability measured parallel and perpendicular to a thin albite vein in the sample from a depth of 937 meters in the Raft River RRGE#2 well. The permeability measurements are strongly dependent on the pressure drop across the sample and show significant hysteresis. These determinations were made at zero confining pressure.

pressure gradients have flushed material out of the flow paths. In spite of the obscuring effect of this pressure dependency, the flow discrepancy between the parallel and perpendicular directions is obvious.

A more graphic example of the effects of veining can be seen in a specimen from 264.6 meters in the Raft River Intermediate well #3 (figure 6-8). This rock is a tuffaceous siltstone. The matrix has had significant development of heulandite and many of the glass shards have been completely replaced. Figure 6-8a is a photomosaic of a portion of this sample that is cut by several veins. The dark, well-developed crystals in the large vein 'A' are euhedral analcime. Light-gray cryptocrystalline analcime (?) with a similar composition surrounds the larger crystals. Both types of analcime are cut by later small quartz veins. Although these veining processes will affect the rock properties, a more illustrative texture can be observed along the smaller calcite veins 'B' shown in detail in figure 6-8b. The variation in luminescence indicates that two different episodes of fracturing and sealing are responsible for the veins '1' and '2'. Note that the veins themselves take up only a small portion of the figure. Most of the calcite has been deposited in the pores of the matrix. This texture has great significance because it indicates that the calcite has been 'absorbed' into the matrix completely filling all voids in the vicinity of the veins. This mechanism would be very efficient in reducing the permeability and conductivity of the sample. The measured values of permeability parallel and perpendicular to the veining do not differ substantially, being 35 and 32 microdarcys, respectively. The measured
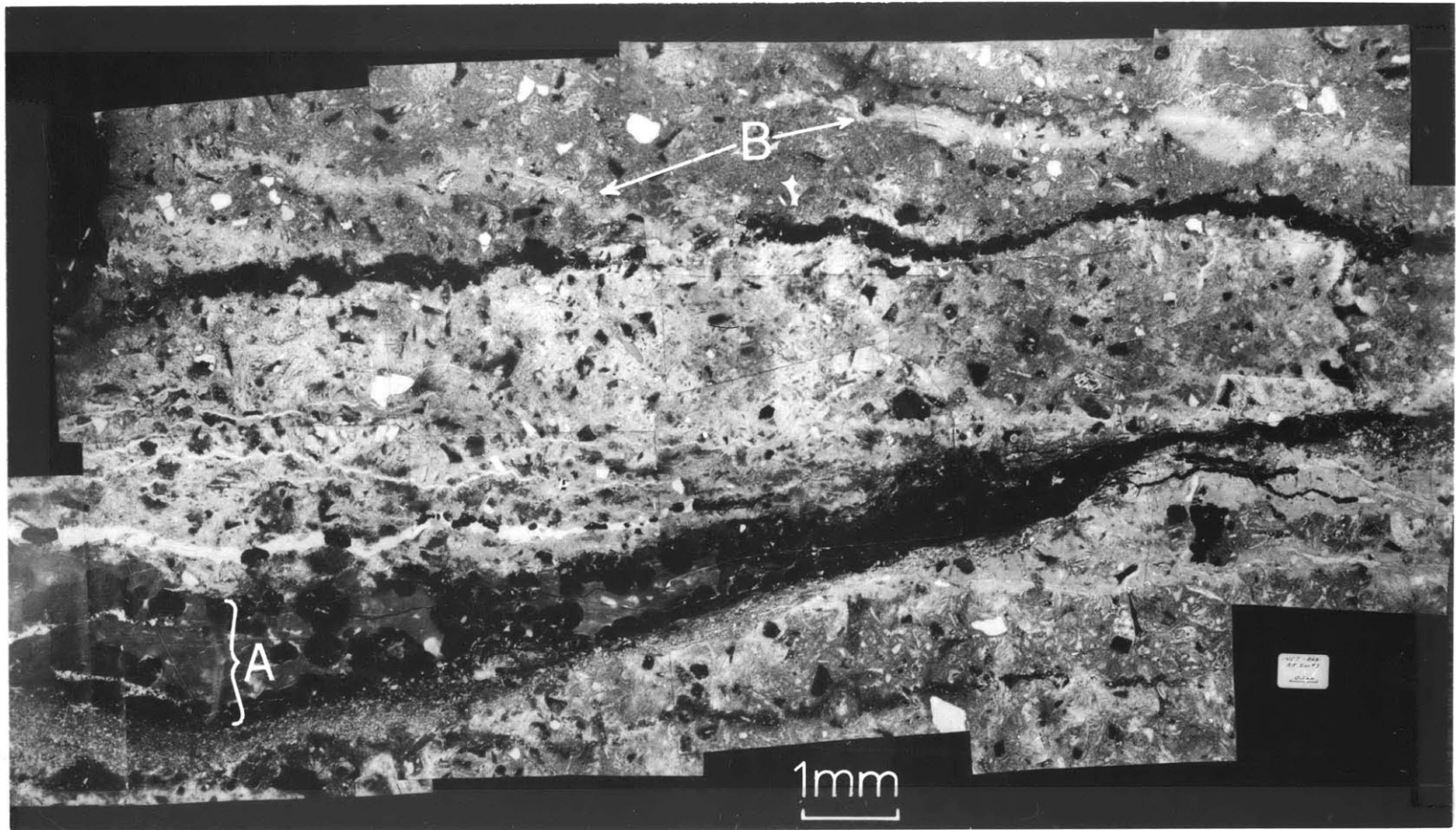
Figure 6-8. Tuffaceous siltstone from a depth of 264.6 meters in the Raft River Intermediate well #3.

(a) Overview of veins under both reflected light and crossed nicols. A - analcime-filled vein; B - calcite-sealed vein.
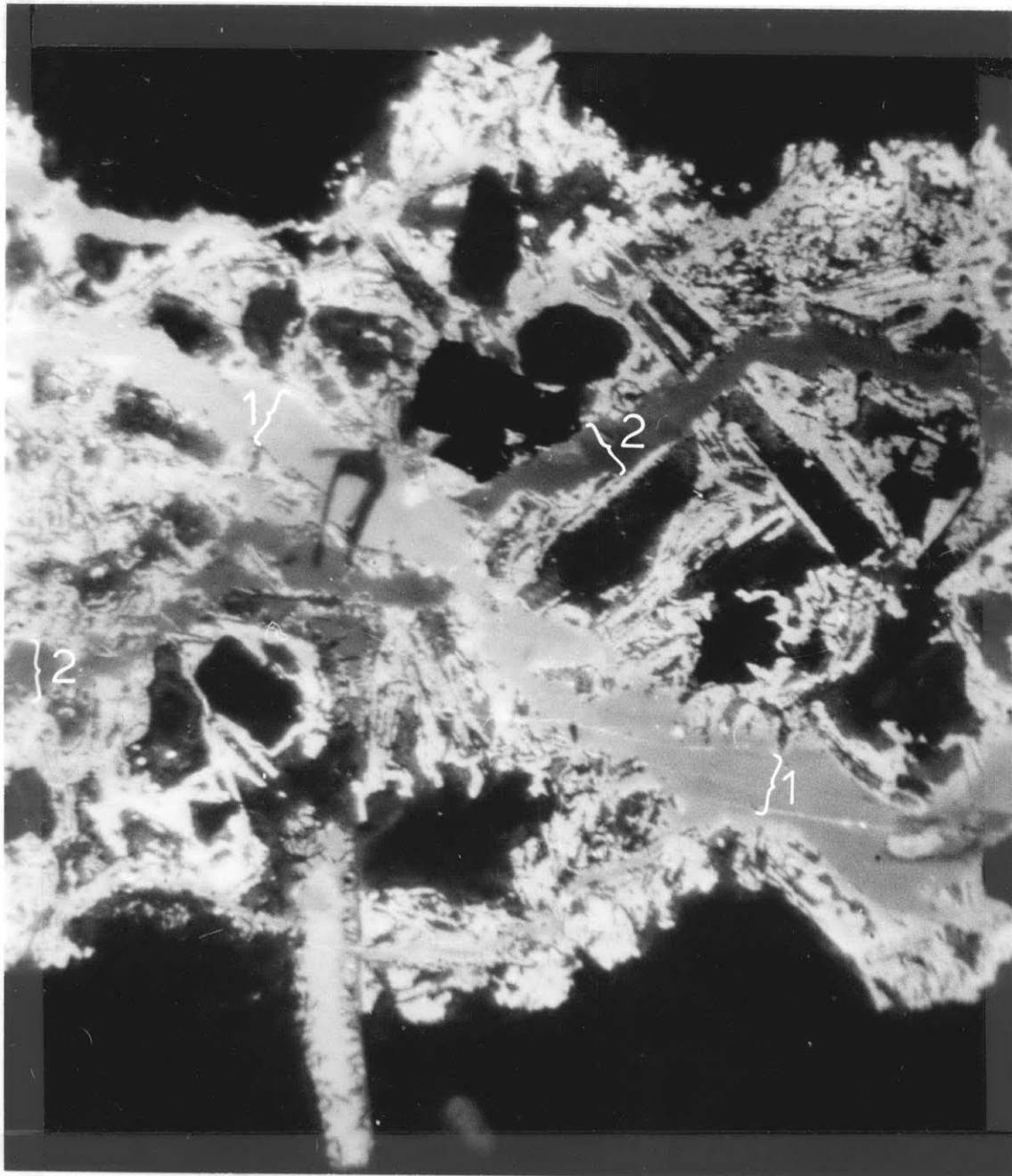
0.3 mm

Figure 6-8b. Cathodoluminescence of the calcite vein intersection showing veining episodes with differing intensity (1 and 2, youngest and oldest). In both, the central vein is surrounded by a light region where calcite has penetrated into the matrix.

values indicate that these sealed fractures are not sufficiently continuous to prevent flow normal to the veins. This calcite veining and the subsequent penetration of calcite into the matrix can be considered a microtextural equivalent to the cementing feature seen previously in figure 6-4.

Intense faulting, crushing, and alteration have occurred in a Coso sample from a depth of 228.6 meters. The cataclastic texture and mixed layer clay alteration of this former granitic rock are apparent in figure 6-9. This rock is typical of many of the faulted and altered zones in the Coso BDH well such as the 285 meter sample examined previously in figures 5-4 to 5-6. The development of finely-granulated quartz and feldspar and the banded clay matrix renders the rock pliant and friable. The DSA curves for this sample are shown in figure 6-10. These curves are remarkable in that this formerly dense crystalline plutonic rock now deforms like the sedimentary rocks analyzed in Chapter IV. The specimen has been so thoroughly crushed and altered that considerable compaction can occur at low pressure. In spite of the porous and open properties of this and other samples from the Coso well, temperature continues to rise with depth. Free circulation and convection must therefore be impeded. The clays developed must block flow effectively. The permeability of this sample could not be measured due to the friable nature. Hence, this sample demonstrates that the processes occurring in geothermal systems can not only indurate but also can weaken and produce a more 'sedimentary-like' behavior. This Coso specimen could be representative of the locations marked '5' in the generalized system (figure 1-3) if the indicated faulting and alteration are
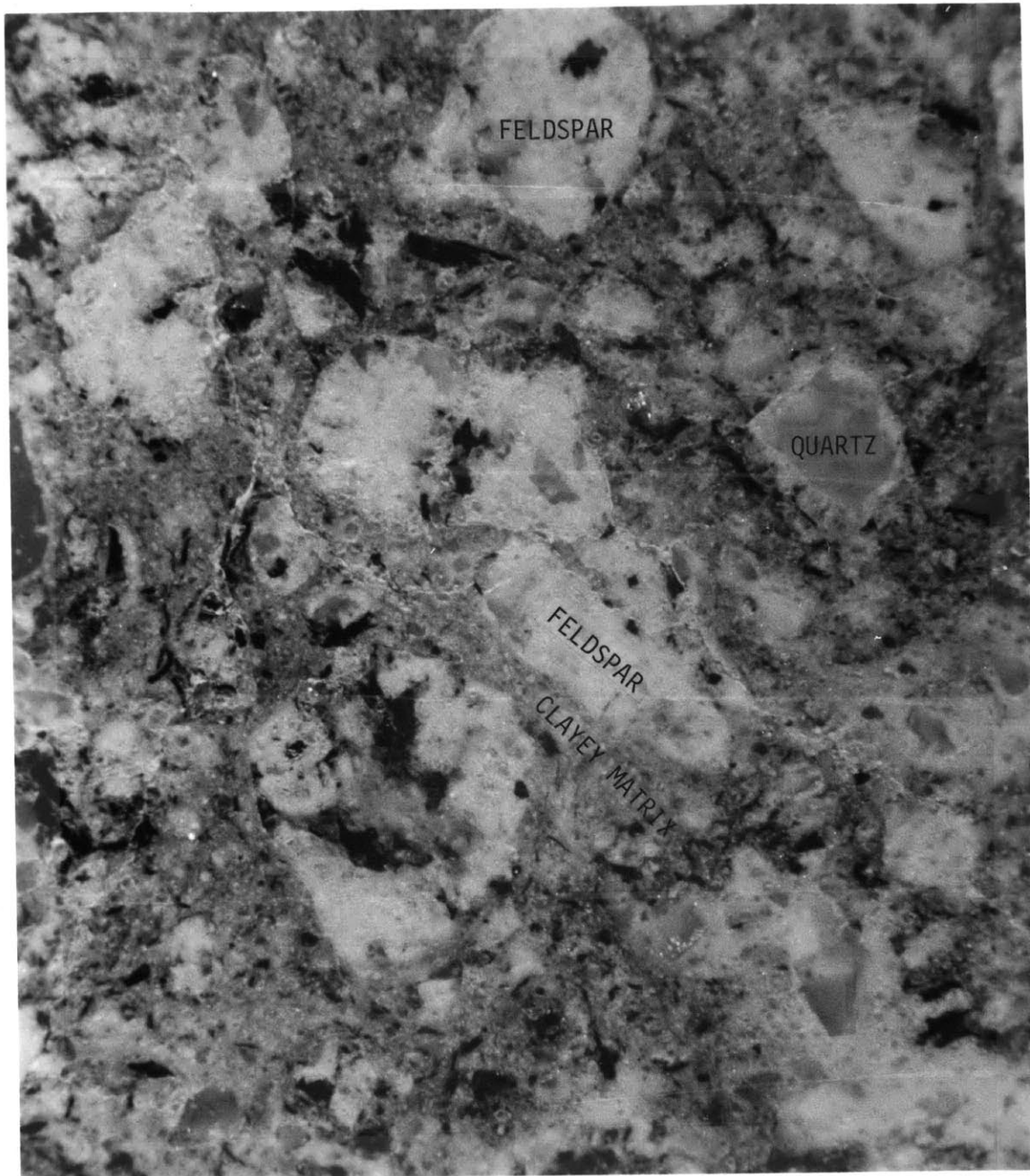
Figure 6-9. Sample from a depth of 228.6 meters in the Coso BDH#1 well viewed under reflected light. Light grains are broken and rotated clasts embedded in the gray-green mixed layer clay matrix.
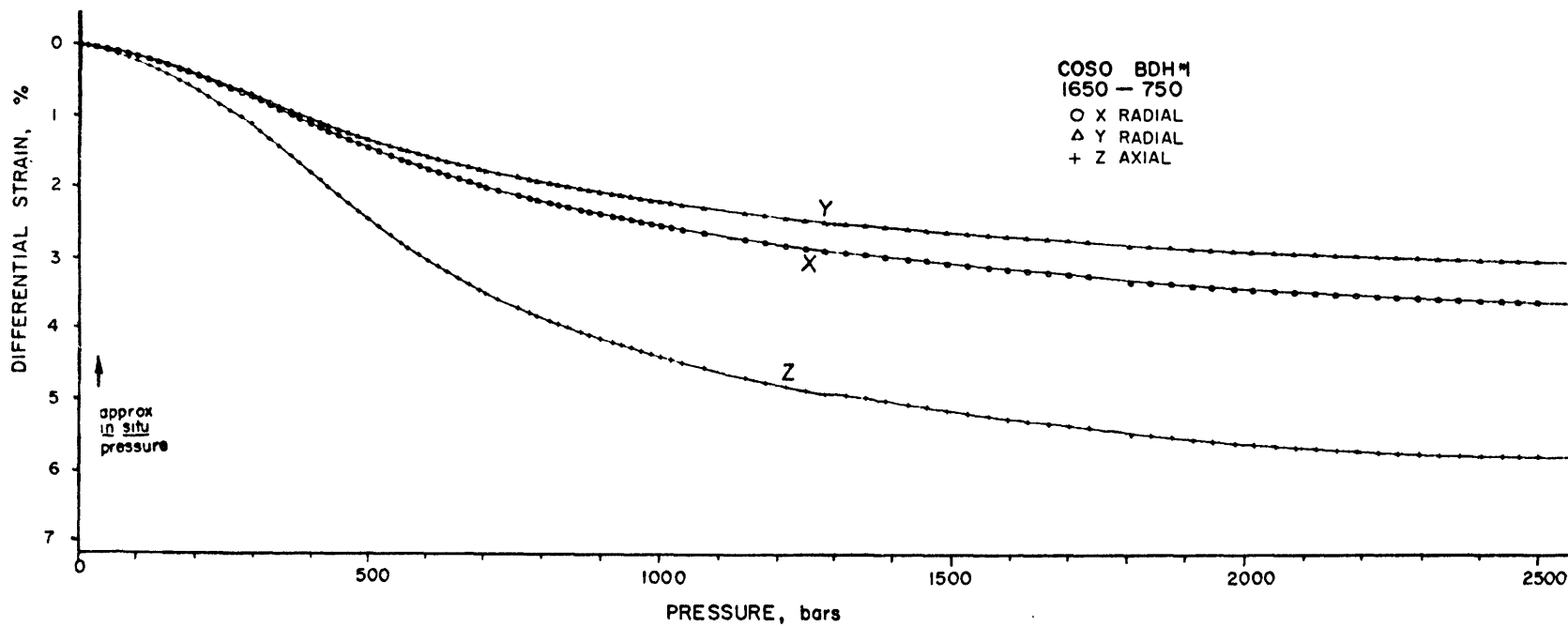
Figure 6-10. Differential strain curves for the Coso sample from a depth of 228.6 meters. Note that the strain curve has behavior similar to porous sedimentary rocks.

extensive.

Marysville is the one location with the suitably uniform characteristics which allow the physical properties to be presented meaningfully as a function of depth. A reasonably complete and representative sample suite was obtained. The country rock at this location was granitic and originally fairly uniform. Any variations in physical properties would therefore result from the observed fracturing and alteration. These variations are not overdominated by original lithologic characteristics. The Empire Creek Stock is a porphyritic granite composed mostly of albite, orthoclase, quartz, and biotite. The stock can be divided into several zones of fracturing and alteration (Blackwell et al., 1975; Blackwell and Morgan, 1976). Above 1200 meters, the rocks have been heavily altered. Below 1200 meters, only light alteration is encountered. Numerous small veins of a wide variety of minerals permeate much of the stock. Details of the well stratigraphy were presented in Chapter II, figure 2-14.

The measured values of permeability, formation factor, and fracture porosity are shown as a function of depth in figure 6-11. A pattern is developed which is dependent on the alteration and clay content. In the upper portion of the Empire Creek Stock, the pores and fractures are filled with alteration material. As a result, the measured fracture porosities are small, less than 10^{-3}. The permeabilities are correspondingly small, ranging from about two hundred nannodarcys down to below the limit of measurement, about half a nannodarcy. Below 1200 meters depth, the fractures are open and clean. The measured fracture porosity increases abruptly to more than. 2×10^{-3} in several specimens.
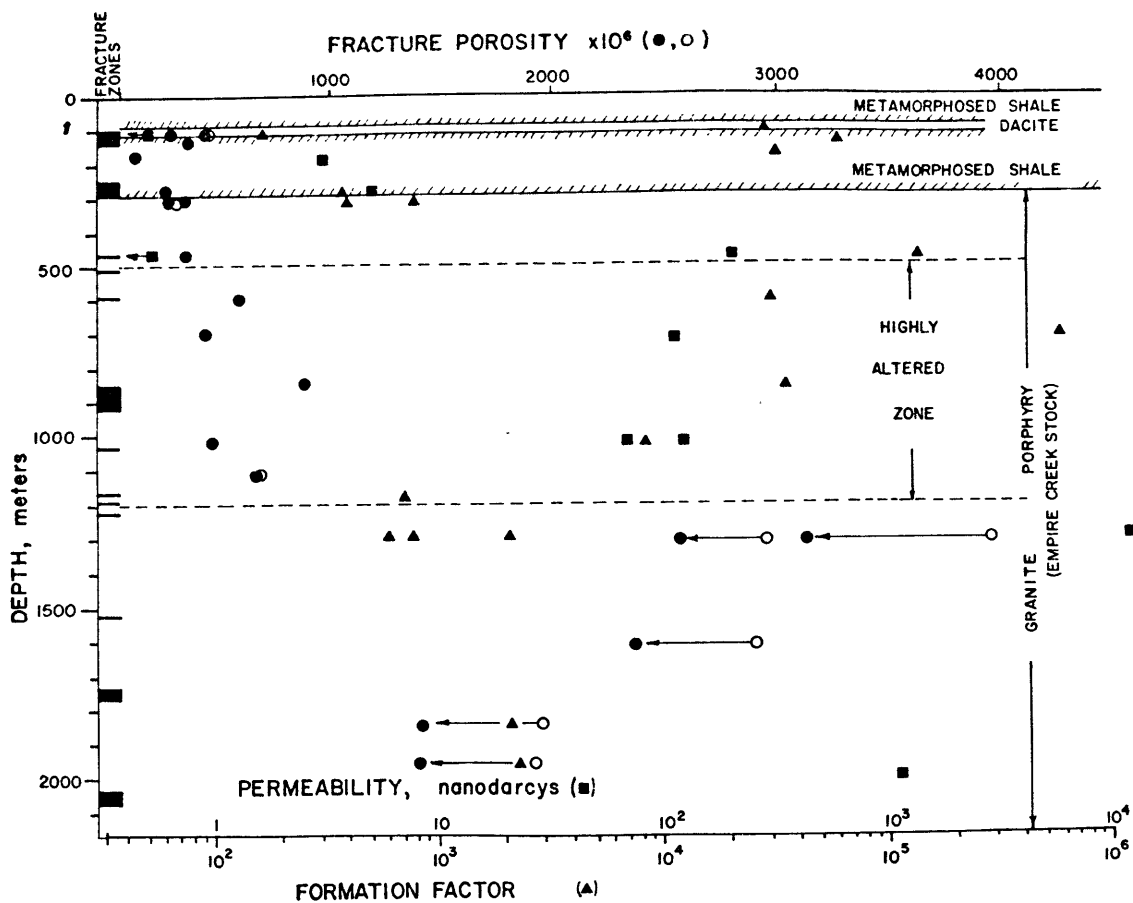
Figure 6-11. Fracture porosity, formation factor, and permeability plotted as a function of depth for the Marysville MGE#1 well. Fracture porosity is shown as both raw and corrected for approximate in situ pressure. Sample resistivities were measured with 1.8 to 2.0 Ωm saturating fluid. Several of the permeabilities were measured as a function of confining pressure. Open circles represent the total fracture porosity at zero confining pressure. Solid circles represent the fracture porosity adjusted for in situ pressure.

The permeability also increases, becoming as large as ten microdarcys in one sample. The conductivities show similar variations but the values are dependent on the fluid properties. Peeples (1975) measured resistivity on numerous Marysville core samples with the rocks saturated with 10 Ωm fluid. He found no significant variations in the conductivity values with depth. In the present study, the samples were saturated with 1.8 to 2.3 Ωm solutions. The resultant formation factors (figure 6-11) decrease below 1200, another indication of open fractures at depth. The approximately constant values measured by Peeples were probably the result of surface conduction through clays in the altered zones. This surface conduction has a more pronounced effect with the dilute solutions he used. The variations in formation factor detected with the more conducting solutions used in this present investigation more accurately indicate the degree of alteration of the rocks.

The textures and exact nature of the alteration materials filling the microcracks in the Empire Creek Stock can be seen in figure 6-12. This figure is a scanning electron photomicrograph mosaic of a sample (#1467) from a depth of 305 meters. The sample is from the shallow portion of the stock just below the shale contact. The large fracture that crosses the figure is filled with a very fine-grained material. The platy habit and microbeam analysis are consistent with montmorillonite. The numerous small cracks in this clay may be due to dessication. The clay filling the fracture results in a low fracture porosity and a low permeability would be expected. Montmorillonite has a large specific surface area and so would have a large surface conduction. The clay content is unusually high in this sample and may account for

orthoclase

clay

clay

albite

orthoclase

30 um
1467
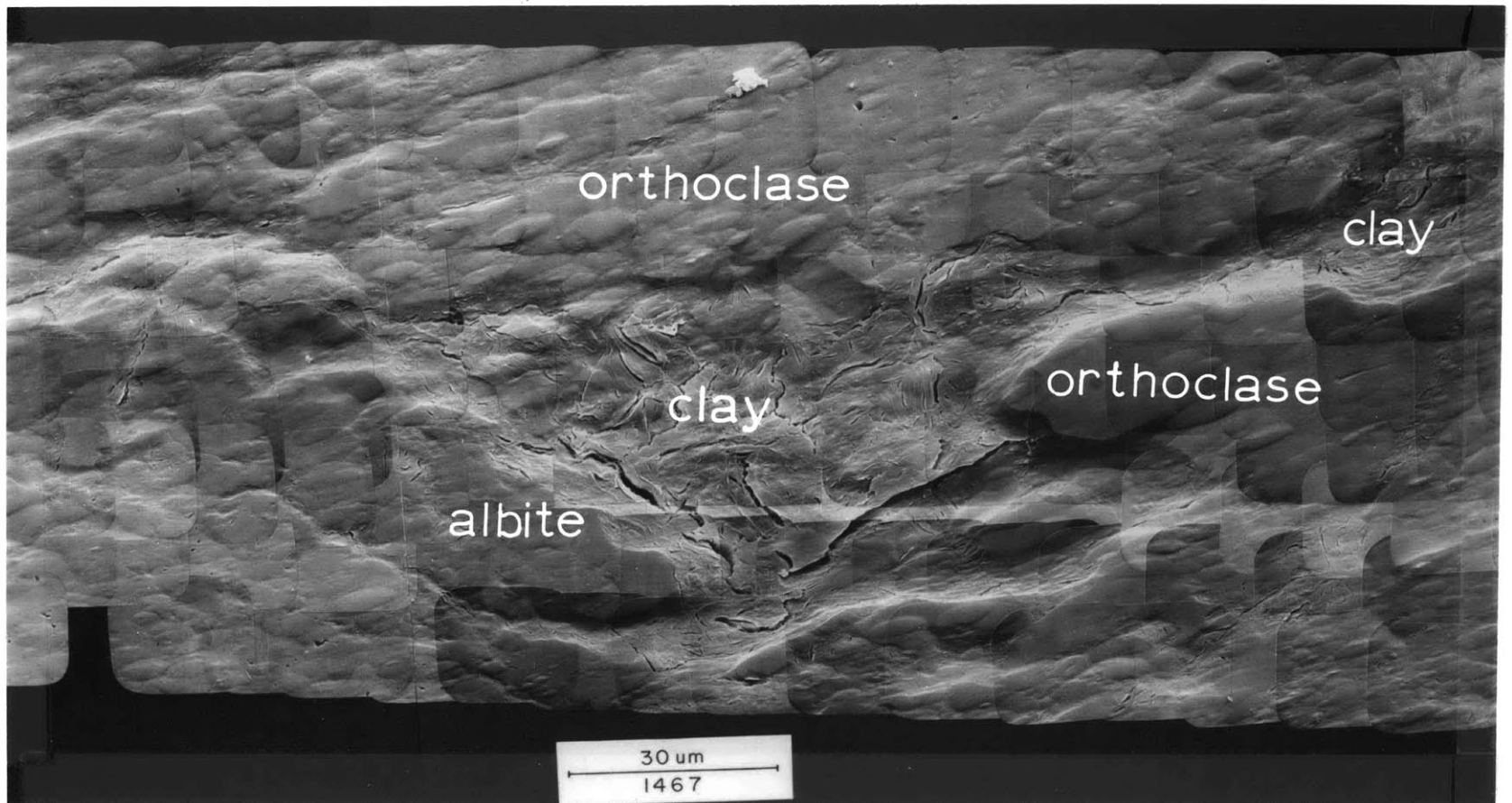
Figure 6-12. SEM mosaic of a Marysville sample from a depth of 305 meters (photomosaic by Steve Shirey). The fracture diagonally crossing the sample is sealed with clay. Smaller openings within the clay may be dessication cracks.

the low value of formation factor. This clay-filled fracture from 305 meters can be contrasted with the open, clean fracture previously examined in figure 5-6. The latter sample is from 1298 meters, below the alteration zones. The fracture porosity and permeability values are relatively large and formation factor correspondingly low. Hence, the clays and alteration products have a dominant role in determining the physical properties of the Empire Creek Stock.

Conclusions

Sealing, alteration, and healing of the fractures and matrix were observed in all the geothermal systems investigated. This sealing and modification may be confined to specific fractures and permeable units invaded by hydrothermal fluids. Distinct silicified and indurated zones or cap rocks may be developed. The sealing can confine fluid flow to specific horizons. Occasionally, as in the Raft River sample of figure 6-3, fractures are modified by etching and leaching. The etching widens fractures and enhances the flow characteristics. Such dissolution is not common in the ascending cooling limbs of the system. The typical effect observed is to close both fractures and nearby matrix. Not only is the permeability of the matrix reduced, but the sealed fractures can become effective barriers to flow normal to the plane of the fracture. This behavior can make the process of sealing and flow inhibition more efficient than just bulk pore filling. Veins can form impermeable planes which give rise to significant permeability and conductivity anisotropy and inhomogeneities.

The observations and results can be summarized in several specific

conclusions:

(1) Fracturing and matrix closure by sealing, healing, and alteration is typical of geothermal systems.

(2) Sealing and alteration can lower permeability, conductivity, and fracture porosity by orders of magnitude and make the rock dense, hard, and more susceptible to brittle fracturing.

(3) These processes will require refracturing to keep the system open to fluid circulation. Systems can thus be involved in repeated cycles of fracturing and fracture sealing.

(4) The type and characteristics of sealing and alteration can vary significantly with time as a result of variations in fluid properties and physical conditions.

(5) Occasionally leaching, crushing, and alteration may occur, which makes rocks more porous and less brittle. Rocks may be rendered weak and friable.

CHAPTER VII

CONCLUSIONS AND APPLICATIONS

Introduction

In this last brief chapter, observations and interpretations are summarized and several specific conclusions are discussed. The results of previous chapters were derived for the specific sampled sites but most of these results can be generalized to other systems. This chapter will close with several proposed applications of the techniques and data of this investigation. This thesis has demonstrated the interrelationships among the evolution and characteristics of geothermal systems, fracturing and faulting, sealing and alteration, and the properties of the enclosing rocks. Although the different processes observed were the topics of separate chapters, all can occur simultaneously within the system.

General Summary

Several distinct processes or features were observed in all the investigated geothermal systems. In general, these systems involve circulation in broad and complex convection cells. Heated fluids rise along fractures and fault zones and invade permeable rock units. The generalized system was discussed in Chapter I and figure 1-2 showed the basic components and flow patterns that occur. Figure 1-4 indicated the evolution of the conceptual system and the effects on physical properties. For convenience, the processes have been categorized here although they need not occur in any specific order or independently of

one another. (1) Compaction, lithification, and cementation processes are predominantly confined to sedimentary rocks and may be unrelated to the geothermal system. The permeability is usually lowered which significantly inhibits flow. Cementation and intense diagenesis may be the first stages brought about by invading hydrothermal fluids. (2) The fracturing and crushing of rocks can increase both the permeability and conductivity by several orders of magnitude. The fracturing is often repeated and varies greatly in morphology and extent. (3) Cracks and pores are usually filled and closed with phases precipitated out of hydrothermal fluids. Water-rock reactions cause alteration and metasomatism resulting in low density, hydrous phases which cause further filling and sealing. The type and degree of sealing and alteration can vary greatly with time. The permeability can be lowered by many orders of magnitude. Conductivity may be lowered similarly depending upon the mineralogy developed. Thin veins can act as effective barriers to flow normal to the plane of the vein. (4) The lowering of permeability by sealing and alteration requires renewed fracturing of rocks to maintain fluid circulation. The system may thus enter a cycle with multiple episodes of fracturing and subsequent sealing.

In detail, the individual geothermal systems are more variable and complex than indicated in this simple summarization. Etching and dissolution can occur instead of sealing. Intensive shearing and alteration can make rocks soft and porous. The development of clays along fractures can lower permeability significantly but leave conductivity relatively unaffected.

Fracturing and sealing processes have a cause and effect relation-

ship with the local geologic environment. The effect of the environment is demonstrated by the wide variety of reactions which have occurred within cracks and veins. Minerals are precipitated and the surrounding rocks are altered or indurated. Induration makes the rock more susceptible to brittle fracturing. The fracture morphology and properties can be substantially changed. Fracturing, on the other hand, can strongly influence many of the physical parameters which control the reactions. Permeability can be increased by more than five orders of magnitude by a single partially sealed fracture. Thus, the flow of hydrothermal fluids is controlled by the same cracks and pores that these fluids will alter or modify.

Applications

The observations and results of the investigation can be applied to several of the problems encountered in the development of a geothermal site. Problems include both the exploration for and evaluation of the high temperature reservoir. The size and heat content of the system must be determined. Future changes of system characteristics due to development must be estimated. Only a brief discussion of some possible applications will be presented here because either the sample suite is inadequate for complete evaluation or the application must be specifically modified for use in each individual area.

The strain analyses and laboratory flow measurements might be used to predict future reservoir behavior. The withdrawal of fluid from producing horizons will lower pore pressure and increase the effective pressure. The increased effective pressure can cause collapse of porous

rocks resulting in land subsidence and decreased permeability. The friable, weak rocks encountered in many wells indicate that such collapse could be a serious problem of large-scale geothermal production. The present sample set is somewhat restricted and not well-suited for this type of evaluation. The specimens were generally well-indurated, or macroscopically fractured, or veined. As a result, softer, more permeable rocks, or open fracture zones are underrepresented. Such softer units are largely responsible for subsidence and changes in fluid production characteristics. Two basic observations can be made however. No samples from within the active portions of the hydrothermal systems showed large strains under the increased confining pressure (a few bars) expected during production. Usually the initial identifiable geothermal processes involved induration and cementation. Such processes prevent collapse under increasing pressure. The induration tends to stabilize the rocks and prevent compaction and reduction in permeability.

The planned development of several areas calls for reinjection of used geothermal fluids. These spent fluids may invade the reservoir and replace the high temperature fluids (Schroeder, 1966; Kettenacker, 1977; Kasameyer et al., 1977). However, the sealing textures seen previously, as well as the thermal inversions in several wells, indicate that hot water flow is often restricted to distinct horizons and zones. Used fluids could be injected into isolated aquifers with little probability of subsequent contamination of the high temperature reservoir.

Resistivity measurements are commonly used in exploration for geothermal resources. Obviously, as discussed previously, these measurements will be dependent on the fracture and pore content of the rocks.

The resistivity will also be dependent on fluid and mineral content.
Usually the object of electrical exploration is to map the location
of hot or briny fluids. However, the results of resistivity deter-
minations may be only a measure of alteration. For example, in a
fractured feldspar-rich rock, the alteration products are often clay
minerals. Clays have large specific surfaces and therefore their sur-
face conduction is large. Hence, as the feldspars become coated with
clays, the resistivity will drop significantly, even with a relatively
small amount of bulk alteration. This effect is shown qualitatively
in figure 7-1. For our hypothesized feldspar-rich rock, the resistivity
will initially be within the range of values typical for granite. As
alteration proceeds, the rock resistivity will decrease to values more
typical of clays. However, the degree to which this 'alteration con-
duction' will affect the overall conductivity of the rock is dependent
on pore size and specific fluid conductance. For rocks saturated with
fluids having a very low specific conductance, the surface conduction
effects dominate (Brace et al., 1965; Williams, 1976). With highly ·con-
ductive fluids, the fluid properties dominate. The relative importance
of this 'alteration conduction' can be compared to the fluid resistivity
as in figure 7-2. In figure 7-2, typical 'granite' and 'clay' resis-
tivities are shown (see, for example, Keller and Frischknecht, 1966,
p. 41; Keller, 1968) along with the measured resistivities of several
fluids, including many geothermal brines. For fluid resistivities less
than 1 Ωm, surface conduction is unimportant. However, with fluid
resistivity greater than approximately 100 Ωm, surface conduction will
dominate (Brace et al., 1965). The field resistivity measurements made
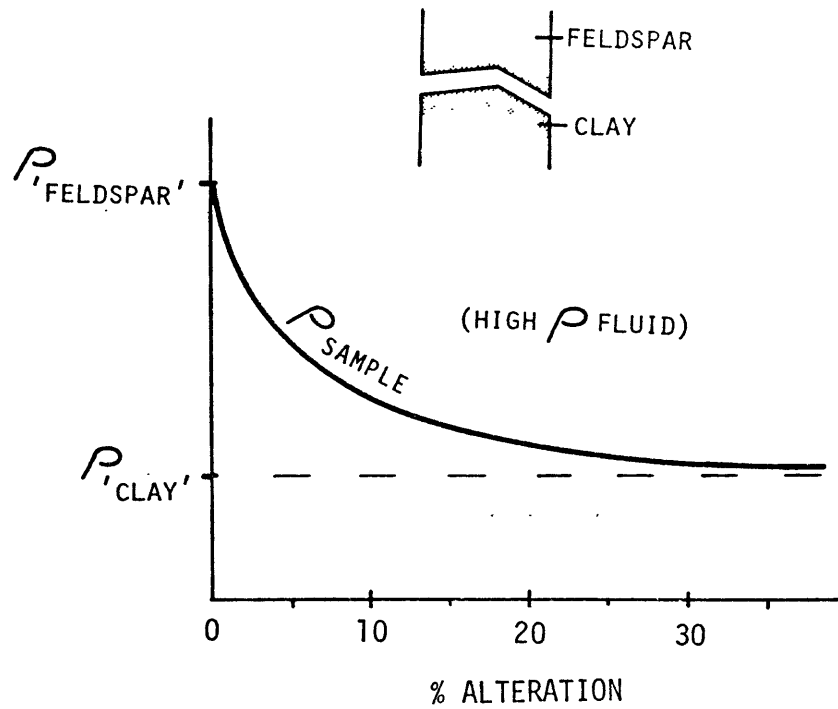
Figure 7-1. Resistivity versus degree of alteration for the idealized feldspar-rich rock in the upper right. The rock is saturated with a highly resistive fluid.
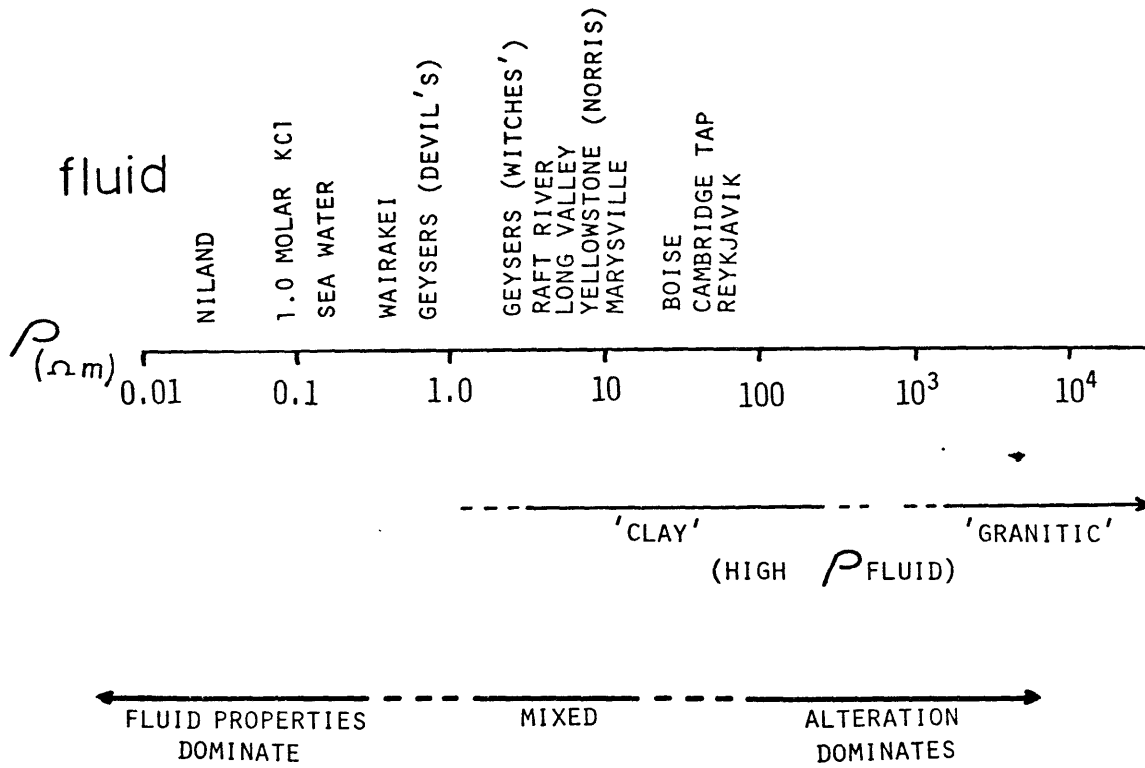
Figure 7-2. Schematic diagram of the relative importance of fluid properties versus clay alteration to resistivity measurements. See text for details.

in geothermal exploration commonly have values in the region of 'clay' of figure 7-2. Hence, if such alteration has occurred, and if the fluid resistivity is high, the resistivity measurements made in geothermal areas will produce values resulting from the combined effects of fluid properties, clay alteration, and pore content. Although these results are very qualitative, they are an indication of the dominant role that can be taken by alteration within fractures.

The fracturing and sealing processes observed in the geothermal systems may be used as a possible exploration technique. The repeated fracturing and subsequent veining with a variety of minerals typifies active systems. Therefore, if such features are observed, the specimen was subjected to active circulation in situo. Hot fluids may presently be circulating nearby. The Coso sample from 190.1 meters shown in figure 6-5 of Chapter VI is an excellent example. Several mineral species are developed within the vein and one, calcite, is intensely zoned. Evidence for repeated fracturing exists in the form of the broken and fragmented calcite seen in figure 6-5d. The minerals must have been precipitated from fluids with rapidly varying chemistry or under fluctuating physical conditions. These features are probably not isolated events but may be characteristic of active systems. If such fabrics are observed in shallow test holes, futher exploration nearby is indicated. Similarly, such features in cores or cuttings from dry or poorly producing wells imply that further drilling or hydrofracturing may intersect productive fracture zones or rock units. The observations necessary for such evaluations can be simply and quickly performed. The techniques may be adaptable for use in the field. These observa-

tions of physical characteristics could be used in conjunction with

any mineralogic indicators developed for individual geothermal areas.

APPENDIX 1

SAMPLE DATA AND DESCRIPTIONS

In this appendix, the physical parameters measured on each sample will be summarized and the sample will be described briefly. The well stratigraphic columns in Chapter II should be referred to for a graphic representation of sample characteristics and the surrounding geologic settings. Several features are noted here for use in the following table. The numbers refer to the superscripts in the column headings in Table Al-la and also apply to the remaining portions (b through f) of the table.

1. In situ effective pressure (EP) is estimated as lithostatic pressure minus fluid pressure calculated for uniform columns of dry rock and water respectively. Dry rock densities were the averages of the measured values for each area and the fluid was assumed to have a density of one gram per cubic centimeter. Any reported well fluid pressure was also included.

2. Fracture or crack porosity (FP) is the sum of the strain due to fracture closure at high pressure in three orthogonal directions. The volume fraction is reported in units of 10^{-6} unless otherwise noted. Total high pressure sample volume change is reported for specimens with large amounts of compaction and consolidation. Compaction volume decreases are noted with a 'C'. If three orthogonal strain measurements were not available, sample symmetry was assumed to deduce the other direction(s) needed to estimate volumetric strains. The maximum pressure for all strain measurements was 2.5 kbars unless otherwise indicated.

3. 'Raw' fracture porosity and consolidation data are for strain mea-
   surements extrapolated back to atmospheric pressure.

4. Adjusted (ADJ.) fracture porosity and consolidation data are the
   strain data adjusted for the estimated in situ pressure. In other
   words, the strains due to fractures that would be closed under
   in situ pressures or the consolidations at less than in situ pres-
   sures are subtracted. Often, the in situ pressures are small and
   no adjustments (NA) to the raw data are necessary.

5. Abbreviations used:

   no Y gage: strain measured in only two orthogonal directions.

   frx: fracture or fractures.

   fracture closure behavior: the sample has stress-strain curves
       with shapes typical of fractured rocks (see Chapter III).

   compaction behavior: the sample has stress-strain curves with
       shapes typical of compaction and consolidation.

   bumps: irregularities and deflections in the general trend of
       strain curves.

   b: bars.

   C: volumetric consolidation.

6. The schematic DSA diagram shows the generalized behavior of the
   measured strain curves. The scale for each diagram is arbitrary.
   The overall behavior is emphasized, not the absolute size.

7. Porosity (POR.) and Density (DENS.) by immersion in water. The
   porosity measured is therefore the interconnected porosity and
   the values are given in void volume fraction. Density values
   are in grams per cubic centimeter. .

8. Permeability (k) values are in darcys ($10^{-8} cm^2$) or standard subdivisions. Values were adjusted (A) for in situ pressure only for samples used for permeability versus confining pressure determinations.

9. Formation factor (For. Fac.) is equal to the rock resistivity (ρ_r) divided by the fluid resistivity (ρ_f). Exponents indicate the power of ten multiplier, i.e., $2.3^3 = 2.3 \times 10^3$ (ρ in Ωm).

10. The well stratigraphies of Chapter II should be referred to for the surrounding physical settings and for the identification of alteration and veining minerals within samples.

Abbreviations:

gr: grained.

frx: fracture or fractures.

<: less than.

>: greater than.

qtz: quartz.

TABLE A1-1. SAMPLE DATA AND DESCRIPTIONS
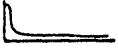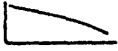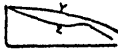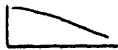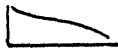
(a) DUNES (well #1452)

Sample (Depth, m)	In situ[1] Effective Pressure	FP or C[2] Raw[3]	FP or C[4] Adjusted[4]	Remarks[5]	Schematic[6] Diagram	Porosity[7] Density	Perm., k[8]	For. Fac.[9] (ρf)	Sample Description and Remarks[10]
281 (85.7)	12.9	C 3%	NA	Smooth consolidation, Z gage failed.		.24 2.01	25 md A	24.4 (2.3)	Pink, medium-grained, lighted cemented lithic arenite with several partially sealed fractures (see figure 4-10).
380 (116)	17.4	507	NA	To 2kb, no Y gage, curve has several linear segments.		.030 2.52	2.8 nd -unfrx -7520 8.2 md - frx - 1130		(ρf = 28) Red-gray, indurated, lithic wacke with several partially sealed fractures (see figure 5-8).
487 (148.4)	22.3	1514	NA	Rough curve, fracture closure behavior.		.038 2.63			Gray, medium-grained, lithic arenite with 2mm wide, pyrite-sealed fracture (see figure 5-17).
495 (151)	22.7	340	NA	To 2kb, no Y gage, some initial grain crushing and linear segments		.075 2.43			Gray, coarse-grained, lithic wacke, well-indurated and no visible fractures or veins.
792 (241.4)	36.2	371	NA	To 2kb, numerous gages show similar magnitude and behavior.		.059 2.49	.45 md -cen - 2510 10 md - edg - 1507		(cen = center of core, edg = edge; ρf = 2.1) Gray, indurated arenite with open and adularia-sealed fractures (see figure 5-12).
942 (287)	43.1	392	NA	To 2kb, no Y gage, smooth fracture closure behavior.		.086 2.41			Gray, well-indurated, lithic arenite with numerous .1mm wide, calcite-sealed fractures.
957 (291.7)	43.8	1710	NA	Very rough, fracture closure behavior, largely anisotropic.		-- --			Gray, well-indurated, medium-grained lithic arenite grading into a conglomerate with quartz and adularia-sealed fractures.
1325 (404)	60.7			Failed due to oil leak.		.13 2.28			Gray-green, medium-grained argillaceous wacke with large clay clasts and calcite-sealed fractures (see figure 5-10).
1998 loose (609)	91.3	C 13%	NA	Compaction and grain crushing, onset of rapid comp. about 850 b.		.35 1.59	3.2 md	3.7 (28)	Gray-green, medium to coarse-grained, friable, argillaceous lithic wacke (see figure 4-14).
1998 indur. (609)	91.3	C 1.5%	C 1.2%	Compaction similar to the initial portion of the 1998 loose curve.		.059 2.53	.34 µd	2.9 (28)	Same as 1998. Loose but well-indurated with calcite cement.
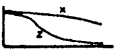
234

Sample	In situ EP	FP or C Raw	FP or C ADJ.	Remarks	Schematic Diagram	POR. / DENS.	k	For. Fac. (ρf)	Sample Description and Remarks
HEBER GTW#1 well (#1459)									
3167 (965.3)	145			Not run.		.25 / 2.08			Light gray, homogeneous, silty mudstone weakly consolidated and readily breaks up into clumps.
3177 (968.4)	145	C 6.9%	NA	Increased rate of compaction at about 550 bars.		.20 / 2.18			Light gray, homogeneous, silty mudstone similar to 3167, several small calcite veins (figure 5-9).
3181 (969.6)	145			Not run.		.25 / 2.01			Light gray, friable, argillaceous sandy siltstone; one vertical ~1mm wide calcite vein.
3184 (970.5)	146	C 13%	NA	Massive compaction occurs at 1500 b. (DSA on different sample gives c = 9.1%.)		.26 / 1.97			Light gray, homogeneous, weakly-indurated argillaceous, sandy, pyritic siltstone.
3193 (973.2)	146	C 12%	NA	Increased rate of compac. at about 1270 b. (DSA on different sample gives c = 13%.)		.29 / 1.89			Light gray, medium-grained, slightly pyritic qtz. arenite.
HEBER GTW#3 well (#1460)									
3885 (1184)	177	410	368	Small fracture content with straight consolidation. c = 1.9%.		.13 / 2.34	15 μd-∥vein - 40 / 5 μd-⊥vein-120		(ρf = 2.0) Gray, moderately-indurated, sandy siltstone with small chlorite (?)-filled faults and many mm wide calcite veins.
3888 (1185)	178	3250	1750	Fracture closure + compaction above 800 b. c = 1.8%.		.086 / 2.47			Gray, moderately-indurated argillaceous siltstone with several vertical cm wide calcite veins.
3891 (1186)	178	8900	6140	Fractures + compaction. Bump in data at 1900 b.		.15 / 2.37			Dark gray, friable, silty, pyritic claystone with small <mm chlorite (?) and calcite veins.
3894 (1187)	178	3100	2000	Fractures + compaction. c = 5.8%.		.13 / 2.39			Dark gray, friable, argillaceous siltstone with many cm wide and smaller calcite veins (figure 6-2).
3905 (1190)	178	5750	3500	Compaction. c = 1.7%.		.16 / 2.23	65 μd	25 (2.0)	Light gray, moderately-indurated, silty sandstone with two <mm wide vertical calcite veins.
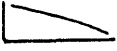
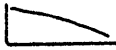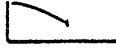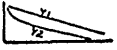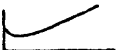| Sample	In situ EP	FP or C Raw	FP or C ADJ.	Remarks	Schematic Diagram	POR. DENS.	k	For. Fac. (ρf)	Sample Description and Remarks
Intermediate well #3 (#1457)									
212 (64.6)	9.7	C 18%	NA	Slight compaction followed by abrupt collapse after about 65 b.		.51 1.22			Light green, silty claystone with soft sed. deformation and small sand lens.
507 clay (154.5)	23			Not run.		.36 1.70			Light green, friable, bedded mudstone; in fault contact with 507 indurated below (see figure 6-4).
507 loose (154.5)	23		NA	Not run.		.10 2.36			Light green, friable, argillaceous lithic wacke, uncemented (see figure 6-4).
507 indur. (154.5)	23	C 1.42%	NA	Smooth consolidation behavior.		.092 2.38			Dense, gray-green, same rock as 507 loose but well cemented with calcite (see figure 6-4).
594 sand (181)	27	C 1.2%	NA	Smooth consolidation. X gage failed. Bump in Z at 1500 b.		.26 1.92			Light green, argillaceous lithic wacke; cemented at distinct spots with calcite similar to 507.
594 clay (181)	27	C 10%	NA	Increased rate of compaction at approximately 250 b.		.34 1.71			Light green mudstone with several 3mm wide calcite veins; directly contacts 594 sand, 45° bedding planes.
868 (264.6)	40	C 15%	NA	Increased rate of compaction at approximately 200 b.		.39 1.50	35 µd - ∥ vein - 32 32 µd - ⊥ vein - 146		(ρf = 2.3) Altered tuffaceous siltstone; many 3 mm wide calcite and analcime veins (see figure 6-8).
982 (299.3)	45	C .38%	NA	Smooth simple compaction.		.094 2.39			Dark gray, well-indurated, laminated, argillaceous siltstone with numerous <2mm analcime veins.
991 (302.1)	45.5			Not run.		.32 1.64			Light green, indurated, argillaceous siltstone with many <2mm wide fractures partially sealed with calcite and analcime.
1067 (325.2)	49	610		2kb max. Mixed consol. and fracture behavior. c = .32%.		.14 2.13			Light green, indurated, sandy, argillaceous siltstone, numerous 2mm wide fractures coated with analcime.
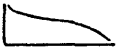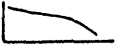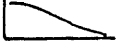
Sample	In situ EP	FP or C Raw	FP or C ADJ.	Remarks	Schematic Diagram	POR. DENS.	k	For. Fac. (ρf)	Sample Description and Remarks
1107 (337.4)	51	C 6.6%	NA	2kb max. increased rate of compaction above 500 b.		.36 1.56			Light green, friable, argillaceous wacke with one 6mm wide multilayered vein with analcime and hematite.
1132 loose (345)	52	C .36%	NA	2kb max., minor fracture behavior.		.36 1.44			Light green, friable, argillaceous, sandy siltstone with many calcite and analcime veins (see figure 6-3).
1132 indur. (345)				See 1132 loose.		.13 1.99			Same as 1132 loose but cemented with analcime. Cementation boundaries along small veins (see figure 6-3).
1159 (353.3)	53			Not run.		.39 1.55			Pale yellow, friable, argillaceous, sandy siltstone; numerous fractures and vugs coated with analcime.
1204 (367)	55	C .6%	NA	Simple compaction behavior with slight increase in rate above 200 b.		.15 2.21	1.1 μd	5.8 (52)	Light to dark green indurated mudstone with <mm wide chlorite veins and small analcime crystals in matrix.
1217 (370.9)	56			Not run.		.49 1.32			Light green, soft, argillaceous siltstone, few fractures partially filled with analcime and calcite.
1247.5 (380.2)	57	C 15%	NA	Compaction with fairly abrupt structural collapse above 375 b.		.39 1.58			White to green, soft mudstone, a few <mm wide open fractures, prominent soft sed. deformation.
1257 (383.1)	58	C 5%	NA	Simple smooth compaction until sample failed at 1000 b.		.-- .--	2.5 μd	1.5 (28)	Gray, soft bedded mudstone with a few <1mm wide calcite veins.
1387 loose (422.8)	64			Not run.		.39 1.65	.2 d	20 (2.0)	Pale gray, friable, poorly sorted argillaceous pebble conglomerate (see figure 4-15).
1387 indur. (422.8)	64			Not run.		.13 2.32	2.1 md	47 (2.0)	Same as 1387 loose but heavily indurated with calcite cement; abrupt cementation boundary (figure 4-15).

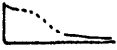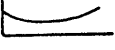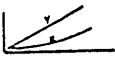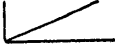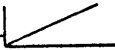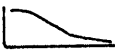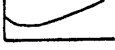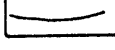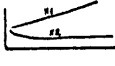| Sample	In situ EP	FP or C Raw	FP or C ADJ.	Remarks	Schematic Diagram	POR. DENS.	k	For. Fac. (ρf)	Sample Description and Remarks
Intermediate well #1 (#1456)									
308 (93.9)	14	C 27%	NA	Abrupt increase in comp. above 55 b., almost constant strains after 1300 b.		.48 1.27			Tan, very friable, poorly sorted, argillaceous, sandy siltstone grading into a coarse sandstone.
Intermediate well #4 (#1458)									
175 (53.3)	8	2810	NA	Fracture closure behavior anisotropic and very rough.		.061 2.45			Purple-gray porphyritic volcanic; many open fractures and vugs with thin coatings of clay and qtz.
RRGE#1 well (#1453)									
4495-4500 (1371)	196	C 8.8%	NA	Increased rate of compaction above 600 b.		.29 1.88			Light green, indurated, tuffaceous siltstone with many mm wide vugs and a 6mm albite vein, broken fragments only.
4690 (1430)	205			Not run.		.-- .--			White-gray, banded quartz-feldspar mica schist; some irregular fractures and open, coated vugs.
4694 (1431)	205	400	360	Small fracture content, large 24 hour temp. oscillations.		.0049 2.73			Gray, layered, dense quartz mica schist; several <1mm wide quartz and chlorite veins (see figure 5-3).
RRGE#2 well (#1454)									
3075 (937)	130	C 9.4% FP 9800	NA 5500	Mixed fracture + consolidation behaviors, break at -270 bars.		.45 1.45	22 md ‖ vein - 6.8 .6 md ⊥ vein - 7.3		(ρf = 2.3) Light green, friable, argillaceous siltstone with several . <mm albite veins.
3082 (939)	131	C 17%	NA	Consolidation behavior, data missing between 255 and 776 b.		.51 1.29			Light green, argillaceous tuffaceous wacke with several <mm vertical albite veins.
3725 (1135)	160	C 3.5%	NA	Smooth consolidation behavior; Y and Z gages failed.		.20 2.11			Light green, moderately-indurated, argillaceous, sandy siltstone; faulted bedding and numerous calcite veins.
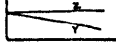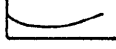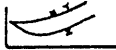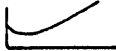
Sample	In situ EP	FP or C Raw	FP or C ADJ.	Remarks	Schematic Diagram	POR. DENS.	k	For. Fac. (ρ_f)	Sample Description and Remarks
4224 (1287)	183	C 3.4% FP 1500	NA 400	Mixed fracture + consolidation behavior. Increased comp. above 1700 b.		.19 2.43	A 9.8 µd	18 (4.2)	Light green, moderately-indurated, argillaceous, sandy siltstone; a few <mm calcite and clay-sealed fractures.
4370-4376 (1333)	190	4810	NA	Increased rate of consolidation above 1500. Y gage failed.		.089 2.43			Dark gray, dense, indurated, silty shale with many <mm chlorite (?) sealed fractures.
RRGE #3 well (#1455)									
2811 (857)	118	C 11%	NA	Consolidation behavior, increased compaction above 350 to 650 b.		.20 2.14			Light green, moderately-indurated, argillaceous, micaceous, lithic wacke, one <mm wide calcite vein.
3365-3380 (1026)	144	C 8.0%	NA	Slightly increasing rate of comp. at high pressures.		.21 2.06	2.9 md	17.1 (3.1)	Light green, moderately-indurated, argillaceous, tuffaceous wacke with many <mm calcite-filled vugs and frx.
3974 (1211)	172	C 15%	NA	Increasing rates of compression above 550 to 650 b.		.30 1.84	3.2 md	8.75 (3.9)	Light green, argillaceous, micaceous wacke with interbedded siltstones, no visible fractures.

(d) COSO HOT SPRINGS

Sample	In situ EP	FP or C Raw	FP or C ADJ.	Remarks	Schematic Diagram	POR. DENS.	k	For. Fac. (ρf)	Sample Description and Remarks
BDH#1 well (#1650)									
502.5 (153.2)	23	2100	NA	Fracture closure behavior for clast in breccia, Y and Z gages failed.		.014 2.78			Dark gray, fine-grained diorite, intensely broken and sheared with development of clays and slickensides.
624 (190.1)	28.5	1270	NA	Rough fracture closure behavior, X gage failed, large anisotropy.		.0065 2.86			Dark green, veined, metashale in fault contact with medium-grained, slightly altered diorite (see figure 6-5).
667 (203.3)	30.5	635	NA	Straight elastic compression.		.063 2.71			Medium to fine-grained, dark gray diorite with many felsic and clay-filled mm wide fractures.
721 (219.8)	33	200	NA	Linear compression, measurements made on intact clast inside breccia.		.-- .--			Cataclastic granodiorite, very friable and heavily altered to light green clays.
750 (228.6)	34	C 12.5%	NA	Has a behavior like the compaction of sedimentary rocks.		.11 2.49			Cataclastic, original felsic rock, broken into small clasts surrounded by dark green clays (see figure 6-9).
890 (271.3)				Not run.		.084 2.50			Fine-grained, equigranular, gray diorite with many <mm veins and one 5mm calcite and zeolite vein.
934 (285)	43	11600	10120	Fracture closure behavior; two gages in each direction.		.18 2.17	A 70 μd	20.8 (2.3)	Cataclastic, yellow and pink, granodiorite clasts in a matrix of yellow clays (see figure 5-4).
1033 (314.8)	47	1930	NA	Fracture closure behavior, some crushing in X direction.		.032 2.58			Light gray meta-wacke(?) heavily broken with <3mm calcite and clay-filled fractures.
1051 (320.3)	48	1450	1400	Typical fracture closure behavior, anisotropic.		.059 2.50			White, sheared, friable, aplite(?) with many branching fractures filled with muscovite.

Sample	In situ EP	FP or C Raw	FP or C ADJ.	Remarks	Schematic Diagram	POR. DENS.	k	For. Fac. (ρf)	Sample Description and Remarks
1139 (347.2)	52	770	NA	Almost linear compression, some minor compaction in Y direction.		.-- .--			Dark gray, fine, equigranular, metased(?) with numerous <mm chlorite-filled veins.
Heat Flow well #3 (#1651)									
36 (11.0)	-0	6820	NA	Smooth fracture closure behavior.		.026 2.59			Medium-grained, pink, slightly altered quartz monzonite, very few small fractures with hematite.
Heat Flow well #13 (#1652)									
299 (91.1)	13.7	8910	NA	Consol. behavior at low pressure; break in slope at 1200 b. leak?		.037 2.74			Medium to fine-grained, gray green diorite(?) with two <3mm calcite and chlorite(?) veins, one shows offset.
Heat Flow well #15 (#1653)									
150 (45.7)	7	1660	NA	Rough fracture closure behavior.		.010 2.70			Fine-grained, equigranular granodiorite with few small clay filled fractures.
Heat Flow well #1 (#1654)									
150 (45.7)	7	4900	NA	Smooth fracture closure behavior.		.014 2.59			Pink, medium-grained, equigranular quartz monzonite with slight oxidation of mafics.
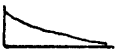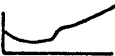
Sample	In situ EP	FP or C Raw	FP or C ADJ.	Remarks	Schematic Diagram	POR. DENS.	k	For. Fac. (pf)	Sample Description and Remarks
1462 (101)	25.0	473	463	Almost linear compression.		.00047 2.67	<.5 nd	2.6^4 (1.8)	Dark gray, porphyritic dacite with several small vertical veins and 5mm wide shear zone.
1462A (101)	25.0	286	NA	Almost linear compression.		.0078 2.71		150 (1.8)	Green-gray, banded dacite; numerous near vertical mm wide veins with bleached zones.
1463 (134)	33.6	360	NA	Almost linear compression.		.00028 2.79		5.8^4 (1.8)	Dark gray, indurated metashale with numerous intersecting <mm wide veins.
1464 (178)	44.6	124	NA	Almost linear compression.		.00036 2.73	3 nd	3.1^4 (1.8)	Dark gray, indurated metashale similar to 1463, dark mm wide bands surround veins.
1465 (282)	60.3	263	NA	Slightly increasing rate of compression at high pressure.		.0013 2.69	5 nd	375 (1.8)	Dark gray, indurated, silty metashale with numerous mm wide veins.
1466 (304)	63.8	358	NA	Increased rate of compression after few hundred bars.		.0019 2.59		390 (1.8)	Very fine-grained, porphyritic granite with rounded phenocrysts, many veins, dark stained zone.
1467 (304)	63.8	320	270	Anisotropic with Z closure strains larger by factor of 7.		.0016 2.59		795 (1.8)	Fine-grained, altered, porphyritic granite with several vertical mm wide veins (figure 6-12).
1468 (465)	87.8	366	NA	Anisotropic with Z closure strains larger by factor of 2 1/2.		.-- .--	<.5 nd	6.0^4(?) (3)	Fine-grained, altered, porphyritic granite with dark wavy veins (a fractured sample had k = .2 μd).
1478 (592)	107	508	498	Typical fracture closure behavior.		.0038 2.55		3.0^4 (1.8)	Medium-grained, altered porphyritic granite with zoned phenocrysts; single 5mm wide vein.
1469 (700)	123	450	NA	Typical fracture closure behavior.		.00085 2.57	.11 μd	1.1^4 (2.3)	Medium-grained, altered porphyritic granite, single mm wide vein (another sample had For. Fac. = 6^5).
1470 (849)	145	880	NA	Smooth fracture closure behavior.		.0080 2.58		3.5^3 (1.8)	Coarse-grained, altered granite with numerous veins surrounded by darkly stained zones.

Sample	In situ EP	FP or C Raw	FP or C ADJ.	Remarks	Schematic Diagram	POR./DENS.	k	For. Fac. (f)	Sample Description and Remarks
1471 (1010)	170	485	476	Typical fracture closure behavior; X gage failed.		.0018 2.60	A .12 µd	A 6.3^4 (3)	Coarse-grained, altered granite with numerous <mm wide, sealed frx (another sample had k = 67 nd).
1472 (1165)	193	670	655	Almost linear compression dominates frx closure behavior.		.046 2.56		735 (1.8)	Medium-grained, sheared, and altered porphyritic granite with numerous >mm wide dark veins.
1473 (1298)	213	2951	2566	Typical fracture closure behavior.		.027 2.57	12 µd	2.0^3 (1.8)	Medium-grained granite porphyry with numerous >mm wide veins; many feldspars altered to clay.
1474 (1298)	213	3960	3120	Smooth fracture closure behavior until gage failures at about 1200 b.		.-- .--		750	Coarse-grained granite with numerous open clay-lined frx; many altered feldspars (figure 5-7).
1475 (1607)	259	2905	2350	Smooth fracture closure behavior		.011 2.60		-- --	Pink, fresh coarse-grained granite with open vugs and numerous open fractures.
1476 (1836)	294	1950	1413	Smooth fracture closure behavior.		.0069 2.60		2.1^3 (1.8)	Pink, fresh, equigranular medium-grained granite; many small frx within and between larger grains.
1477 (1954)	311	1910	1410	Fracture closure behavior with small bumps at 222 b.		.-- .--	A 1.1 µd	A 4.1^3 (3.7)	Pink, fresh, equigranular, medium-grained granite; many small frx within larger grains.

Sample	In situ EP	FP or C Raw	FP or C ADJ.	Remarks	Schematic Diagram	POR. DENS.	k	For. Fac. (ρf)	Sample Description and Remarks
OBSERVATION HOLE #2									
1997 (608.7)	91(?)	975	NA	Somewhat rough fracture closure behavior.		.0031 2.70			Gray-green, medium-grained, equigranular granodiorite, some alteration of mafics, feldspathic, and hematite veins (see figure 6-6).
WELL 9-1									
5002 (1525)	230(?)	2280	1930	Fracture closure behavior but with significant bumps at 800 b.		.0026 2.67			Gray, medium-grained granodiorite, slight alteration of mafics, many small fractures visible in larger grains.

APPENDIX 2

GEOMETRIC MEAN MODEL

A detailed description of the geometric mean model is presented in this appendix. This model is used to interpret the dependence of permeability and conductivity of rocks on a homogeneous fracture population. The development is patterned after the geometric mean conductivity model of Madden (1976) which can be considered an extension of work done previously by Parsons (1966). The model variables include the measured fracture parameters of aspect ratio and fracture porosity derived from differential strain analysis (DSA). This method is applied to Westerly granite because this rock is fine-grained, homogeneous, approximately isotropic (to within the measurement errors of permeability and conductivity), and the characteristics are well-known. The results of the modeling are used in Chapter V to examine the interaction and dependence of transport properties on various fracture paramaters.

The general scheme for the modeling is developed in several distinct steps:

(1) The appropriate equations are developed for the dependence of permeability and conductivity on individual fractures and on the fracture population in general.

(2) The dependence is reduced to the three parameters (porosity, width, length) that need to be determined.

(3) Parameters are measured on a sample, in this case Westerly granite. Only porosity can be determined directly; aspect ratio is determined indirectly.

(4) Estimates of relative values of length versus aspect ratio are made in order to match the rock conductivity.

(5) The absolute values of length are adjusted to match the rock permeability.

(6) The model fractures are then closed with increasing pressure by two distinct mechanisms and the result compared to measured values.

The modeled rock is constructed of a large number of microscopic zones or cubes with edges of length L. Each cube is either solid matrix material or contains a single fracture. Each fracture is a rectangular 'box' with one dimension, L, common to all fracture sizes (see figure A2-1a). Using the parallel plate analogy for a single fracture of size 'i' gives

$$K_i = \frac{w_i^3 \ell_i}{12 \mu A}$$

where w_i and ℓ_i are the width and length (both variable) of the fracture, respectively, μ is the fluid viscosity, and A is the surface area of the zone. Expanding the equation gives

$$K_i = \frac{w_i^2}{12 \mu} \frac{w_i \ell_i}{L \cdot L} = \frac{w_i^2}{12 \mu} \cdot \frac{w_i \ell_i L}{L \cdot L \cdot L} = \frac{w_i^2}{12 \mu} \cdot \frac{V_i}{V_z}$$

V_i is the volume of the crack and V_z is the volume of the zone; hence, the ratio of V_i to V_z is the single fracture porosity ϕ_{si}. The permeability is then

$$K_i = \frac{w_i^2}{12 \mu} \phi_{si}$$
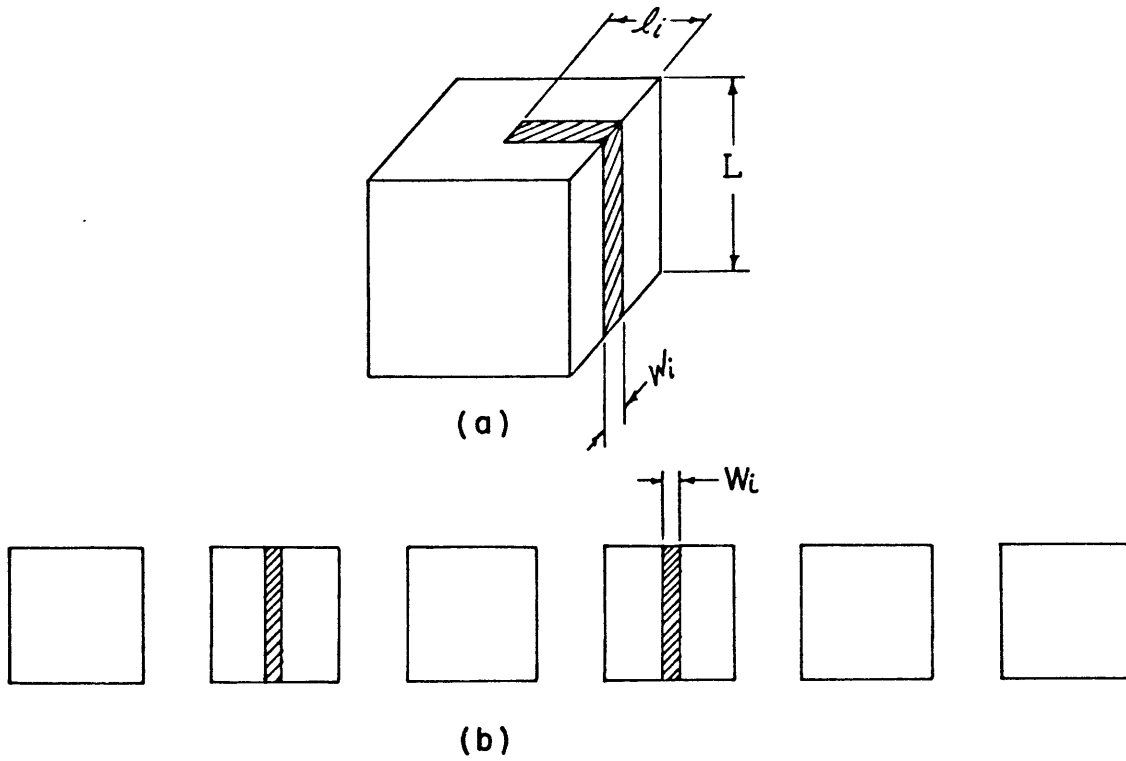
Figure A2-1. (a) Unit zone with modeled fracture dimensions.

(b) Six zones with a 0.33 fracture probability.

or equivalently

$$\phi_{si} = k_i(12\mu/w_i^2)$$.

For many zones, the total porosity, ϕ_i, of all the fractures with this same width is proportional to the probability that the zones contain such fractures

$$\phi_i = P_i\phi_{si} = P_ik_i(12\mu/w_i^2) \tag{A2-1}$$

Here, P_i is the probability that a fracture with a width w_i occurs in a zone. For example, in figure A2-1b, $P_i = 2/6 = .33$. Hence, for the total crack porosity of the rock, ϕ,

$$\phi = \sum_i \phi_i = 12\mu \sum_i P_ik_i/w_i^2$$

The total number of ith-sized cracks in the rock is equal to the total volume of ith-sized cracks divided by the volume of a single such fracture:

$$\frac{\phi_i}{w_i\ell_iL}$$

For the entire rock, the probability of the ith fractures is then the total number of ith-sized cracks divided by the total number of fractures within the rock or

$$P_i = \frac{\phi_i}{w_i\ell_iL}\,[\sum_j(\frac{\phi_j}{w_j\ell_jL})]^{-1} = \frac{\phi_i}{w_i\ell_i}\,[\sum_j(\frac{\phi_j}{w_j\ell_j})]^{-1} .$$

Substituting in equation (A2-1) and cancelling yields

$$k_i = \frac{w_i\ell_i}{12\mu}\,(\frac{\phi_j}{w_i\ell_i}) \tag{A2-2}$$

Equation (A2-2) is only valid when all fractures are oriented parallel to the direction of flow. In an isotropic rock, many of the fractures will not be oriented parallel to flow. The model zones will have fractures oriented along all three of the coordinate axes. An inefficiency factor must be added due to the approximately one-third of the fractures (in a cubic system) that are oriented normal to flow.

$$k_i = \frac{w_i \ell_i}{12\mu} \left(\frac{2}{3-\phi}\right) \sum \left(\frac{\phi_j}{w_i \ell_i}\right)$$

For small porosities the equation can be simplified to

$$k_i = \frac{w_i \ell_i}{18\mu} \sum \left(\frac{\phi_i}{w_j \ell_j}\right) \qquad (A2-3)$$

The resulting geometric mean permeability, $<<k>>$ for the rock will then be the product of all the individual permeabilities exponentiated to the respective probability:

$$<<k>> = \prod_i K_i^{P_i} \qquad (A2-4)$$

A similar derivation will occur for the individual fracture conductance, Y_i.

$$Y_i = \sigma_f \frac{2w_i \ell_i}{3} \sum \left(\frac{\phi_i}{w_j \ell_j}\right) \qquad (A2-5)$$

where σ_f is the saturating fluid conductivity. The resulting geometric mean rock conductivity is then

$$<<\sigma>> = \prod_i Y_i^{P_i} \qquad (A2-6)$$

The use of the geometric mean model requires the values of porosity,

width, and length for each fracture set. Porosity can be derived

directly from strain data. The width and length can only be measured

by stress-strain techniques coupled together in the aspect ratio,

$\alpha_i = w_i/\ell_i$. Values of either w_i or ℓ_i must then be estimated. The

aspect ratio is determined through the relationship derived by Walsh

(1965), as was mentioned in Chapter III. This relation can be expressed

in the form

$$\alpha = \beta P_c \frac{4(1-\nu^2)}{3\pi(1-2\nu)}$$
(A2-7)

where β and ν are the compressibility and Poisson's ratio, respectively,

of the fracture-free matrix and P_c is the crack closure pressure. Sever-

al investigations have improved on this formula recently, but considering

the crudeness of this model, equation (A2-7) is quite adequate. Sub-

stituting the values $\nu = 0.21$ and $\beta = 2.06$ Mb^{-1} (Brace, 1965) gives

$\alpha = 1.44 \times 10^{-6} P_c$.

Porosity as a function of aspect ratio can thus be determined from

strain data through the closure pressure-shape relation of equation

(A2-7). A graph of cumulative fracture porosity derived from DSA on

Westerly granite is shown in figure A2-2. As pressure increases,

according to equation (A2-7), cracks with larger aspect ratios close

with a subsequent drop in total porosity. For use in this model,

closures are grouped into 5 sets centered (logarithmically) about dis-

tinct closure pressures of 20, 70, 200, 700, and 2000 bars. These

closure pressures correspond roughly to the aspect ratios $10^{-4.5}$,

10^{-4}, $10^{-3.5}$, 10^{-3}, and $10^{-2.5}$ ($10^{.5} \approx 3.16$). The result is the tabu-

lation of porosity versus aspect ratio shown in figure A2-3.
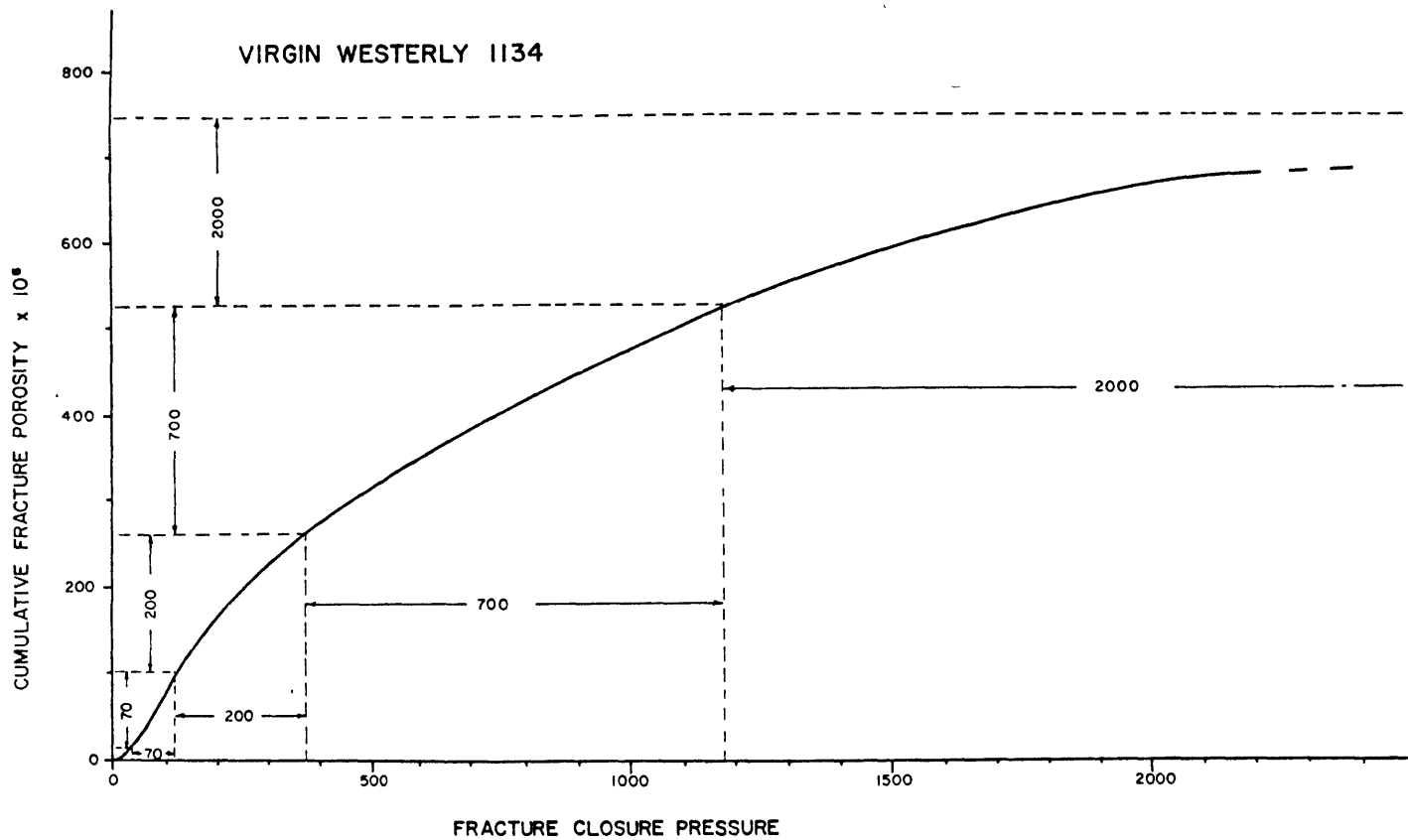
Figure A2-2. Cumulative fracture porosity from DSA of Westerly granite. Intersecting vertical and horizontal lines are used to measure fracture content for logarithmically increasing fracture closure pressures (DSA data from Cooper, personal communication, 1976).
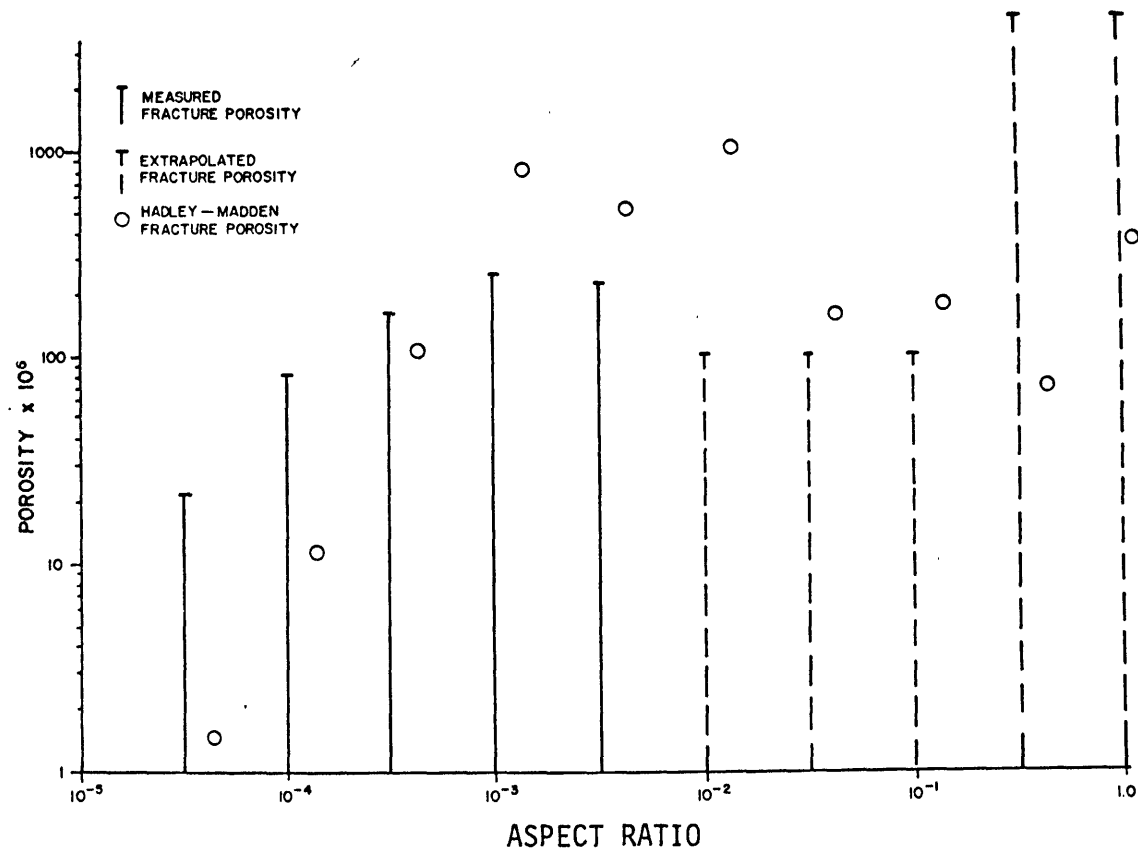
Figure A2-3. Aspect ratio versus porosity as calculated from Figure A2-2 and total rock porosity. The values of Hadley (1976) as tabulated by Madden (1976) are included.

Three comments should be made about the distribution shown in

figure A2-3. First, measurement above an aspect ratio of about

3.16×10^{-3} is not possible with the equipment available for this study.

Porosity values of cracks with aspect ratios of 0.01 and larger must

be extrapolated based on the general trend of the curve of figure A2-2

and on other less precise high pressure data (Brace, 1965). Secondly,

the total porosity of Westerly granite is approximately one percent.

This porosity is contained mostly in the more spherical pores and void

spaces (Sprunt and Brace, 1974; Montgomery and Brace, 1975). This

porosity is measured by an immersion technique which requires that the

voids be interconnected. These pores will play a significant role in

the transport properties. The porosities attributed to the 0.316 and

1.0 aspect ratio pores are increased to accommodate these more equidi-

mensional voids. Finally, the fracture porosity has also been surveyed

under the scanning electron microscope by Simmons and Richter (1976),

Feves et al. (1977), Feves (1977), and Hadley (1976). Hadley's values

were used in investigations by Brace (1977) and Madden (1976). The values

reported by Madden are included in figure A2-3 for comparison. The

two distributions in figure A2-3 are in approximate agreement in the

mid-range of aspect ratios but differ considerably at the extremes.

The total porosity measured with the SEM is too low because of the low

reported values for the more equidimensional voids. At very small

aspect ratios, Hadley's porosity is also much lower than the values

determined with DSA. With the SEM, fractures under approximately

0.03 μm in width cannot be observed due to the conductive coating.

Since a considerable proportion of small aspect ratio cracks may have

correspondingly small widths, Hadley's distribution probably under-estimates the number of these small fractures.

Aspect ratio is the ratio of length to width and so the length distribution needs to be estimated. One possibility is to hold length constant and let width vary according to aspect ratio. However, this distribution results in too large a number of small narrow cracks. A very large number of narrow cracks of length ℓ will be created for the same value of porosity that produces a single spherical pore with the same diameter ℓ (figure A2-4a). The result is a very strong pressure dependence. At very low pressures the calculated values of both permeability and conductivity decrease by many orders of magnitude. Hence, the length must decrease with increasing aspect ratio (figure A2-4b). The width will not then increase as rapidly with increasing aspect ratio. This kind of length-width relationship is observed in the several SEM studies mentioned previously. Dependence is now spread more evenly among all the fractures and pores. The result is a smaller decrease in permeability and conductivity at low pressure.

Once the length distribution has been established to fit conductivity values, the absolute size of the cracks can be altered to match zero pressure permeability. Conductivity is independent of absolute size if the relative sizes stay the same. By equation (A2-5) any increase in $w_i\ell_i$ will be cancelled by the equal increase in $w_j\ell_j$. Permeability is very sensitive to even slight changes in width, which is apparent from equation (A2-3). The result will be a length versus aspect ratio distribution similar to the type shown in figure A2-5.

The final step is to actually close fractures with pressure.

(a)

(b)
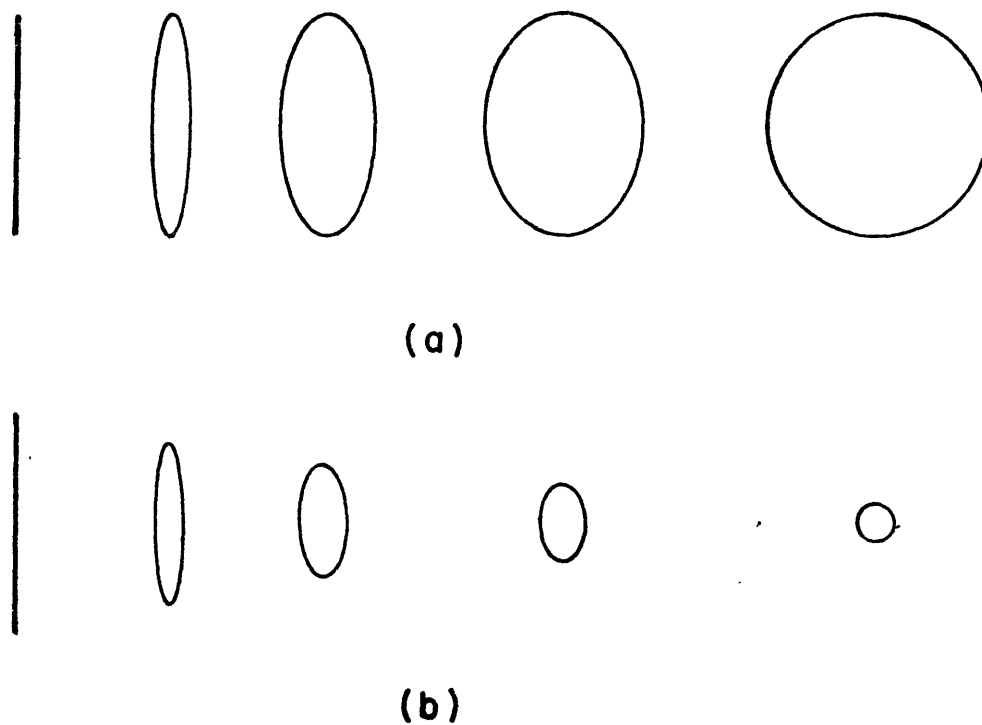
Figure A2-4. Schematic width-length relationships.

(a) Length constant with increasing aspect ratio.

(b) Length decreasing with increasing aspect ratio.

To increase the number or probability of the more spherical voids for a given porosity, the relative sizes must decrease with increasing aspect ratio as in (b). The actual values used are given in Figure A2-5.
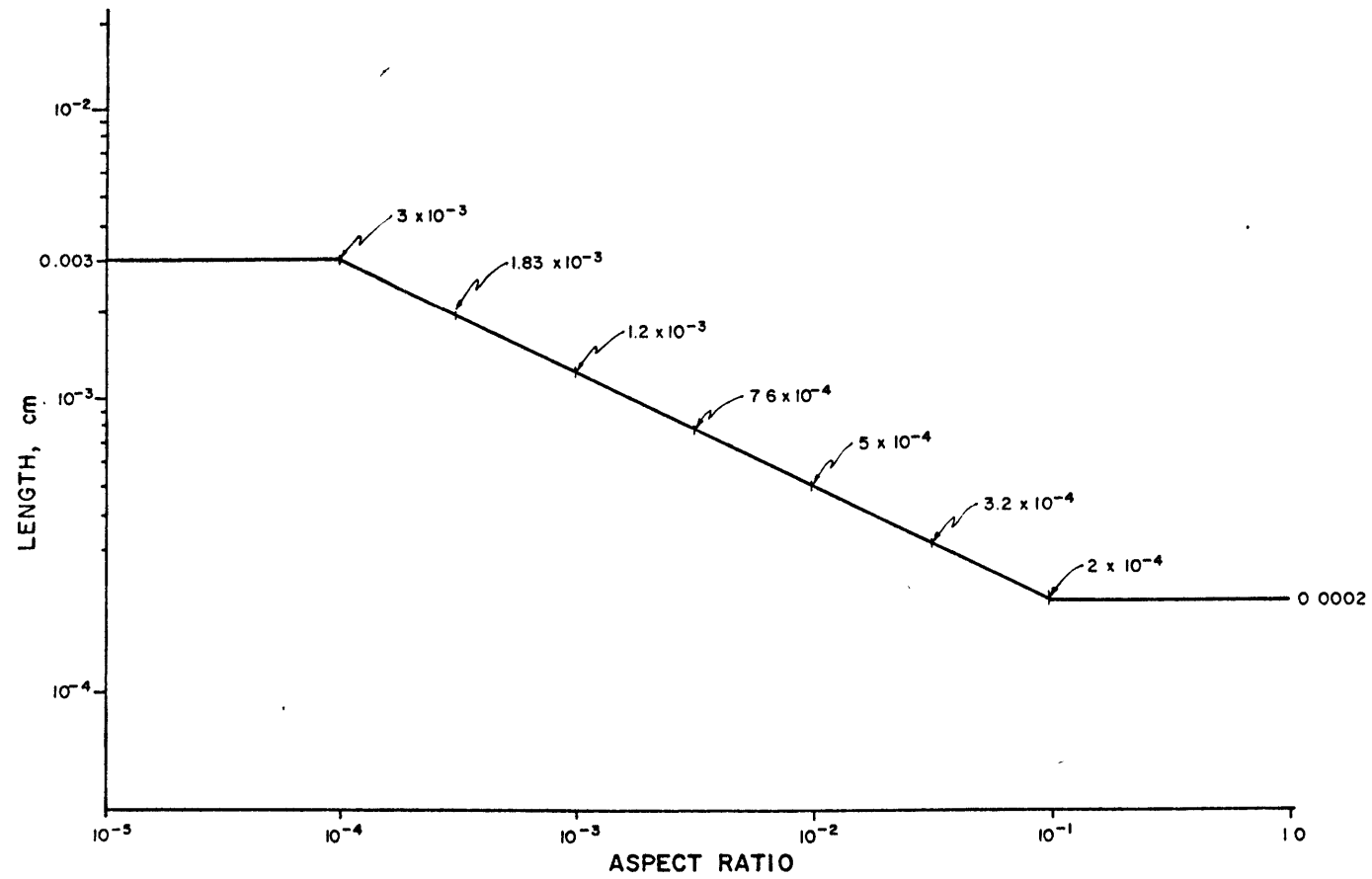
Figure A2-5. Final model length distribution versus aspect ratio.

Although the fractures are closed, they must remain in the system with the same probability. The cracks are still interconnected but have much smaller permeability and conductivity values. The first type of closure mechanism, the type that seems most obvious, is to reduce widths to some small fraction of the initial width. The pressure is increased in logarithmic increments to close the sets of cracks with logarithmically increasing aspect ratios. Since the cracks close linearly with pressure, the result is that the width is first reduced to 1/3 of the original value and then to the final closure value of 1/25 after the next pressure increment. The calculated values are shown in figure 5-15b and are given in Table A2-1. The results are not very satisfactory. The reduction to 1/25 of the former width is a 'best fit' for this type of closure mechanism. Permeability is too strongly affected by confining pressure, but conductivity is not decreased sufficiently. Another closure scheme, type 2, is to make all the closed fractures have the same small constant value of permeability and conductivity. The 'best fit' of this second type of mechanism is also presented in figure 5-15b and in Table A2-1. This type of closure gives a fit to the observed values well within the limits of measurement error. This latter type is characteristic of very inefficient closure, especially for small aspect ratio fractures. The effect is the same as if the fracture closed as much by length as by width. Such inefficient closure would be the case for contorted, crenulated fractures. The two closure types are fundamentally different.

This model is somewhat crude, but some valid interpretations can be drawn. Fracture closure can explain the decrease in permeability

and conductivity. The fractures in Westerly granite are probably rough and irregular as closure is inefficient. Larger pores and voids play a significant role in the flow properties. The geometric mean model needs more thorough testing before more detailed conclusions can be drawn. In the present form, the model is too specific to Westerly granite.

Table A2-1. Geometric mean fracture probability, permeability, and conductivity.

(a) No confining pressure, all cracks open and using the distribution of figures A2-3 and A2-5.

Aspect ratio	Length (cm)	Width (cm)		Por.		Prob.	Cond. $(\Omega m)^{-1}$		Perm. (cm^2)	
α	ℓ_i	w_i	w_i^3	ϕ_i	$\phi_i/w_i\ell_i$	P_i	Y_i	$Y_i^{P_i}$	k_i	$k_i^{P_i}$
10^{-5}	.003	3.0×10^{-8}	2.0×10^{-23}	0	0	0	--	1.0	--	1.0
3.16×10^{-5}	.003	9.5×10^{-8}	8.5×10^{-22}	21.5	7.5	0.064	7.5×10^{-4}	.633	1.7×10^{-19}	6.4×10^{-2}
10^{-4}	.003	3.0×10^{-7}	2.7×10^{-20}	81	9.0	0.076	2.36×10^{-3}	.630	5.3×10^{-18}	4.8×10^{-2}
3.16×10^{-4}	1.9×10^{-3}	5.9×10^{-7}	2.1×10^{-19}	159	14.3	0.121	2.9×10^{-3}	.493	2.6×10^{-17}	9.8×10^{-3}
10^{-3}	1.2×10^{-3}	1.2×10^{-6}	1.7×10^{-18}	265	18.4	0.156	3.8×10^{-3}	.419	1.34×10^{-16}	3.35×10^{-3}
3.16×10^{-3}	7.6×10^{-4}	2.4×10^{-6}	1.4×10^{-17}	222	12.2	0.103	4.8×10^{-3}	.576	7.0×10^{-16}	2.7×10^{-2}
10^{-2}	5.0×10^{-4}	5.0×10^{-6}	1.25×10^{-16}	100	4.0	0.034	6.55×10^{-3}	.843	4.1×10^{-15}	0.325
3.16×10^{-2}	3.2×10^{-4}	1.0×10^{-5}	1.0×10^{-15}	100	3.1	0.026	8.4×10^{-3}	.882	2.1×10^{-14}	0.44
10^{-1}	2.0×10^{-4}	2.0×10^{-5}	8.0×10^{-15}	100	2.5	0.021	1.05×10^{-2}	.908	1.05×10^{-13}	0.53
3.16×10^{-1}	2.0×10^{-4}	6.3×10^{-5}	2.5×10^{-13}	4500	35.7	0.303	3.3×10^{-2}	.356	3.3×10^{-12}	$3.35 \times 10{-4}$
1	2.0×10^{-4}	2.0×10^{-4}	8.0×10^{-12}	4500	11.3	0.096	1.05×10^{-1}	.805	1.05×10^{-10}	0.11
				$\sum$ 118			$\prod$ 9.18×10^{-3}		$\prod$ 7.7×10^{-15}	

Table A2-1 (continued).

(b) Type 1 closure with increasing pressure (see text).

Note: Blank spaces indicate no change from preceding lower pressure values.

				70 BARS CONFINING PRESSURE						
α	ℓ_i	w_i	w_i^3	ϕ_i	$\phi_i/w_i\ell_i$	P_i	Y_i	$Y_i^{P_i}$	k_i	$k_i^{P_i}$
10^{-5}										
3.16×10^{-5}	.003	3.8×10^{-9}	5.5×10^{-26}			0.064	3.0×10^{-5}	.513	1.1×10^{-23}	.034
10^{-4}	.003	1.2×10^{-8}	7.7×10^{-24}			0.076	9.4×10^{-5}	.494	3.4×10^{-22}	.023
3.16×10^{-4}	1.9×10^{-3}	3.9×10^{-7}	5.9×10^{-20}	.159	14.3	0.121	1.9×10^{-3}	.470	7.4×10^{-18}	8.46×10^{-3}
10^{-3}								.419		3.35×10^{-3}
3.16×10^{-3}								.576		2.7×10^{-2}
10^{-2}								.843		.325
3.16×10^{-2}								.882		.44
10^{-1}								.908		.53
3.16×10^{-1}								.356		3.35×10^{-4}
1								.805		.11
								$\prod \overline{5.6 \times 10^{-3}}$		$\prod \overline{1.7 \times 10^{-14}}$

				200 BARS CONFINING PRESSURE						
α	ℓ_i	w_i	w_i^3	ϕ_i	$\phi_i/w_i\ell_i$	P_i	Y_i	Y_i^{Pi}	k_i	k_i^{Pi}
10^{-5}										
3.16×10^{-5}								.513		.034
10^{-4}								.494		.023
3.16×10^{-4}	1.9×10^{-3}	2.4×10^{-8}	1.3×10^{-23}			0.121	1.2×10^{-4}	.334	1.7×10^{-21}	3.1×10^{-3}
10^{-3}	1.2×10^{-3}	8.0×10^{-7}	5.1×10^{-19}			0.156	2.5×10^{-3}	.393	4.0×10^{-17}	2.8×10^{-3}
3.16×10^{-3}								.576		2.7×10^{-2}
10^{-2}								.843		.325
3.16×10^{-2}								.882		.44
10^{-1}								.908		.53
3.16×10^{-1}								.356		3.35×10^{-4}
1								.805		.11
								$\prod\ 3.7\times10^{-3}$		$\prod\ 5.1\times10^{-6}$

700 BARS CONFINING PRESSURE

α	ℓ_i	w_i	w_i^3	ϕ_i	$\phi_i/w_i\ell_i$	P_i	Y_i	$Y_i^{P_i}$	k_i	$k_i^{P_i}$
10^{-5}										
3.16×10^{-5}								.513		.034
10^{-4}								.494		.023
3.16×10^{-4}								.334		3.1×10^{-3}
10^{-3}	1.2×10^{-3}	4.8×10^{-8}	1.1×10^{-22}			.156	1.5×10^{-4}	.253	8.6×10^{-21}	7.4×10^{-4}
3.16×10^{-3}	7.6×10^{-4}	1.6×10^{-6}	4.1×10^{-18}			.103	3.2×10^{-3}	.553	2.1×10^{-16}	2.4×10^{-2}
10^{-2}								.843		.325
3.16×10^{-2}								.882		.44
10^{-1}								.908		.53
3.16×10^{-1}								.356		3.35×10^{-4}
1								.805		.11
								$\prod\ 2.3\times10^{-3}$		$\prod\ 1.2\times10^{-16}$

				2000 BARS CONFINING PRESSURE						
α	ℓ_i	w_i	w_i^3	ϕ_i	$\phi_i/w_i\ell_i$	P_i	Y_i	$Y_i^{P_i}$	k_i	$k_i^{P_i}$
10^{-5}										
3.16×10^{-5}								.513		.034
10^{-4}								.494		.023
3.16×10^{-4}								.334		3.1×10^{-3}
10^{-3}								.253		7.4×10^{-4}
3.16×10^{-3}	7.6×10^{-4}	9.6×10^{-8}	8.8×10^{-22}			.103	1.9×10^{-4}	.414	4.5×10^{-20}	.0102
10^{-2}	5.0×10^{-4}	3.3×10^{-6}	3.7×10^{-17}			.034	4.4×10^{-3}	.831	1.2×10^{-15}	.312
3.16×10^{-2}								.882		.44
10^{-1}								.908		.53
3.16×10^{-1}								.356		3.35×10^{-4}
1								.805		.11
								$\prod\ 1.7\times10^{-3}$		$\prod\ 4.9\times10^{-17}$

Table A2-1 (continued).

(c) Type 2 closure with increasing pressure (see text).

Note: Blank spaces indicate no change from preceding lower pressure values.

70 BARS CONFINING PRESSURE										
α	ℓ_i	w_i	w_i^3	ϕ_i	$\phi_i/w_i\ell_i$	P_i	Y_i	$Y_i^{P_i}$	k_i	$k_i^{P_i}$
						.140	1×10^{-5}	.20	2×10^{-20}	1.75×10^{-3}
3.16×10^{-5}										
10^{-4}										
3.16×10^{-4}	1.9×10^{-3}	3.9×10^{-7}	5.9×10^{-20}	.159	14.3	.121	1.94×10^{-3}	.470	7.4×10^{-18}	8.46×10^{-3}
10^{-3}								.419		2.35×10^{-3}
3.16×10^{-3}								.576		2.7×10^{-2}
10^{-2}								.843		.325
3.16×10^{-2}								.882		.44
10^{-1}								.908		.53
3.16×10^{-1}								.356		3.35×10^{-4}
1								.805		.11
								$\prod\ 4.38\times10^{-3}$		$\prod\ 3.74\times10^{-15}$

(c) Type 2 (continued)

					200 BARS CONFINING PRESSURE					
α	ℓ_i	w_i	w_i^3	ϕ_i	$\phi_i/w_i\ell_i$	P_i	Y_i	$Y_i^{P_i}$	k_i	$k_i^{P_i}$
10^{-5}						.261	1×10^{-5}	4.96×10^{-2}	2×10^{-20}	7.22×10^{-6}
3.16×10^{-5}										
10^{-4}										
3.16×10^{-4}										
10^{-3}	1.2×10^{-3}	8.0×10^{-7}	5.1×10^{-19}	265	18.4	0.156	2.5×10^{-3}	.393	4.0×10^{-17}	2.8×10^{-3}
3.16×10^{-3}								.576		2.7×10^{-2}
10^{-2}								.843		.325
3.16×10^{-2}								.882		.44
10^{-1}								.908		.53
3.16×10^{-1}								.356		3.35×10^{-4}
1								.805		.11
								$\prod$ 2.17×10^{-3}		$\prod$ 1.51×10^{-15}

(c) Type 2 (continued)

α	ℓ_i	w_i	w_i^3	ϕ_i	$\phi_i/w_i\ell_i$	P_i	Y_i	$Y_i^{P_i}$	k_i	$k_i^{P_i}$
						.417	1×10^{-5}	8.2×10^{-3}	2×10^{-20}	6.1×10^{-9}
3.16×10^{-5}										
10^{-4}										
3.16×10^{-4}										
10^{-3}										
3.16×10^{-3}	7.6×10^{-4}	1.6×10^{-6}	4.1×10^{-18}	222	12.2	.103	3.2×10^{-3}	.553	2.06×10^{-16}	2.42×10^{-2}
10^{-2}								.843		.325
3.16×10^{-2}								.882		.44
10^{-1}								.908		.53
3.16×10^{-1}								.356		3.35×10^{-4}
1								.805		.11
								$\prod$ 8.77×10^{-4}		$\prod$ 4.12×10^{-16}

2000 BARS CONFINING PRESSURE

α	ℓ_i	w_i	w_i^3	ϕ_i	$\phi_i/w_i\ell_i$	P_i	Y_i	$Y_i^{P_i}$	k_i	$k_i^{P_i}$
						.520	1×10^{-5}	2.5×10^{-3}	2×10^{-20}	4.0×10^{-11}
3.16×10^{-5}										
10^{-4}										
3.16×10^{-4}										
10^{-3}										
3.16×10^{-3}										
10^{-2}	5.0×10^{-4}	3.33×10^{-6}	3.7×10^{-17}	100	4.0	.034	4.4×10^{-3}	.831	1.22×10^{-15}	0.312
3.16×10^{-2}								.882		0.44
10^{-1}								.908		$\cdot$0.53
3.16×10^{-1}								.356		3.35×10^{-4}
1								.805		0.11
								$\prod\ 4.77\times10^{-4}$		$\prod\ 1.07\times10^{-16}$

267

REFERENCES

Abey, A.E., A model for predicting the hydrostatic loading and unloading relationship of porous materials containing various amounts of fluid, J. Geophys. Res., 82, 5418-5422, 1977.

Austin, C.F. and J.K. Pringle, Geologic investigations at the Coso Thermal Area, Naval Weapons Center, China Lake, California, TP 4878, 40 pp., 1970.

Austin, C.F., W.H. Austin, Jr., and G.W. Leonard, Geothermal science and technology - a national program, Naval Weapons Center, China Lake, California, TP 45-029-72, 95 pp., 1971.

Austin, C., personal communication, Naval Weapons Center, China Lake, California, 1977.

Bailey, R.A., G.B. Dalrymple, and M.A. Lanphere, Volcanism, structure, and geochronology of Long Valley caldera, Mono County, California, J. Geophys. Res., 81, 725-744, 1976.

Barnes, H.L. and G.K. Czamanske, Solubilities and transport of ore minerals, in Geochemistry of Hydrothermal Ore Deposits, edited by H.L. Barnes, Holt, Rinehart, and Winston, New York, 334-381, 1967.

Batzle, M.L. and G. Simmons, Microfractures in rocks from two geothermal areas, Earth Planet. Sci. Lett., 30, 71-93, 1976.

Batzle, M.L. and G. Simmons, Geothermal systems: rocks, fluids, fractures, in The Earth's Crust: Its Nature and Physical Properties, Geophys. Monogr. Ser., vol. 20, edited by J.G. Heacock, AGU, Washington, DC, 233-242, 1977.

Bear, J., Dynamics of Fluids in Porous Media, American Elsevier Pub-

lishing Co., Inc., New York, 764 pp., 1972.

Belk, J.A., The x-ray mode and basic microanalysis, in Quantitative Scanning Electron Microscopy, edited by D.B. Holt, M.D. Muir, P.R. Grant, and I.M. Boswarva, Academic Press, London, 389-402, 1974.

Biehler, S., R.L. Kovach, and C.R. Allen, Geophysical framework of northern end of Gulf of California structural province, in Marine Geology of the Gulf of California, edited by T.H. Van Andel and G.G. Shor, Jr., Am. Assoc. Pet. Geol. Mem. 3, 126-143, 1964.

Biehler, S., Gravity studies in the Imperial Valley, in Rex, R.W. et al., Cooperative geological-geophysical-geochemical investigations of geothermal resources in the Imperial Valley area of California: Final Report (FY 1971), Contr. No. 14-06-300-2194, U.S. Bureau of Reclamation, 29-42, 1971.

Bird, D.K., Geology and geochemistry of the Dunes hydrothermal system, Imperial Valley of California, Masters thesis, University of California at Riverside, IGPP-UCR-75-2, 123 pp., 1975.

Black, W.E., J.S. Nelson, and J. Combs, Thermal and electrical resistivity investigations of the Dunes geothermal anomaly, Imperial Valley, California, (ABS), Trans. Am. Geophys. Union, 54, 1214, 1973.

Blackwell, D.D. and C.-G. Baag, Heat flow in a 'blind' geothermal area near Marysville, Montana, Geophysics, 38, 941-956, 1973.

Blackwell, D.D., M.J. Holdaway, P. Morgan, D. Petefish, T. Rape, J.L. Steele, D. Thorstenson, and A.F. Waibel, Results and analysis of exploration and deep drilling at Marysville geothermal area, NSF-RANN Final Technical Report #23111-01410, E1-E116, 1975.

Blackwell, D.D. and P. Morgan, Geological and geophysical exploration

of the Marysville geothermal area, Montana, USA, in Proceedings, Second United Nations Symposium on the Development and Use of Geothermal Resources, 2, 895-902, 1976.

Blackwell, D.D., Marysville geothermal project workshop, in Geothermal: State of the Art, Geothermal Resources Council, Transactions, 21-22, 1977.

Brace, W.F., Some new measurements of linear compressibility of rocks, J. Geophys. Res., 70, 391-398, 1965.

Brace, W.F., A.S. Orange, and T.R. Madden, The effect of pressure on the electrical resistivity of water-saturated crystalline rocks, J. Geophys. Res., 70, 5669-5678, 1965.

Brace, W.F., J.B. Walsh, and W.T. Frangos, Permeability of granite under high pressure, J. Geophys. Res., 73, 2225-2236, 1968.

Brace, W.F., E. Silver, K. Hadley, and C. Goetze, Cracks and pores: a closer look, Science, 178, 162-163, 1972.

Brace, W.F., Permeability from resistivity and pore shape, J. Geophys. Res., 82, 3343-3349, 1977.

Browne, P.R.L. and W.A. Elders, Hydrothermal alteration of diabase, Heber geothermal field, Imperial Valley, California, Geol. Soc. Am., Abstracts with Programs, 8, 793, 1976.

Bruce, J., personal communication, Battelle Northwest Laboratories, Richland, Washington, 1977.

Bryant, N.L. and W.T. Parry, Hydrothermal alteration at Roosevelt Hot Springs KGRA-DDH 1976-1, University of Utah - ERDA, TR 77-5, 87 pp., 1977.

Chilingarian, G.V. and K.H. Wolf (editors), Compaction of Coarse-

Grained Sediments, I, Elsevier Scientific Publishing Co., Amster-
dam, 552 pp., 1975.

Combs, J., Heat flow and geothermal resource estimates for the Imperial
Valley, in Rex, R.W. et al., Cooperative geological-geophysical-
geochemical investigations of geothermal resources in the Imperial
Valley area of California: Final Report (FY 1971), Contr. No.
14-06-300-2194, U.S. Bureau of Reclamation, 5-28, 1971.

Combs, J., Thermal studies, in Rex, R.W. et al., Cooperative investi-
gation of geothermal resources in the Imperial Valley area and
their potential value for desalting water and other purposes:
Institute of Geophysics and Planetary Physics, University of
California, Riverside, California, no. 72-33, B1-B23, 1972.

Combs, J., Heat flow determinations and implied thermal regime of the
Coso geothermal area, California, (ABS), EOS, Trans. Am. Geophys.
Union, 57, 1009, 1976.

Combs, J. and Y. Rotstein, Microearthquake studies at the Coso geother-
mal area, China Lake, California, in Proceedings, Second United
Nations Symposium on the Development and Use of Geothermal Re-
sources, 2, 909-916, 1976.

Combs, J. and D. Hadley, Microearthquake investigation of the Mesa
geothermal anomaly, Imperial Valley, California, Geophysics, 42,
17-33, 1977.

Combs, J. and D. Jarzabek, Seismic evidence for a deep heat source
associated with the Coso geothermal area, California, in Geother-
mal: State of the Art, Geothermal Resources Council, Transactions,
41-43, 1977.

Cooper, H., personal communication, Massachusetts Institute of Technology, Cambridge, Massachusetts, 1976.

Cooper, H. and G. Simmons, The effect of cracks on the thermal expansion of rocks, Earth Planet. Sci. Lett., 36, 404-412, 1977.

Coplen, T.B., Cooperative geochemical investigation of geothermal resources in the Imperial Valley and Yuma areas: University of California at Riverside, Institute of Geophysics and Planetary Physics, report no. 73-84, 22 pp., 1972.

Crebs, T.J. and K.L. Cook, Gravity and ground magnetic surveys of the central Mineral Mountains, Utah, University of Utah - NSF Final Report, volume 6, contract GI-43741, 129 pp., 1976.

Crosby, G.W., Nomographic solution for preliminary economic evaluation by geothermal prospects, in Geothermal: State of the Art, Geothermal Resources Council, Transactions, 69-71, 1977.

Crosthwaite, E.G., H.R. Covington, and S. Kluender, Raft River geothermal - intermediate hole no. 3, unpublished stratigraphic section, U.S. Geological Survey, 1974.

Domenico, S.N., Elastic properties of unconsolidated porous sand reservoirs, Geophysics, 42, 1339-1368, 1977.

Duffield, W.A., Late Cenozoic ring faulting and volcanism in the Coso Range area of California, Geology, 3, 335-338, 1975.

Dupuy, L.W., Bucket-drilling the Coso mercury deposit Inyo County, California, U.S. Bureau of Mines Report of Investigation #4201, 45 pp., 1948.

Elders, W.A., R.W. Rex, T. Meidav, P.T. Robinson, and S. Biehler, Crustal spreading in southern California, Science, 178, 15-24, 1972.

Elders, W.A. and D.K. Bird, Investigations of the Dunes geothermal
     anomaly, Imperial Valley, California, II. Petrological studies,
     presented at the International Symposium on Water-Rock Interac-
     tion of the International Union of Geochemistry and Cosmochem-
     istry, Prague, 14 pp., 1974.

Elders, W.A., Petrology as a practical tool in geothermal studies, in
     Geothermal: State of the Art, Geothermal Resources Council,
     Transactions, 85-87, 1977.

Evans, S.H., Jr. and W.P. Nash, Low temperature rhyolites from the Roose-
     velt geothermal area, Utah, (ABS), Geol. Soc. Am., Astracts with
     Programs, 7, 1070, 1975.

Facca, G. and F. Tonani, The self-sealing geothermal field, Bull. Vol-
     canol., 30, 271-273, 1967.

Feves, M. and G. Simmons, Effects of stress on cracks in Westerly
     granite, Bull. Seism. Soc. Am., 66, 1755-1765, 1976.

Feves, M., G. Simmons, and R. Siegfried, Microcracks in crustal igneous
     rocks: physical properties, in The Earth's Crust: Its Nature and
     Physical Properties, Geophys. Monogr. Ser., vol. 20, edited by
     J.G. Heacock, AGU, Washington, DC, 95-118, 1977.

Feves, M.L., Characterization of stress-induced cracks in rocks,
     PhD thesis, M.I.T., 123 pp., 1977.

Fournier, R.O., D.E. White, and A.H. Truesdell, Convective heat flow
     in Yellowstone National Park, in Proceedings, Second United
     Nations Symposium on the Development and Use of Geothermal Re-
     sources, 1, 731-739, 1976.

Furgerson, R., Resistivity profiling in the Imperial Valley geo-

thermal area, California, in Rex, R.W. et al., Cooperative inves-
tigation of geothermal resources in the Imperial Valley area and
their potential value for desalting of water and other purposes:
Institute of Geophysics and Planetary Physics, University of
California, Riverside, California, no. 72-33, section J, 1972.

Furgerson, R.B., Progress report on electrical resistivity studies,
Coso geothermal area, Inyo County, California, Naval Weapons Cen-
ter, China Lake, California, TP 5497, 66 pp., 1973.

Gale, J.E., A numerical, field, and laboratory study of flow in rocks
with deformable fractures, PhD thesis, University of California,
Berkeley, 225 pp., 1975.

Garfunkel, Z., Tectonics of the Salton Trough, preliminary results,
in Rex, R.W. et al., Cooperative geological-geophysical-geochemi-
cal investigations of geothermal resources in the Imperial Valley
area of California: Final Report (FY 1971), Contr. no. 14-06-
300-2194, U.S. Bureau of Reclamation, 129-138, 1971.

Garfunkel, Z., The structure of the Salton Trough in southern Califor-
nia, in Rex, R.W. et al., Cooperative investigation of geothermal
resources in the Imperial Valley area and their potential value
for desalting of water and other purposes: Institute of Geophysics
and Planetary Physics, University of California, Riverside, Califor-
nia, no. 72-33, section I, 1972.

Grindley, G.W. and P.R.L. Browne, Structural and hydrological factors
controlling the permeabilities of some hot-water geothermal
fields, in Proceedings, Second United Nations Symposium of the
Development and Use of Geothermal Resources, 1, 377-386, 1976.

Hadley, K., Comparison of calculated and observed crack densities and seismic velocities in Westerly granite, J. Geophys. Res., 81, 3484-3494, 1976.

Hamilton, W., Origin of the Gulf of California, Bull. Geol. Soc. Am., 72, 1307-1318, 1961.

Healy, J. and M.P. Hochstein, Horizontal flow in hydrothermal systems, J. Hydrology, 12, 71-82, 1973.

Helgeson, H.C., Geologic and thermodynamic characteristics of the Salton Sea geothermal system, Am. J. Sci., 266, 129-166, 1968.

Hoagland, J.R., Applications of solute equilibrium models to the study of geothermal reservoirs, in Geothermal: State of the Art, Geothermal Resources Council, Transactions, 143-145, 1977.

Hubbert, M.K., Darcy's law and the field equations of the flow of underground fluids, Petroleum Transactions, AIME, 207, 222-239, 1956.

Hyde, J., personal communication, University of Utah, Salt Lake City, Utah, 1978.

Jackson, D.B., J.E. O'Donnell, and D.I. Gregory, Schlumberger soundings, audio-magnetotelluric soundings and telluric mapping in and around the Coso Range, California, U.S. Geological Survey Open File Report 77-120, 9 pp. plus appendix, 1977.

Jennings, C.W., Geologic map of California, Death Valley sheet, Cal. State Dept. of Natural Resources, 1958.

Jennings, C.W., J.L. Burnett, and B.W. Troxel, Geologic map of California, Trona sheet, Cal. State Dept. of Natural Resources, 1962.

Kasameyer, P., L. Thorson, and C. McKee, Modeling thermal and flow

fronts for arbitrary well arrays, in Geothermal: State of the Art, Geothermal Resources Council, Transactions, 163-165, 1977.

Keller, G.V. and F.C. Frischknecht, Electrical Methods in Geophysical Prospecting, Pergamon Press, Oxford, 519 pp., 1966.

Keller, G.V., Electrical prospecting for oil, Quarterly of the Colorado School of Mines, 63, 268 pp., 1968.

Kendall, C., Petrology and stable isotope geochemistry of three wells in the Buttes area of the Salton Sea, geothermal field, Imperial Valley, California, USA, UCR/IGPP report 76/17, 211 pp., 1976.

Kettenacker, W.C., Two-dimensional simulation of the Raft River geothermal reservoir and wells, Idaho National Engineering Laboratory, report no. TREE-1085, 41 pp. plus appendices, 1977.

Koenig, J.B., S.J. Gawarecki, and C.F. Austin, Remote sensing survey of the Coso geothermal area, Inyo County, California, Naval Weapons Center, China Lake, California, TP 5233, 32 pp., 1972.

Kunze, J.F., L.G. Miller, and J.F. Whitbeck, Moderate temperature utilization project in the Raft River Valley, in Proceedings, Second United Nations Symposium on the Development and Use of Geothermal Resources, 3, 2021-2030, 1976.

Kunze, J.F., Idaho geothermal development projects annual project for 1976, Idaho National Engineering Laboratory, 38 pp., 1977.

Ladd, C.C., Strength parameters and stress-strain behavior of saturated clays, M.I.T. Special Summer Program 1.34S, Soft Soil Construction, Research Report R71-23, Soils Publication 278, 1971.

Ladd, C.C., Estimating settlements of structures supported on cohesive soils, paper presented April 9-10, 1973, Metropolitan Section,

Am. Soc. Civil Engineers, 99 pp., 1973.

Lambe, T.W. and R.V. Whitman, Soil Mechanics, John Wiley and Sons, Inc., New York, 553 pp., 1969.

Lambert, S., Stable isotope studies of some active hydrothermal systems, PhD thesis, California Institute of Technology, 362 pp., 1976.

Lanphere, M.A., G.B. Dalrymple, and R.L. Smith, K-Ar ages of Pleistocene rhyolitic volcanism in the Coso Mountains, California, Geology, 3, 339-341, 1975.

Lee, K.L. and I. Farhoomand, Compressibility and crushing of granular soil in anisotropic triaxial compression, Canadian Geotech. J., 4, 68-86, 1967.

Low, P.F., Viscosity of water in clay systems, in Clays and Clay Minerals, Proceedings of the Eighth National Conference on Clays and Clay Minerals, 170-182, 1959.

McNitt, J.R., The role of geology and hydrology in geothermal exploration, in Geothermal Energy: Review of Research and Development, edited by H.C.H. Armstead, UNESCO, Paris, 33-40, 1973.

McSpadden, W.R. and others, The Marysville, Montana Geothermal Project Final Report, NSF-RANN Final Technical Report #23111-01410, 1975.

Madden, T.R., Random networks and mixing laws, Geophysics, 41, 1104-1125, 1976.

Madden, T., R. McEuen, G. Olhoeft, and W. Sill, Rock properties team report, in Workshop on Electrical Methods in Geothermal Exploration, University of Utah Geothermal Workshop (ERDA contract 14-08-0001-G-359), 17-35, 1977.

Mann, L., personal communication, Chevron Resources Corp., San Fran-

cisco, California, 1977.

Matthews, C.S. and D.G. Russell, Pressure Buildup and Flow Tests in Wells, Monograph Volume 1, H.L. Doherty Series, Society of Petroleum Engineers, Dallas, Texas, 1967.

Maxwell, J.C., Experiments on compaction and cementation of sand, in Rock Deformation (A Symposium), edited by D. Griggs and J. Handin, Geol. Soc. Am. Mem. 79, 105-132, 1960.

Meidav, T. and R. Furgerson, Electrical resistivity for geothermal exploration in the Imperial Valley, in Rex, R.W. et al., Cooperative geological-geophysical- geochemical investigations of geothermal resources in the Imperial Valley area of California: Final Report (FY 1971), Contr. No. 14-06-300-2194, U.S. Bureau of Reclamation, 43-88, 1971.

Mercado, G.S., Chemical changes in geothermal well M-20, Cerro Prieto, Mexico, Bull. Geol. Soc. Am., 80, 2623-2630, 1969.

Miller, R.L., Corrosion engineering in the utilization of the Raft River geothermal resource, Aerojet Nuclear Company report no. ANCR-1342, 1976.

Montgomery, C.W. and W.F. Brace, Micropores in plagioclase, Contrib. Mineral. Petrol., 52, 17-28, 1975.

Morlier, P., Description de l'etat de fissuration d'une roche a partir d'essais non-destructifs simples, Rock Mech., 3, 125-138, 1971.

Moskowitz, B. and D. Norton, A preliminary analysis of intrinsic fluid and rock resistivity in active hydrothermal systems, J. Geophys. Res., 82, 5787-5795, 1977.

Mudie, J., in Gulf of California Rift System and Its Implications for

the Tectonics of western North America, W.A. Elders and S. Biehler, convenors, Geology, 3, 85-87, 1975.

Muffler, L.J.P. and D.E. White, Active metamorphism of upper Cenozoic sediments in the Salton Sea geothermal field and the Salton Trough, southeastern California, Bull. Geol. Soc. Am., 80, 157-182, 1969.

Muffler, L.J.P., Summary of Section I, present status of resources development, Proceedings, Second United Nations Symposium on the Development and Use of Geothermal Resources, 1, xxxiii-xliv, 1976.

Narasimhan, T.N. and P.A. Witherspoon, Reservoir evaluation tests on RRGE 1 and RRGE 2, Raft River geothermal project, Idaho, Lawrence Berkeley Laboratory report no. LBL-5958, 50 pp., 1977.

Nash, W.P., Petrology of the Quaternary volcanics of the Roosevelt KGRA, and adjoining area, Utah, University of Utah - NSF Final Report, volume 1, contract GI-43741, 99 pp., 1976.

Nathenson, M. and L.J.P. Muffler, Geothermal resources in hydrothermal convection systems and conduction-dominated areas, in Assessment of Geothermal Resources of the United States - 1975, edited by D.E. White and D.L. Williams, U.S.G.S. Circular 726, 104-121, 1975.

Norton, D., Fluid circulation in the earth's crust, in Exploration Criteria for Low Permeability Geothermal Resources, ERDA, Progress report no. COO-2763-1, 103-130, 1977.

Norton, D. and R. Knapp, Transport phenomena in hydrothermal systems: the nature of porosity, Am. J. Sci., 277, 913-936, 1977.

Norton, D. and J. Knight, Transport phenomena in hydrothermal systems:

cooling plutons, Am. J. Sci., 277, 937-981, 1977.

O'Connell, R.J. and B. Budiansky, Seismic velocities in dry and satu-
rated cracked solids, J. Geophys. Res., 79, 5412-5426, 1976.

Palmer, T.D., J.H. Howard, and D.P. Lande, Geothermal development of
the Salton Trough, California and Mexico, Lawrence Livermore Lab-
oratory report no. UCRL-51775, 45 pp., 1975.

Papadopulos, S.S., R.H. Wallace, Jr., J.B. Wesselman, and R.E. Taylor,
Assessment of onshore geopressured-geothermal resources in the
northern Gulf of Mexico basin, in Assessment of Geothermal Re-
sources of the United States - 1975, edited by D.E. White and
D.L. Williams, U.S.G.S. Circular 726, 125-140, 1975.

Parry, W.T., N.L. Benson, and C.D. Miller, Geochemistry and hydrother-
mal alteration at selected Utah hot springs, University of Utah -
NSF Final Report, voluem 3 (revised), contract GI-43741, 131 pp.,
1976.

Parsons, R.W., Permeability of idealized fractured rock, Soc. Pet.
Engineers J., 6, 126-136, 1966.

Peeples, W.J., Magnetotelluric sounding - Marysville, Montana, NSF-
RANN Final Technical Report #23111-01410, E117-E148, 1975.

Pratt, H.R., H.S. Swolfs, R. Lingle, and R.R. Nielsen, In situ and
laboratory measurements of velocity and permeability, in The
Earth's Crust: Its Nature and Physical Properties, Geophys.
Monogr. Ser., vol. 20, edited by J.G. Heacock, AGU, Washington,
DC, 215-231, 1977.

Raghavan, R. and F.G. Miller, Mathematical analysis of sand compaction,
in Compaction of Coarse-Grained Sediments, I, edited by G.V.

Chilingarian and K.H. Wolf, Elsevier Scientific Publishing Co., Amsterdam, 403-524, 1975.

Randall, W., Percent volume of sand bodies in the Imperial Valley (Preliminary Report), in Rex, R.W. et al., Cooperative geological-geophysical-geochemical investigations of geothermal resources in the Imperial Valley area of California: Final Report (FY 1971), Contr. No. 14-06-300-2194, U.S. Bureau of Reclamation, 119-128, 1971.

Reed, M., A preliminary report on the geology and geochemistry of the Cerro Prieto geothermal field, in Rex, R.W. et al., Cooperative investigation of geothermal resources in the Imperial Valley area and their potential value for desalting water and other purposes: Institute of Geophysics and Planetary Physics, University of California, Riverside, California, no. 72-33, G1-G40, 1972.

Reed, S.J.B., Electron Microprobe Analysis, Cambridge University Press, Cambridge, 400 pp., 1975.

Renner, J.L., D.E. White, and D.L. Williams, Hydrothermal convection systems, in Assessment of Geothermal Resources of the United States - 1975, edited by D.E. White and D.L. Williams, U.S.G.S. Circular 726, 5-57, 1975.

Rex, R.W., The waters of the Imperial Valley, in Rex, R.W. et al., Cooperative geological-geophysical-geochemical investigations of geothermal resources in the Imperial Valley area of California: Final Report (FY 1971), Contr. No. 14-06-300-2194, U.S. Bureau of Reclamation, 89-106, 1971.

Richter, D. and G. Simmons, Thermal expansion behavior of igneous rocks,

Int. J. Rock Mech. Min. Sci., 11, 403-411, 1974.

Richter, D. and G. Simmons, Microcracks in crustal igneous rocks: microscopy, in The Earth's Crust: Its Nature and Physical Properties, Geophys. Monogr. Ser., vol. 20, edited by J.G. Heacock, AGU, Washington, DC, 149-180, 1977.

Rieke, H.H., III, and G.V. Chilingarian, Compaction of Argillaceous Sediments, Elsevier Scientific Publishing Company, Amsterdam, 424 pp., 1974.

Ross, C.P. and R.G. Yates, The Coso quicksilver district Inyo County, California, U.S. Geological Survey Bulletin 936-Q, 395-416, 1943.

Schroeder, R.C., Reservoir engineering report for the Magma-SDG&E geothermal experimental site near the Salton Sea, California, Lawrence Livermore Laboratory, report no. UCRL-52094, 62 pp., 1976.

Sharp, J.C. and Y.N.T. Maini, Fundamental considerations on the hydraulic characteristics of joints in rocks, in Symposium Proceedings: Percolation through Fissured Rock, Stuttgart, 1972, section T1-F, 15 pp., 1972.

Siegfried, R.W., II, Differential strain analysis: application to shock-induced microfractures, PhD thesis, M.I.T., 158 pp., 1977.

Sigvaldason, G.E., Geochemical methods in geothermal exploration, in Geothermal Energy: Review of Research and Development, edited by H.C.H. Armstead, UNESCO, Paris, 49-59, 1973.

Simmons, G., R.W. Siegfried, III, and M. Feves, Differential strain analysis: a new method for examining cracks in rocks, J. Geophys. Res., 79, 4383-4385, 1974.

Simmons, G., R. Siegfried, and D. Richter, Characteristics of microcracks in lunar samples, Proc. Sixth Lunar Sci. Conf., 3, 3227-3254, 1975.

Simmons, G. and D. Richter, Microcracks in rocks, in The Physics and Chemistry of Minerals and Rocks, edited by R.G.J. Strens, Wiley-Interscience, New York, 105-137, 1976.

Sipple, R.F., Sandstone petrology, evidence from luminescence petrography, J. Sed. Pet., 38, 530-554, 1968.

Smith, J.V. and R.C. Stenstrom, Electron-excited luminescence as a petrologic tool, J. Geol., 73, 627-635, 1965.

Smith, R.L. and H.R. Shaw, Igneous-related geothermal systems, in Assessment of Geothermal Resources of the United States - 1975, edited by D.E. White and D.L. Williams, U.S.G.S. Circular 726, 58-83, 1975.

Snow, D.T., Rock fracture spacings, openings, and porosities, J. Soil Mech. Found. Div. Amer. Soc. Civil Eng., 94 (SMI), 73-91, 1968.

Sommer, S.E., Cathodoluminescence of carbonates, 2. Geological applications, Chem. Geol., 9, 275-284, 1972.

Spencer, S.G. and W.W. Hickman, Environmental program, in Geothermal R&D Project Report for Period July 1, 1976 to September 30, 1976, Idaho National Engineering Laboratory, report no. TREE-1030, 15-17, 1976.

Sprunt, E.S. and W.F. Brace, Direct observation of microcavities in crystalline rocks, Int. J. Rock Mech. Min. Sci. & Geomech. Abstr., 11, 139-150, 1974.

Stanley, W.D., J.E. Boehl, F.Z. Bostick, and H.W. Smith, Geothermal

significance of magnetotelluric sounding in the eastern Snake
River Plain - Yellowstone region, J. Geophys. Res., 82, 2501-
2514, 1977.

Stoker, R.C., D. Goldman, and S.J. Prestwich, Reservoir engineering,
in Geothermal R&D Project Report for Period July 1, 1976 to Sep-
tember 30, 1976, Idaho National Engineering Laboratory, report
no. TREE-1030, 3-14, 1976.

Stoker, R.C., D. Goldman, and J.F. Kunze, Deducing production zones
from well logs, in Geothermal: State of the Art, Geothermal
Resources Council, Transactions, 279-280, 1977.

Todd, T., H. Wang, W.S. Baldridge, and G. Simmons, Elastic properties
of Apollo 14 and 15 rocks, Proc. Third Lunar Sci. Conf., 3, 2577-
2586, 1972.

Toksöz, M.N., C.H. Cheng, and A. Timur, Velocities of seismic waves in
porous rocks, Geophysics, 41, 621-645, 1976.

Tsvetkova, M.A., Influence of mineralogic composition of sandy rocks
on filtration capacity and oil production, Tr. Inst. Nefti, Acad.
Nauk, S.S.S.R., 3, 1954.

Van de Kamp, P.C., Holocene continental sedimentation in the Salton
Basin, California, Bull. Geol. Soc. Am., 84, 827-848, 1973.

Walsh, J.B., The effect of cracks on the compressibility of rocks,
J. Geophys. Res., 70, 381-389, 1965.

Ward, S.H. and W.R. Sill, Dipole-dipole resistivity delineation of
the near-surface zone at the Roosevelt Hot Springs area,
University of Utah - ERDA, volume 76-1, contract EY-76-S-07-1601,
5 pp., 1976.

Ward, S.H., W.R. Sill, R.B. Smith, K.L. Cook, and W.J. Peeples, Geophysics and photogeology at Roosevelt Hot Springs KGRA, Utah, (ABS), Conference on Exploration for the Geothermal Reservoir, May 4-5, 1976.

Warren, J.E. and H.S. Price, Flow in heterogeneous porous media, Soc. Pet. Engineers J., 1, 153-169, 1961.

Weaver, C.E. and K.C. Beck, Clay water diagenesis during burial: how mud becomes gneiss, Geol. Soc. Am. Spec. Paper 134, 78 pp., 1971.

White, D.E., Hydrology, activity, and heat flow of the Steamboat Springs thermal system, Washoe County, Nevada, U.S. Geological Survey Prof. Paper 458-C, 109 pp., 1968.

White, D.E., L.J.P. Muffler, and A.H. Truesdell, Vapor-dominated hydrothermal systems compared with hot-water systems, Econ. Geol., 66, 75-97, 1971.

White, D.E., R.O. Fournier, L.J.P. Muffler, and A.H. Truesdell, Physical results of research drilling in thermal areas of Yellowstone National Park, Wyoming, U.S. Geological Survey Prof. Paper 892, 70 pp., 1975.

Williams, E., The surface conduction contribution to pore fluid electrical conduction, unpublished general examination paper, M.I.T., 34 pp., 1976.

Willliams, P.L., K.L. Pierce, D.H. McIntyre, and P.W. Schmidt, Preliminary geologic map of the southern Raft River area, Cassia County, Idaho, unpublished geologic map, U.S. Geological Survey, Denver, 1974.

Williams, P.L., D.R. Mabey, A.A.R. Zohdy, H. Ackermann, D.B. Hoover,

K.L. Pierce, and S.S. Oriel, Geology and geophysics of the southern Raft River Valley geothermal area, Idaho, USA, in Proceedings, Second United Nations Symposium on the Development and Use of Geothermal Resources, 2, 1273-1282, 1976.

Wilson, H.D.B. and N.W. Hendry, Geology and quicksilver deposits of Coso hot springs area, (ABS), Bull. Geol. Soc. Am., 51, 1965, 1940.

Wilt, M.J., An electrical survey of the Dunes geothermal anomaly and surrounding region Imperial Valley, California, Masters thesis, University of California at Riverside, 128 pp., 1975.

Zoback, M.D. and J.D. Byerlee, Effect of high-pressure deformation permeability of Ottawa Sand, Amer. Assoc. Pet. Geol. Bull., 60, 1531-1542, 1976.

BIOGRAPHICAL NOTE

Born (but not again) in November 1950, the author spent most of his youth in and around the community of Riverside in southern California. Raised in the orange groves, early employment was in the associated fields of orange grove irrigation and weed control. A dyed-in-the-wool desert rat, he tried to determine if there was a way to make a living by wandering around the boondocks. So, never having been adequately warned, he chose to enter the realm of geoscience. Bachelor of science degrees were obtained in 1973 in geology and geophysics from that noble branch of the University of California at Riverside. Heeding the advice to 'head east, young man' by assorted professorial types around the above-mentioned institution, this young man loaded his life in his Willys pick-up and headed east. Eventually, he encountered the Atlantic by the small, sleepy coastal village of Boston, Massachusetts. There being no immediate openings for orange grove irrigationers, he settled for a position as an overpaid and underworked graduate student at MIT. During his tenure at MIT, the author spent several summers with the U.S. Geological Survey performing assorted geoelectric magic at several geothermal areas in the golden west. The author was also a Chevron Graduate Fellow for one year. More than 0.166 of his entire life was spent in the process of completing his PhD requirements.

Publications:

Batzle, M.L. and G. Simmons, Microfractures in rocks from two geothermal areas, Earth Planet. Sci. Lett., 30, 71-93, 1976.

Batzle, M.L. and G. Simmons, Fracturing and sealing in geothermal

systems, Proceedings Volume, NSF-RANN Geothermal Conference, Golden, Colorado, May 1976, submitted.

Batzle, M.L. and G. Simmons, Geothermal systems: rocks, fluid, fractures, in The Earth's Crust: Its Nature and Physical Properties, Geophys. Monogr. Ser., vol. 20, edited by J.C. Heacock, AGU, Washington, DC, 233-242, 1977.

Batzle, M.L. and G. Simmons, Assessing geothermal areas during drilling, in Geothermal: State of the Art, Geothermal Resources Council, Transactions, 13-15, 1977.

Padovani, E.R., M.L. Batzle, and G. Simmons, Characteristics of microcracks in samples from the drill hole Nördlingen 1973 in the Ries Crater, Germany, (ABS), Lunar Science IX, 847-849, 1978.

Batzle, M.L., S.B. Shirey, and G. Simmons, Correlation of physical properties with microfracture characteristics, (ABS), Geol. Soc. Am., Abstracts with Programs, Rocky Mountain Section, in press, 1978.

Quasi-Publications (U.S.G.S. Open File Reports):

Hoover, D.B., M. Batzle, and R. Rodriguez, Self potential map, Steamboat Hills, Nevada, TRU 75-446, 1975.

Hoover, D.B., J. O'Connell, M. Batzle, and R. Rodriguez, Telluric profiles, Steamboat Hills, Nevada, TRU 75-445, 1975.

Long, C.L. and M.L. Batzle, Station location map and audiomagnetotelluric data log for Monte Neva KGRA, Nevada, Project no. 9730-01714, 1976.

Long, C.L. and M.L. Batzle, Station location map and audiomagnetotelluric data log for Rye Patch KGRA, Nevada, Project no. 9730-

01714, 1976.

Long, C.L. and M.L. Batzle, Station location map and audiomagnetotel-
luric data log for Ruby Valley KGRA, Nevada, Project no. 9730-
01714, 1976.

Hoover, D.B. and M.L. Batzle, Station location map and audiomagnetotel-
luric data log for Pinto Hot Springs KGRA, Nevada, unreleased,
1976.

Batzle, M.L., S.E. Hammond, and V.N. Farkash, Telluric traverse location
map and profiles for Ruby Valley KGRA, Nevada, Project no. 9730-
01714, 1976.

Batzle, M.L., S.E. Hammond, and V.N. Farkash, Telluric traverse location
map and profiles for Pinto Hot Springs KGRA, Nevada, report 76-701A,
1976.

Batzle, M.L., S.E. Hammond, and K.R. Cristopherson, Telluric traverse
location map and profiles for Breitenbush KGRA, Oregon, report
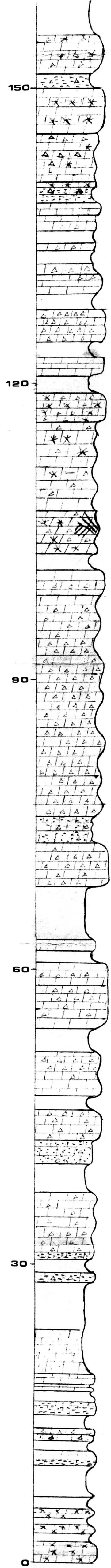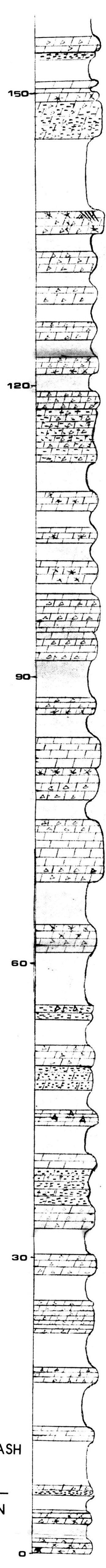76-701D, 1976.

Batzle, M.L., S.E. Hammond, and K.R. Cristopherson, Telluric traverse
location map and profiles for Wendel-Amedee KGRA, California,
report 76-701C, 1976.
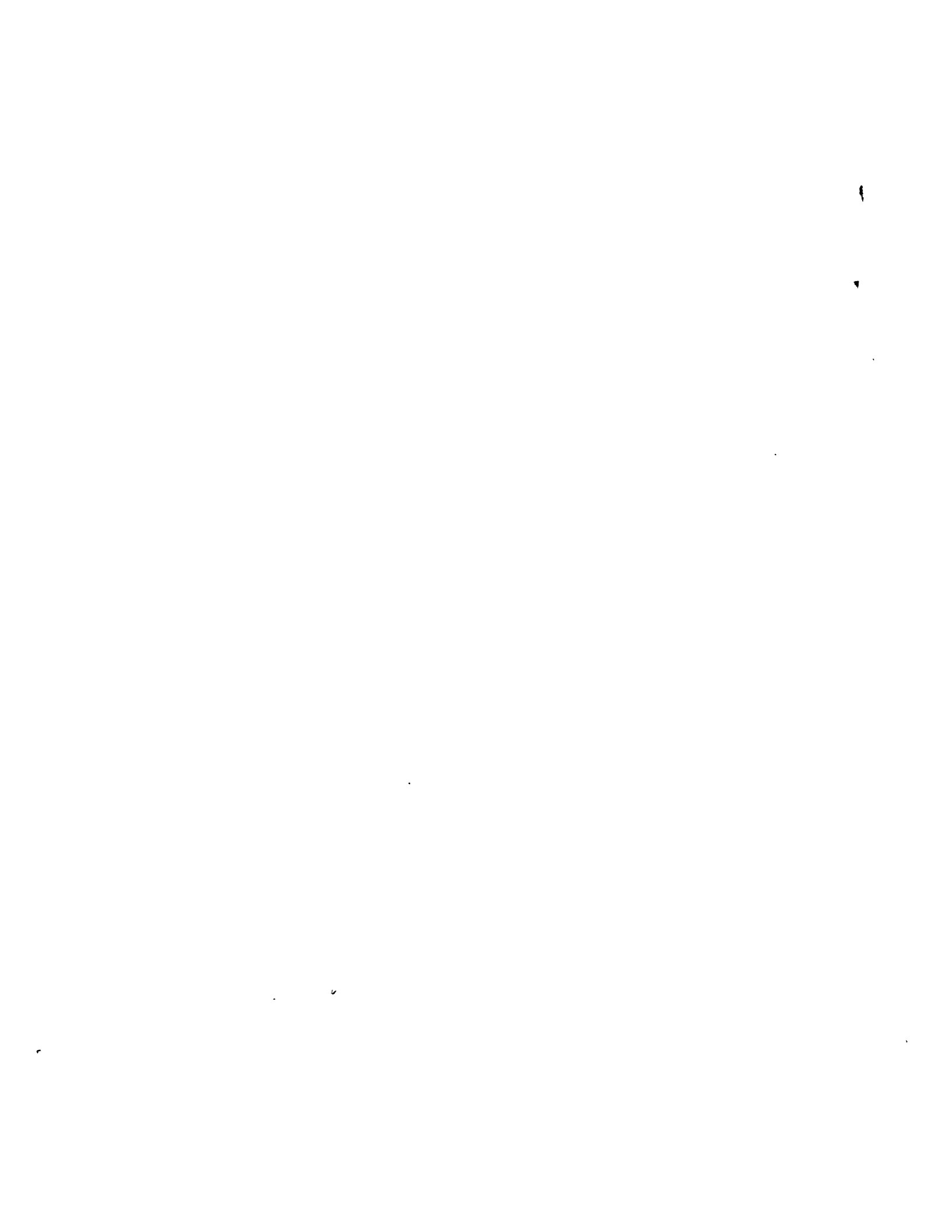
Commerford, J.
Comparative
Stratigraphy...

BIRD SPRING

STRATIGRAPHIC

COLUMNS

METERS

150

120

90

60

30

0

△ CHERT

SILT

✳ FOSSIL HASH

CROSS—
STRATIFI—
CATION

LEE CANYON

150

120

90

60

30

0

PAHRUMP